

**DESIGN OF NOVEL MESOPOROUS NANOCAPSULES AND  
THEIR THERAPEUTIC EFFICIENCIES AS A DRUG  
DELIVERY CARRIER AND TO ENHANCE THE  
IMMUNOLOGICAL RESPONSES**

*Dissertation submitted in partial fulfillment of the requirements for the degree of*

Doctor of Philosophy (Ph.D.)

in

**NANOSCIENCE AND TECHNOLOGY**

By

Himadri Medhi

11ENPT04

Under the guidance of

Dr. PRADIP PAIK

(Associate Professor)



SCHOOL OF ENGINEERING SCIENCES AND TECHNOLOGY

**UNIVERSITY OF HYDERABAD**

HYDERABAD-500046

India

November 2018

## Declaration

I hereby declare that the work reported in this Ph.D. dissertation entitled “**Design of novel mesoporous nanocapsules and their therapeutic efficiencies as drug delivery carrier and to enhance the immunological responses**” submitted to **University of Hyderabad** for the award of Doctor of Philosophy in **Nano Science and Technology** is original and was carried out by me during my tenure as a Ph.D. scholar under the supervision of **Dr. Pradip Paik**, Associate Professor, School of Engineering Sciences and Technology, University of Hyderabad, India. This dissertation has not formed the basis for the award of any degree, diploma, associateship, membership or similar title of any university or institution. Finally, plagiarism of this dissertation has been checked and satisfied the requirements.

Himadri Medhi  
School of Engineering Sciences and Technology  
University of Hyderabad  
Hyderabad 500046, India

Place:

Date:



## Certificate

This is to certify that the dissertation entitled “**Design of novel mesoporous nanocapsules and their therapeutic efficiencies as drug delivery carrier and to enhance the immunological responses**” submitted by **Himadri Medhi**, bearing registration number **11ENPT04** in partial fulfilment of the requirements for the award of **Doctor of Philosophy** in the **School of Engineering Sciences and Technology** is a bonafide work carried out by her under my supervision and guidance.

This dissertation is free from plagiarism and has not been submitted previously in part or in full to this or any other University or Institute for the award of any degree or diploma.

### Outcome of the dissertation

A. Parts of this dissertation have published in the following publications:

1. **Himadri Medhi et al.**, *Nanoscale*, 2017, 9, 14641-14653.
2. **Himadri Medhi et al.**, *Biomedical Physics and Engineering Express (IOP)*, 2018, 4-3.
3. **Himadri Medhi et al.**, Paper to be communicated (Part-III of chapter-3).

B. Parts of this dissertation have presented at the following conferences:

4. **Himadri Medhi et al.**, Presented (Poster) in ACIN 2018, Namur, Belgium.
5. **Himadri Medhi et al.**, presented (Poster) in NanoSciTech-2016, Punjab, India.
6. **Himadri Medhi et al.**, Presented (Poster) in “Advanced Nanomaterials and Nanotechnology”-2015, IITG, Guwahati, Assam, India.
7. **Himadri Medhi et al.**, Presented (Poster) in ICAPM-2013, Kottayam, India.
8. **Himadri Medhi et al.**, Presented (Poster) in IUMRSICA-2013, IISc, Bangalore, India.

The student has passed the Research Methodology course towards the fulfilment of the requirement for Ph.D. work.

Course Code	Name	Credits	Pass/Fail
MT601	Research Methodology	4.00	Pass

Further, the student has passed the following courses towards the fulfilment of coursework requirement for Ph.D.

<b>Course Code</b>	<b>Name</b>	<b>Credits</b>	<b>Pass/Fail</b>
NT401	Thermodynamics and Phase Equilibria	4.00	Pass
NT402	Concepts of Materials Science	4.00	Pass
NT403	Characterization of Materials	4.00	Pass
NT404	Seminar	2.00	Pass
NT405	Advanced Engineering Mathematics	2.00	Pass
NT406	Materials Processing & Characterization Lab	4.00	Pass
NT407	Concepts of Nano Science and Technology	4.00	Pass
NT408	Synthesis and Applications of Nanomaterials	4.00	Pass
NT451	NanoBiotechnology	4.00	Pass
NT452	Mechanical Behaviour of Nanomaterials	4.00	Pass
NT453	Modelling and Simulation	4.00	Pass
NT454	MEMS and NEMS Nanofabrication Tech	4.00	Pass
NT455	Surface Engineering	4.00	Pass
NT456	Polymer Science and Technology	2.00	Pass
NT457	Laboratory	4.00	Pass
NT458	Seminar	2.00	Pass
NT550	Dissertation	18.00	Pass

**Supervisor**

**(Dr. Pradip Paik)**

**DEAN**

**(School of Engineering Sciences and Technology)**

## Acknowledgements

I am using this opportunity to express my deepest gratitude to the people with whom I become associated with during my Ph. D. tenure and received advice, support, encouragement and finally able to accomplish my Ph.D. work with the doctoral dissertation.

I consider myself fortunate enough as I was provided with an opportunity to pursue my doctoral research work under the guidance of Dr. Pradip Paik, who himself is a very hard working person with lots of energy and a big deal of knowledge in almost all topics of science. Dr. Pradip Paik had included few new topics in my research which I have never contemplate to work on and used to be a source of encouragement and always enthusiastic towards my work. The most important things I have learned from him to do hard work, writing research papers and presentation skills and to be patience for good results as everyday can't be a good day in research.

I am deeply indebted to my doctoral review committee members Dr. Swati Ghosh Acharyya (SEST) and Dr. Mrinal K Bhattacharyya (SLS, UoH) for their guidance, support and help during my Ph.D. years. I am thankful to Dean of School of Engineering Sciences and Technology (SEST) Prof. M. Ghanashyam Krishna and all faculties in the department for providing me the facilities and the advice for the completion my research work.

Completion of my biological collaboration research works were possible due to the help and support of School of Life Sciences faculties Dr. Mrinal K Bhattacharyya, Dr. Nooruddin Khan and Dr. Brahmanandam Manavathi. Therefore, I would like to express my humble thank to them along with their students who helped me to carry out my biological application work.

I would also like to thank the technicians and non-teaching staff of SEST Mr. Mallesh, Mr. Balakishan, Mrs. Kranthi, Mrs. Malathi and Mr. S. Venu as well as TEM technicians Mr. Durga Prasad and Mr. Pankaj.

A positive work environment is unavoidable for a fruitful research and I am thankful to Dr. Pradip Paik's research group and my labmates Dr. Koushi Kumar, Dr. Santosh Kumar, Dr. Chander A, Debasrita, Somedutta, Monica, Monami and Anil for cooperation and help during my Ph. D. years. It was great sharing the Lab with you all during these years.

Friends make the things go easy. I am glad I have few friends who constantly encouraged, supported, helped and advised me during all these years and I am taking this opportunity to thank Naveen, Bikash, Nilam, Vikholienuo, Wabangienla and Gayatri. I want to express my special thanks to my friend Praxanta who unfortunately left us last year and went to eternity but his encouragement will always remain with me.

I express my deepest gratitude to my dear friends Dr. Daniel Yeggoni and Dr. Pangkita Deka for their precious advices, support, appreciation and trust on me to achieve my goal.

My family is the persistent source of moral and emotional support for me and I want to acknowledge them for believing me and my choice of this career. I would like to express my deepest gratitude to my parents Mr. Dwijendra kumar Medhi and Mrs. Amala Medhi, my sisters Dr. Mithu Medhi and Mrs. Rituparna Medhi, my brother in laws Dr. Pranjal Sonowal and Mr. Anupam Barua for their constant encouragement throughout my life.

Himadri

# Contents

<b>SI No.</b>	<b>Title</b>	<b>Page No.</b>
I	Contents	<i>i</i>
II	List of Figures	<i>vii</i>
III	List of Tables	<i>xiii</i>
IV	Abbreviations	<i>xiv</i>
V	List of Publications	<i>xvi</i>
VI	Abstract	<i>xvii</i>

## **Chapter 1: Introduction and Literature Review**

- 1.1. Introduction** 2
- 1.2. Nanomaterials 3
  - (A) Inorganic nanomaterials 3
  - (B) Organic nanomaterials 3
- 1.3. Drug delivery system 4
- 1.4. Mesoporous nanocapsules for drug delivery applications 10
- 1.5. Inorganic metal oxide Zinc Oxide (ZnO) 11
- 1.6. Polymer Polycaprolactone (PCL) 12
- 1.7. Brief introduction of the drugs/protein used 13
  - (A) Chloroquine diphosphate salt (CQDP) 13
  - (B) Dihydroartemisinin (DHA) 13
  - (C) Sulfadoxine (SD) 14
  - (D) Ovalbumin (Ova) 15
  - (E) Paclitaxel (Ptaxel) 15
- 1.8. Brief introduction of the cell line used 16
  - (A) *Plasmodium falciparum* (*P. falciparum*) 16
  - (B) MCF7 (Michigan Cancer Foundation 7) 17
  - (C) MDA-MB-231 18

- 1.9. Immunology 18
- 2. Literature Review 20**
- 2.1. Malaria parasite *P. falciparum* resistivity towards antimalarial drugs 20
- 2.2. Nano drug carriers for suppressing malaria infection 22
- 2.3. Nanotechnology in immunology 25
- 2.4. Ova protein in immunology 27
- 2.5. Nano carriers against cancer therapy 30
- 2.6. Paclitaxel drug loaded nanocarriers against cancer therapy 32
- 2.7 The motivation behind this work 36**
- 2.8 Objectives of this dissertation 38**

## **Chapter 2: Materials and methods: Experimental procedures and Characterization techniques**

- 2.1. Introduction 40
- 2.2. Materials and reagents used for experiments 41
- 2.3. Experimental procedure 42
  - 2.3.1. Synthesis procedures 42
    - (A) Synthesis of hollow porous PCL NCs 42
      - (i) Loading of Rh6G, DHA, CQDP and SD in hollow mesoporous PCL NCs and corresponding release study 43
    - (B) Synthesis of mesoporous ZnO NCs 44
      - (i) Loading of Ova protein in mesoporous ZnO NCs and corresponding release kinetics 44
      - (ii) Loading of dye, antimalarial drugs and anticancer drugs in mZnO NCs and corresponding release study 44
    - (C) Synthesis of porous PCL NCs 45
      - (i) Loading of anticancer drug Paclitaxel in mesoporous PCL NCs and corresponding drug release profile 46
- 2.4. Characterization Techniques 46
  - 2.4.1. X-Ray Diffraction (XRD) 46
  - 2.4.2. Electron microscopic imaging techniques (SEM, FESEM and TEM) 47
  - 2.4.3. Energy dispersive X-ray spectroscopy (EDS or EDX) 50
  - 2.4.4. Thermogravimetric analysis (TGA) 51

- 2.4.5. Differential Scanning Calorimetry (DSC) 52
- 2.4.6. Brunauer-Emmet-Teller (BET) 52
- 2.4.7. Fourier Transform Infrared (FTIR) spectroscopy 54
- 2.4.8. Zeta potential analysis 55
- 2.4.9. Confocal microscopy 56
- 2.4.10. Ultraviolet-Visible spectroscopy (UV-Vis) 57
- 2.4.11. Fluorescence activated cell sorting (FACS) analysis 58
- 2.4.12. Multimode microplate reader 58

### **Chapter 3: Result and discussion Part I (section A)**

#### **Synthesis of SiO<sub>2</sub> templated mesoporous PCL NCs and loaded with various antimalarial drugs (CQDP and DHA) for suppressing malaria.**

- 3.1A.1. Introduction 62
- 3.1A.2. Synthesis procedure 63
  - (a) Synthesis of template SiO<sub>2</sub> NPs 63
  - (b) Synthesis of solid core shell polymer NPs 64
  - (c) Formation of hollow porous PCL capsules 64
- 3.1A.3. Synthesis mechanism of hollow mesoporous PCL capsules 64
- 3.1A.4. Loading of Rh6G, DHA and CQDP in hollow mesoporous PCL capsules 66
- 3.1A.5. Effect of drug loaded NCs with *P. falciparum* cell line 67
- 3.1A.6. Designing hollow mesoporous PCL capsules: Size, Morphology and porous structure of NCs 68
- 3.1A.7. BET surface area analysis 70
- 3.1A.8. Surface chemical structure of hollow mesoporous PCL capsules 71
- 3.1A.9. Thermal stability, solid state crystal structure study and zeta potential analysis 73
- 3.1A.10. Cell viability analysis of bare hollow mesoporous PCL capsules with *P. falciparum* culture medium 76
- 3.1A.11. *P. falciparum* inhibition with PCL-DHA and PCL-CQDP formulation 77
- 3.1A.12. Hollow mesoporous PCL capsules facilitate releasing of DHA and CQDP in the medium 79
- 3.1A.13. Release kinetics and diffusion coefficients of PCL-DHA and PCL-CQDP nanoformulations 81

3.1A.14. PCL-DHA and PCL-CQDP formulation actively inhibit *P. falciparum* 86

3.1A.15. Summary of Part I (Section A) 87

### **Chapter 3: Result and discussion Part I (Section B)**

#### **Efficiency of hollow mesoporous PCL NCs loaded with antimalarial drug Sulfadoxine against *P. falciparum* cell line**

3.1B.1. Introduction 91

3.1B.2. Loading of Sulfadoxine in hollow mesoporous PCL capsules 91

3.1B.3. Cell inhibition study of hollow mesoporous PCL capsules loading with Sulfadoxine 92

3.1B.4. Hollow mesoporous PCL capsules facilitate releasing of SD in the culture media RPMI 1640 93

3.1B.5. Release kinetics and diffusion coefficients of SD from PCL-SD nanoformulations 94

3.1B.6. Summary of Part I (Section B) 96

### **Chapter 3: Result and discussion Part II (Section A)**

#### **Designing of mesoporous ZnO NCs incorporated with protein for the enhancement of immune responses**

3.2A.1. Introduction 98

3.2A.2. Synthesis procedure mesoporous ZnO NCs 99

3.2A.3. Synthesis mechanism of mesoporous ZnO NCs 99

3.2A.4. Designing hollow mesoporous PCL capsules: Size, Morphology and porous structure of NCs 101

3.2A.5. BET surface area analysis 103

3.2A.6. Surface chemical structure analysis of mZnO NCs 104

3.2A.7. Phase, solid state crystal structure study and zeta potential analysis 104

3.2A.8. Photoluminescence analysis, UV absorbance, optical band gap and Raman analysis 107

3.2A.9. Loading of OVA protein in mZnO NCs 109

3.2A.10. Entrapment efficiency and release of mZnO NCs 110

3.2A.11. Study of OVA release kinetics from mZnO NCs 111

- 3.2A.12. Immunization of mice with mZnO-Ova to analyze Immune responses *112*
- 3.2A.13. Splenocytes and PBMC isolation from immunized mice *113*
- 3.2A.14. Lymph node isolation *114*
- 3.2A.15. Nanoformulation of mZnO-Ova elicit enhanced antigen-specific T cell responses upon immunization in mice *114*
- 3.2A.16. mZnO-Ova nanoformulation elicit enhanced antigen-specific CD8<sup>+</sup> and CD4<sup>+</sup> T-cell effector responses without a booster *115*
- 3.2A.17. mZnO-Ova nanoformulation elicit enhanced antigen-specific CD8<sup>+</sup> and CD4<sup>+</sup> T-cell effector responses with a booster *117*
- 3.2A.18. Ova loaded mZnO NCs trigger amplified antigen specific antibody responses *118*
- 3.2A.19. Summary of Part II (Section A) *120*

### **Chapter 3: Result and discussion PART II (Section B)**

#### **Mesoporous ZnO NPs incorporated with different drugs for cancer therapy**

- 3.2B.1. Introduction *123*
- 3.2B.2. Loading of dye, antimalarial drugs and anticancer drugs in mZnO NCs *124*
- 3.2B.3. Biocompatibility of mZnO studied with two breast cancer cell lines *124*
- 3.2B.4. Time dependent release profile of Rh6G from nanoformulation mZnO-Rh6G *128*
- 3.2B.5. Time and temperature dependent drug release profiles of antimalarial drugs from mZnO NCs *129*
- 3.2B.6. Time dependent drug release profile of anticancer drug from the nanoformulation of mZnO- Paclitaxel NCs *132*
- 3.2B.7. Ultramicrotome HRTEM analysis of antimalarial and anticancer drugs loaded mZnO NCs interaction with cancer cell line K562 *133*
- 3.2B.8. Summary of Part II (Section B) *136*

### **Chapter 3: Result and discussion Part III**

#### **Synthesis of porous PCL nanocapsules by template removing approach to eradicate Breast Cancer cells**

- 3.3.1. Introduction *139*

- 3.3.3. Synthesis procedure *140*
  - (a) The synthesis method of mesoporous ZnO NCs *140*
  - (b) Synthesis of core shell NCs *141*
  - (c) Etching of core from core shell NCs *141*
- 3.3.3. Mechanism of formation of porous PCL NCs *141*
- 3.3.4. Designing mesoporous PCL NCs: Size, Morphology and porous structure of NCs *143*
- 3.3.5. Surface chemical structure of PCL-mZnO and hollow mesoporous PCL NCs *145*
- 3.3.6. BET surface area analysis of porous PCL NCs *146*
- 3.3.7. Phase, solid state crystal structure study and zeta potential analysis *147*
- 3.3.8. Loading of anticancer drug Paclitaxel in mesoporous PCL NCs *149*
- 3.3.9. Time dependent drug release behavior of anticancer drug from core shell PCL-mZnO (PZ) and porous PCL (HPZ) NCs. *149*
- 3.3.10. Biocompatibility of core shell PCL-mZnO (PZ) studied with two breast cancer cell lines *150*
- 3.3.11. Biocompatibility of mesoporous PCL (HPZ) NCs studied with two breast cancer cell lines *153*
- 3.3.12. Interaction of Paclitaxel with Cancer cell lines MCF 7 and MDA-MB-231 *156*
- 3.3.13. Interaction of Paclitaxel loaded HPZ with Cancer cell lines MCF 7 and MDA-MB-231 *158*
- 3.3.14. Summary and Conclusions of Part III *162*

## **Chapter 4: Summary and Conclusions**

- 4.1. Summary and conclusion *164*

## **References *165***

# List of Figures

## Chapter 1: Introduction and Literature Review

Schematic 1.1. Schematic diagram of the life cycles of *P. falciparum* with different stages.

Figure 1.1. Schematic representation of the fields involved in the current dissertation work.

Figure 1.2. Comparison of three drug delivery mechanisms.

Figure 1.3 A schematic representation of the *Liposome* with different therapeutic agents inside its aqueous core as well as on its hydrophilic surface.

Figure 1.4. Schematic representation of functional block copolymers *Micelles*.

Figure 1.5 A schematic representation of *Dendrimer* for therapeutic application.

Figure 1.6 A schematic representation of *Hydrogel* with decreasing size and porous structure.

Figure 1.7 A schematic representation of multifunctional polymer encapsulated *Quantum dot* and PEG functionalized gold *Nanorod* for platinum delivery.

Figure 1.8 A schematic representation of drug interaction with *Nanosphere* and NC for drug delivery system.

Figure 1.9 Chemical structure of Polycaprolactone.

Figure 1.10 Chemical structure of Chloroquine diphosphate salt (CQDP).

Figure 1.11. Chemical structure of *Dihydroartemisinin (DHA)*.

Figure 1.12. Chemical structure of *Sulfadoxine (SD)*.

Figure 1.13 Chemical Structure of Paclitaxel (Ptaxel).

Figure 1.14. Nanotechnology applied in immunology (a-c) NPs (d-f) nanoemulsions and (g and h) virus-like particles.

Figure 1.15. Metal NPs interaction in Immune system.

## Chapter 3: Result and discussion Part I (section A)

Schematic 3.1.1. Step by step synthesis mechanism of core shell PCL-SiO<sub>2</sub> NPs and hollow mesoporous PCL capsules after removal of template SiO<sub>2</sub>.

Schematic 3.1.2. a) Life-cycle of *P. falciparum*, (b) early Trophozoite stage of *P. falciparum* at which stage PCL-DHA/PCL-CQDP nanoformulations added for treatment and (c) schematic of different steps of making nanoformulations and treatment.

Schematic 3.1.3. (a and b) Representative schematic showing with a change in body temperature how the DHA/CQDP release happened with “on” and “off” mode from the PCL-

DHA and PCL-CQDP nanoformulations, and (c) a proposed “*temperature clock*” showing the different extent of release with temperature.

Figure 3.1.1. Chemical structural representation of SiO<sub>2</sub> surrounded by PCL forming core shell structure.

Figure 3.1.2. TEM image of (a) SiO<sub>2</sub> NPs-1 (10-15nm), FESEM images of (b) SiO<sub>2</sub> NPs-2 with (c) corresponding particle size distribution (455 nm) and (d) core shell PCL-SiO<sub>2</sub> NPs with (e) corresponding particle size distribution (510 nm), TEM images of (f) PCL-SiO<sub>2</sub> NPs and (g) single core shell PCL-SiO<sub>2</sub> NP.

Figure 3.1.3. (a) and (b) FESEM images of mesoporous PCL at low and high magnification, respectively, (c) and (d) confocal microscopy images of mesoporous PCL loaded with Rhodamine 6G at lower and higher magnification, respectively.

Figure 3.1.4. BET results (a) BJH adsorption-desorption isotherm and (b) pore size distribution of mesoporous PCL capsules, respectively. (c) and (d) BJH adsorption-desorption isotherm and pore size distribution of DHA loaded capsules, respectively.

Figure 3.1.5. FTIR results for (a) SiO<sub>2</sub> NPs, (b) PCL- SiO<sub>2</sub> NPs and (c) hollow porous PCL capsules.

Figure 3.1.6. FTIR spectrum of pure PCL polymer (commercial) with all characteristic bands.

Figure 3.1.7. (a) TGA for SiO<sub>2</sub>NPs, pure PCL (commercial), PCL- SiO<sub>2</sub> NPs and hollow porous PCL capsules and (b) DTGA for the same, respectively.

Figure 3.1.8. XRD for (a) SiO<sub>2</sub> NPs, (b)core shell PCL-SiO<sub>2</sub> NPs, (c)hollow porous PCL capsules and for (d) pure PCL (commercial).

Figure 3.1.9. DSC for (a) SiO<sub>2</sub> NPs, (b) PCL- SiO<sub>2</sub> NPs and (c) hollow porous PCL capsules.

Figure 3.1.10. Zeta potential analysis of hollow porous PCL capsules.

Figure 3.1.11. Cell viability of porous PCL capsules (bear) with different concentrations of capsules in *P. falciparum* cells.

Figure 3.1.12. Cell inhibition by PCL-DHA nanoformulation while treated with *P. falciparum* infected cells by maintaining lower to higher concentrations of drug DHA (2 nM to 1000 nM) at 37°C after 48h of incubation.

Figure 3.1.13. Cell inhibition by PCL-CQDP nanoformulation while treated with *P. falciparum* infected cells by maintaining lower to higher concentrations of drug CQDP (100 to 500 µg/mL) at 37°C after 48h of incubation.

Figure 3.1.14. The release profile of (a) DHA from PCL-DHA and (b) CQDP from PCL-CQDP nanoformulations at different temperatures, respectively.

Figure 3.1.15. The release profile of DHA drugs from PCL-DHA nanoformulation at room temperature for 30 days.

Figure 3.1.16. First order release kinetics at 30°C and 37°C for PCL-DHA nanoformulation.

Figure 3.1.17. Zero order release kinetics at 40°C and 43°C for PCL-DHA nanoformulation.

Figure 3.1.18. First order release kinetics at all 4 temperatures for PCL-CQDP nanoformulation.

Figure 3.1.19. Anti-malarial activity of (a) PCL-DHA nanoformulation and (b) PCL-CQDP nanoformulation in a dose dependent manner.

### **Chapter 3: Result and discussion Part I (Section B)**

Figure 3.1.20. Cell inhibition by PCL-SD nanoformulation while treated with *P. falciparum* infected cells by maintaining lower to higher concentrations of sulfadoxine at 37°C after incubating for 48h.

Figure 3.1.21. Drug release profile of SD drug from PCL-SD nanoformulation at room temperature for a period of one month.

Figure 3.1.22. First order release kinetics of SD from PCL-SD nanoformulations maintain experiment condition at room temperature (25°C) for the duration of 30days.

### **Chapter 3: Result and discussion Part II (Section A)**

Scheme 3.2.1. Schematic illustration of mesoporous ZnO formation mechanism.

Scheme 3.2.2. Ova loading mechanism in mZnO NCs.

Figure 3.2.1. HRTEM micrographs of (a), (b) mZnO NCs and (c), (d) showed high magnification HRTEM images of a single mZnO NCs with distinct pores present inside.

Figure 3.2.2. Histogram for the average particle size distribution of mZnO NPs calculated from HRTEM micrograph (Figure 1a).

Figure 3.2.3. HRTEM micrographs of (a) SAED pattern of mZnO NCs and (b) lattice d-spacing(c) which counted as 0.35nm from the TEM histogram.

Figure 3.2.4. BET results (a) N<sub>2</sub> absorption-desorption isotherm of mZnO NCs with (b) BJH pore size distribution from an adsorption isotherm.

Figure 3.2.5. FTIR spectrum of mZnO NCs.

Figure 3.2.6. XRD powder diffraction pattern of mesoporous ZnO NCs.

Figure 3.2.7. Zeta potential results of mZnO NC recorded at 25°C in DI water.

Figure 3.2.8. Zeta potential of nanoformulation of mZnO-Ova recorded at 25°C in DI water.

Figure 3.2.9. UV-Vis absorbance spectrum of mZnO NCs recorded at 25°C in PBS (~7.2 pH).

Figure 3.2.10. Tauc plot for the optical band gap measurement of mZnO NCs drawn from the UV-Vis absorbance spectrum of mZnO NCs (Figure 3.2.9).

Figure 3.2.11. PL spectra of unloaded (bare) mZnO and mZnO-Ova NCs.

Figure 3.2.12. Raman spectrum for mZnO NCs at room temperature on the powdered sample.

Figure 3.2.13. UV spectrum of time dependent OVA release from mesoporous ZnO-Ova NCs at 37°C for 3days in media in RPMI 1640 medium.

Figure 3.2.14. mZnO-Ova induce efficient antigen specific T-cells.

Figure 3.2.15. Nanoformulation of mZnO-Ova elicit enhanced antigen-specific CD8<sup>+</sup> and CD4<sup>+</sup> T-cell effector responses.

Figure 3.2.16. mZnO-Ova nanoformulations trigger synergistic enhancement of antigen-specific IFN- $\gamma$  producing CD8<sup>+</sup> and CD4<sup>+</sup> effector T-cells upon secondary immunization.

Figure 3.2.17. mZnO-Ova NCs elicit amplified antigen specific antibody responses.

### **Chapter 3: Result and discussion Part II (Section B)**

Figure 3.2.18. Percentage of cell survival analyzed by MTT assay while mZnO NCs were incubated with MCF7 cell line at 37°C for 24h.

Figure 3.2.19. Percentage of cell survival analysed by MTT assay while mZnO NCs were incubated with MDA-MB-231 cell line at 37°C for 24h.

Figure 3.2.20. Microscopic images of the MDA-MB-231 cancer cells after incubation with increasing concentration of mZnO at 37°C for 24h.

Figure 3.2.21. Dye release profile of Rh6G from mZnO NCs at 25°C temperatures for 7h in PBS medium (pH 7.2).

Figure 3.2.22. Temperature and time dependent drug release profile of CQDP loaded in nanoformulation mZnO-CQDP at 30°C, 35°C, 37°C, 40°C temperatures for 8h in RPMI 1640 medium.

Figure 3.2.23. Drug release profile of DHA loaded in the nanoformulation of mZnO-DHA at 37°C for 30days in PBS medium (pH 7.2).

Figure 3.2.24. Drug release profile of Sulfadoxine loaded in the nanoformulation of mZnO-Sul at 37°C for 30days in PBS medium (pH 7.2).

Figure 3.2.25. Drug release profile of Paclitaxel loaded in the nanoformulation of mZnO-ptaxol at 37°C for 30days in PBS medium (pH 7.2).

Figure 3.2.26. Cell sectioning HRTEM images of pure cancer cell line K562 (a-d) from lower to higher magnification. (c) and (d) showing single cells with all distinct cell components.

Figure 3.2.27. Cell sectioning images of bare mZnO NCs dispersed in PBS (pH 7.2) treated with K562 cell lines at 37°C from (a-d) lower to higher magnifications. (c) and (d) showing the single cell deformed after interaction with mZnO NCs.

Figure 3.2.28. Cell sectioning HRTEM images of mZnO –CQDP nanoformulations dispersed in PBS (pH 7.2) treated with K562 cells at 37°C from (a-d) from lower to higher magnifications. (c) and (d) showing the single cell deformation after interaction with mZnO-CQDP nanoformulation.

Figure 3.2.29. Cell sectioning HRTEM images of mZnO-DOX nanoformulations dispersed in PBS (pH 7.2) treated with K562 cells at 37°C (a-d) from lower to higher magnifications. (c) and (d) showing cell membrane deformation after interaction with mZnO-DOX nanoformulation.

### **Chapter 3: Result and discussion Part III**

Schematic 3.3.1. Step by step synthesis mechanism of core shells PCL-mZnO NPs and mesoporous PCL NCs after removal of core mZnO NPs.

Figure 3.3.1. TEM images of core shell PCL- mZnO NPs (PZ) from lower to higher magnifications (a-d).

Figure 3.3.2. Histogram for the average particle size distribution of core shell PCL-mZnO NPs (PZ), calculated from HRTEM results (Figure 3.3.1a).

Figure 3.3.3. TEM images of hollow porous PCL NCs (HPZ) (a-d) from lower to higher magnifications and (e) average particle size distribution of HPZ calculated from the TEM micrograph (Figure 3.3.3a).

Figure 3.3.4. FTIR spectra of (a) PCL-mZnO core shell (PZ) NPs and (b) porous PCL (HPZ) NCs. FTIR experiments were performed on KBr pallet.

Figure 3.3.5. BET results (a) N<sub>2</sub> absorption-desorption isotherm of porous PCL NCs with (b) BJH pore size distribution from adsorption isotherm.

Figure 3.3.6. XRD powder diffraction pattern of mZnO, PCL-mZnO (PZ) and porous PCL NCs.

Figure 3.3.7. Zeta potential of mesoporous PCL NC recorded at 25°C in DI water.

Figure 3.3.8. The release profile of Paclitaxel from PCL-mZnO (PZ) and mesoporous PCL NCs at 25°C temperatures for 72h in RPMI 1640 medium.

Figure 3.3.9. Percentage of cell survival analyzed by MTT assay while PCL-mZnO (PZ) NCs were incubated with MCF7 cell line at 37°C for 24h. For this experiment calculated IC<sub>50</sub> value is 35.49 (±0.25)nM.

Figure 3.3.10. Percentage of cell survival analyzed by MTT assay while PCL-mZnO (PZ) NCs were incubated with MDA-MB-231 cell line at 37°C for 24h. For this experiment calculated IC<sub>50</sub> value is 32.8 (±0.29)nM.

Figure 3.3.11. Microscopic images of the MDA-MB-231 cancer cells after incubation with increasing concentration of PZ at 37°C for 24h.

Figure 3.3.12. Percentage of cell survival analyzed by MTT assay while mesoporous PCL NCs were incubated with MCF7 cell line at 37°C for 24h. For this experiment calculated IC<sub>50</sub> value is 52(±1.0)nM.

Figure 3.3.13. Percentage of cell survival analysed by MTT assay while mesoporous PCL NCs (HPZ) were incubated with MDA-MB-231 cell line at 37°C for 24h. For this experiment calculated IC<sub>50</sub> value is 55 (±1.05)nM.

Figure 3.3.14. Microscopic images of the MDA-MB-231 cancer cells after incubation with increasing concentration of HPZ at 37°C for 24h.

Figure 3.3.15. Percentage cell survival of MCF 7 while incubated with pure Paclitaxel drug for 24h at 37° C. For this experiment calculated IC<sub>50</sub> value is 31.9 (±1.3)nM.

Figure 3.3.16. Percentage of cell survival of MDA-MB-231 while incubated with pure Paclitaxel drug for 24h at 37°C. For this experiment calculated IC<sub>50</sub> value is 37.52(±1.8) nM.

Figure 3.3.17. Optical microscopic images of MDA-MB-231 cancer cells at different concentrations (1.95-250 µg.mL<sup>-1</sup>) of Paclitaxel.

Figure 3.3.18. Percentage of cell survival analyzed by MTT assay while HPZ-Paclitaxel nanoformulation incubated with MCF 7 cell lines at 37°C for 24h. The IC<sub>50</sub> value is found in this case as 33.9(± 1.5)nM.

Figure 3.3.19. Percentage of cell survival analyzed by MTT assay while HPZ- Paclitaxel nanoformulations were incubated with MDA-MB-231 cell line at 37°C for 24h. The IC<sub>50</sub> value is found in this case as 45.62(±1.86)

Figure 3.3.20. Microscopic images of the MDA-MB-231 cancer cells after incubation with increasing concentration of HPZ at 37°C for 24h.

# List of Tables

## **Chapter 1: Introduction and Literature Review**

Table 1. Nanodrug carriers against Malaria infection.

Table 2. Ova protein incorporation with NPs in immunology.

Table 3. Paclitaxel encapsulated nanodrug carrier for cancer therapy.

## **Chapter 2: Materials and methods: Experimental procedures and Characterization techniques**

Table 1. List of chemicals, solvents and reagents used for nanomaterial synthesis.

## **Chapter 3: Result and discussion Part I (section A)**

Table 1: Zeta potential results of hollow porous PCL capsules

Table 2: Diffusion coefficient ( $D_T$ ) of PCL-DHA nanoformulation with a range of time and temperature.

Table 3: Diffusion coefficient ( $D_T$ ) of PCL-CQDP nanoformulation with a range of time and temperature.

## **Chapter 3: Result and discussion Part I (Section B)**

Table 4: Diffusion coefficient ( $D_T$ ) of PCL-SD nanoformulation with a range of time.

## **Chapter 3: Result and discussion Part II (Section A)**

Table 1: Zeta potential results of mZnO NCs.

Table 2: Zeta potential of nanoformulation of mZnO-OVA.

## **Chapter 3: Result and discussion Part III**

Table 1: Zeta potential of mesoporous PCL NCs.

## List of Abbreviations

nm	= nanometer ( $10^{-9}$ m)
$\mu\text{m}$	= micrometer ( $10^{-6}$ m)
mm	= millimetre
NP	= nanoparticle
MNP	= metal nanoparticle
NC	= Nanocapsule
FDA	= Food and drug administration
Rh6G	= Rhodamine 6G
Ova	= Ovalbumin
CQDP	= Chloroquine diphosphate salt
<i>DHA</i>	= Dihydroartemisinin
SD	= Sulfadoxine
PEG	= Polyethylene glycol
PLGA	= poly(D,L-lactic-co-glycolic acid)
PLA	= poly(D,L-lactide)
PCL	= Poly- $\epsilon$ -caprolactone
MCF7	= Michigan Cancer Foundation 7
K562	= Myelogenous Leukemia Cell Line
TLR	= Toll like receptor
XRD	= X-ray diffraction
SEM	= Scanning electron microscopy
FESEM	= Field emission electron microscopy
TEM	= Transmission electron microscopy
TGA	= Thermogravimetric analysis
DSC	= Differential scanning calorimetry
EDS or EDX	= Energy dispersive X-ray spectroscopy
BET	= Brunauer-Emmet-Teller

BJH = Barret-Joyner-Halenda

FTIR = Fourier Transform Infrared

PL = Photoluminescence

UV-Vis = Ultraviolet-Visible spectroscopy

dH<sub>2</sub>O = deionized water

# List of publications/ Conferences

## Publications/ Manuscripts

- ❖ Sumbul Afroz\*, **Himadri Medhi\***, Somedutta Maity, Gillipsie Minhas, Srikanth Battua, Jeevan Giddaluru, Koushi Kumar, Pradip Paik and Nooruddin Khan, Mesoporous ZnO nanocapsules for the induction of enhanced antigen-specific immunological response.  
\* **These authors contributed equally to this work**, *Nanoscale*, 2017, **9**, 14641-14653.
- ❖ **Himadri Medhi**, Mrinal K. Bhattacharyya, Pradip Paik, Hollow mesoporous polymer capsules with Dihydroartemisinin and Chloroquine diphosphate for knocking down Plasmodium falciparum infection, *Biomedical Physics and Engineering Express (IOP)*, 2018, 4-3.
- ❖ Vijay Bhooshon Kumar, **Himadri Medhi**, Zhang Yong, Pradip Paik, Designing idiosyncratic hmPCL-siRNA Nanoformulated Capsules for Silencing and Cancer Therapy, *Nanomedicine: Nanotechnology, Biology and Medicine*, 12(2016) 579-588.
- ❖ Santhosh Kumar K, **Himadri Medhi**, Dhiman Banik, M. B Suresh, Pramod Borse, Pradip Paik, Novel mesoporous SiO<sub>2</sub> conjugated Graphene Oxide 2D layers: Frequency and temperature dependent dielectric properties, *Materials Chemistry and Physics* (Submitted).
- ❖ **Himadri Medhi**, Pradip Paik, Polymer based drug delivery vehicle encapsulating Paclitaxel against Brest Cancer therapy. (Manuscript under preparation).

## Conferences

1. Poster presentation in international conferences of Advanced Nanomaterials and Nanotechnology-2015, IITG entitled “Mesoporous nanocapsules for suppressing the activity of Malaria *P. falciparum* ” **Himadri Medhi**, S. Chalapareddy, M. K. Bhattacharyya, P. Paik
2. Poster presentation in international conferences *NanoSciTech-2016*-Panjab University entitled “Mesoporous polymer capsules for preventing activity of Malaria *P. falciparum*”. **Himadri Medhi**, S. Chalapareddy, M. K. Bhattacharyya, P. Paik.
3. Poster presented entitled “Surface Functionalized Porous Polymer Nanocapsules for Drug Delivery Applications” **Himadri Medhi**, Chandar A, Koushi Kumar, Pradip Paik in International Conference on Advanced Polymeric Materials (ICAPM-2013), at Mahatma Gandhi University, Kottayam.
4. Poster presented entitled “Porous Surface Functionalized Nanocapsules for Drug Delivery” **Himadri Medhi**, Chandar A, Koushi Kumar, Pradip Paik in International Union of Materials Research Society-International Conference in Asia (IUMRSICA-2013), at Indian Institute of Science, Bangalore.
5. Poster presented entitled “Designing of mesoporous ZnO nanocarrier for the improvement of the induction of enhanced antigen-specific immunological responses” **Himadri Medhi**, Somedutta Maity, Nooruddin Khan and Pradip Paik in Fourth International Conference on Advanced Complex Inorganic Nanomaterials (ACIN 2018) Namur, Belgium.

## Abstract

With passing time medical field has been improving rapidly, because of incessant new inventions by researches in this particular field. Presently, nanotechnology has strengthened its root in all trajectory of the biomedical field with a focused persistence for human healthcare and together it can be termed as nanobiotechnology. Consequently, it has shown potential in drug formation, preventing and curing any disease, cancer therapy, drug delivery system, tissue engineering, MRI contrast agent and many more. Biocompatible and biodegradable nanomaterials play a noteworthy part in this trait. Currently, porous nanomaterials have enlightened the tremendous possibilities in the applied field of biotechnology by offering void space to encapsulate or entrapped particles in it like a nanocargo followed by delivery those encapsulated particles in the site of interest by a sustained controlled release and after unloading that nanocargo in physiological condition without leaving any side effects. Encapsulated particles can be drugs, biomolecules, gene, protein and a range of therapeutics. From a healthcare point of view, these nanomaterials with characteristic porous structures can decrease the doses of drugs thereby reducing toxicity occurred due to the therapeutics and also increase the possibility of bioavailability of therapeutics. Then the challenge occurred with the size of the nanocarrier along with the size of the pores. Therefore, synthesis of nanomaterials with all required characteristics as a carrier has become vital. However, polymer nanostructures are getting additional highlights because of their biocompatible and biodegradable nature but few metal NPs like silica, zinc oxide, quantum dots, titanium dioxide, iron oxide, etc. have also proved their efficiency as nanodrugcarrier with small size, rigid arrangements, long shelf life as well as interact with cellular biomolecules thereby facilitates admittance into the cell.

This dissertation comprises a detail synthesis approach of three types of polymeric and inorganic nanomaterials with varying sizes, followed by a complete systematic characterization for the biomedical application. Conventional sole gel techniques, chemical synthesis by using nanotemplates and surfactant free sonochemical technique have been followed for the synthesis of nanomaterials with different characteristics such as core-shell, hollow porous and mesoporous. Three different therapeutic fields have been included in this work for the

application purpose of synthesized porous structured nanomaterials and the fields are Malaria, Immunology and Cancer Therapy.

Malaria is becoming a big threat in human by becoming resistant to almost all available malaria medications and thereby causing about 216 million cases in 91 countries annually with 445000 deaths according to WHO. There instant proper up gradation in the Malaria treatment is becoming a very urgent issue. The first part of this dissertation includes the development of a core-shell nanostructure where different sizes of SiO<sub>2</sub> NPs synthesized by sole gel technique have been used as core and PCL polymer formed the outer shell layer. Later the templates SiO<sub>2</sub> NPs have been etching out to create a new PCL NC with hollow porous morphological characteristics. This novel amorphous hollow porous PCL NCs are biocompatible biodegradable and have a great encapsulation efficiency while loaded with antimalarial drugs Dihydroartemisinin and Chloroquine and Sulfadoxine. Their antimalarial activities have been studied with Malaria causing *P. falciparum* parasitic cell culture where these NCs have efficiently inhibit the growth of the parasite-infected RBCs compared to free drugs. These NCs are unique because they can be tuned as a “time temperature clock” module i.e., they can be tuned with predetermined drug doses obligatory for the Malaria treatment with an increase of body temperature due to the infection. This nanodrugcarrier has the potential to control the release of confined drugs from it as soon as the temperature arises gradually reduces the release of drug with a gradual decrease in the temperature to normal. Therefore, this unique polymer based NCs can be used as nanodrug carrier for eradicating *P. falciparum* growth efficiently.

In the field of nanobiotechnology, nanostructures based on metal have received importance recently for the formation of vaccines. Moreover, nanostructured with porous morphology is an excellent candidate in that regard. The second part of this dissertation included designing of nanostructured ZnO with mesoporous morphology by surfactantfree sonochemical method. This unique stable mesoporous ZnO NCs showed outstanding loading efficiency by encapsulating protein Ova. These protein loaded metal oxide NCs have immunized in mice model to investigate the enrichment of immunological responses. Ova has worked as an antigen in this regard for improvement in CD8<sup>+</sup> and CD4<sup>+</sup> T-cell effector responses. Antigen-specific IgG levels and IgG2a or IgG2b levels in serum has also increased when lymph node and serum of Ova loaded mZnO immunized mice have studied. The role of mesoporous ZnO NCs in enriching the immune response makes it as a good promoter to design nanovaccines in the field of medicine to prohibit various ailments. Later these mesoporous nanocarriers have been used to encapsulate antimalarial drugs Dihydroartemisinin,

Chloroquine and Sulfadoxine and anticancer drugs DOX and paclitaxel and a systematic sustained controlled drug release pattern can be observed in each drug conjugate nanoformulations. The cellular level interaction of drugs loaded mZnO NCs with cancer cell line K562 have been studied where these NCs entirely deformed the malignant cell structures and thereby proved their efficiency as a drug carrier.

With the development of biomedical field, the therapeutic field Cancer has also developed. A part of credit can be claimed by the involvement of nanotechnology in this particular medical field with new innovative researches to avoid complications related to the treatment. The third part of this dissertation includes engineering of a core-shell nanostructure with mesoporous ZnO NCs as a template and polymer PCL as coating layer where 2-3 templates were coated by a polymeric shell. Later these temples were etched out by leaving pores in the polymer nanostructures. This amorphous NC is biocompatible and biodegradable in nature with a great drug encapsulation efficiency. Biocompatibility of this NCs with the templates as well as without templates were investigated with two different breast cancer cell lines MCF 7 and MDA-MB-231 respectively. The drug Paclitaxel has been used to load inside the NCs pores and cell inhibition assay have been conducted by using MCF 7 and MDA-MB-231 where drug loaded with NCs performed more malignant cell inhibition property compared to free Paclitaxel drug. Moreover, this nanocarrier showed lower IC<sub>50</sub> compared to free drug. Thus these polymer-based nanodrug carriers can decrease the toxic drug doses thereby reducing side effects and also can increase the bioavailability of therapeutics.

# Chapter 1: Introduction and Literature Review

## 1.1 Introduction

- 1.2. Nanomaterials
- 1.3. Drug delivery system
- 1.4. Mesoporous nanocapsules for drug delivery applications
- 1.5. Inorganic metal oxide: Zinc Oxide (ZnO)
- 1.6. Polymer Polycaprolactone (PCL)
- 1.7. Brief introduction of the drugs/protein used
- 1.8. Brief introduction of the cell line used
- 1.9. Immunology

## 2. Literature Review

- 2.1. Malaria parasite *P. falciparum* resistivity towards antimalarial drugs
- 2.2. Nano drug carriers for suppressing malaria infection
- 2.3. Nanotechnology in immunology
- 2.4. Ova protein in immunology
- 2.5. Nano carriers against cancer therapy
- 2.6. Paclitaxel drug loaded nanocarriers against cancer therapy

## 3. The motivation behind this work

## 4. Objectives of this dissertation

# Chapter 1

## Introduction and Literature Review

### 1.1 Introduction

A few decades ago the term “Nanotechnology” itself was unfamiliar to the world. In 1959, a talk delivered by prominent physicist Richard Feynman about the possibility of manipulating and controlling smaller scale [1] had exposed the research platform for nanotechnology. Later, rapid research works have been started and still going on in the field of nanotechnology. Since then it catches the attention of researchers from all areas of science, trying to explore nanotechnology field in their concern research field and consequently today nanotechnology has proved it’s supremacy over all extents of scientific research by accomplishing a prominent place in science and technology globally. Currently, the most advanced technology field is nanotechnology and it comprises more or less all scientific research domains of physics, chemistry, biology and engineering together with their their sub applied fields.

Presently in biomedical field a lot of research is going on based on the nanotechnology (popularly known as ‘Nanobiotechnology’) whether to form a drug or to cure any disease or cancer therapy or in drug, other biomolecules delivery or tissue engineering or MRI contrast enhancement or in any device making, etc. which are particularly used in this field [2–14]. Since the biomedical field is a very broad area of science and therefore the rapid enhancement of nanotechnology in this filed makes it challenging to do research in this area. Hence we have chosen the area ‘drug delivery’ from the biomedical field as the concern research area by applying the concept of nanotechnology.

This introduction includes a brief summary about nanomaterials and their use in drug delivery system focusing on inorganic and polymer nanocarriers and also the application of these nanocapsules (NCs) in immunology. Further, it comprises a brief introduction of the drugs, protein and cell line used for the work.

## 1.2. Nanomaterials

The basic of nanotechnology is the designing of nanomaterials by following different physical or chemical routes and their applications in appropriate fields. While describing a nanomaterial, these are materials having the scale of  $10^{-9}$ m (nanometer) and size range about 1-100nm in any of x, y and z dimension. These are designed or fabricated to a smaller scale than atomic level since they possessed more advanced and unique characteristics compared to their other bulk counterparts of size scale micrometer ( $\mu\text{m}$ ) or millimeter (mm) in all aspects and hence can have better multidisciplinary applications.

Since, research works on nanotechnology have tremendously enhanced with time, simultaneously various synthesis techniques for the production of the nanomaterials have also developed very promptly. Basically, these synthesis techniques have followed two basic routes, namely as ‘top down approach’ where breaking down the bulk structure to nanometer size range and ‘bottom up approach’ where self-assembly of atomic or molecular components for the production of desired nanostructured material [15]. Specifically ‘bottom up approach’ has followed for designing nanomaterials in this research work.

Further considering the purpose of this research work, category of nanomaterials production have been limited to inorganic nanomaterials and organic nanomaterials.

**(A) Inorganic nanomaterials:** When nanomaterials are synthesized from metal, semiconductors and metal oxides those nanomaterials are categorized as inorganic nanomaterials. Metal oxide NPs have been chosen for synthesis for particular use in drug delivery applications in the present research work.

**(B) Organic nanomaterials:** When nanomaterials are synthesized from organic materials like lipid or polymers those nanomaterials are categorized as organic nanomaterials [16]. Since polymeric NPs are the most appropriate candidates for several applications in biological domain, therefore, polymer NPs have been chosen to synthesis for particular use in drug delivery applications in the present research work.

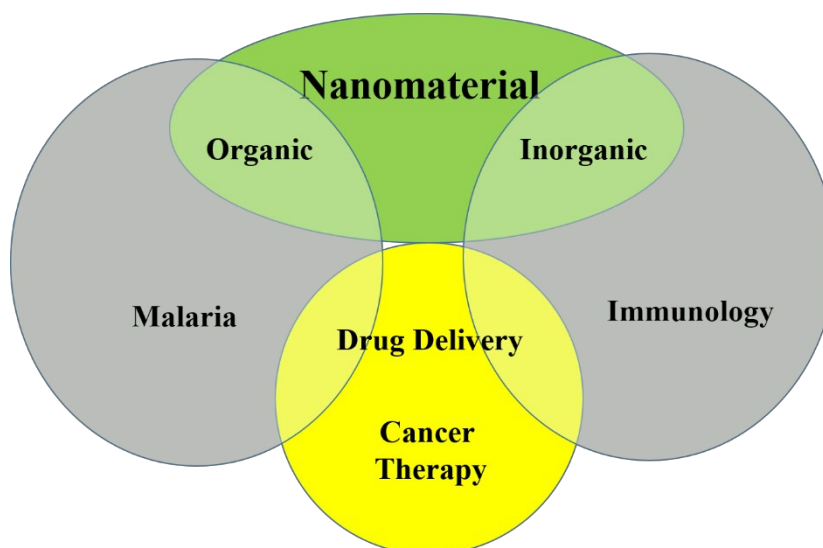


**Figure 1.1.** Schematic representation of the fields involved in the current dissertation work.

### 1.3. Drug delivery system

Drug delivery is a most frequently used term in the field of biomedical. Like the term depicts, the approach or system where administrating a drug or therapeutic compound within the human or animal body with respect to the desired safety purpose to the site of action is termed drug delivery system. Exclusively, it focuses on both dosages of drugs and the drugs administration routes.

While focusing on drug delivery, the key concern goes to the drug administration routes by which drugs are transporting within the organs as per requirement of the therapeutic condition. Further, this system can be classified into two categories as *conventional drug administration approach* and *novel drug administration approach*. The conventional approach of drug administration comprises of a number of approaches mainly, *oral* i.e., via the mouth (also is the most common path), *injection* (injecting by a needle), *transdermal* i.e., via skin [17], *nasal* via nose [18] etc. However, these approaches further include few more drug administration paths by following injecting drugs or other pharmaceutical products through *sublingual* (via tissues present under the tongue), *buccal* (via oral mucosa), *rectal* (via the rectum), *intravenous* (via veins), *intramuscular* (via muscles) [19–22]. However, till date conventional approach of drug administration is widely followed worldwide still, it has many disadvantages which lead to the development of more advanced as well as up-to-date drug administration approach is intended for the betterment of mankind. Few limitations can occur as a result of the conventional doses of drugs administrated by conventional paths are

mentioned here such as, (i) lesser dose interval which gives less bioavailability, (ii) maintaining the drug concentration inside the body become more challenging due to immediate release of drug once the dose is given, (iii) interval of giving doses have shorter half-life than the drug itself and thus resulting increased other side effects to the patient like irritations, discomfort, inflammations to the applied area, (iv) problems associated with drug degradation, (v) poor drug permeability through cell walls, (vi) toxicity of the drugs, (vii) enzymatic degradation of few drugs and also (viii) few drug administration paths as well as drugs are very expensive and not cost efficient for general people to take repeated number of times for optimal result.

Hence, to overcome all these limitations of the *conventional drug delivery system*, as stated earlier, the requirement of a *nonconventional or novel drug administration approach* arises using most improved, modern technologies and design less toxic, biocompatible formulations. It can also provide the solution of problems allied with doses of existing drugs with the concept of controlled, sustained as well as targeted drug delivery/release path. These modes of drug release systems are specially designed to obtain more bioavailability of existing drugs and to acquire the desirable therapeutic effects by decreasing quantity of doses for longer period of time.

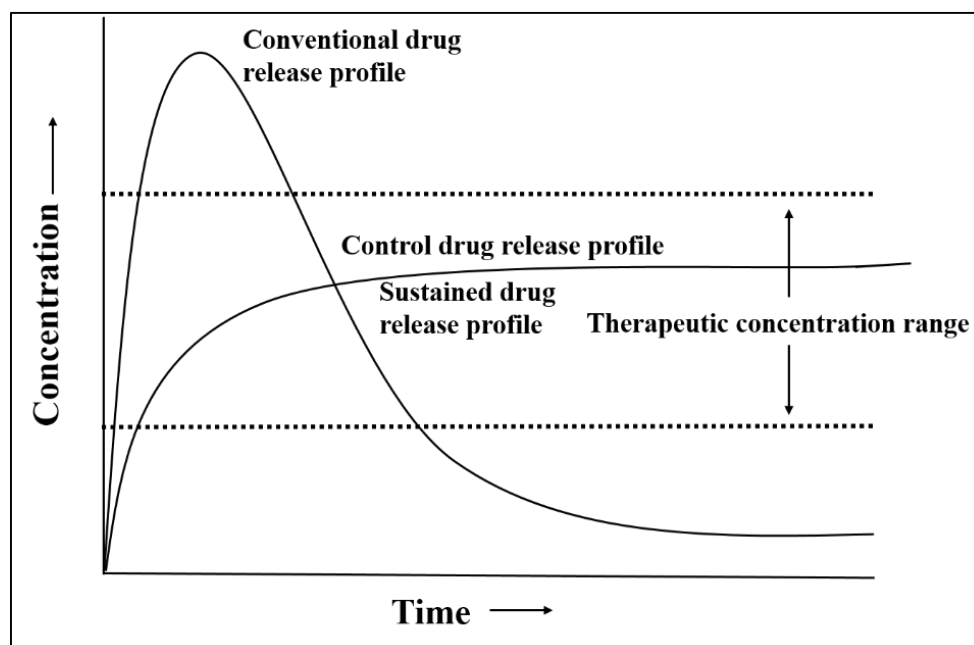


**Figure 1.2.** Comparison of three drug delivery mechanisms.

During the controlled drug release or delivery, the concentration of the drug is made persistent in the blood flow throughout the treatment period for a predetermined extent of the

time period and the release of drug is also predetermined. In sustained release or delivery of drug, the interval of the time period of drug dose is constant throughout the treatment period for an extended time [23,24]. With the advanced techniques from last few years, bioengineers are constantly trying to combine these both drug release systems by achieving required therapeutic response below the toxicity level which can arise because of an overdose of the applied drugs as like conventional drug delivery system. Targeted drug delivery is the current achievement in the biomedical fields which can direct drugs or other therapeutic substances towards the affected or desired area of interest and thereby helps to protect the other uninfected area of the body from the harmful side-effects of drugs [25,26]. The great example can be the cancerous tissues, where the whole body is going through severe side effects during the treatment. The chief mechanism behind these modes of drug release can be diffusion, dissolution, degradation, osmosis and also based on ion affinity.

Further to improve the mechanism of drug and other therapeutic substances delivery to the desired sites of action certain carriers are required which are known as drug carriers or drug vehicles. With the advancement of nanobiotechnology, these nanodrug carriers are able to seek all the attention of researchers to solve various problems concerned with biomedical science. There are some benefits to use NPs as the nanodrug carriers over other drug carriers. Size is the biggest advantage of these NPs and additionally, biocompatibility, stability, efficiency, unique drug release pattern of each NP, site specific targeted drug delivery as well as their very fast growth in the research helps to find new development in them, in a regular basis.

A brief introduction about some nanocarriers is mentioned here, i.e., liposome, micelle, dendrimers, hydrogels, nanospheres, quantum dots, nanorods, NCs etc.

*Liposome* formation occurred due to the self-assembly of colloidal lipid substances in a spherical pattern in the aqueous medium. It composed of lipid bilayers where hydrophilic part of the first layer has made a thick shell and the hydrophobic part of the second layer got attached to the hydrophobic part of the first layer by forming a hydrophilic core. Thus it can encapsulate water soluble therapeutic agents inside it safely. These liposomes take the drugs to the cell either releasing the drugs by attaching to the cell membranes or be taken up by cells followed by open up to liposomes by releasing drugs to the cells (in case of phagocytic cells) [25,27].

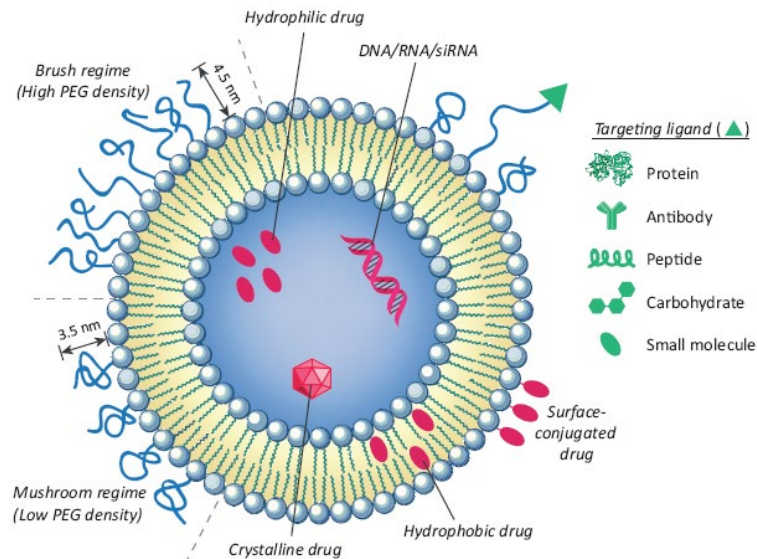


**Figure 1.3.** A schematic representation of the Liposome with different therapeutic agents inside its aqueous core as well as on its hydrophilic surface [28].

Micelle formation is also occurred because of the self-assembly or aggregation by hydrogen bonds of amphiphilic polymers in an aqueous medium forming a hydrophilic shell and a hydrophobic core formed by the hydrophobic part of the polymer structure. Hence, drugs and other biological substances can load inside it safely for drug delivery [27,29].

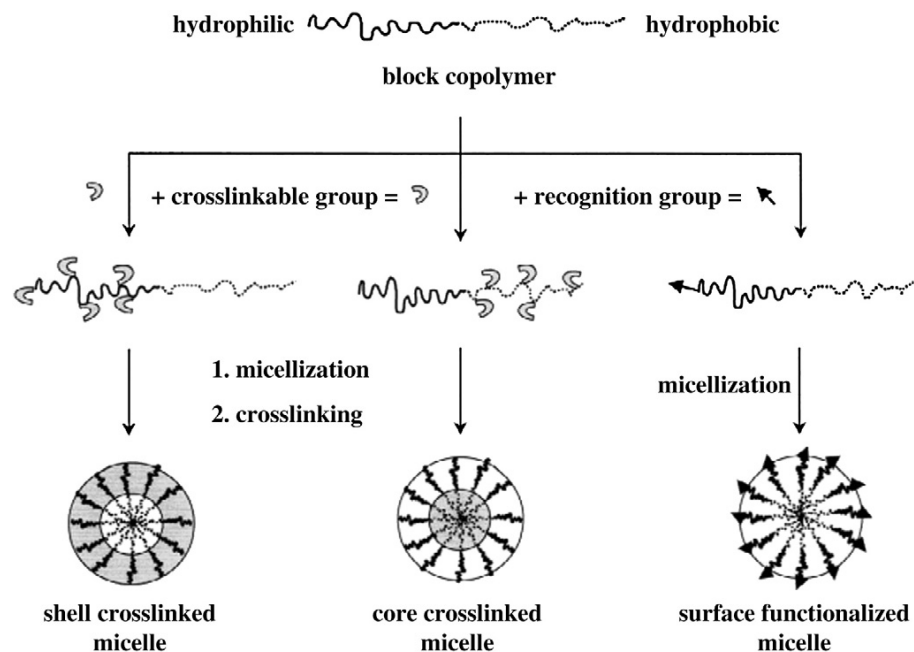


**Figure 1.4.** Schematic representation of functional block copolymers Micelles [29].

*Dendrimers* are branched nanostructures made up of synthetic biodegradable globular molecules [25]. Different kinds of therapeutic agents, antibodies, functional groups etc., can be attached to the specific branched structure of *dendrimers* and hence showed its potential as an efficient platform for drug delivery. These branched structures can also be used for the trans-membrane transport as well as gene transfer.

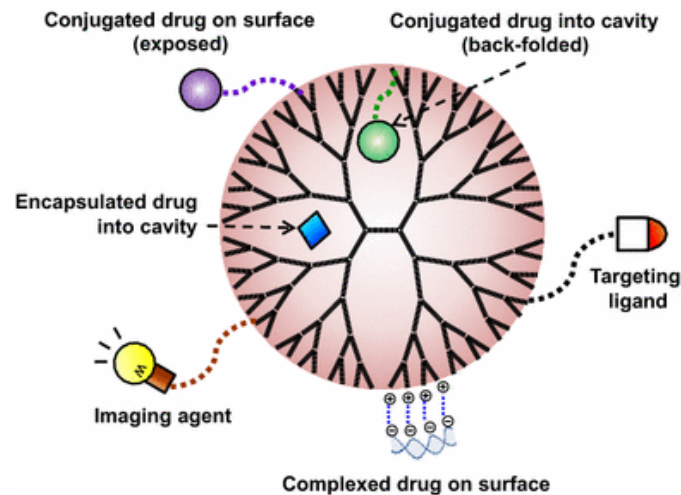


**Figure 1.5.** A schematic representation of Dendrimer for therapeutic application [30].

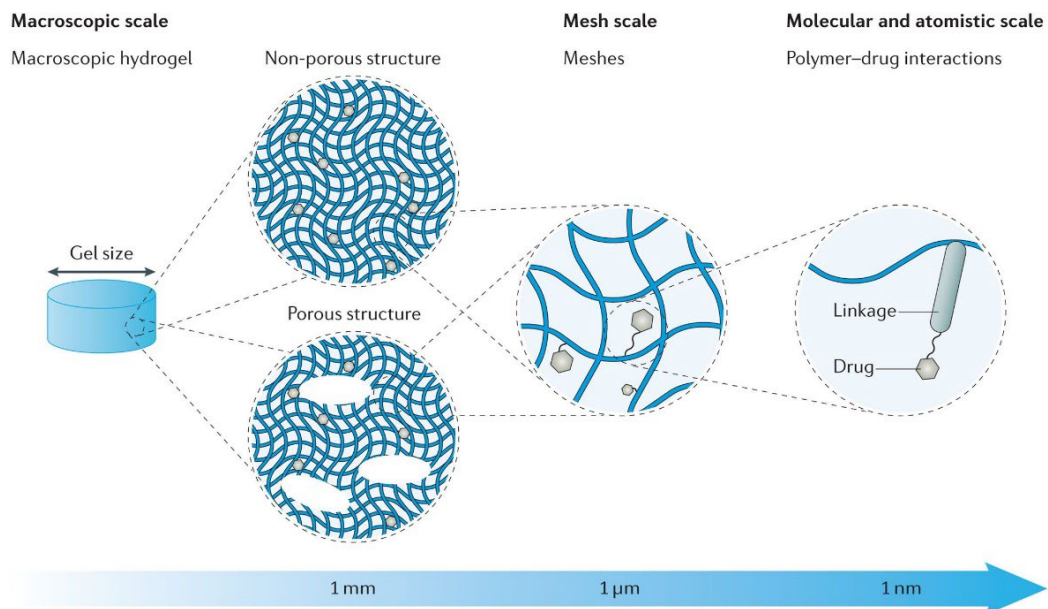


**Figure 1.6.** A schematic representation of Hydrogel with decreasing size and porous structure [31]. At the molecular (or atomistic) scale, therapeutics can be incorporated with the polymer chains via a covalent linkage.

*Hydrogels* or nanogels are formed by 3D cross linked polymer networks possessing hydrophilic properties. Therapeutic substances are loaded into the pores present in the matrix of the gel [25]. About 70-90% water content structure of *hydrogels* makes them resemble with the structure of tissues and thus makes it a biocompatible drug carrier for encapsulating drug molecules with hydrophilic nature. However, after functionalization of the surface of the *hydrogel*, they are utilized for the delivery of hydrophobic drug molecules. The crosslinking of the polymer network gives them a solid structure with good mechanical strength.

*Quantum dots* are semiconductor nanocrystals with 1-10nm in size have unique fluorescence property by which it can help in imaging purpose [25]. *Quantum dot* by itself or functionalised with other complexes can be used as drug carriers also [32]. Amphiphilic polymers can be functionalised over the *quantum dot* by considering it as the inorganic core which serves to embed molecules of imaging contrast agents and also hydrophobic drug molecules. Whereas therapeutic agents with hydrophilic nature (like siRNA, oligodeoxy nucleotide i.e., ODN etc.) as well as bioligands (like antibodies, peptides, inhibitors etc.) can be immobilized to the hydrophilic polymer shell over *quantum dot* [33].

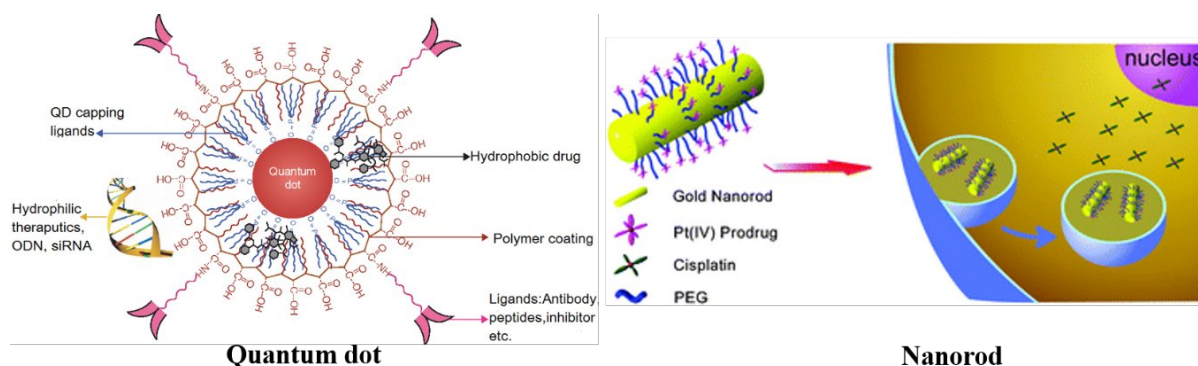


**Figure 1.7.** A schematic representation of multifunctional polymer encapsulated *Quantum dot* (where hydrophobic therapeutic agents can be entrapped inside the hydrophobic core whereas hydrophilic therapeutic compounds can be attached to the outer polymer coating layer) [33] and PEG functionalized gold *Nanorod* for platinum delivery [34].

*Nanorods* are rod shaped nanostructures of inorganic materials and semiconductors with nanometre range diameter. All therapeutic substances are loaded on the surface of this NPs for drug delivery purpose. Bioinert, nontoxic Gold *nanorod* structures possess extended circulation time period *in vivo* thereby increase the percentage of nanostructure accumulation inside the tumors and also they are used for near infra-red imaging due to their excellent optical

property, gene delivery etc. Moreover, *nanorods* can be functionalized with polymers to enhance the efficiency of drug delivery [34].

*Nanospheres* are NPs with nanometer size and spherical in shape. This nano drug carrier is used to absorb, encapsulate drug molecules inside its polymer matrix as well as attached pharmacological agents on the surface of the *nanosphere* to prevent from chemical and enzymatic degradation of the therapeutics inside the cell [35]. These nanostructures possess either amorphous or crystalline nature. Hydrophilic polymer PEG, Poloxamine nanospheres have been used to target tumours [36].

*Nanocapsules* are also made up of either inorganic or polymeric nanostructures with spherical in shape and drug molecules can be inserted inside the solid/liquid core by a protective outer membrane made of polymer nanomaterials while the hollow core offers great opportunities for encapsulating different therapeutics [35]. Porous NCs of PCL polymer have been used to encapsulate siRNA for enhanced siRNA transfection on HepG2 using EGFP (enhanced green fluorescent protein) [37].

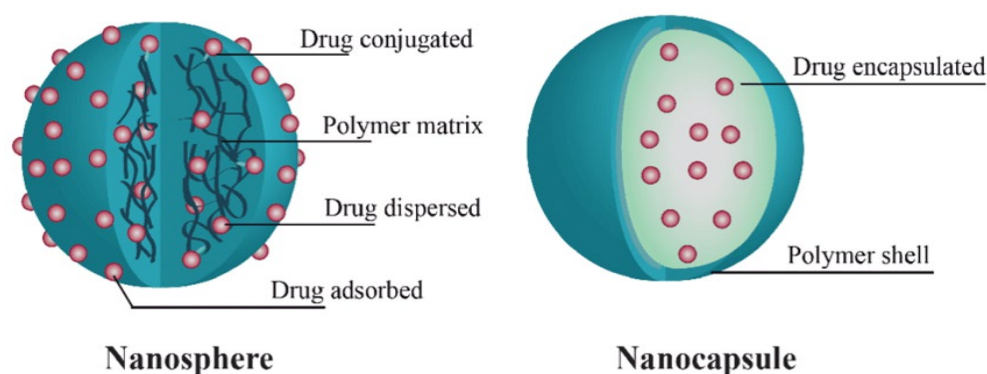


**Figure 1.8.** A schematic representation of drug interaction with Nanosphere and NC for drug delivery system [35].

#### 1.4. Mesoporous nanocapsules for drug delivery applications

When nanomaterials possess features like pores/cavities in their structure then they are acknowledged as porous nanomaterials. There may be one or more pores occur in individual nanostructure. Subsequently, in the post discovery era of porous nanomaterials, where it has brightened up tremendous possibilities of porous nanomaterials in the applied fields. Again, according to the size of the pores i.e., the diameter of the pores, the nanomaterials are classified

into three categories such as, *microporous nanomaterials* having pore width less than 2nm, then *mesoporous nanomaterials* having pore width in the range of 2nm to 50nm and *macroporous* nanomaterials having pore width greater than 50nm [38]. The main benefit of the extensive use of microporous and mesoporous nanomaterials in various applications from past decades, is their nanoscale range pore width. Therefore, our main interest also lies in mesoporous NCs (pore width approx. 2nm-50nm) as a delivery vehicle for biomedical applications.

### **1.5. Inorganic metal oxide: Zinc Oxide (ZnO)**

A well-known inorganic metal oxide is Zinc oxide nanopowder. It has molecular formula ZnO and molar mass 81.40g/mol. It possesses a melting point is 1975°C and boiling point is 2360°C. Its physical appearance is white solid powder without any odour. It is insoluble in aqueous medium, can dissolve in acidic (very slow) and basic medium.

ZnO nanopowder has a vast range of applications in nanotechnology. This nanopowder exhibits some remarkable properties like UV-filtering, antibacterial, antifungal as well as anti-corrosive [39]. Synthetically produced ZnO nanopowders have various commercial utilizations like optical devices, rubber and plastic industries; glass, ceramics and cement industries; various paint industries, cosmetics products, lotion and ointment industries [40] etc.

Apart from all these ZnO NPs are also famous as a semiconductor (II–IV type semiconductor) in the material science field and used as liquid crystal display, energy storage, and as nanosensor in the electronic field. It possesses some exclusive properties like wide band gap (3.3eV), high binding energy, high electron mobility and very favorable transparency [41].

The hydroxyl rich surface of ZnO NPs with excellent biocompatible nature made easy functionalization of other complexes, therapeutics, biological agent to the ZnO surface and thus they can perform a large number of applications in biomedical domains such as bio-imaging, delivery of drugs and gene, biosensors etc [32]. The reduction in the size of MNPs to nanoscale levels predominantly alters the electromagnetic, structural, morphological and chemical properties, which allows these MNPs to interact in diverse ways with cellular bio-molecules and facilitates entry into the cells [42]. The MNPs have increased surface reactivity due to the presence of a large number of atoms at their surface which boost their capacity to be loaded with therapeutic agents and deliver them to target cells [43].

## 1.6. Polymer Polycaprolactone (PCL)

Since a few decades earlier, only polycaprolactone (PCL) has been used in the biomedical field as a promising platform of drug carrier amongst all other polymers. The combination of both biodegradable and biocompatible nature makes it favourable for all biological applications, besides it is correspondingly accepted by FDA (Food and drug administration) for the delivery of the drug.

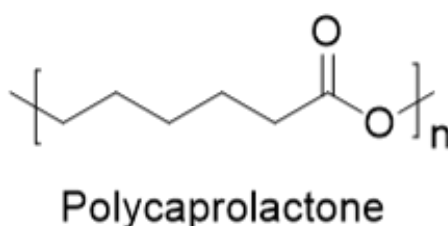


*Figure 1.9. Chemical structure of Polycaprolactone.*

Manufacture of PCL is not complicated, inexpensive and one of the oldest most used polymers from the time of its synthesis since around 1930's [44]. PCL belongs to the polyester family and can be synthesized by following the “ring opening polymerization” route of  $\epsilon$ -caprolactone by the utilization of a catalyst of nature either cationic, anionic or pseudo anionic (coordination-insertion) [45].

Few unique properties made PCL preferable over other biodegradable polymers, like viscoelastic property and rheological property [46]. PCL is semicrystalline (with increasing molecular weight crystallinity decreases) possess low glass transition temperature ( $T_g$  about -60°C), low modulus [47] and low melting point (around 59-64°C). Basically, PCL is a water and alcohol insoluble polymer. At room temperature, it shows solubility in chloroform, benzene, cyclohexane, dichloromethane, toluene, carbon tetrachloride etc. and sparingly soluble in acetone, ethyl acetate etc [48]. The thermal stability of PCL polymer increased in its composite formulations with other materials.

## 1.7. Brief introduction of the drugs/protein used

### (A) Chloroquine diphosphate salt (CQDP)

**Structure:** Molecular formula  $C_{18}H_{26}ClN_3 \cdot 2H_3PO_4$ . This is a member of the quinoline compound family.

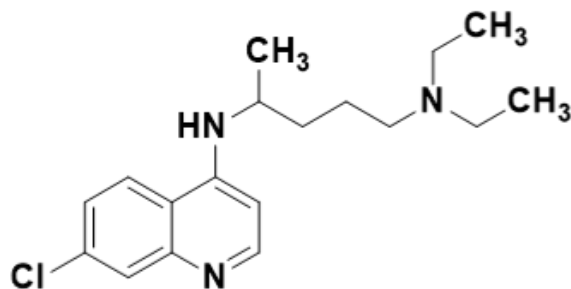


**Figure 1.10.** Chemical structure of Chloroquine diphosphate salt (CQDP).

**Properties:** Molecular weight 515.86 g/mol and melting point 193°C. It is soluble in water and almost insoluble in alcohol, ketone, ether, chloroform etc. It is photosensitive in nature.

**Application:** Primarily CQDP has extensively used as an antimalarial drug to inhibit the growth of malaria parasite in blood because of its inexpensiveness, high stability, high efficiency and less toxic in the body. However, with the improvement of research in the medical field, it has proved that CQDP has applications beyond malaria cure like, to inhibit cell growth in breast and lung cancer, antitumor activity, autophagy and apoptosis inhibitor etc [49–51].

### (B) Dihydroartemisinin (DHA)

**Structure:** Molecular formula  $C_{15}H_{24}O_5$ . It is a derivative of artemisinin family.

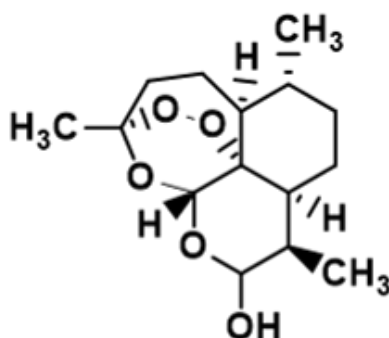


**Figure 1.11.** Chemical structure of Dihydroartemisinin (DHA).

**Properties:** Molecular weight 284.35 g/mol and melting point of 140°C. It possesses less solubility in water and showed high solubility in acetone, chloroform and all alcohols. It is quite unstable in nature. It has less toxicity compared to other artemisinin derivative combination of drugs.

**Application:** DHA is used as an intermediate in the formation of other antimalarial drugs belongs to the family of artemisinin. It is commonly known for the prevention of malaria infection when combination with piperazine for commercial use, although it has other medical importance like CQDP [52–54]. DHA is toxic to cancer cells, active towards chemotherapeutics and can treat with human melanoma cells.

### (C) Sulfadoxine (SD)

**Structure:** Molecular formula is C<sub>12</sub>H<sub>14</sub>N<sub>4</sub>O<sub>4</sub>S. It belongs to the drug group Sulfanilamide.

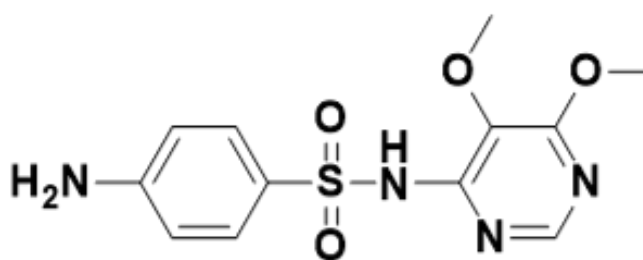


**Figure 1.12.** Chemical structure of Sulfadoxine (SD).

**Properties:** Molecular weight is 310.32896g/mol, melting point 190°C-194°C. It shows solubility in aqueous medium.

**Applications:** The combination of SD with drug Pyrimethamine is used to inhibit as well as a treatment for Malaria infection instigated by *P. falciparum* when the parasite is showing resistant to the drug Chloroquine. It prevents bacterial enzyme dihydropteroate synthase enzyme activity thereby indirectly prevents the cell growth of *P. falciparum* and thus reproduction of the parasite stops [55]. Although SD can be used to treat liver stock, urinary tract as well as respiratory infection, by combining with other drugs [56].

#### (D) Ovalbumin (Ova)

**Structure:** Molecular formula is  $C_{66}H_{105}N_{21}O_{23}$ . It is a part of Serpin family of protein and consists of 385 amino acids. Ovalbumin (Ova) is a glycoprotein and the source of it is chicken egg white comprising 54% of the total amount of protein.

**Properties:** Molecular weight is 45kDa.

**Applications:** Ova is mainly used in immunology as antigen and in vaccination [57]. It is a very cost efficient, low maintenance, easy to available in large quantity and a stable protein. It can also be used as a molecular marker in gel electrophoresis calibration as well as in the study of structures and properties of other proteins.

#### (E) Paclitaxel (Ptaxel)

**Structure:** Molecular formula is  $C_{47}H_{51}NO_{14}$ . It belongs to the Taxane drug group.

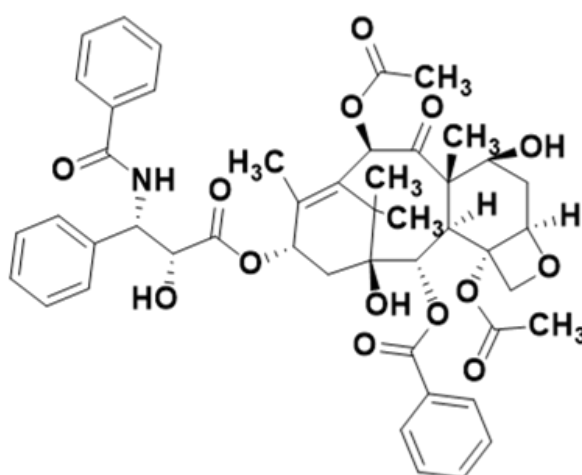


**Figure 1.13.** Chemical Structure of Paclitaxel (Ptaxel).

**Properties:** Molecular weight 853.91g/mol, melting point 216°C –217°C. Ptaxel shows solubility in DMSO, ethanol etc. It is insoluble in water and little bit soluble in aqueous buffer.

**Applications:** Presently, Ptaxel is a well-known and bestselling anticancer medication for a number of cancer treatments and also used as a chemotherapeutic agent. It possesses antitumor action. For the treatment of breast, pancreatic, lung, ovarian, melanoma, cervical, stomach, prostate cancer and Kaposi's sarcoma, Ptaxel drug is widely utilized. It is toxic in nature. Similar to all other anticancer drugs it also has severed side effect [58,59].

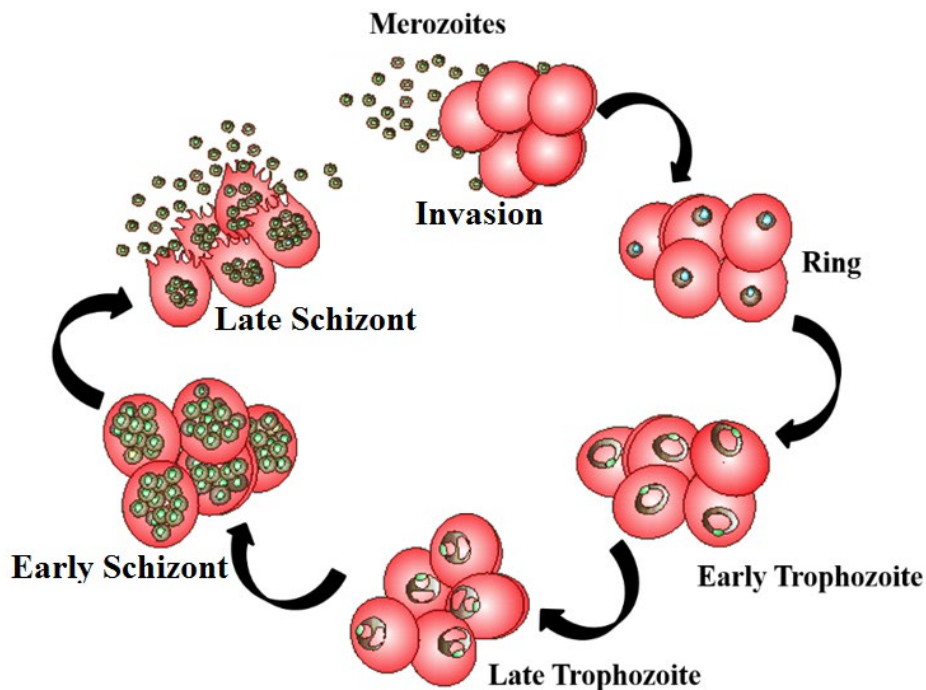
## 1.8. Brief introduction of the cell line used

### (A) *Plasmodium falciparum* (*P. falciparum*)

*Plasmodium falciparum* also is known as *P. falciparum* is a member from the protozoan parasite *Plasmodium* responsible for the spreading one of the most life threatening sickness malaria in a human being. *Plasmodium* comprises altogether four species i.e., *Plasmodium falciparum* (*P. falciparum*), *Plasmodium vivax*, *Plasmodium malariae* and *Plasmodium ovale*. Among all these four species *P. falciparum* is the most fatal one for causing more complications and highest mortality rate. Symptoms of malaria are high fever with chills, headache, anaemia, diarrhea, muscle ache, vomiting, nausea etc. Through the female Anopheles mosquito, it is migrated to the human body during the bite of the mosquito [60]. Additionally, the fifth *Plasmodium* species *P. knowlesi* which was previously known for causing infection in animals (macaque monkeys), has found infecting human as well in some parts of Southeast Asia region, Malaysian Borneo, Singapore and Philippines [61,62].

The life cycle of *P. falciparum* is considered as a complicated one, where both mosquito and the human body are included and then parasite goes through differentiation for a multiple number of times during the whole transmission and infection process. Salivary gland of the female Anopheles mosquito is the habitat of the sporozoites form of the *P. falciparum* parasite which passes to the human body after mosquito bite and directly enters to the blood stream of the human. Thereafter, these sporozoites attack the hepatocytes, i.e., liver cells by transforming into trophozoites during next 16 days of mosquito bite. After performing a multiple number of divisions these parasites produce merozoites of tens to thousands in number and comes out of the hepatocytes by blasting the cell wall. Further, each merozoite infects erythrocytes, i.e., red blood cell and performs another round of cell division process and produced around 12-16 number of merozoites within schizont in next 48h which causes the indications of malaria infection. In the first stage of additional cell differentiation inside erythrocyte, trophozoites also known as ring stage forms before schizogonic differentiation [63]. After blasting out from infected erythrocytes, merozoites goes to infect other healthy erythrocytes. Thus infection is spreading through the human erythrocytes. Some merozoites are only differentiated to schizonts, some of them participated into sexual cell division by forming gametocytes which are later collected by anopheles mosquito during the feeding. Male gametocytes performs fast nuclear division in mosquito midgut by producing flagellated microgametes which later fertilize female macrogametes and thus generating ookinetes which crosses the mosquito gut

and enclosed on the outer wall of the gut in the form of oocyst. Rupturing of oocyst produces around hundreds of sporozoites and accumulated in the salivary glands of the female anopheles mosquito [64,65].



**Schematic 1.1.** Schematic diagram of the life cycle of *P. falciparum* with different stages.

The **schematic diagram 1.1** represented all stages of *P. falciparum* life cycle which started with the invasion of erythrocyte by merozoites of parasites. In the following stage, parasites appear as a thin ring inside the erythrocyte and because of the shape of the parasite this stage is considered as ring stage. In the next stage i.e., early trophozoites, parasites develop trophozoites and on the surface of the host erythrocytes, an electron dense portion appears till it enters to late trophozoite stage. Then in the early schizont stage, parasites division started to form merozoites and finally with the completion of 48h in the late schizont stage, merozoites release due to the outbursts of host erythrocytes.

**(B) MCF 7 (Michigan Cancer Foundation 7)**

Since the past decades cancer has been occupying the peak position continuously among all the life threatening diseases globally. Consequently researches on cancer study becoming most challenging and the great positive accomplishment is in degradation of the mortality rate by 2% per year including both men and women [66]. When considering all types

of cancers, breast cancer is the most common occurring form of malignancy in females worldwide. In modern research, Michigan Cancer Foundation 7 shortly MCF 7, is a well-recognized, broadly studied and thoroughly characterized epithelial breast cancer cell line derived from human breast adenocarcinoma. These adherent cells are large enough with 20-25 micron cell size. The growth of this cancer cell line is very slow measuring approximately 30-40hr. While mentioning about the application of MCF 7 cell line, it is extensively used in cell culture for *in vitro* studies. Receptors like progesterone, estrogen as well as glucocorticoid are expressed by MCF 7 cell line and are sensitive to cytokeratin. Along with its all multiple uses, MCF 7 cell line is widely used to estimate cell cytotoxicity study with the help of MTT assay [67].

### **(C) MDA-MB-231**

Presently, MDA-MB-231 is also a well-studied most commonly used epithelial breast cancer cell line in medical research. It is derived from a pleural effusion of a metastatic mammary adenocarcinoma [68] and it is devoid of receptor expressions like oestrogen, progesterone and human epidermal growth factor receptor 2 amplification (HER2). Therefore, it was categorized as basal breast cancer cell line initially but later kept in the claudin-low molecular subtype. MDA-MB-231 is a form of triple negative invasion breast cancer cell line intermediated by proteolytic degradation of extracellular matrix [69] and having the limited curing possibility. It appears as endothelial like morphology under 3D culture. It is a recognized tool in the research of bone metastasis. It is also widely used cell line to estimate cell cytotoxicity study with the help of MTT assay.

## **1.9. Immunology**

Immunology is a very significant area of biomedical field. Immunology concerns with the defense system of a multicellular organism (which is the host) against infection causes because of the exposure of foreign objects which can be any organisms or materials. The defense system of host organism works for all sorts of properties like physiological, chemical, physical and any sudden change in these, the defense system becomes activated to fight against that change. Illness in organism is the result of poor immune system which failed to protect the body against pathogens. With the constant research and growth in the field of nanotechnology, it is able to include almost all areas of science in it and even in the development of immunology also.

Almost all sort of nanostructured materials are engineered to form immunomodulatory agents, adjuvants and even vaccines, as nanostructured materials have the advantage of small size to go to the targeted side and deliver the immunologically active components. Thus with the involvement of nanotechnology in the field of immunology it can help to improve clinical outcomes thereby preventing the ailments.

As we cruise into an era of modern vaccines, the use of nanotechnology has open the platform for researchers to design NPs varying in shape, size, composition and surface properties [70] for improving efficiency of antigen delivery, antigen immunogenicity by augmenting antigen processing/presentation, enhancing antigen stability, and sustained release of antigens [71].

Nanovaccines are virus like NPs being used extensively as therapeutics for the treatment of various autoimmune diseases as well as degenerative diseases such as Alzheimer's, cancer treatment, cardiovascular diseases [72] and nicotine addiction [73–79]. In European countries, MF59 nanoemulsion is used as a vaccine adjuvant is used against influenza infection [80]. Different nanostructured particles such as PLGA NPs, polymer based nanospheres, NCs, hydrogels, liposomes etc. have been widely used by means of vaccines carriers, antibody immunomodulator agents. In the development of a vaccine, PEGylated PLGA of size 150-200nm have been designed to encapsulate hepatitis B antigen i.e., HBsAg [81] and thus it promotes the vaccine antigen uptake as well as induce the production of antigen specific antibodies in the cell. Currently, nanotechnology has been used to engineer versatile nanostructured materials to improve immune responses. Recently various NPs have been engineered to be administered as a prophylactic nanovaccines for the prevention and treatment of infectious diseases [82] like HIV, influenza and Tuberculosis [83].

In immunology, some other nanostructured materials are also used such as PLGA, PEG, natural polymers like alginate, inulin and chitosan, liposome-based liposome-polycation-DNA NPs (LPD) which are coordinated as an adjuvant delivery system for most of DNA vaccines, virus-like particles (VLPs) [67–69]. Additionally, inorganic and non-biodegradable NPs such as silica-based NPs (Si NPs), metal-based NPs (MNPs) such as nano-metallic oxides (zinc oxide, titanium dioxide, iron oxide, and quantum dots), offer many good properties such as rigid structures, long shelf life and capability to modify immune-stimulatory property of an antigen [87–90].

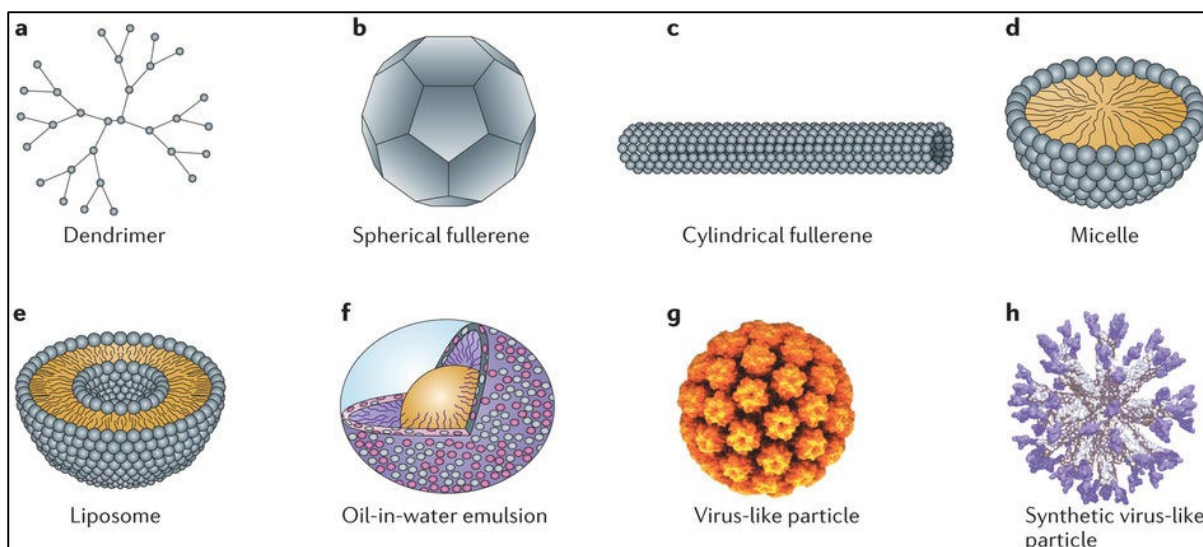


**Figure 1.14.** Nanotechnology applied in immunology (a-c) NPs, (d-f) nanoemulsions and (g and h) virus-like particles [86].

## 2. Literature Review

### 2.1. Malaria parasite *P. falciparum* resistivity towards antimalarial drugs

Malaria is one of the most life threatening ailment in human which causes annually about 216 million cases and 445000 deaths across the globe according to WHO [91]. It is an intermittent fever instigated by protozoan parasites of female Anopheles mosquito bite. Among the five protozoan malaria parasite species i.e., *Plasmodium falciparum* (*P. falciparum*), *Plasmodium vivax*, *Plasmodium malariae*, *Plasmodium ovale* and *Plasmodium knowlesi* which are responsible for causing malaria in human, *P. falciparum* is the most deadly one.

Currently, to eradicate *P. falciparum* is becoming the most concerned topic for biomedical researchers. There are many clinical approaches have been proposed till now to eradicate *P. falciparum* infection, among them the array of alkaloids possess antimalarial properties chosen as treatment like artemisinin-based combination therapy (ACT), CQDP undermining malaria control efforts and reversing gains in child survival and vector control are the potent intervention that can reduce malaria. Moreover, Peter *et al.* informed that quinine the first licensed antimalarial drug to prevent *P. falciparum*, became tolerant to the disease malaria through the treatment in Brazil in the year 1910 itself [92] and likewise the amount of drug dose varied from area to area to overturn the infection. In later years, according to Packard *et al.*, after the development of CQDP in 1930, it took the prime responsibility to eradicate the

parasitic infection during 1950-1970, although soon it was found out that Southeast Asia (in 1957 Thailand and 1959 Colombia-Venezuela border) took all attention for developing resistance for this drug, reported in Packard *et al.* and Farooq *et al.* [93,94]. Zalis *et al.* have also explained that the drug resistance in *P. falciparum* spread rapidly, it shows resistance for drug CQDP, which is used as the first-line drug for treatment in most of the epidemic areas [95]. Farooq *et al.* have mentioned the development of combination drug artemisinin in the 1990's due to the gradual growth of lenience towards all established antimalarial treatments [94].

Consequently, from the research of last decades, it has emerged out the resistivity of *P. falciparum* infection towards nearly all available treatments. The report given by Arjen *et al.*, suggested the *P. falciparum* resistance to artemisinin-based combination therapies [96], which are recommended first-line treatment used for malaria [97]. They selected Thailand-Cambodian border region for study over 40 patients, where *P. falciparum* has abridged *in-vivo* susceptibility to its treatment by artemisinin. In Mu *et al.*, *P. falciparum* genome-wide association study suggested that it is more resistant to drugs and moreover drug resistivity differs from continent to continents where they have included Asia (Thailand and Cambodia), America, Africa and Papua New Guinea [98]. They have investigated on 189 *P. falciparum* genome, isolated from these different continents to study against seven clinically approved available antimalarial drugs Dihydroartemisinin, chloroquine, mefloquine, sulfadoxine-pyrimethamine, quinine, amodiaquine, piperazine.

It is also noticed that antimalarial drugs enforce strong selective pressure on *P. falciparum* parasite and leave a signature of selection in the parasitic genome according to John *et al.* and Roper *et al.* [99,100]. Vreden *et al.* has reported the presence of Artemisinin resistance has found  $\geq 5$  h of parasitic half-life during artesunate monotherapy in Surinam [101]. Till date no remarkable vaccination is known, only one research vaccine against *P. falciparum* is known as RTS, S/AS01 and is in a clinical trial in 7 countries in Africa and has been submitted to the European Medicines Agency under art. 58 for regulatory review [102].

## 2.2. Nano drug carriers for suppressing malaria infection

The new treatment approach for the malaria infection, via antimalarial drugs has become an urgent requirement clinically, due to the increased resistance of *P. falciparum* against the available treatments. Moreover, extensively used antimalarial drugs like Dihydroartemisinin (DHA) possess few physical properties like short lifetime, low stability and also has low bioavailability [103] in its free therapeutic form. Additionally, encapsulation of antimalarial drugs has become urgency since an overdose of these free drugs are very risky as they have numerous side effects like gastrointestinal problems, stomach ache, itch, headache, postural hypertension, nightmares, blurred vision etc.

Jeong *et al.* and Venkataraman *et al.*, have mentioned that the concept of polymer based nanomedicine and also the drug delivery vehicles [104,105]. Further, as described by Avnesh *et al.* and Mora-Huertas *et al.*, the drugs confined in polymeric NCs increase the stability, bioavailability as well as the effectiveness of the treatment [106,107].

Till date, many researchers have reported the polymeric antimalarial drug carriers to suppress the malaria infection across the world. Polyester based PLGA capsules are used in the controlled delivery of malaria drugs due to their biocompatibility and biodegradability reported by Fredenberg *et al.* [108]. However, according to Makadia *et al.*, PLGA can degrade under hydrolytic conditions due to the hydrolysis of its ester group [109]. Recently, Golenser *et al.* reported the rigid block copolymer (PCL-b-MPEG) with artemisin in has been used for cerebral malaria treatment, but, (i) the polymer used there was not hollow and mesoporous in structure and (ii) temperature dependent monitoring of doses were not confirmed [110].

According to Foger *et al.*, to date, many NP based research works for antimalarial activities have been reported such as phosphorothionate antisense oligodeoxyribo-nucleotide and chitosan based NPs for silencing of malaria but those NPs found are very unstable [111].  $\beta$ -arteether lipid based NP formulation of curcumin is also reported by Memvanga *et al.* and used for malaria therapy [112]. However, because of the poor solubility and bioavailability of curcumin, this formulation found inefficient to achieve the expected efficiency to overpower the infection.

Owais *et al.* explained the use of liposome based drug carrier against the malaria parasite. They have designed liposome by Egg phosphatidyl choline, cholesterol and gangliosides where they have attached two mouse monoclonal antibodies MAbsD2 and

MAbsF10 separately along with antimalarial drug Chloroquine [113] and reported that this combination of nanocarrier efficiently controls drug susceptibility as well as the malaria infection. Urbán *et al.*, engineered a lipid based immunoliposome with size 200nm to encapsulate quantum dots further functionalized with *P. falciparum* specific half- antibodies against infected RBC's as well as non-infected RBC's as targeted delivery nanovector [114]. In the later work, they have checked the liposome based nano vector efficiency with antimalarial drugs chloroquine and fosmidomycin [115].

Mosqueira *et al.* reported a formulation involved NCs of an oily core of PLA where antimalarial drug halofantrine base was entrapped and outer shell surface was functionalized with grafted PEG chains [116]. Bakker-Woudenberg *et al.*, has reported about PEG-coated liposome NCs [81] have also been used against parasites, however their short-life in physiological conditions has become a major concern. Liposome based nanoformulations of halofantrine has also been studied for malaria treatment and found that due to the uncontrolled doses of halofantrine, it caused the cardiac side effects (cardiac arrhythmias) explained by Wesche *et al.* [118] and it required the correct administration which was explained by Bouchaud *et al.* [119].

Jacob *et al.* has report the antiplasmodial prospective of metal oxide NPs such as  $Al_2O_3$ ,  $ZrO_2$ ,  $Fe_3O_4$ ,  $MgO$  and  $Fe_3O_4$  and later coated by PDDS against *P. falciparum* infection where they mentioned coated NPs exhibited superiority as antiplasmodial activity over non-coated metal oxide [120]. But only PDDS coated  $Fe_3O_4$  NP has shown a better result than other four metal oxides by showing low  $IC_{50}$  value. However, metal oxide NPs are found not suitable for abrogating *P. falciparum*, since they are not biodegradable.

Further, Singh *et al.* have studied anti-malarial activity by using lipid nanoemulsion of the size range of 10–200nm combined with Primaquine (PQ) [121]. They reported that this oral nanoemulsion with antimalarial drug provides low dose and enhanced bioavailability of the drug in the liver.

Few more recently reported research works for suppressing malaria infection have been listed in **Table 1**.

**Table 1.** Nanodrug carriers against Malaria infection.

Material	Type of nanocarrier	Drug used	Purpose	Reference
Poly- $\epsilon$ -caprolactone (PCL)	NCs	Artemether (ATM)	Investigated free drug and efficiency of drug loaded NCs on <i>P. berghei</i> infected mice to improve oral efficacy and to reduce cardiovascular toxicity. ATM-NCs have shown a reduced signal of QT (28%) and QTc (27%) interval compared to free ATM during ECG.	Souza <i>et al.</i> [122]
Poly- $\epsilon$ -caprolactone (PCL)	NCs (~200nm)	Curcumin, Quinine	Investigated codelivery of both drugs via polysorbate 80 functionalized NCs on <i>P. falciparum</i> and evaluated the toxicity level of the drugs-NC on <i>Caenorhabditis elegans</i> . The worm has shown 30% improved life span and no effect on reproduction after the treatment with nanoformulation compared to free drugs.	Velasques <i>et al.</i> [123]
Poly- $\epsilon$ -caprolactone (PCL), Eudragit®	NCs	Curcuma aromatic, Quinine	Developed a set of cationic anionic based NCs with quinine present in the oily core composed of Curcuma oil by changing different reaction parameters like drugs conc., precursor conc., amount of surfactant against <i>P. berghei</i> infected mice by using polymers PCL Eudragit® and showed an improvement in physicochemical characteristics, drug loading efficiency with better quinine photostability.	Gomes <i>et al.</i> [124]
PLA-PEG diblock copolymer, Poly- $\epsilon$ -caprolactone (PCL)	NCs	Halofantrine chlorhydrate	Evaluated the toxicity of halofantrine in cardiovascular system by encapsulating the drug in NCs where a drug with PCL NC has shown better efficiency compared to the drug with PLA-PEG formulation in <i>P. berghei</i> infected mice.	Leite <i>et al.</i> [125]
Chitosan, Polyvinyl alcohol	Solid lipid NPs bellow 500 nm	Chloroquine diphosphate	Developed heparin functionalized Chloroquine loaded solid-lipid NPs thereby investigated efficiency against <i>P. falciparum</i> .	Muga <i>et al.</i> [126]

Chitosan hydrochloride	NCs	Triclosan an anti-microbic agent	Developed Triclosan loaded colloidal chitosan nanocarrier as an oral delivery system against malaria <i>P. falciparum</i> infection and also suggested this chitosan nanovehicle as a potential carrier with controlled release of the drug.	Maestrelli <i>et al.</i> [127]
Dextran	NPs Less than 70nm	CQDP	Developed drug loaded with Dextran NP which performed potential in antimalarial activities on <i>P. falciparum</i> by depositing in food vacuoles of parasites as well as intercellular uptake analysis and also suggested nanoformulation can perform prolong drug release via intravenous drug administration route.	Kashyap <i>et al.</i> [128]

### 2.3. Nanotechnology in immunology

The research in the field of modern medicine has attained a new advanced era with the discovery of vaccines [129] by receiving a solution to defeat pathogens against the human race. However, in spite of this greatest achievement over microbes development of potent vaccines against several emerging and re-emerging diseases [130] continue to be a formidable challenge. As a result, the limitations such as antigen selection, proper antigen delivery and adjuvant engineering approaches are used to advance the vaccine development. Nanotechnology has attained significant importance in the past few decades in the area of biomedical sciences especially in “nano vaccinology”.

It has been documented by Smith *et al.* and Kasturi *et al.*, that NPs (NPs) have inherent immunomodulatory functions thereby acting as co-adjuvants, stimulating immunological reactions. In addition, NPs can be incorporated with other immunodominant structures such as Toll-like Receptors (TLRs) ligands, cell-targeting moieties or other biologically active mediators, to enhance vaccine efficacy [86,131]. Kasturi *et al.* has reported about a NP based vaccine using PLGA of approximately 300nm sized enclosing the TLR ligands either R837 (TLR7) or MPL (TLR4) or both together with an antigen and found out that antigen and TLR ligands together in single NP didn't show much good antibody response like the antibody responses given by antigen, TLR ligands in separate NPs [131].

The NPs enable efficient cross-presentation of peptides [132] and trigger the activation of APCs like dendritic cells according to Fahmy *et al.* and Mant *et al.* [133], respectively.

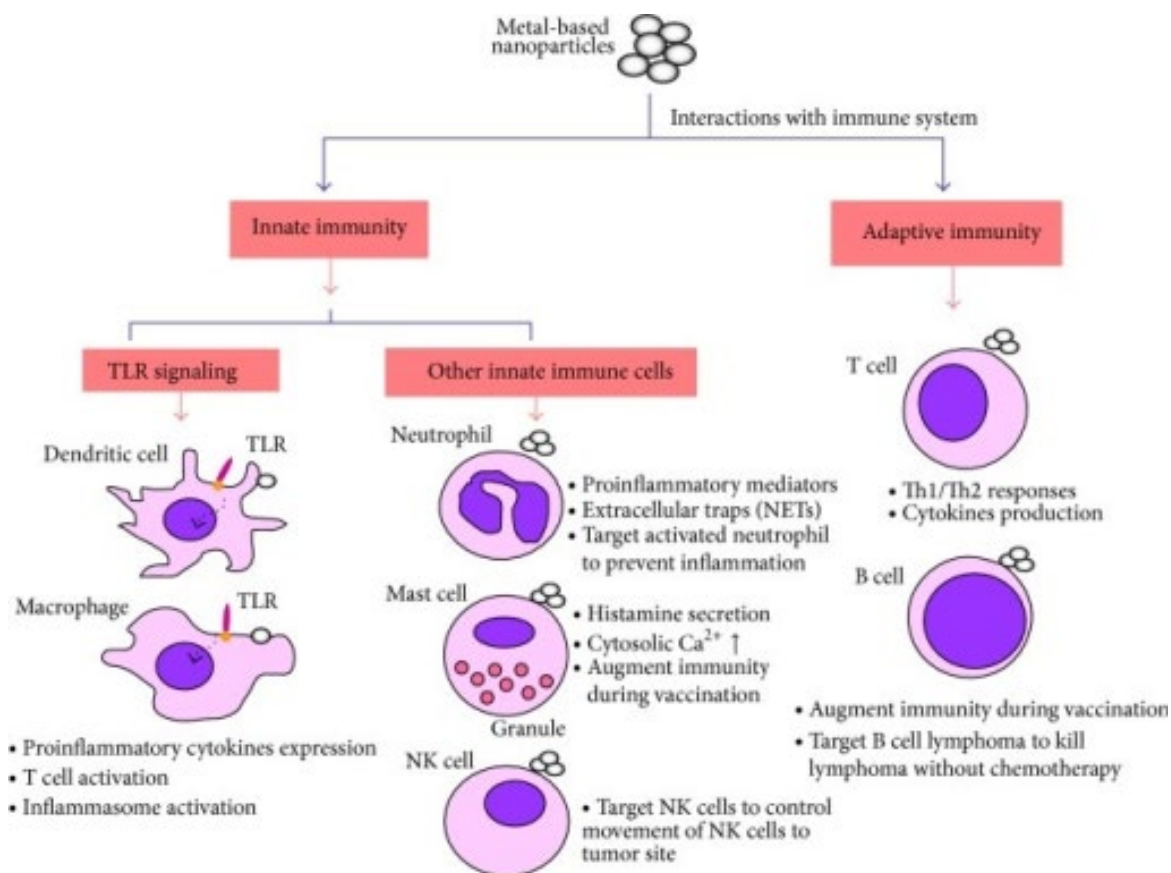


**Figure 1.15.** Metal NPs interaction in Immune system [134].

Intrinsically, MNPs have been shown to modulate immune responses via TLR signaling. Lucarelli *et al.* and Cui *et al.* have explained that Titanium dioxide ( $TiO_2$ ) and Zirconium dioxide ( $ZrO_2$ ) NPs were found to regulate TLR 7 and TLR 10 transcripts in human macrophage U-937 cells and TLR 2 and TLR 4 transcripts in the mouse liver cells [111,112]. However, Petrarca *et al.* suggested that in spite of several benefits of these MNPs, some of the MNPs might induce non-specific immunological reactions, cell cytotoxicity, immuno suppressant and autoimmunity. They may even cause morphological alterations of the immunologically active tissues which are basically attributed to their physical (size) and chemical characteristics (through released ions) [137]. It is, therefore, pertinent to carefully select and effectively engineer the MNPs, which have greater antigen carrying capability together with immunostimulatory properties for vaccine development.

According to Vigneshwaran *et al.* and He *et al.*, a metal oxide such as Zinc Oxide NP ( $ZnO$ ) have been widely used for several biomedical applications including bioimaging, drug

delivery, due to their excellent biocompatibility with human body, non-toxicity, stability and cost effectively [114,115]. Moreover, ZnO has been well documented as an FDA approved material as mentioned by Emamifar *et al.* [140] and has already been shown to have antibacterial, antifungal and UV protection features. As mentioned by Chang *et al.*, ZnO NPs have been proved to induce MyD88-dependent pro-inflammatory cytokines production via a TLR signaling pathway [141]. Also, Cho *et al.* reported, multifunctional core-shell NPs comprising of as core ZnO have been effectively used in DCs based cancer immunotherapy [142]. Further, elemental Zn has been found to regulate human body growth, bone metabolism, collagen synthesis and vision and can be easily excreted out from the body through various routes including sweat and urine thereby reducing the chances of accumulation within the body. Previous studies highlight that spherical particles larger than 200nm size can be filtered out by bone marrow, liver, and spleen while particle size smaller than 10nm can be efficiently filtered by the kidney as reported by Liu *et al.* [143].

Hence, it has been postulated that the ZnO NPs in the range of 10-200nm might be considered as an optimal size range for drug delivery. As reported by Paik *et al.*, and Meier *et al.*, the formation of hollow, porous mesoporous NCs with precise size have attracted researchers due to their exclusive capacity for encapsulation of a wide range of biomolecules including drugs, proteins, nucleic acids together with sustained release of these encapsulated biomolecules at the target sites with high efficiency [143,144]. Recently, Kupferschmidt *et al.* has reported, mesoporous SiO<sub>2</sub> NPs (MSNs) have been shown to efficiently potentiate the immunological response against an antigen and hence lead to a decrease in the antigen amount needed for vaccine formulation [146]. Additionally, MSNs have been shown to be an attractive vehicle for targeted delivery and release of biomolecules such as proteins, peptides, drugs and nucleic acids reported by Heidegger *et al.* and Kupferschmidt *et al.* [147,148].

## **2.4. Ova protein in immunology**

Ovalbumin shortly Ova, is basically a protein extracted from the chicken egg has plenty of applications in both *in-vivo* and *in-vitro* pathways due to its nontoxic, easy availability and cost efficiency. In immunology, for the analysis of antigen specific immune response, Ova protein is used as T cell dependent antigen. During the *in-vivo* study, if there is a condition of absence of an immune response, the Ova antigen will not cause any toxic effect on the living organism [149].

Zhang *et al.*, reported the immunization of Ova antigen in mice model for 10 days where ova specific proliferation of lymphocyte was inhibited by cathepsin D inhibitor pepstatin A and thereby suppressed both cellular responses Th1 as well as Th2. Their study has revealed the role of Ova to activate the inhibitor activities as there was no direct influence of the cathepsin D inhibitor to the function of lymphocyte *in-vivo* [150].

Slütter *et al.*, have studied on the efficiency of crosslinker CpG DNA over tripolyphosphate (TPP) to design Ova encapsulated TMC (N-trimethyl chitosan) NPs and its capacity to induce Th2 response for antibody response in mice after nasal administration [151]. In another work Slütter *et al.* and Keijzer *et al.*, have reported a comparative study of physicochemical properties of NPs by developing three sets of NPs loaded with Ova such as PLGA-Ova, TMC (N-trimethyl chitosan)-Ova and PLGA/TMC-Ova in mice for the purpose of nasal vaccination [152,153]. Compared to other two NPs, Ova loaded TMC has shown a better immune response after nasal administration [152]. PLGA NPs are efficient to enhance CD4<sup>+</sup> T-cell immunoregulatory responses thereby inducing Foxp3 expression present in the nasopharynx of lymphoid tissue as well as cervical lymph nodes [153].

Rahimian *et al.* have reported about an Ova antigen polymeric delivery mechanism where they have developed a spherical polymeric nanocarrier poly(lactide-co-hydroxymethyl glycolic acid) a hydrophilic polyester of diameter 300nm to 400nm to encapsulate Ova to dendritic cells in mice by covalently binding fluorescent dyes both to the nanocarrier and the antigen Ova. Antigen loaded NPs showed efficient CD8<sup>+</sup> T cells response in lymph nodes than bare protein antigen [154]. In a similar way, Kim *et al.* have designed synthetic vaccine nanomaterial of polymer PGA, 20-70nm in diameter for the lymph node delivery of antigen Ova and TLR3 in tumour bearing mice. The sole purpose of these synthetic vaccine nanomaterial to trigger the immune responses in lymph nodes as well as improve the adaptive and innate antitumor immunity [155]. Anne *et al.* have also reported Ova-PLGA with TLR3 and also without TLR3 to prompt immune response for the intradermal administration of vaccines [156]. A new synthesis route of Ova loaded  $\gamma$ -PGA NPs for inter cellular pathway of cross presentation efficiency has been reported by Mukai *et al.* [157].

Few more recently reported research works for Ova protein incorporation with NPs in immunology have been listed in **Table 2**.

**Table 2.** Ova protein incorporation with NPs in immunology.

Material	Type of nanocarrier	Drug used	Purpose	Reference
$\gamma$ -PGA, cholesterol-amine polyinosinic-polycytidylic acid	NPs Diameter of 120nm	Ova, TLR3	Developed vaccine NPs loaded with Ova for improvement for both cancer vaccine and antitumoral immune response in lymph nodes. After a great cellular uptake by lymph nodes, these antigen loaded NPs instigate high pro-inflammatory cytokines and also Immunization of these loaded NPs induced cancer therapy essential natural killer cell expansion with the response of CD8 <sup>+</sup> T cell thereby preventing the growth of a tumor.	Kim <i>et al.</i> [155]
$\gamma$ -PGA	NPs Size ~200nm	Ova	Developed $\gamma$ -PGA NPs with Ova antigen boost up a fusion of endoplasmic reticulum endosome for cross-presentation. Loaded NPs again retrotranslocated through translocon sec 61 from endoplasmic reticulum endosome to cytoplasm	Mukai <i>et al.</i> [158]
Poly(propylene sulfide)	NPs Size ~30nm	Ova	Described Pluronic-stabilized NP covalently bound with Ova delivered via lungs instigate T cell response. Adjuvant CpG influenced cellular uptake of antigen by lungs thereby enhanced antigen cross presentation and protect mice morbidity due to infection of influenza virus.	Nembrini <i>et al.</i> [159]
1,2-dimyristoyl-sn-glycerol-3-phosphocholine, 1-palmitoyl-2-oleoyl-sn-glycerol-3-phosphocholine	Lipoprotein nanodiscs	Ova, Peptide	Designed lipoprotein nanodiscs for multiloading of MPLA, CpG, TLR4 agonist, TLR9 agonist and combined with Ova as well as some peptides improved dendritic cells activation, promote strong humoral responses, IgG response, reduction of plasma cholesterol rate upto 17-30% and also promote responses of CD8 <sup>+</sup> T cell by 8fold.	Kuai <i>et al.</i> [160]

## 2.5. Nano carriers against cancer therapy

In modern field of scientific research, the field nanotechnology has achieved rapid development as it emphasizes on the coalescence of diverse disciplines of science under one distinct domain. The constant effort of nanotechnology to improve cancer therapy by eradicating the malignant cells and by controlling toxicity of therapeutics on unaffected cells are going on and recently progresses in this aspect prove the potential of reduced size material in cancer therapy. Although NPs are used as drug delivery vehicles [161], diagnostics of cancer cell [162], therapeutics [163] etc.

Huang *et al.* reported about the gold nanorods (aspect ratio of 3.9) for the use as a contrast agent. They have synthesized gold nanorods with the help of modified seed-mediated growth approach and conjugate with antiepidermal monoclonal antibodies against oral epithelial HOC313 clone8 and HSC3 malignant cell lines along with epithelial HaCat non-malignant cell line. Gold nanorods were synthesized by modified seed-mediated growth method and used as contrast agent in this case. However, due to the presence of over expressed EGFR (anti-epidermal growth factor receptor) on the cytoplasmic membrane of infected cells, the nanorod-antibody conjugation attached directly there and gold nanorods scattered red light in dark field laboratory microscope, thus clearly distinguished the malignant cells from non-malignant cells [164]. Similar work has reported by El-Sayed *et al.*, where they have developed Au NPs conjugated with anti-EGFR antibodies using HaCat, HOC313 clone8, and HSC3 cell lines. The nanoconjugate bind to the malignant cells with greater affinity than non-malignant cells. They have suggested that nanoconjugates could be used as molecular biosensor due to their surface plasmon resonance scattering imaging as well as absorption [165]. Chen *et al.*, have also reported using Au nanocage about 45nm as a photothermal agent for treating cancer by attaining absorption cross section area of  $3.48 \times 10^{-14} \text{ m}^2$  in NIR region. The conjugation of nanocage with monoclonal antibodytargeted to over expressed EGFR present on the surface of SK-BR-3 a breast cancer cell line [166].

Nadine *et al.* have shown that the strong absorbance for the SWNTs were used for optical simulation the nanotubes inside the living cells. They have also reported that for oligonucleotides the oligos can be translocated into the cell nucleus by rupturing caused by NIR laser pulses as the repeated NIR laser pulse radiation can cause cell death due to localized heating of SWNTs. They have reported that the light sources from 700 to 1100nm range can be used for efficient excitation of SWNTs *in vitro* [167].

Substantial importance of magnetic NPs for cancer treatment as heat nanomediator have been discussed by Hyun Ball *et al.* while designing 30nm sized iron oxide nanocubes stabilized by surface modification of chitosan oligosaccharide. This conjugate nanostructure of size  $103 \pm 15$  have improved the total magnetic moment thereby exhibiting 2614W/g specific loss power value greater than the value 83W/g of super paramagnetic iron oxide NPs available commercially. Low toxic nanoconjugate exhibit exceptional antitumoral behavior by decreasing the number of target malignant cells in A549 tumor-bearing mice [168]. Creixell *et al.* have also developed magnetic NP iron oxide heaters conjugated to EGF (epidermal growth factor) which leads to a reduction of cell viability without a necessity to raise the temperature. They have reported that these MNHs kill cancer cells by altering magnetic fields which are considered impossible in previous conditions [169]. Chu *et al.* have synthesized Fe<sub>3</sub>O<sub>4</sub> NPs of different shapes like hexagonal, spherical and wire shaped, functionalized with PEG for both *in vitro* and *in vivo* esophageal cancer cells. These NPs showed low toxicity without harming the structure of the cells. At 808nm irradiation, the cell viability can be affected by damaging cellular organelles by the magnetic NPs. Esophageal tumor growth in mouse inhibited due to the photothermal effect possessed by these functionalized NPs [170].

Liang *et al.* have fabricated a photosensitizer of porphyrinlipid bilayer cerasomes with the help of sol-gel as well as self-assembly process. This conjugate structure has performed drug loading efficiency 33.46% superior to the physical entrapment of cerasomes which is less than 10% [171].

Cheng *et al.*, have developed conjugate of PEGylated Au NP of diameter 32nm to encapsulate a PDT hydrophobic drug Silicon phthalocyanine 4 to the photodynamic therapy (PDT) site. The release mechanism they have checked together *in vitro* and *in vivo* tumor bearing mice model [172].

Nam *et al.*, have engineered smart Au NPs of size 10nm by changing pH for both positive and negative charges and the electrostatic attractions of the Au NPs resulted by accumulating them in the mild acidic intercellular atmosphere. Au NPs have performed an efficient killing of cancerous cells with an intensity threshold of 5W/cm<sup>2</sup> [172].

Chu *et al.*, have developed quantum dots of CdTe and CdSe coated by different silica thickness layers. They convert light energy to the heat form at laser radiation of 671nm both in case of *in vivo* as well as *in vitro*. Silica coated CdTe inhibit the growth of mouse melanoma tumors followed by after laser irradiation [174].

## 2.6. Paclitaxel drug loaded nanocarriers against cancer therapy

Amid all other anticancer therapeutic agents, Paclitaxel is the most diversely used and known for its outstanding effect against a number of solid tumors malignant cells like breast, lung, ovarian, cervical, pancreatic cancer [175] etc. However, like all other anticancer therapeutic agents, it is not devoid of side effects. Severe side-effects are associated with this toxic anticancer drug. Though the advanced nanotechnology research domain has come out with one solution for this complicated cytotoxic problem with its tremendous research achievement in a very limited period of time, many researchers have recently reported that the side effect caused by the Paclitaxel response to the normal body tissues can be minimized by encapsulating drug inside a nanocarrier or conjugating the drug on the surface of a nanocarrier by physical or chemical conjugation.

Tao *et al.*, have designed hollow nanosphere of chitosan (diameter ~ 150nm) functionalized by alginate (shell thickness ~ 20nm) synthesized by hard template method for the co-delivery of two different anticancer drugs, one was doxorubicin loaded on the negatively charged surface of the nanosphere by electrostatic interaction and the other drug paclitaxel was loaded inside the nanosphere adsorption. They have investigated the cytotoxicity effect of the carriers and inhibition effect of these drugs loaded nanostructures on the lung cancer cell line A549 and they reported that these nanospheres are accumulated in the cytoplasm and its biodegradable in nature [176]. Shixian *et al.*, have also reported about co-delivery of antimalarial drugs doxorubicin and paclitaxel by using nanodrug carrier of triblock copolymer methoxypoly(ethylene glycol)-b-poly(L-glutamic acid)-b-poly(L-lysine) functionalized with deoxycholate (mPEsG-b-PLG-b-PLL/ DOCA). Cytotoxicity assays have been checked on lung adenocarcinoma A549 cell line and combination drug therapy has shown the synergistic effect to the growth of cancer cell apoptosis [177].

Zhang *et al.* have synthesized a multifunctional NP based on polyphosphoester and loaded paclitaxel physically as well as the same drug conjugated chemically to the NP. They have expected the physically loading paclitaxel could initiate the killing of tumor cells thereby controlling the growth and the chemically conjugated drug can perform gradual release for a longer period of time in tumor tissues [178].

Yao *et al.* have synthesized two sets of nanocarriers to carry drug paclitaxel, such as PEG-PLA and PEG-PLA-Folic acid. They have studied *in vitro* slow release effect and *in vivo* pharmacokinetic and tissue-distribution studies by using three ovarian cancer cell lines SK-

OV-3, A2780 and HO8910 [179]. Xiaolin *et al.* have designed block copolymers of tetrandrine (Tet) coloaded/amphiphilic methoxy poly(ethylene glycol)–poly(caprolactone) for the delivery of paclitaxel against mice hepatoma H22 cells [180].

Rejinold *et al.* have formulated Mn doped ZnS NPs to coat paclitaxel drug and to check its efficiency on both *in-vivo* as well as *in-vitro*. MTT assay, apoptosis assay as well as DNA fragmentation analysis have performed with paclitaxel/Mn/ ZnS NPs with cell penetration peptides like PEN, pVEC, and R9. *In-vivo* studies have been done on breast cancer xenograft where R9/Mn/ ZnS NPs have performed better than other conjugates [181].

Marcial *et al.* have analyzed the effect of three lipid formulations like solid lipid nanostructures, lipid nanocarriers and nanoemulsion by hot melting homogenization and ultrasonication to load drug paclitaxel. Lipid nanocarriers have performed efficiently on breast cancer cell lines MCF 7 (with IC<sub>50</sub> 25.33 ± 3.17 nM) and MDAMB-231 (with IC<sub>50</sub> 2.13 ± 0.21 nM) [182].

Mo *et al.* have developed a nanocarrier of folic acid-PEG-p-phosphonated calixarene for co-drug delivery of drugs paclitaxel and carboplatin against Ovarian cancer cells SKOV-3 cells [183]. Rosière *et al.* have formulated a solid lipid nanocarrier of PEG-Chitosan (diameter 250nm) to encapsulate drug paclitaxel. For *in vitro* they have used M109-HiFR and HeLa cell lines and for *in vivo* M109 cell line has been used [184]. Gupta *et al.* have designed solid lipid core nanocarriers for co-delivery of paclitaxel and erlotinib against NCI-H23 cell line *in vitro* by pH dependent release of drugs [184]. Liu *et al.* have reported about the formation of nanocrystals (D- $\alpha$ -tocopheryl polyethylene glycol 1000 succinate) for the delivery of paclitaxel. Effects of these nanocrystals have been checked on H460, NCI/ADR-RES, KB cell lines [185].

Song *et al.* have conjugated hyaluronic acid-disulfide-vitamin E succinate nanocarrier which is redox sensitive for loading paclitaxel against lung cancer therapy. The efficiency of drug loaded nanoconjugate have been investigated by using CD44 over-expressed A549 cells in both *in vivo* and *in vitro* [185].

Xiaolin *et al.* have mentioned about the formation of core shell PEG-PCL polymeric NPs by precipitation method for the co-delivery of paclitaxel and tetrandrine against BGC-823 gastric cancer cell line [186]. Jiang *et al.* have reported self-assembled vitamin E succinate NPs for co-delivery of paclitaxel as well as tetrandrine against MCF 7 cells and MCF 7/Adr cells (breast carcinoma) *in vitro* study [187]. Mingji *et al.* have reported about the co-delivery of chemotherapeutic agents paclitaxel and siRNA to A549 cells by preparing polyethyleneimine-block-poly lactic acid NPs (with size 82.4nm), where paclitaxel was encapsulated in the core and siRNA conjugated to the NP through electrostatic interaction [188].

Few more recently reported research works for Paclitaxel encapsulated nanodrug carrier for cancer therapy have been listed in **Table 3**.

**Table 3.** Paclitaxel encapsulated nanodrug carrier for cancer therapy.

Material	Type of nanocarrier	Drug used	Purpose	Reference
DNA, Cyclo(Arg-Gly-Asp-d-Phe-Lys; cRGD)	Biocomplex of DNA nanotube-peptide	Paclitaxel, DOX	Developed a biocomplex with high drug loading efficiency and suggested that this biocomplex can be efficient for multidelivery of different drugs than the traditional multidrug-delivery system, transport of receptor, cell imaging and drug delivery.	Xiaoting <i>et al.</i> [189]
mPEG-b-pAsp	Solid Lipid Core NCs Size 195nm	Paclitaxel, Erlotinib	Developed a multidrug carrier with high loading efficiency, pH dependent (high release in acidic pH 5) sustain release, inhibit NCI-H23 cell line as well as with lower IC <sub>50</sub> value 50 fold lower than the free drugs.	Gupta <i>et al.</i> [190]
Polydopamine Linoleic acid Arginine	Colloidal capsules Size 100 nm	Paclitaxel, DOX	Developed NC has been used for cytosolic delivery by loading hydrophobic Paclitaxel in the linoleic acid core while DOX was absorbed on the PDA shell against Hep-G2 cells	Tao <i>et al.</i> [191]
Triblock copolymers F127 (PEO106PPO7 OPEO106) micelle	Micelle Size ~90 nm	Paclitaxel, Functionalized CuS nanodisk (photothermal agent)	Developed a NC for coencapsulation of CuS nanodisks with paclitaxel and can perform high stability, biocompatibility, less toxicity with great NIR absorbance and also exhibit sustained drug release pattern stimulated via NIR-photothermal irradiation. Drug encapsulation efficiency showed 41.25% and showed remarkable antitumoral effect in mice.	Jian <i>et al.</i> [192]

Poly(lactide)-poly(ethyleneglycol) (PLA-PEG)	Magnetically responsive nanocarriers	Paclitaxel, Nanocrystal organophilic iron oxide (7nm)	Designed a magnetic nanocarrier for codelivery of drug, iron oxide and performed a good loading efficiency with sustained responsive to the alternating magnetic field, cytotoxicity against A549 cells which is more than free drug. The performance of the nanocarrier on malignant cells further improved by functionalized with cysteine TAT peptide.	Koutsiouki <i>et al.</i> [193]
Chitosan Amino acid derivatives	NCs	Paclitaxel, green fluorescent protein, Nile Red, Casp-3 protein	Designed chitosan aminoacid derivative nanocarriers linoleic Acid as the core for multiple deliveries of drug and protein to HeLa cells with improved stability, biocompatibility, biodegradability, lower IC50 value and good % of apoptotic cells than aminoacidfunctionalized gold NPs and mondrugdelivery system as well.	Wu <i>et al.</i> [194]
Chloroauric acid Pluronic-b-poly(L-lysine)	NPs	Paclitaxel	Developed gold NPs surface modified by Pluronic-PLL encapsulating drug for chemo-photothermal therapy where irradiating MDA-MB-231 malignant cells with NIR light and <i>in vivo</i> study confirmed these drug loaded nanocarriers have possessed better biocompatibility, more cytotoxicity by improving cellular uptake than free drug.	Sun <i>et al.</i> [195]

### 3. The motivation behind this work

This dissertation consists of three parts i.e., designing of polymeric and inorganic NCs followed by characterizing them and application of those NCs in different biomedical fields. Basically, three different biomedical areas of application have been included in this research work and those are Malaria, Immunology and Cancer therapy.

***Application field-Malaria:*** A polymer with moderate degradation rate could advance the sustained delivery of anti-malarial drugs in physiological conditions under periodic enhancement of body temperature. Using the nanoemulsion droplets of lipid molecules were found not possible since without using surfactants the emulsion cannot be formed and it is toxic in nature. Thus extensive efforts have been made to find out a suitable nanocarrier for anti-malarial drugs to facilitate the treatment and for killing the *P. falciparum* where each having individual drawbacks. It is worth mentioning that, till date only the poly(N-Isopropylacrylamide) based copolymers were reported which control the temperature dependent release of drugs [196] but not for the hollow PCL capsules. The disadvantages of poly(N-Isopropylacrylamide) for treatment of malaria is that the critical transition temperature ( $T_c$ ) of drug release for this polymer is  $32^\circ\text{C}$ , which is very low compared to the normal body temperature ( $37.4^\circ\text{C}$ ) and hence poly(N-isopropylacrylamide) may not useful for control release of DHA/CQDP for treatment of the *P. falciparum* as most of the drug released below the body temperature, rather the excess release of drugs from poly(N-Isopropylacrylamide) at low temperature ( $33^\circ\text{C}$ ) caused side effects and increased the resistance of drugs to the *P. falciparum* [197]. Not to be ignored the issue with all antimalarial drugs is their bioavailability, which is very less in conventional drug administration system. However, the main challenge occurred when all *Plasmodium* species have shown the resistivity towards the available antimalarial drugs and an overdose of these drugs resulting with side effects like gastrointestinal problems, stomach ache, itch, headache, postural hypertension, nightmares, blurred vision etc. Therefore, engineering of an appropriate drug carrier is becoming very essential.

***Application field-Immunology:*** In the past decade diverse nanostructure materials irrespective of polymers or inorganic materials have been administered as adjuvant delivery systems. Inorganic NPs such as (zinc oxide, titanium dioxide, iron oxide, quantum dots etc.) [88] possess many advantages due to rigid structures, long shelf life and the capability to tailor the immune-stimulatory property of an antigen and also to interact in diverse ways with cellular

biomolecules and facilitates entry into the cell. Despite several benefits of MNPs, emerging evidence suggests that some of the MNPs might induce non-specific immunological reactions, cell cytotoxicity, immunosuppression and autoimmunity, morphological alterations of the immunologically active tissues [137]. It is, therefore, pertinent to carefully and effectively engineer the NPs with greater antigen carrying capability together with immunostimulatory properties for vaccine development. Additionally, for *in vivo* application of nanomaterials, there are few immunology consequences like immune-mediated destruction or rejection, induced by a defensive immune reaction ensuing in the removal of the nanomaterials and the next is immunotoxicity, resulting by damaging the immune system with effecting pathological changes and immunocompatibility, not related to immune response [198]. While delivering Ova antigen in this current research work, is predominantly released from the hollow core (or pores), to avoid a burst-effect for Ova release which can be observed in case of SBA-15 with non-functionalized and relatively large mesoporous size (above 10nm).

***Application field-Cancer Therapy:*** Polymer is the most promising and potent candidate when the focus goes to drug delivery because of their biocompatibility with living cells, biodegradability in the physicochemical environment together with their convenient engineering procedure by encapsulating or attaching therapeutic agents as well as other biomolecules inside or on the surface of it. Life threatening cancer therapy includes all therapeutics with a lot of side effects. Administration of anticancer drugs is effecting healthy normal cells along with malignant subsequently causing unavoidable severe side effects. In that concern, a carrier with all required properties for delivering the anticancer therapeutic agents during the treatment of cancer is becoming very much urgent. The biggest challenge for the utilization of anticancer therapeutic agents is their solubility, as few of them are non-water soluble. Widely used drug Paclitaxel is also possessing the same characteristic. To improve the solubility of this drug non-ionic surfactant Cremophor EL and dehydrated ethanol can add to it which in return can cause clinical complications [59]. Additionally, progressive resistance of ovarian carcinoma A2780 cell line against Paclitaxel [199] is becoming a serious medical issue and to minimize all these limitations of the anticancer therapeutic appropriate delivery vehicle is becoming necessary.

#### 4. Objectives of this dissertation

1. Designing of core-shell NPs of SiO<sub>2</sub> as template coated with PCL and followed by the formation of hollow mesoporous PCL NCs and systematic characterizations of these NCs to analyze their chemical, physical properties.
2. Loading of hollow mesoporous PCL NCs with two antimalarial drugs (DHA and CQDP) and checking their efficiencies in suppressing malaria infection with *P. falciparum*.
3. To study the drug release efficiency and cell inhibition of hollow mesoporous PCL NCs while loaded with antimalarial drug Sulfadoxine against *P. falciparum*.
4. Designing of mesoporous ZnO NCs and study their chemical physical properties with all characterization results.
5. Mesoporous ZnO NCs incorporated with protein Ova for the enhancement of immunological responses.
6. Mesoporous ZnO NPs incorporated with different drugs (DHA, CQDP, SD, Paclitaxel, DOX) for cancer therapy.
7. Designing of core shell PCL-mZnO NPs (mZnO as core and PCL as shell) followed by porous PCL NCs by template removing technique and characterize their physical, chemical properties.
8. Analysis of biocompatibility and interaction of these porous PCL capsules with anticancer cell lines by encapsulating antimalarial drugs.

## **Chapter 2: Materials and methods: Experimental procedures and Characterization techniques**

### **2.1. Introduction**

### **2.2. Materials and reagents used for experiments**

### **2.3. Experimental procedure**

#### 2.3.1. Synthesis procedures

### **2.4. Characterization Techniques**

#### 2.4.1. X-Ray Diffraction (XRD)

#### 2.4.2. Electron microscopic imaging techniques (SEM, FESEM and TEM)

#### 2.4.3. Energy dispersive X-ray spectroscopy (EDS or EDX)

#### 2.4.4. Thermogravimetric analysis (TGA)

#### 2.4.5. Differential scanning calorimetry (DSC)

#### 2.4.6. Brunauer-Emmet-Teller (BET)

#### 2.4.7. Fourier Transform Infrared (FTIR) spectroscopy

#### 2.4.8. Zeta potential analysis

#### 2.4.9. Confocal microscopy

#### 2.4.10. Ultraviolet-Visible spectroscopy (UV-Vis)

#### 2.4.11. Fluorescence activated cell sorting (FACS) analysis

#### 2.4.12. Multimode microplate reader

# Chapter 2

## Materials and methods:

### Experimental procedures and Characterization techniques

#### 2.1 Introduction

This chapter of the dissertation encloses three parts. First part includes all materials and reagents used for nanomaterial synthesis with their purity and brand names, second part includes details of all experimental procedures to formulate the nanomaterials and third part includes different characterization techniques. All these three parts have been explained in detail in the subsequent sections.

In this work, both organic and inorganic mesoporous NCs have been synthesized by using different synthesis methods like template removal method, by using surfactant and without using surfactant etc.

The sole persistence of these mesoporous nanostructures is to introduce them as proficient carriers for various drugs and biomolecules in the field of nanobiotechnology. Therefore, an immense characterization of various properties, efficiencies and efficacy of these produced mesoporous NCs have been required.

The utilized characterization techniques are **X-ray diffraction (XRD)** to study crystallinity of the nanomaterials; to study morphology, size, and shape of the nanomaterials **Scanning electron microscopy (SEM)**, **Field emission electron microscopy (FESEM)** and **Transmission electron microscopy (TEM)** techniques have been used; thermal properties like weight loss with an increase of temperature, heat flow, phase transition etc., have been checked by using **Thermogravimetric analysis (TGA)** and **Differential scanning calorimetry (DSC)** techniques. **Energy dispersive X-ray spectroscopy (EDS or EDX)** used for the elemental study of these nanomaterials. **Brunauer-Emmet-Teller (BET)** and **Barret-Joyner-Halenda (BJH)** analysis have been followed to determine specific surface area and pore size analysis of the mesoporous NCs respectively. To identify chemical bonding and

functional groups present in the polymer and inorganic NCs **Fourier Transform Infrared (FTIR)** spectroscopy technique has used. To determine the surface charge of the NCs **Zeta potential** analysis has been used. **Photoluminescence (PL) spectroscopy** has been used for the determination of a chemical property of NCs. To study the vibrational and rotational mode of nanomaterials **Raman spectroscopy** technique has been used.

For the biological applications, NCs were loaded with drugs, biomolecules and **Confocal microscope** technique has been used to determine the loading efficiency of porous NCs. **Ultraviolet-Visible spectroscopy (UV-Vis)** has used to calculate the concentration of drugs and other biomolecules inside the nanocarriers. Biocompatibility of prepared mesoporous NCs is very essential to use it in biomedical applications. Biocompatibility of NCs has studied with different cell assays. Different cell based studies have been performed to establish the proposed NCs as an efficient carrier of various biomaterials and all these experimental procedures have been represented in the consecutive sections of this chapter.

## 2.2. Materials and reagents used for experiments

In this section, all chemicals, solvents and reagents used for the synthesis purpose have been mentioned in tabular form with make and percentage of purities. All chemicals are used with original purity as purchased and further purification was avoided.

**Table 1.** List of chemicals, solvents and reagents used for nanomaterial synthesis

Sl. No.	Name	Make	Purity (%)
1	TEOS (Tetraethyl Orthosilicate)	Sigma Aldrich	98
2	Ammonium hydroxide (NH <sub>4</sub> OH)	Sigma Aldrich	99.9
3	Ethanol	SRL	98
4	PCL (Poly caprolactone)	Sigma Aldrich	99.9
5	Igepal CO_50	Sigma Aldrich	99.9
6	Hydrofluoric acid (HF)	Fisher Scientific	98.3
7	Acetone	SRL	99
8	Isopropanol	SRL	99.3
9	Rhodamine 6G	Sigma Aldrich	95

10	CQDP	Sigma Aldrich	98
11	DHA	Sigma Aldrich	99
12	Sulfadoxine (SD)	Sigma Aldrich	95
11	RPMI 1640	Sigma Aldrich	99.8
12	Parasitic cells	Human	100
13	Zinc acetate dihydrate ( $Zn(OOCH_3)_2 \cdot 2H_2O$ )	Alfa Aesar	98.5
14	Sodium hydroxide (NaOH) pallet	SDFCL	97
15	Ovalbumin (Ova)	Sigma Aldrich	99
16	Paclitaxel (Ptaxel)	Sigma Aldrich	99

## 2.3. Experimental procedure

In this work, two organics and one inorganic porous NCs have been synthesized, i.e.,

- Hollow porous PCL NCs by removing template  $SiO_2$  NPs.
- Mesoporous ZnO NCs (mZnO) without using any template.
- Hollow mesoporous PCL NCs by removing template mZnO.

### 2.3.1. Synthesis procedures

#### (A) Synthesis of hollow mesoporous PCL NCs

For the synthesis of hollow mesoporous PCL NCs,  $SiO_2$  NPs were used as a template. These templates were synthesized by following Stöber method. 2mL of TEOS was added to 30mL of ethanol and stirred at room temperature (25°C). Then 1mL of  $H_2O$  was added to the mixture and left for half an hour under stirring (600RPM). Finally,  $NH_4OH$  was added drop wise to the mixture and the whole mixture was kept under vigorous stirring for overnight. The resulting white colloidal solution was centrifuged at 5000RPM for 10min and  $SiO_2$  NPs were separated and washed thoroughly using  $dH_2O$  and Isopropyl alcohol mixture to remove unreacted reactants. Then  $SiO_2$  NPs were dried at 120°C.  $SiO_2$  NPs of two different sizes such as (i) average size of ~10nm named as  $SiO_2$  NPs-1 (ii) average size of ~ 450nm named as  $SiO_2$  NPs-2 were prepared.  $SiO_2$  NPs-2 were prepared to take a high concentration of TEOS (5mL), keeping all other reaction parameters same. It is worth mentioning here that the larger sizes of

SiO<sub>2</sub> (SiO<sub>2</sub> NPs-2) have been used to create the hollow core and the smaller sizes particles (SiO<sub>2</sub> NPs-1) have been used to create pores on the shell of the polymeric capsules.

Core shell NPs were prepared by using SiO<sub>2</sub> NPs as core and polymer PCL as a shell. For that, 50mg of synthesized SiO<sub>2</sub> NPs-1 was thoroughly dispersed in acetone through ultra-sonication. Then 50mg PCL (average M<sub>n</sub> 45,000) was also dissolved in acetone at 45°C. Thereafter, dispersed SiO<sub>2</sub> NPs-1 and dissolved PCL were mixed together. Then, 50mg SiO<sub>2</sub> NPs-2 was dispersed in 20mL acetone separately through ultra-sonication and the homogeneous dispersion of SiO<sub>2</sub> NPs-2 was added to the mixture of SiO<sub>2</sub> NPs-1 and PCL under constant stirring at 45°C. Then the resultant mixture of SiO<sub>2</sub> NPs-1, PCL and SiO<sub>2</sub> NPs-2 was added continuously to a 150mL (water/surfactant, Igepal CO 50) emulsion under sonication at the feeding rate of 150μL.min<sup>-1</sup>. Finally, the mixture was kept under stirring for 24h (1000RPM). The resultant product is core shell NPs of SiO<sub>2</sub> and PCL (PCL-SiO<sub>2</sub>NPs) which were collected after repeated washing and centrifugation (at 5000RPM) followed by drying through lyophilization.

Above synthesized core-shell, NPs were treated with HF (5M solution) for 12h to etch out the SiO<sub>2</sub> NPs-1 from polymer shell and NPs-2 from the core of the NPs. After 12h of incubation, the etched core-shell polymeric NPs were centrifuged (at RPM 10000) to separate the particles from the solution followed by repeated dispersion and washing. Finally, the product was collected after freeze drying.

#### **(i) Loading of Rh6G, DHA, CQDP and SD in hollow mesoporous PCL NCs and corresponding release study**

The dried mesoporous PCL NCs were collected and used for loading dye and anti-malaria drugs. The mesoporous PCL NCs were incubated with Rh6G and DHA, CQDP, SD separately, with a concentration of dye/ drugs to hollow mesoporous PCL capsules of 1:1 mg.mL<sup>-1</sup> in PBS (pH 7.4). The suspensions were stirred for 1h and then kept for another 24h in dark place without stirring. The Rh6G, DHA, CQDP, SD loaded PCL NCs were separated from PBS solution through centrifugation (at 8000RPM). These loaded NCs were then washed three times with PBS to remove the free dye/drug molecules from the surface of the NCs followed by air drying in dark for further experiments.

PCL-DHA, PCL-CQDP and PCL-SD formulations were suspended in medium (RPMI 1640) and the release behavior has been studied. Maintaining a fixed time interval the absorbance of the released drugs in the medium was recorded at different temperatures such as

30, 37, 40 and 43°C using UV-Vis spectrometer and the extent of release of DHA, CQDP and SD were calculated. Release amounts were calculated for 6h in case of DHA, CQDP and for 30days in case of SD with a fixed time interval and then investigated the kinetics for the release. To study the release kinetics, 0.6mg of PCL-DHA, PCL-CQDP and PCL-SD for each were taken with 5mL of medium in a cuvette. The release behaviors of the DHA, CQDP and SD from the hollow mesoporous PCL NCs were studied in the medium used for cell culture by using UV-Vis–NIR spectrometer (Perkin-Elmer LAMBDA 750).

### **(B) Synthesis of mesoporous ZnO NCs**

Novel mesoporous ZnO (mZnO) NCs were synthesized using a high energy sonochemical method without using any surfactant. A 1:2 molar ratio of zinc acetate dihydrate and sodium hydroxide was taken for the formation of ZnO NCs.  $Zn(OOCH_3)_2 \cdot 2H_2O$  was dispersed in ethanol. Next, NaOH solution was added drop wise to the zinc acetate solution under continuous sonication (ELMA S60H, peak power: 600W, frequency = 37kHz) at room temperature (25°C) and finally kept for 12h stirring (600RPM). The white precipitate was collected by centrifugation (14000RPM) followed by repeated dispersion and washing with filter sterile water–ethanol mixture (v: v = 50: 50). Finally, the sample was dried for 12h at 80°C and the white powdered sample was collected for further characterization.

#### **(i) Loading of Ova protein in mesoporous ZnO NCs and corresponding release kinetics**

The mZnO NCs were loaded with Ova protein in the ratio 1 : 1 ( $mg \cdot mL^{-1}$ ) in  $1 \times$  PBS (pH 7.2) and incubated for 24h at room temperature. The Ova loaded mZnO NCs were separated from the supernatant after centrifugation. Repeated washing was done to remove the protein particles from the surface of the NCs. The Ova protein loaded mZnO NCs were collected and dried using a vacuum. The entrapment efficiency of the prepared mZnO NCs was calculated as:

$$\% \text{ Entrapment efficiency} = [\text{weight of protein in NCs} / \text{weight of protein fed initially}] \times 100$$

The release kinetics of Ova from mZnO NCs was evaluated by suspending NCs in culture media (RPMI 1640) at room temperature (25°C) and absorbance was taken at fixed time intervals up to 72h, maintaining similar conditions, until no change in the absorbance was observed for release profiles.

#### **(ii) Loading of dye, antimalarial drugs and anticancer drugs in mZnO NCs and corresponding release study**

Dried mZnO NCs were used for loading dye as well as different drugs. The mZnO NCs were incubated with dye Rh6G and drugs like CQDP, DHA, SD, DOX, Paclitaxel with a concentration of dye/drugs to mZnO NCs were kept in the ratio of 1:1 mg.mL<sup>-1</sup> in PBS (pH 7.2). The suspensions were mixed for an hour separately and kept for another 24h without further stirring and stored in a dark place. The dye and drug particles were then separated through centrifugation (at 5000RPM). These loaded NCs were washed thrice with PBS to remove the free dye and drug molecules from the surface of the mZnO NCs followed by lyophilization (at temperature -40°C and vacuum 1Pa) and stored in dark at room temperature for further experiments.

mZnO-Rh 6G (450µg), mZnO-CQDP, mZnO-DHA and mZnO-SD (500µg) were suspended in RPMI 1640 medium and the release behavior has been studied individually. The encapsulation efficiencies for mZnO-CQDP, mZnO-DHA and mZnO-SD NCs have been calculated by using [% Entrapment efficiency = {weight of drug in NPs/weight of drug fed initially}×100]

### **(C) Synthesis of porous PCL NCs**

The mZnO NC has been synthesised by a surfactant free ultrasonication technique. The synthesized mesoporous ZnO NCs were used as template for the formation of core shell PCL-mZnO NPs. For the synthesis of core shell structure, firstly 50mg of synthesized mZnO was thoroughly dispersed in 20mL acetone through ultra-sonication. Then 50mg PCL was dissolved in 20mL acetone at 45°C under constant stirring. Thereafter, dispersed mZnO and dissolved PCL were mixed together in another beaker. Then the resultant mixture of mZnO NPs and PCL were added continuously to 150mL (water/surfactant) emulsion under sonication at a constant rate of 150µL.min<sup>-1</sup>. After addition, the mixture was kept under vigorous stirring for 24h. The resultant core shell NPs formed consisted of mZnO as core and PCL formed the outer shell, which was washed with water and isopropanol. The final product was collected after repeated washing and centrifugation (at 5000RPM) followed by drying through lyophilization.

Above synthesized core-shell PCL-mZnO NPs were treated with NaOH (5M) and incubated in the same for 6h to etch out the mZnO and which leaving the porous polymeric shell. After 6h of incubation in 5M NaOH at room temperature, the etched core-shell NPs were then centrifuged to separate the particles from the solution and repeated washing was done to remove the dissolved mZnO/NaOH. Finally, mesoporous PCL NCs were collected after freeze drying.

### **(i) Loading of anticancer drug Paclitaxel in mesoporous PCL NCs and corresponding drug release profile**

The dried mesoporous PCL NCs were collected and loaded with drug Paclitaxel. The mesoporous PCL NCs were incubated with Paclitaxel with a concentration of drug to NCs of 1:1mg.mL<sup>-1</sup> in PBS (pH 7.4). The drug NC and PBS mixture were stirred for 1h and then kept for another 24h in a dark place without stirring at room temperature. The paclitaxel loaded mesoporous PCL NCs were separated from PBS solution through centrifugation (at 8000RPM). These loaded particles were then washed three times with PBS to remove the excess free drug molecules from the surface of the NCs followed by air drying (at room temperature) for the further experiments. The whole drug loading process has been done at room temperature.

0.5mg of anticancer drug loaded NCs were suspended in RPMI 1640 medium in a cuvette and the drug release behavior of Paclitaxel drug loaded NCs have been studied by maintaining a time interval for 3 days at room temperature (25°C).

## **2.4. Characterization Techniques**

Different characterization techniques have been used to examine synthesized nanomaterials are **X-ray diffraction (XRD)**, **Scanning electron microscopy (SEM)**, **Field emission electron microscopy (FESEM)**, **Transmission electron microscopy (TEM)**, **Thermo gravimetric analysis (TGA)**, **Differential scanning calorimetry (DSC)**, **Energy dispersive X-ray spectroscopy (EDS or EDX)**, **Brunauer-Emmet-Teller (BET)**, **Fourier Transform Infrared (FTIR) spectroscopy**, **Zeta potential analysis**, **Photoluminescence (PL) spectroscopy**, **Raman spectroscopy**, **Confocal microscopy**, **Ultraviolet-Visible spectroscopy (UV-Vis)**, **FACS** and **Multimode reader**. A brief explanation of the working principle of these instruments with sample preparation procedures has mentioned in the following section below.

### **2.4.1. X-Ray Diffraction (XRD)**

XRD is a commonly used characterization technique to investigate the information of nanomaterials like crystallinity, crystalline phase, inter planner distance in a solid state crystal, average crystallite size etc. X-rays are produced in a typical cathode ray tube, where tungsten

filament is heated to generate electrons which are later accelerated by applying voltage and directed towards the anode target and finally high energy electrons remove inner shell electrons of target materials by generating characteristic X-ray spectra. These produced X-rays are filtered to monochromatic radiations and directed on the synthesized nanomaterials which were placed in the sample holder of the XRD unit, where both sample and detectors are in rotational motion. This constructive interference of monochromatic X-ray with the sample have to satisfy Bragg's Law which was proposed by William Henry Bragg and William Lawrence Bragg in 1912, which is  $n\lambda = 2d \sin \theta$ ..... (2.1)

Where, n is order of the diffracted beam,  $\lambda$  is the wavelength of the incident X-ray beam, d is the distance between adjacent planes of atoms (the d-spacing), and  $\theta$  is the angle of incidence of the X-ray beam.

From the Bragg's law d spacing can be calculated as

$$d = \frac{n\lambda}{2 \sin \theta} \dots\dots\dots (2.2)$$

Nanomaterial samples with the sample holder rotate in the direction of monochromatic X-ray by making an angle  $\theta$  and the detector rotated at an angle  $2\theta$  to collect the diffracted rays from the rotating sample. Intensity of the X-rays which are diffracted from the rotating sample is collected in detector while scanning the sample thoroughly for a range of  $2\theta$  angle. Then intensity peaks occur which later compared with standard reference patterns of materials as each material has unique d spacing like unique figure prints of human being and thus identifying the material of the synthesised sample.

For this work, samples were characterized by using **Bruker D8** Advance X-Ray Diffractometer with X-ray source Cu K $\alpha$  ( $\lambda= 1.5406$ ) operating at 40 kV/30 mA with step size 0.02 and 10 to 90°  $2\theta$  range.

**Sample preparation for XRD analysis:**

All samples were given in fine powdered form for the XRD analysis.

**2.4.2. Electron microscopic imaging techniques (SEM, FESEM and TEM)**

Investigation of morphology, surface topography, texture, elemental composition, crystallinity, crystal planes etc., all physicochemical properties, electron microscopic techniques have used. Scanning electron microscope (SEM), field emission scanning electron

microscope (FESEM) and Transmission electron microscope (TEM) come under electron microscopy.

#### **(A) Scanning electron microscope (SEM)**

As a part of the electron microscopic technique, SEM contains high energy electrons as a source, (unlike light beam source of the optical microscope) which is made up of tungsten electron gun. The electron beam is directed towards the nanomaterial sample surface through a pair of magnetic condenser lenses and scanning coils which deflect the beam and finally bombarded on the sample surface and scan the sample surface in raster scan pattern. As a result of high voltage electron and nanomaterial surface atom interaction, the secondary electrons, backscattered electrons, diffracted backscattered electrons, X-rays, heat etc., which carry different information about the sample occur and later recorded in the detector and after multiple amplifications SEM micrographs of the given material will form. Both secondary and backscattered electrons are used to produce images of the sample in the detector where secondary electrons give the information about surface morphology and topography and backscattered electrons give the phase contrast in the sample. There is no weight loss of the nanomaterials during this characterization technique therefore SEM is a nondestructive technique can be used for the same nanomaterial characterization, repetitively.

#### **Sample preparation for SEM analysis:**

In SEM analysis, a coating of the nanomaterial sample is mandatory for nonconductive nature samples since nonconducting samples have the tendency to build up the high voltage, charge on the surface of the sample thus by making it difficult to scan the sample surface and get the expected information from the micrograph. Generally, gold (Au), gold-palladium (Au-Pd), Platinum (Pt) etc., conducting metals are used for coatings through sputtering to avoid charging effect on the NP surface. For this research work, nanomaterials were dispersed properly in a suitable solvent and taken a drop on a clean glass slide followed by drying it appropriately. As the nanomaterials are nonconducting in nature so a coating layer of Au-Pd has done for 30sec before sending for SEM analysis. The voltage used 15kV to capture SEM images of synthesized nanomaterials. SEM model HITACHI S-3400 N has used for the characterization of nanomaterials.

#### **(B) Field emission electron microscopy (FESEM)**

Field emission electron microscopy technique is also a part of the electron microscopy technique. It is an improved microscopic technique than a scanning electron microscope in terms of a narrow probe, resolution, magnification and diminished sample damage due to charge while exposed under a microscope. Like SEM it uses electron beam as a source instead of the light beam used in optical microscopy technique. Electron gun contains a field emission cathode as a source of high energy electrons, where vacuum and an electric field is maintained accurately. A narrow spot of 1 to 5 microns is formed by focusing and deflected field emission electron beams through electronic lenses inside FESEM chamber and finally directed to scan the nanomaterial sample surface in a raster scanning manner. Accelerating voltage range is 1 to 30kV magnification upto 10,00000X. Secondary electron signals ejected from the nanomaterial surface are recorded in the detector, transformed to electronics signals and after multiple times of amplification FESEM micrographs, carrying all morphological, topological etc., information about the nanomaterials, will be formed.

#### **Sample preparation for FESEM analysis:**

The same sample preparation for FESEM is same as SEM characterization. The voltage used 15kV has used to capture FESEM micrographs of the synthesized nanomaterials. FESEM model ZEISS ULTRA 55 is used for the characterization of nanomaterials.

#### **(C) Transmission electron microscope (TEM)**

Transmission electron microscope (TEM) is also an electron microscope where finer, magnified images can be obtained with more minute detail of the nanomaterials than the other two electron microscopes SEM and FESEM. High voltage electron beam produced by tungsten filament (diameter 0.1mm) is used as the source which interacts with the ultra-thin sample and transmitted through the nanomaterial sample inside a high vacuum chamber to reduce the interaction of moisture and produced signal is detected on fluorescence screen and fine well magnified TEM micrographs will be produced. Two pairs of condenser lenses are used to demagnify first by decreasing the spot size and later magnifying the electron beam in the TEM apparatus. Additionally, there are another lenses that are also present in TEM apparatus like an objective lens, intermediate lens and projector lens for further magnification of the electron beam. Some areas on nanomaterial sample scatter fewer electrons, consequently form bright field image on the contrary areas which scatter more electrons, form dark field image in the

TEM micrographs. Generally, these high resolution transmittance electron microscopes are used to find out all structural details of materials with very fine size like in nanometer range.

For a crystalline sample, TEM analysis can produce selected area electron diffraction (SAED) pattern which is formed due to the diffraction of high energy electron beam by atoms present in the sample to a specific angle considering the structure of the crystal. Thus a series of spots will generate due to the diffracted electrons by considering each spot as the crystal planes of the crystalline material.

#### **Polymer sample preparation for TEM:**

Drop casting method is following for the preparation of the TEM sample. Polymer NCs have dispersed properly in a suitable solvent and one drop of it cast on a carbon coated grid followed by a drop of stain phosphotungstic acid (PTA) added to the grid to form a contrast in the micrograph. After 10sec, excess PTA on the sample grid was washed out with Milli-Q water and allowed to air dry in vacuum. For the TEM analysis nanomaterial sample loaded copper grid has placed into the sample holder of the instrument and images are captured at different places of the nanomaterial with different magnifications. Approximately 200kV accelerating voltage has used to capture TEM micrographs. TEM micrographs of nanomaterials have been obtained from a high resolution transmission electron microscope (HRTEM) model FEI TECHNAI G2 has been used.

#### **Inorganic sample preparation for TEM:**

Inorganic NCs have dispersed properly in a suitable solvent and one drop of it cast on a carbon coated grid followed by proper air drying in vacuum. The same TEM model has used as mentioned above.

### **2.4.3. Energy dispersive X-ray spectroscopy (EDS or EDX)**

With the help of non-destructive energy dispersive X-ray spectroscopy (EDS or EDX) technique, the information about the elemental composition of nanomaterials can be acquired. Basically, this instrument unit is attached to the SEM, FESEM and TEM instruments to gather the elemental composition of the sample used for the imaging. When nanomaterial sample is exposed under high energy electron beam, atoms present on the sample excited out with a number of different signals, among those X-rays are used by EDS detector by producing peaks

corresponding to the atoms of sample surface which are responsible for X-ray production. Consequently, a spectrum of peaks will form due to the different elements present in the sample. Since a specific site of the sample surface is exposed under narrow electron beam in an electron microscope, EDS will give the information about the elements present on that specific region of the sample surface in percentage amount. Therefore, a number of the spectrum of peaks will form due to the selection of different regions present across the same sample surface. Sometimes, the discrete element can produce more than one peak for the corresponding selected region of the sample surface and sometimes peaks corresponding to different elements can intersect with each other.

#### **Sample prepared for EDS or EDX:**

The samples used for electron microscopic analysis can be used for EDS analysis side by side. As EDS unit is attached to the electron microscopic unit therefore same instrumental models are used for EDS analysis also which are used for electron microscopic techniques (SEM, FESEM and TEM).

#### **2.4.4. Thermogravimetric analysis (TGA)**

It is necessary to determine the thermal stability of a nanomaterial to prove their efficiency in different thermal environments. With the help of thermogravimetric analysis (TGA), the thermal stability of synthesized nanomaterials is measured. With an increase of temperature, a material loses its weight or mass due to evaporation, dehydration, reduction or decomposition. In TGA technique, this variation of the weight of the nanomaterial sample with respect to the change in temperature or time in a specific environment can be determined. In TGA, the nanomaterial samples are placed on a microgram balance in an N<sub>2</sub> environment while for a specific heating rate (5-20°/min) for an increase of temperature 1000°C inside a furnace which can be monitored by using a thermocouple. Thus formed data can give a plot of percentage weight loss vs. temperature in Celsius or time which is called as TGA thermogram of the corresponding nanomaterial. As result of analysis of a TGA thermogram, the stability of the nanomaterials, as well as kinetic degradation parameter of a nanomaterial sample have been calculated by using Friedman and Freeman-Carroll technique.

#### **Sample preparation for TGA:**

Powder nanomaterial samples around 100mg are used for TGA characterization technique where flow rate was fixed at 10°/min upto 1000°C. Thermogravimetric analysis was done in a TA Instrument.

#### **2.4.5. Differential Scanning Calorimetry (DSC)**

Differential scanning calorimetry (DSC) technique is used to measure the physical transformation like phase transition of a nanomaterial with heat flow within it with an increase in temperature. The transformation of the nanomaterial includes glass transition temperature, exothermic processes (release heat), endothermic processes (absorb heat) and change in heat capacity of the sample with increasing heat and temperature. In DSC instrument, one reference pan (empty) is used along with the sample pan where both reference and samples are maintained in the same temperature whether temperature linearly increased or decreased. With the increase in temperature, sample will experience physical transition by heat flow to maintain the same temperature like a reference. In an endothermic reaction, heat is absorbed by the nanomaterial sample to experience a phase transition i.e., solid to liquid. Likewise, in an exothermic reaction, the amount of heat required is less for phase transition by promoting the sample temperature up to reference level. Thus DSC calculates the amount of heat flow absorbed or release throughout the phase transition, also measures melting temperature ( $T_m$ ), the percentage of crystallinity, glass transition temperature ( $T_g$ ) and other chemical reactions occurred during the transition of the nanomaterial sample.

#### **Sample preparation for DSC:**

Differential Scanning Calorimetry (DSC) analysis was performed by Q-100, TA instrument with powder samples.

#### **2.4.6. Brunauer-Emmet-Teller (BET)**

BET stands for Stephen Brunauer, Paul Hugh Emmett and Edward Teller, three scientists who developed the theory, known as BET which measures the specific surface area of a nanomaterial. The same instrument follows Barrett-Joyner-Halenda (BJH) which is used for pore width measurement.

Basically, how physical adsorption of gas molecules occurs on the surface of solid materials is explained by BET theory. Multilayer adsorption of noncorrosive gas (nitrogen, argon, carbon dioxide) on the surface of the adsorbent for the determination of specific surface area can be done with the help of BET theory. For this work, nitrogen gas (N<sub>2</sub>) has used as probe gas and due to the van der Waals force of attraction interaction between nitrogen gas molecule and sample occurs in the liquid nitrogen atmosphere.

BET equation is

$$\frac{1}{[V_a(P_0/P - 1)]} = \left[ \frac{C - 1}{V_m C} \times \frac{P}{P_0} \right] + \left[ \frac{1}{V_m C} \right] \dots \dots \dots (2.3)$$

Where, P is partial vapor pressure of adsorbate gas at the boiling point of liquid nitrogen i.e., 77.4K.

P<sub>0</sub> is the saturated pressure of adsorbate gas.

V<sub>a</sub> is the volume of gas adsorbed at STP.

V<sub>m</sub> is the volume of gas adsorbed at STP to form a monolayer on the adsorbent.

C is a constant (dimensionless) which is related to the enthalpy of adsorption of the probe gas on the sample surface.

Further  $\frac{1}{[V_a(P_0/P - 1)]}$  vs  $\frac{P}{P_0}$  produces a straight line in the approximate relative pressure range of 0.05 to 0.3. The value of V<sub>m</sub> and C are determined from the slope and intercept of BET linear plot. Specific surface area can be calculated by using:

$$S = \frac{V_m N_a}{m \cdot 22400} \dots \dots \dots (2.4)$$

Where N is Avogadro number, a is effective cross-section of adsorbate molecule, m is mass of the solid sample, 22400 is volume occupied by 1 mole of adsorbate gas at STP.

There are six types of adsorption isotherms can achieve from BET analysis. Porous nanomaterials form the type IV isotherm which is in the shape of a hysteresis loop.

**Sample preparation for BET analysis:**

Powder nanomaterials have used for BET analysis. Degassing of samples is essential to remove unwanted gas, moisture from the sample surface to get an accurate specific surface area from BET theory. For the BET analysis model, Tristar II 3020 has used.

#### **2.4.7. Fourier Transform Infrared (FTIR) spectroscopy**

With the help of Fourier Transform Infrared (FTIR) spectroscopy, we can get the information about absorption, emission, functional groups present in the nanomaterial sample. Different frequencies of light are directed on the sample surface and amount of beam absorbed by the sample is recorded in the detector by repeating the process for a number of times with different frequencies. In IR spectroscopy, molecules present in the sample are able to absorb frequencies characteristic for their structure.

Infrared (IR) spectroscopy is an analytical method to record the vibrations of functional groups which can characterize the molecular structure of a material. The absorption and transmittance peaks in the IR spectrum are the fingerprint of the frequencies of molecular vibrations corresponding to different functional groups present in the sample. Therefore, different materials with unique combinations of atoms in the functional groups while interacting with the IR radiation produces different and unique IR spectrum which enables the determination of the type of chemical bond present in the material. The IR spectra can be divided into three regions such as Near IR ( $14000-4000\text{cm}^{-1}$ ), Mid IR ( $4000-400\text{cm}^{-1}$ ), and Far IR ( $400-10\text{cm}^{-1}$ ) respectively. When a molecule absorbs IR radiation of a particular frequency it undergoes a change in its dipole moment upon vibration and when the frequency of the IR radiation coincide with the natural frequency of vibration of the molecule, the amplitude of the vibration changes. The molecular vibrations associated with the fluctuating dipole moment are stretching and bending. The bending vibrations again can be classified into four types such as rocking, twisting, wagging and scissoring. The IR can be utilized for quantitative analysis such as the determination of the concentration of an unknown solution or quantity of material present. Conventional IR spectroscopy works in the frequency domain where the radiant power is measured as a function of frequency. The Fourier transformation IR spectroscopy measures the radiant power as a function of time and the time domain spectrum is mathematically represented into frequency domain spectrum with help of Fourier transform. The Michelson interferometer in the FTIR instrument consists of a fixed mirror, moving mirror, a beam splitter,

IR radiation source and a detector. The beam splitter divides the IR beam into two parts and one half of the beam is reflected by the fixed mirror and the other half is reflected by the moving mirror. The two beams are again recombined at the beam splitter which passes through the cell and finally the beam is focused to the detector. The FTIR instrument used for sample analysis is PerkinElmer FTIR/FIR Spectrometer, Frontier. The analysis was carried out at room temperature in the MIR ( $4000\text{-}400\text{cm}^{-1}$ ) region using absorbance mode.

#### **Sample preparation for FTIR:**

The samples were prepared in the pellet form by mixing the samples with KBr powder.

#### **2.4.8. Zeta potential analysis**

With the help of Zeta potential characterization technique surface charge and electrical stability of the NPs in a colloidal suspension have been investigated. As liquids comprise ions whether cations or anions which interact with the NPs surface charge (even solid particles contains charges in suspension) during the suspension of the NPs in the liquid medium. Movement of the NPs in the suspension medium depends on the interference of charge of the NPs and the applied external electric field. The particle velocity is proportional to the electrical potential of the suspended charged NPs at the diffuse layer of electrical double layer i.e., zeta potential. Therefore, zeta potential can be determined by observing the movement of NPs i.e., NP velocity 'V' and the electrophoresis with a known refractive index of the suspension medium and a known dielectric constant ' $\epsilon$ '. The factor pH of the solvent is affecting the value of zeta potential. Zeta potential value of a nanomaterial is positive at lower pH solvent medium i.e., acidic solvent and negative at higher pH solvent medium i.e., base solvent. The point where NPs possess zero zeta potential value, that point is an Isoelectric point where colloidal suspension of NPs will show the least stability.

A laser source of light is split to an incident beam and reference beam of light. Though the sample cell incident laser beam passes and scattered by making an angle. With the application of an electric field, NPs move through measured sample cell make the intensity of detected light to alter with a frequency proportional to the velocity of the NP. A detector records the information which is analysed by a software zeta sizer to form spectrum from which zeta potential can be calculated.

NPs with small zeta potential value have the tendency to coagulation and thus possessing less stability in colloidal suspension, whereas NPs with a higher value of zeta

potential (may be positive or negative) possess high electrical stability by resisting agglomeration in the colloidal medium. Stability of NPs is considered as having value  $\geq +30\text{mV}$  for positive zeta potential and having value  $\geq -30\text{mV}$  for negative zeta potential.

#### **Sample preparation for zeta potential analysis:**

Solid NPs have been properly suspended in DI water and kept in a capillary cell of the instrument for the determination of zeta potential value. Model Mastersizer 3000 (Malvern Instrument) has been used for the zeta potential analysis.

#### **2.4.9. Confocal microscopy**

By using confocal microscopy loading of any other small particles in the prepared NCs were checked with its good optical resolution, phase contrast ability. In 1955, Marvin Minsky proposed the concept of a confocal microscope to overcome the drawbacks of a fluorescence microscope. In confocal microscope both image and sample i.e., object, have the same focal point with the ability to abolish the lights or information which are out of focus from the focal point of the object by using a pinhole in front of the image formed. The function of this pinhole to eliminate all out of focus lights which are above or below the focal plan of the object and allowing a very narrow beam of light to form images of the only focused portion of the light. Thus, it can give information about the required portion of the sample surface with good clarity and good resolution. In a confocal microscope, the source is a laser beam to form bright light at a specific wavelength and images produced are detected by a sensitive photomultiplier detector. The microscope is interfaced with a computer, which can scan the rectangular area of the sample, focus, collect and finally analyze the micrographs. The confocal microscope can form images of fluorescence which is applied to the sample and produce a contrast in color to the image with the help of that it becomes easy to differentiate fluorescence particles from the other parts of the sample. Thus, it can produce a phase difference within the same image formed in the computer. Therefore, confocal microscopy technique is used to image the prepared mesoporous NPs which were previously loaded with fluorescence dyes.

#### **Sample preparation for confocal microscopy:**

Mesoporous NPs have been treated with fluorescence dye Rh 6G and the washed it with DI water to avoid the presence of dye on the surface of the NPs and so that dye particles can

present only inside the pore of the NPs. After vacuum drying these dye loaded NPs were dissolved in a solvent and taken for confocal microscopy imaging.

#### 2.4.10. Ultraviolet-Visible spectroscopy (UV-Vis)

UV-Vis spectroscopy is based on absorption spectroscopy and it works in the ultraviolet (approximately 190-380nm wavelength range) and visible range (wavelength range approximately 380-800nm) of the electromagnetic spectra. This spectrometer is used to determine the quantity or concentration of different chemical compounds formed the nanomaterials by checking absorbance *w.r.t.* UV-Vis wavelength range. As the wavelength is specific for different molecules, this spectrometer records electrons transition by UV-Vis light from ground state to higher energy state by absorbing at the specific wavelength for that specific molecules. Thus it becomes easy to identify the molecule as well as the concentration of the molecule present in the NP.

The principle of UV-Vis spectroscopy works on Beer-Lambert law where at a specific wavelength the absorbance of a molecule is directly proportional to the absorbing molecule concentration present in solution and the light path length. This can be represented as:

$$A = \text{Log}_{10} \left( \frac{I_0}{I} \right) = \epsilon \times C \times l \dots \dots \dots (2.5)$$

Where, A is the absorbance measured

$I_0$  is the incident light intensity

$I$  is the intensity of transmitted light

$\epsilon$  is the constant called molar absorptivity

$l$  is the path length of light.

The spectrometer contains two sources a tungsten filament for visible range (300nm to 2500nm) and for UV range a radiation source of deuterium arc lamp with 190-400nm, monochromators to monochromatic light by filtering lights to a specific single light wavelength, photomultiplier and a photodiode detector to record the measured light, a sample

holder and a reference sample holder (which has 100% transmission or can say 0% absorbance).

#### **Sample preparation for UV-Vis spectroscopy:**

Powder nanomaterials were dissolved in a suitable solvent to take a reading in UV-Vis spectrometer. Quartz cuvettes were used for both sample and reference sample cell. Baseline correction has done to avoid absorbance peak formed due to solvent before taking data for nanomaterials. Then dissolved nanomaterials have kept in sample quartz cell and reference cuvette has filled with only pure solvent and respective absorbance peak have been checked for each prepared nanomaterials. Model LAMDA 750, Perkin Elmer instrument has been used for the experiment.

#### **2.4.11. Fluorescence activated cell sorting (FACS) analysis**

A fluorescence activated cell sorting (FACS) is a tool comes under flow cytometry, where laser light is utilized to sort, count and detect fluorescence labeled cells from a heterogeneous stream of cells while crossing through a single flow path. It helps to distinguish and to get a quantitative profile of cells in a heterogeneous cell suspension.

Laminar flow of heterogeneous cell suspension exposed to laser light beam by flowing through a narrow path which is designed in such a manner to allow single cell at a time with the help of hydrodynamic focusing. An electromagnetic field is applied to enforce an electric charge on all cell. Under the laser light beam fluorescently labelled biological cells in a stream of fluid, get excited to produce forward scattering, side scattering, fluorescence scattering signals at single or multiple wavelengths and accordingly detecting those signals by several detectors (positioned around the cell stream), count, quantity and sort of cells present in a biological cell sample. Detectors parallel to the laser light beam measures forward scattering signals and detectors perpendicular to the stream measures side scattering signals. The detected scattered signals and fluorescence lights are analyzed by the software of the computer.

It is a very fast method and can determine thousands of particles per second and can collect varying physical and chemical structural information with different parameters of cells of interest.

### **2.4.12. Multimode microplate reader**

The instrument multimode micro plate reader has a varied range of applications like its name. It can be used to determine the physical, chemical and biological properties of nanomaterials as well as biological cells also. However, vastly utilized in the biological field. Samples are kept in 96 well microplates (8×12) where the volume of each well is about 150µL to 200µL, are commonly used. Multimode microplate reader consists of different detection modes like absorbance, fluorescence, luminescence, time resolve fluorescence etc. The detection mode absorbance works for different biological assays. To check the cell viability of synthesized nanomaterials absorbance detection mode has been utilized in the present work. Samples are placed under a light source of specific wavelength and amount of initial light transmitted i.e., the concentration of the sample, through the desired sample can be detected by a detector placed opposite side of well. In case of fluorescence detection mode, samples are placed under a light source of a specific wavelength, fluorescence molecules present in the sample will emit light and collected by an emission system where emitted lights are parted from excitation light with the help of a monochromator and measures the signal. In case of a luminescence detector, emitted light by the sample gives information of chemical properties of the sample or some typical type of biological reactions. This detector has used to check the photoluminescence spectra of the synthesized nanomaterials.

#### **Sample preparation for Multimode multiplate reader:**

In biocompatibility assay, nanomaterials have been treated with cells and seeded in 96 well plate which has been examined under multimode multiplate reader after the specific incubation period.

In PL analysis synthesized nanomaterials have been dispersed in a suitable solvent and studied under the multimode multiplatereader at specific wave length range.

## **Chapter 3**

### **Result and discussion**

**Part I (Section A): Designing of SiO<sub>2</sub> templated hollow mesoporous PCL NCs and loaded with various antimalarial drugs (CQDP and DHA) for suppressing malaria.**

**Part I (Section B): Efficiency of hollow mesoporous PCL NCs loaded with antimalarial drug Sulfadoxine against *P. falciparum* cell line.**

**Part II (Section A): Designing of mesoporous ZnO NPs incorporated with protein for the enhancement of immune responses.**

**Part II (Section B): Mesoporous ZnO NCs incorporated with different drugs for cancer therapy.**

**Part III: Synthesis of porous PCL NPs by template removing approach to eradicate breast cancer cells.**

**Chapter 3: Result and discussion: Part I (Section A)**

**Objective: Designing of SiO<sub>2</sub> templated hollow mesoporous PCL NCs and loaded with various antimalarial drugs (CQDP and DHA) for suppressing malaria.**

3.1A.1. Introduction

3.1A.2. Synthesis procedure

3.1A.3. Synthesis mechanism of hollow mesoporous PCL capsules

3.1A.4. Loading of Rh6G, DHA and CQDP in hollow mesoporous PCL capsules

3.1A.5. Effect of drug loaded NCs with *P. falciparum* cell line

3.1A.6. Designing hollow mesoporous PCL capsules: Size, Morphology and porous structure of NCs

3.1A.7. BET surface area analysis

3.1A.8. Surface chemical structure of hollow mesoporous PCL capsules

3.1A.9. Thermal stability, solid state crystal structure study and zeta potential analysis

3.1A.10. Cell viability analysis of bare hollow mesoporous PCL capsules with *P. falciparum* culture medium

3.1A.11. *P. falciparum* inhibition with PCL-DHA and PCL-CQDP formulation

3.1A.12. Hollow mesoporous PCL capsules facilitate releasing of DHA and CQDP in the medium

3.1A.13. Release kinetics and diffusion coefficients of PCL-DHA and PCL-CQDP nanoformulations

3.1A.14. PCL-DHA and PCL-CQDP formulation actively inhibit *P. falciparum*

3.1A.15. Summary of Part I (Section A)

## Chapter 3

### Result and discussion: Part I (Section A)

**Objective: Designing of SiO<sub>2</sub> templated hollow mesoporous PCL NCs and loaded with various antimalarial drugs (CQDP and DHA) for suppressing malaria.**

#### 3.1A.1. Introduction

Hollow mesoporous nanocarriers typically based on the polymer are becoming a smart delivery vehicle to deliver drugs and other biomolecules because of their recent achievement in the biomedical field. Polymer nanocarriers have advantages over another nanocarrier as they are biodegradable and biocompatible in nature.

From recent reports of WHO it is very clear that the death caused by Malaria is not ignorable as it is increasing every year. To date, many NP based research works for antimalarial activities have been reported such as phosphorothionate antisense oligodeoxyribo-nucleotide and chitosan based NPs for silencing of malaria [111],  $\beta$ -arteether lipid based NP formulation of curcumin [112].

However, it is worth mentioning that, till date only the poly(N-Isopropylacrylamide) based copolymers were reported which control the temperature dependent release of drugs

[196]. But the disadvantages of poly(N-Isopropylacrylamide) for treatment of malaria is that the critical transition temperature ( $T_c$ ) of drug release for this polymer is  $32^\circ\text{C}$ , which is very low compared to the normal body temperature ( $37.4^\circ\text{C}$ ) and hence poly(N-Isopropylacrylamide) may not be useful for controlled release of antimalarial drugs for treatment of the *P. falciparum* as most of the drug is released below the body temperature, rather the excess release of drugs from poly(N-Isopropylacrylamide) at low temperature ( $33^\circ\text{C}$ ) caused side effects and increased the resistance of drugs to the *P. falciparum* [197].

Controlled release of antimalarial drugs DHA and CQDP, at body temperature ( $37^\circ\text{C}$ ) and higher temperature caused by malaria infection, with the help of hollow PCL capsules as delivery vehicles has not been reported yet. Therefore, we have designed an appropriate drug delivery vehicle of polymer PCL through wet chemical template removal technique. A comprehensive analysis of the *in-vitro* cytotoxic effect of the porous PCL capsules and also *P. falciparum* parasitic cell inhibition efficiency of these synthesized hollow mesoporous PCL capsules has been studied here. Their *in-vitro* sustained drug release behavior while loaded with different antimalarial drugs to the *P. falciparum* RBCs with a gradual change in temperature ( $37^\circ\text{C}$ - $43^\circ\text{C}$ ), makes them a suitable contender for the controlled delivery of antimalarial drug to eradicate *P. falciparum* infection.

### 3.1A.2. Synthesis procedure

A detail of the experimental procedure for the synthesis of templates  $\text{SiO}_2$  NPs, Core shell PCL-  $\text{SiO}_2$  NPs and hollow mesoporous PCL NCs has been explained here. The detail of the Chemicals, reagents, solvents used for the experiment has been included in **Chapter 2**.

#### (a) Synthesis of template $\text{SiO}_2$ NPs

$\text{SiO}_2$  NPs were synthesized followed by Stöber method [200]. In brief, 2 mL of TEOS was added to 30 mL of ethanol and stirred at room temperature ( $25^\circ\text{C}$ ). Then 1 mL of  $\text{dH}_2\text{O}$  was added to the mixture and left for half an hour under stirring (600 RPM). Then  $\text{NH}_4\text{OH}$  was added drop wise to the mixture and the whole mixture was kept under vigorous stirring for overnight. The resulting white colloidal solution was centrifuged at 5000 RPM for 10 min and  $\text{SiO}_2$  NPs were separated and washed thoroughly using  $\text{dH}_2\text{O}$  and Isopropyl alcohol mixture to remove unreacted reactants. Then  $\text{SiO}_2$  NPs were dried at  $120^\circ\text{C}$ .  $\text{SiO}_2$  NPs of two different sizes such as (i) average size of  $\sim 10\text{nm}$  named as  $\text{SiO}_2$  NPs-1 (ii) average size of  $\sim 450\text{nm}$  named as  $\text{SiO}_2$  NPs-2 were prepared.  $\text{SiO}_2$  NPs-2 were prepared by taking a higher

concentration of precursor material TEOS (5mL), keeping all other reaction parameters same. It is worth mentioning here that the larger sized SiO<sub>2</sub> (SiO<sub>2</sub> NPs-2) has been used to create the hollow core and the smaller sized particles (SiO<sub>2</sub> NPs-1) have been used to create pores on the shell of the polymeric capsules. Later, these both white powdered SiO<sub>2</sub> NPs were stored properly for further characterizations.

### **(b) Synthesis of solid core shell polymer NPs**

In brief, 50mg of synthesized SiO<sub>2</sub> NPs-1 were thoroughly dispersed in acetone through ultra-sonication. Then 50 mg PCL (avg. M<sub>n</sub> 45,000) was also dissolved in acetone at 45°C. Thereafter, dispersed SiO<sub>2</sub> NPs-1 and dissolved PCL were mixed together. Then, 50mg SiO<sub>2</sub> NPs-2 were dispersed in 20mL acetone separately through ultra-sonication and the homogeneous dispersion of SiO<sub>2</sub> NPs-2 was added to the mixture of SiO<sub>2</sub> NPs-1 and PCL under constant stirring at 45°C. Then the resultant mixture of SiO<sub>2</sub> NPs-1, PCL and SiO<sub>2</sub> NPs-2 was added continuously to a 150mL (water/surfactant, Igepal CO 50) emulsion under sonication at the feeding rate of 150μL.min<sup>-1</sup>. Finally, the mixture was kept under stirring for 24h (1000RPM). The resultant product is core shell NPs of SiO<sub>2</sub> and PCL (PCL-SiO<sub>2</sub> NPs) which were collected after repeated washing and centrifugation (at 5000RPM) followed by drying through lyophilization. In the core shell structure, SiO<sub>2</sub> is in the core and shell is PCL.

### **(c) Formation of hollow mesoporous PCL capsules**

Above synthesized core-shell NPs were treated with HF (5M solution) for 12h to etch out the SiO<sub>2</sub> NPs-1 and NPs-2. After 12h of incubation, the etched core-shell polymeric NPs were centrifuged (at RPM 10000) to separate the particles from the solution followed by repeated dispersion and washing. Finally, the white powdered product was collected after freeze drying.

### **3.1A.3. Synthesis mechanism of hollow mesoporous PCL capsules**

The chemical formation mechanism of hollow mesoporous PCL NCs is briefly explained here. To form a core-shell structure, nucleophilic Oxygen of Igepal-CO 50 is rich in electrons which donate electrons to the tetravalent silicon atom thereby resulting in an intermediate anion. There can be a possibility of two chemical routes to form the final core

shell structure. In the first case, after the addition of another equivalent molecule of  $\text{SiO}_2$  atom, dianion formation takes place, which upon hydrolysis causes the conversion of ionic oxygen to a hydroxyl group.

In another case, the intermediate anion upon hydrolysis is following nucleophilic substitution pathway i.e. the electron rich oxygen of silica attacks the carbonyl center of PCL.

Two equivalent of PCL was added to the above solution to form the product given as,

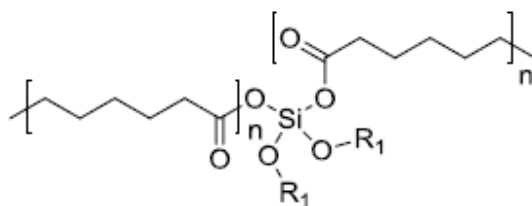
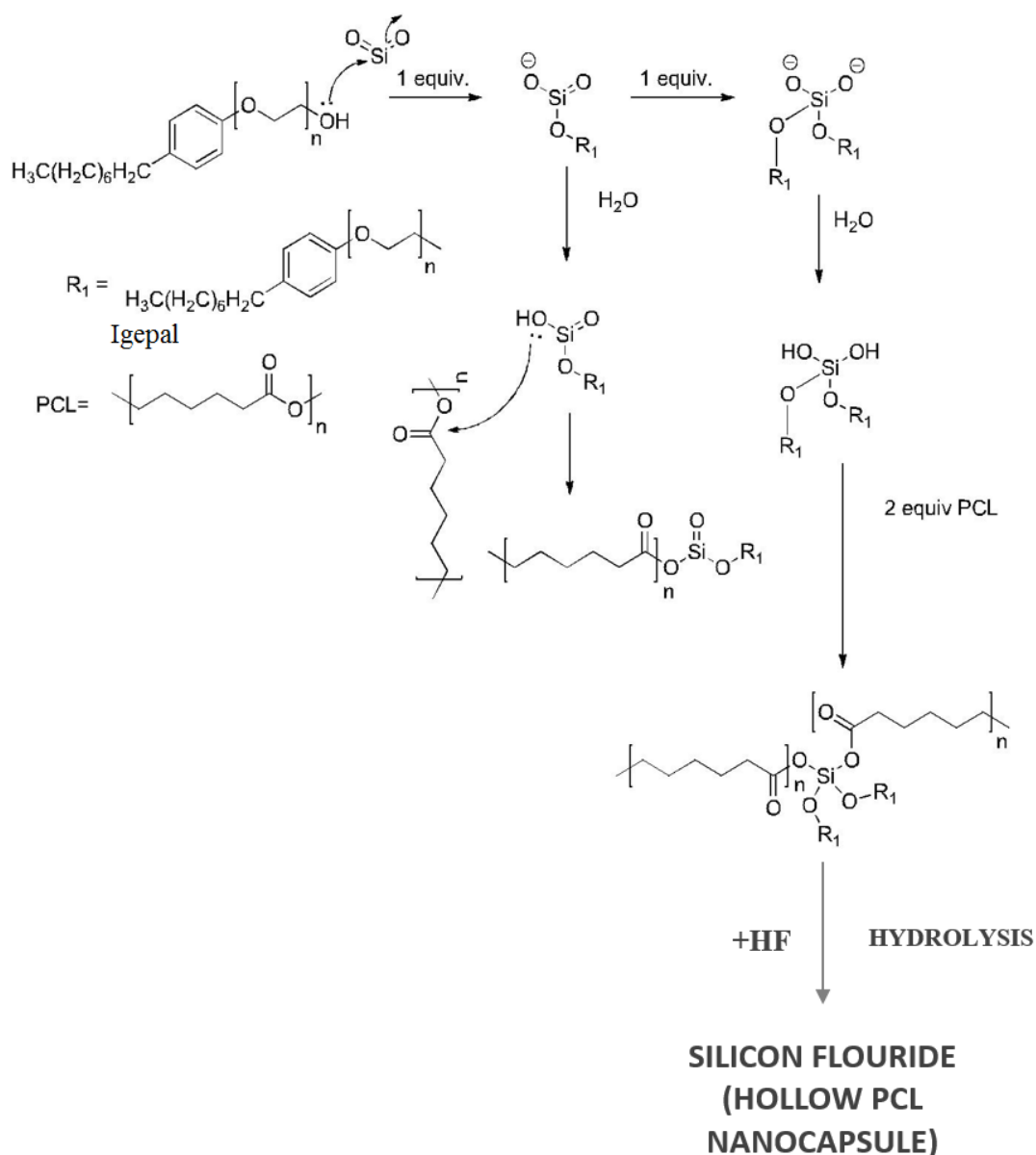


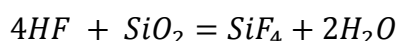
**Figure 3.1.1.** Chemical structural representation of  $\text{SiO}_2$  surrounded by PCL forming core shell structure.



**Schematic 3.1.1.** Step by step synthesis mechanism of core shell PCL-SiO<sub>2</sub> NPs and hollow mesoporous PCL capsules after removal of template SiO<sub>2</sub>. In the first step, nucleophilic Oxygen of Igepal-CO 50 donates electrons to the silicon atom followed by forming an anion. In the second step, dianion formed after addition of an equivalent molecule of SiO<sub>2</sub> atom. In the third step, hydrolysis of dianion converted ionic oxygen to hydroxyl group. In the next step, the electron rich oxygen of silica attacks the carbonyl center of PCL. Simultaneously, in another parallel case, the intermediate anion upon hydrolysis is following nucleophilic substitution pathway where the electron rich oxygen of silica attacks the carbonyl center of PCL. Two equivalent of PCL was added to the above solution to form the final core shell structure. In the

*final step after addition of HF, template SiO<sub>2</sub> removed in the form of silicon fluoride gas thereby forming PCL shell with hollow porous structure.*

Aqueous hydrogen fluoride (HF), is added which reacts with the core shell PCL-SiO<sub>2</sub> (structure represented above) NPs. Template SiO<sub>2</sub> reacts with hydrogen fluoride by resulting silicon tetrafluoride gas (which will be given off) as well as water. Therefore, it leaves behind the porous PCL shell with a hollow core and porous shell. The proposed chemical reaction for the removal of SiO<sub>2</sub> template from the PCL shell after reacting with HF has been mentioned below,



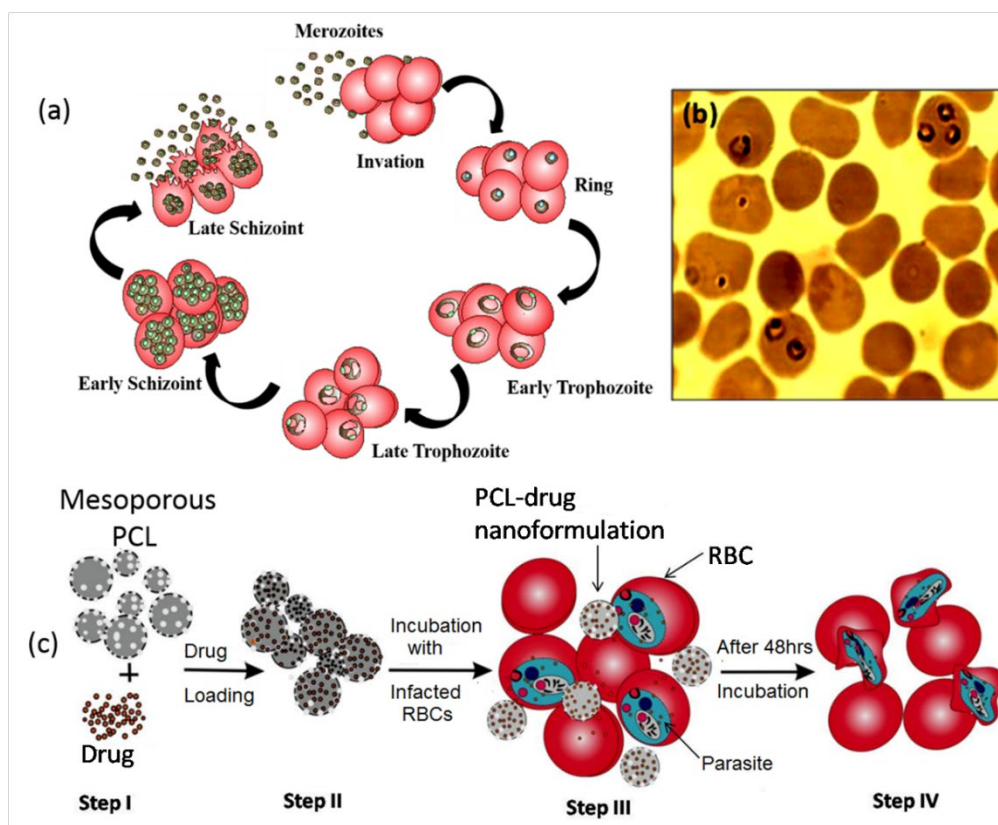
#### **3.1A.4. Loading of Rh6G, DHA and CQDP in hollow mesoporous PCL capsules**

The dried mesoporous hollow PCL capsules were collected and used for loading dye and anti-malaria drugs. The mesoporous PCL capsules were incubated with Rh6G and antimalarial drugs DHA, CQDP separately, with a concentration of dye/ drugs to mesoporous PCL capsules of 1:1 mg.mL<sup>-1</sup> in PBS (pH 7.4). The suspensions were stirred for 1h and then kept for another 24h in dark place without stirring. The Rh6G and DHA/CQDP loaded PCL capsules were separated from PBS solution through centrifugation (at 8000RPM). These loaded particles were then washed three times to remove the free dye/drug molecules from the surface of the capsules followed by air drying in dark for further experiments.

#### **3.1A.5. Effect of drug loaded NCs with *P. falciparum* cell line**

Parasites have a complex cell cycle of growth (48h), which consists of three typical stages such as ring, trophozoite and schizont stages showed in *Schematic 3.1.2a*. After reaching to the schizont stage, merozoites emerge out of the erythrocytic vesicle and once again these merozoites invade an erythrocytic cell and a new life cycle of the parasite repeats again for multiple times. Nano-formulated PCL-DHA and PCL-CQDP were added to the *P.*

*falciparum* infected RBCs at the early trophozoite stage as the ring formed (**Schematic 3.1.2b**). On adding the formulation at ring stage, either DHA or CQDP started to release from the polymer formulations and sustained for a longer time and subsequently starts to inhibit the growth of the parasites. This process can be continued for a longer period of time due to the sustained release of DHA, CQDP and subsequently maintained the killing process as it is shown in the **Schematic 3.1.2c**.



**Schematic 3.1.2.** a) Life-cycle of *P. falciparum*, (b) early Trophozoite stage of *P. falciparum* at which stage PCL-DHA/PCL-CQDP nanoformulations added for treatment and (c) schematic of different steps of development of nanoformulations and treatment with *P. falciparum* infected RBCs resulting deformed structures of infected RBCs after 48h of incubation with drug loaded nanoformulations.

### 3.1A.6. Designing hollow mesoporous PCL capsules: Size, Morphology and porous structure of NCs

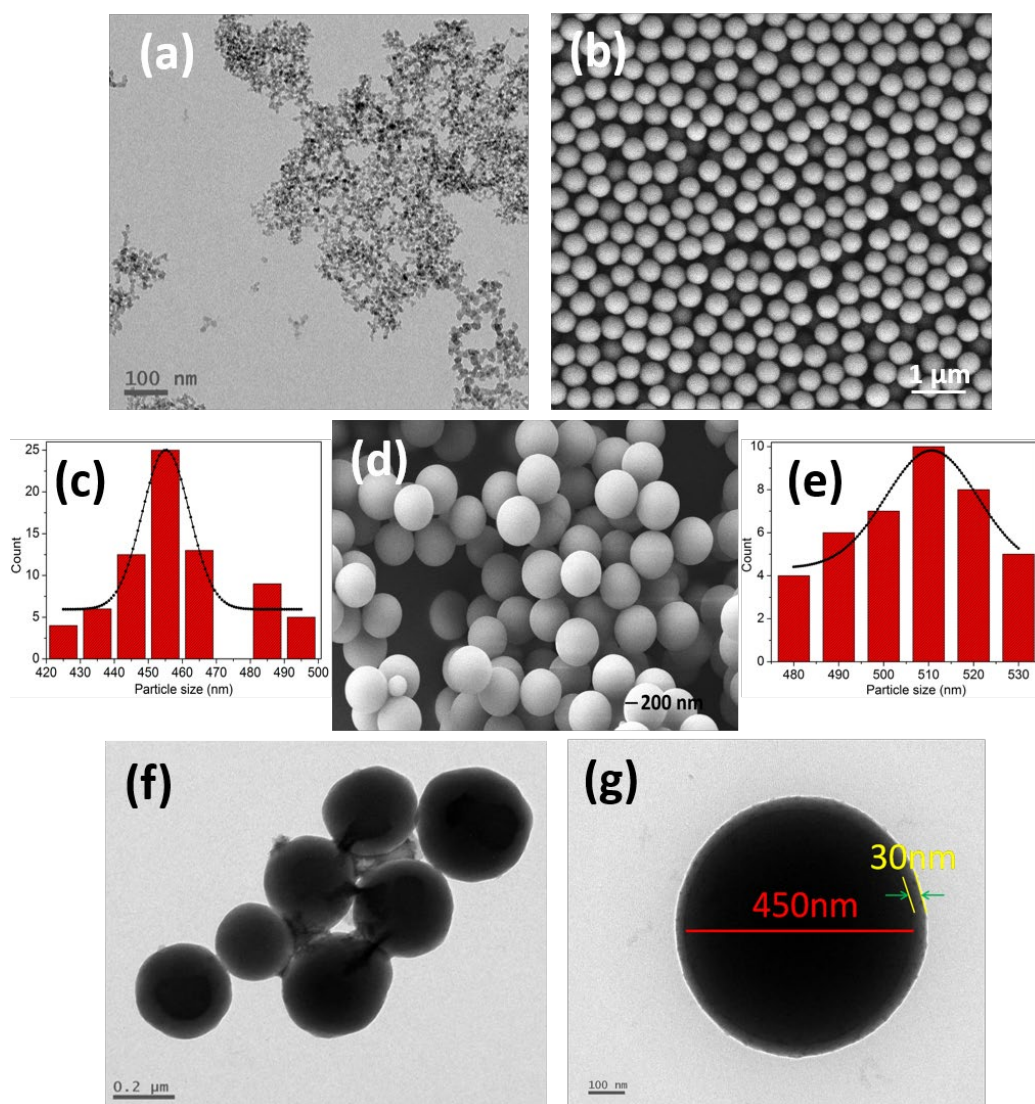


**Figure 3.1.2.** TEM image of (a) SiO<sub>2</sub> NPs-1 (10-15nm), FESEM images of (b) SiO<sub>2</sub> NPs-2 with (c) corresponding particle size distribution (455 nm) and (d) core shell PCL-SiO<sub>2</sub> NPs with (e) corresponding particle size distribution (510 nm), TEM images of (f) PCL-SiO<sub>2</sub> NPs and (g) single core shell PCL-SiO<sub>2</sub> NP.

Hollow mesoporous PCL capsules were synthesized through template synthesis approach as it has been discussed in synthesis procedure part, by using two different SiO<sub>2</sub> templates i.e., SiO<sub>2</sub> NPs-1 (10-15nm) and SiO<sub>2</sub> NPs-2 (~455nm) (**Figure 3.1.2a** and **3.1.2b** respectively). Microscopic images in **Figure 3.1.2a** and **3.1.2b** confirms the spherical morphology of the SiO<sub>2</sub> NPs with uniform dispersion. **Figure 3.1.2c**, average particle size distribution plot has confirmed the average diameter of SiO<sub>2</sub> NP-2 as 455nm. Initially, core-shell structure of PCL-SiO<sub>2</sub> has been designed where the PCL network has been formed surrounding to the SiO<sub>2</sub> NPs-2 core, thus forming the shell structure and the smaller SiO<sub>2</sub> NPs-

1 entrapped in the network of the PCL shell as shown in **Figure 3.1.2d-g**. Consequently, the larger SiO<sub>2</sub> NPs-2 help to create hollow core at the center, whereas the smaller particles (SiO<sub>2</sub> NPs-1) help to create the mesopores on the polymeric shell of PCL.

In **Figure 3.1.2e** the average size of the core shell PCL NPs have shown as 510nm in diameter with the shell thickness of ca. 30-35nm (**Figure 3.1.2g**). In **Figure 3.1.2g** (HRTEM), the entrapped SiO<sub>2</sub> NP-1 are clearly visible which helps to create the mesopores on the PCL shell as well as SiO<sub>2</sub> NP-2 which helps to form the hollow core.

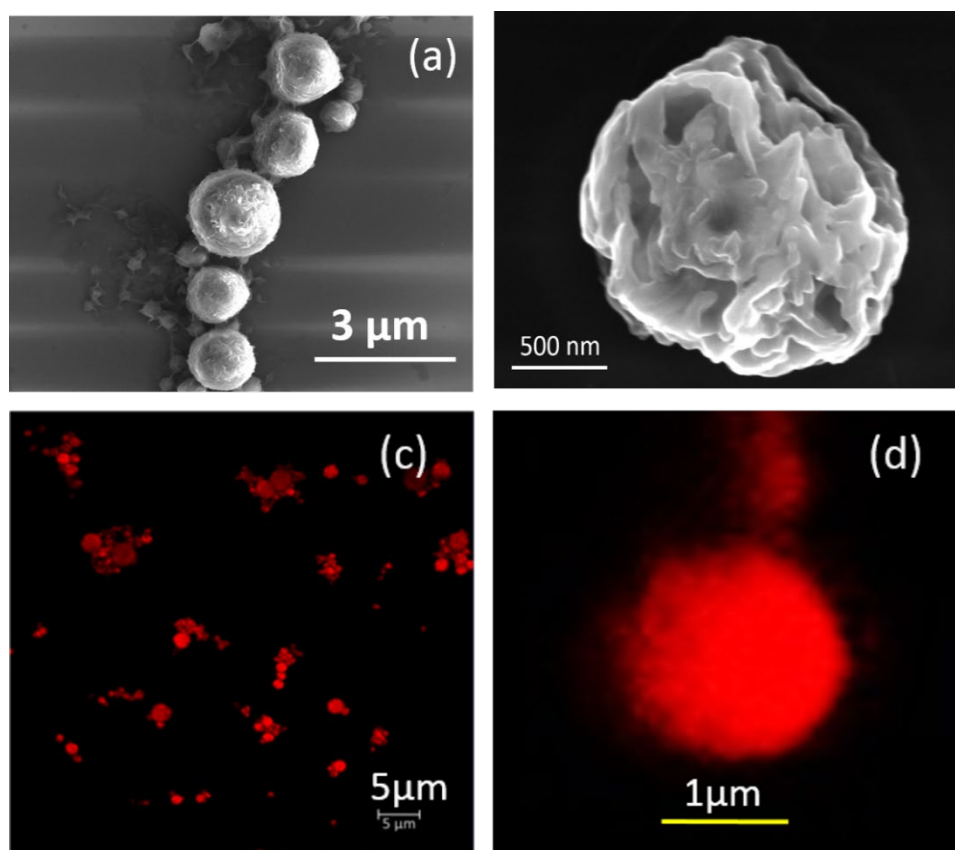


**Figure 3.1.3.** (a) and (b) FESEM images of mesoporous PCL at low and high magnification, respectively, (c) and (d) confocal microscopy images of mesoporous PCL loaded with Rhodamine 6G at lower and higher magnification, respectively.

The FESEM micrograph in **Figures 3.1.3a** and **3.1.3b** clearly showed the spherical morphology with pores on the shell of PCL capsules. The porous nature of the PCL capsules has further been confirmed from BET experiments (**Figure 3.1.4**). Further to confirm the porous structure and to check the loading of small molecules, confocal microscopy analysis has been performed and the results have been shown in **Figures 3.1.3c** and **3.1.3d**. For this study, Rh 6G molecules have been loaded in the NCs and the confocal microscopy images

were acquired. The clear red emission from the capsules is the evidence for the porous structure of the PCL shell (*Figure 3.1.3c* and *3.1.3d*).

### 3.1A.7. BET surface area analysis

The BJH adsorption-desorption isotherm for the polymer capsules were obtained from the BET experiment and acquired a type-IV isotherm with a clear hysteresis showed in *Figure 3.1.4a* and the nature of the isotherm is the evidence for the porous structure.

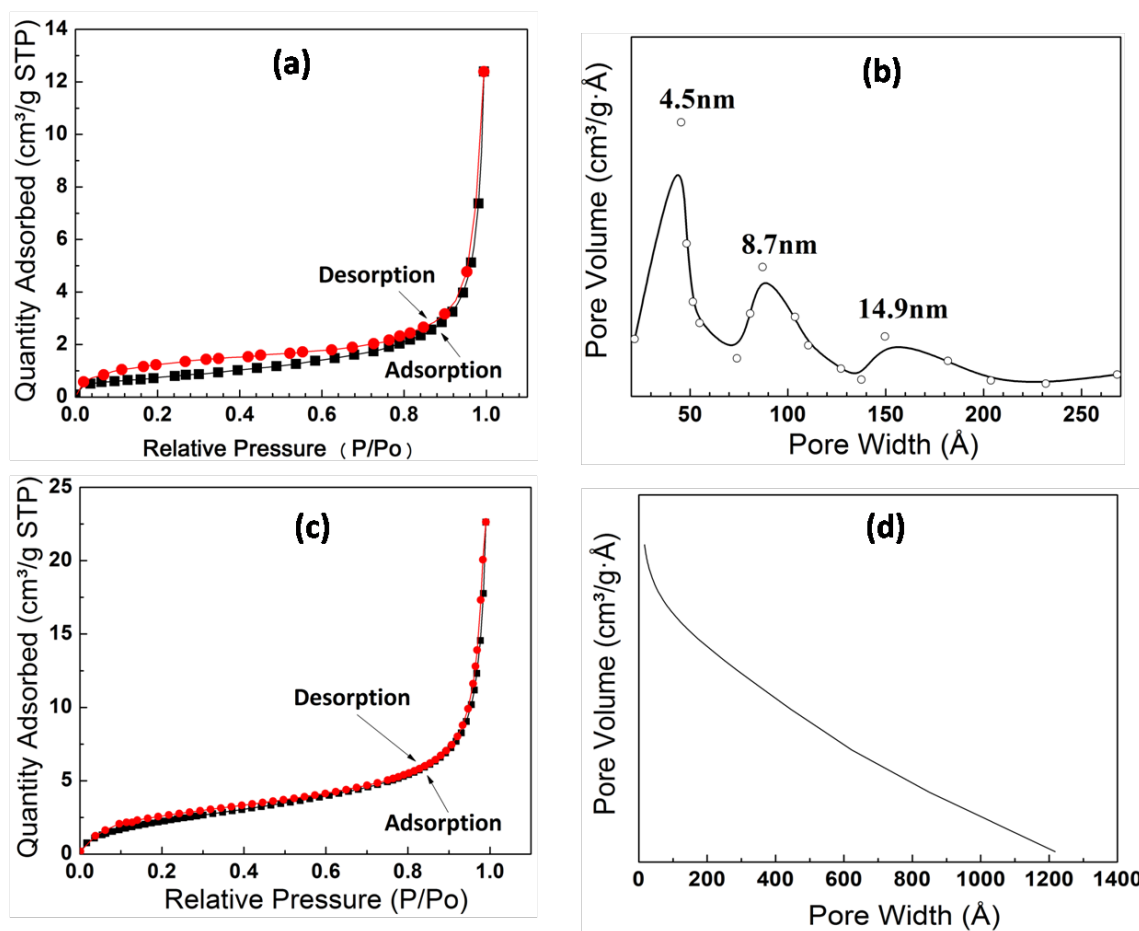


**Figure 3.1.4.** BET results (a) BJH adsorption-desorption isotherm and (b) pore size distribution of mesoporous PCL capsules, respectively. (c) and (d) BJH adsorption-desorption isotherm and pore size distribution of DHA loaded PCL capsules, respectively.

BET surface area for the mesoporous PCL capsules have also been calculated and found to be 50m<sup>2</sup>.g<sup>-1</sup>. The hollow core has been created by the removal of the bigger SiO<sub>2</sub> NPs-2 templates from the core and the porous shell structure created by removing smaller SiO<sub>2</sub> NPs-1 from the core-shell structure of PCL-SiO<sub>2</sub> NPs. From BET, the average pore size has been obtained to be in between 4.5nm to 14.9nm with different sizes of the pores such as 4.5, 8.7

and 14.9nm in diameter as it is in **Figure 3.1.4b**. The pore size ca. 4.5nm has been formed due to the micelles size of the surfactant (Igopal CO 50) and the sizes of the pores 8.7nm and 14.9nm have been formed due to the distribution of the smaller sizes of SiO<sub>2</sub>-1 NPs. It is worth to mention that, the shrinkage of the pore size in mesoporous polymeric shell compared to the size of SiO<sub>2</sub> NPs-1 has occurred due to the relaxation of the strain of the PCL chains (viscoelastic nature), once the SiO<sub>2</sub> (NPs-1) particles have been extracted from the shell. On loading of DHA in mesoporous PCL, the surface area is reduced to 32.2 m<sup>2</sup>.g<sup>-1</sup>. **Figure 3.1.4c** and **3.1.4d** are showing the BJH isotherm and pore size distribution profile for the DHA loaded PCL capsules, respectively. The diminution of hysteresis in **Figure 3.1.4c** compared to the **Figure 3.1.4a** and the nonappearance of peaks for pore size distribution (**Figure 3.1.4d**) are the clear evidence for the loading of DHA in the pores of PCL capsules. Thus, it is confirmed that the drug molecules were loaded in porous and hollow PCL capsules. It can be assumed that the hollow core of the capsules act as a reservoir and the surface mesopores act as the channel for releasing the drug molecules from the core.

### 3.1A.8. Surface chemical structure of hollow mesoporous PCL capsules

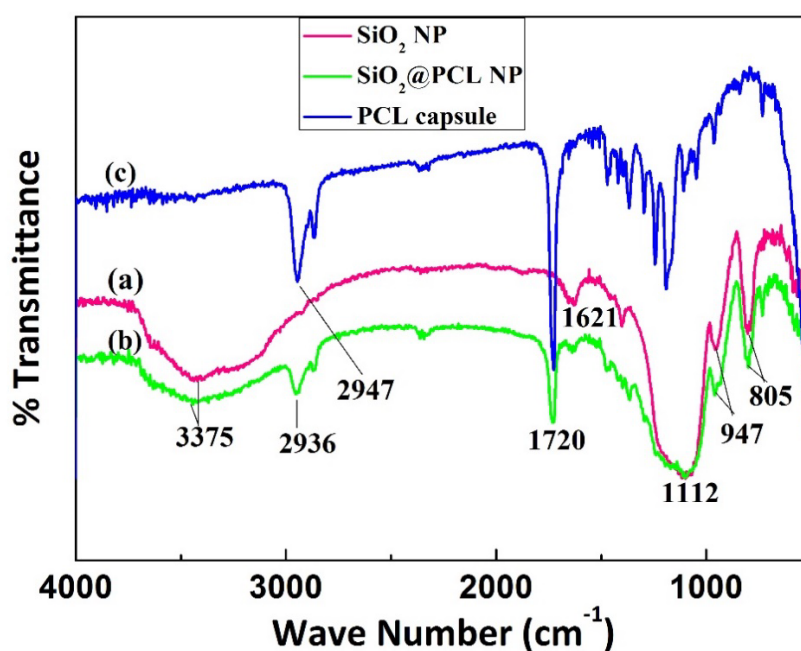


**Figure 3.1.5.** FTIR results for (a) SiO<sub>2</sub> NPs, (b) PCL- SiO<sub>2</sub> NPs and (c) hollow porous PCL capsules.

From the FTIR analysis, we have identified the functional groups present on the surface of the SiO<sub>2</sub> NPs, core-shell PCL-SiO<sub>2</sub> NPs and hollow porous PCL capsules showed in **Figure**

3.1.5 and for commercially available pure PCL showed in **Figure 3.1.6**. In mesoporous PCL the band at  $2936\text{cm}^{-1}$  arises for C-H ( $-\text{CH}_2$ ) group of PCL and band arises at  $1720\text{cm}^{-1}$  is due to the C=O group of PCL [201]. It is worth mentioning that the chemical structure of PCL before and after formation of capsules remained unaltered (**Figure 3.1.6** pure PCL and **Figure 3.1.5b, 3.1.5c**). For  $\text{SiO}_2$  (**Figure 3.1.5a**), the band appeared at  $1112\text{cm}^{-1}$  is for asymmetric vibrations of Si-O, at  $947\text{cm}^{-1}$  for asymmetric vibration of Si-OH and at  $805\text{cm}^{-1}$  for symmetric vibrations of Si-O. An intense absorption band at  $3375\text{cm}^{-1}$  is appeared due to the stretching of O-H bond of water. Also, this band can be cross checked through the  $1635\text{cm}^{-1}$  band appeared due to scissor bending vibration of molecular water. None of the characteristic bands which could be for  $\text{SiO}_2$  (**Figure 3.1.5a**) [202–204] have been identified in hollow mesoporous PCL capsules (**Figure 3.1.5c**), meant  $\text{SiO}_2$  templates have been removed completely from the core shell structure (i.e. from PCL- $\text{SiO}_2$  NPs) and formed the hollow mesoporous PCL capsules as it has been shown in the FESEM, SEM and TEM images.

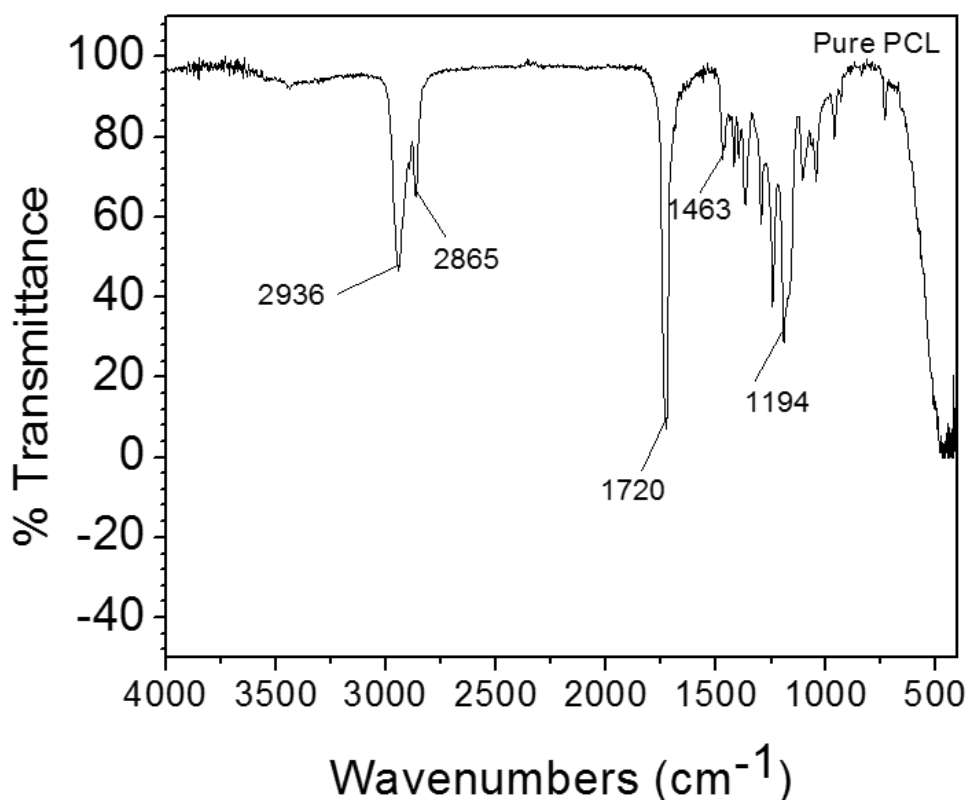


**Figure 3.1.6.** FTIR spectrum of pure PCL polymer (commercial) with all characteristic bands.

### 3.1A.9. Thermal stability, solid state crystal structure study and zeta potential analysis

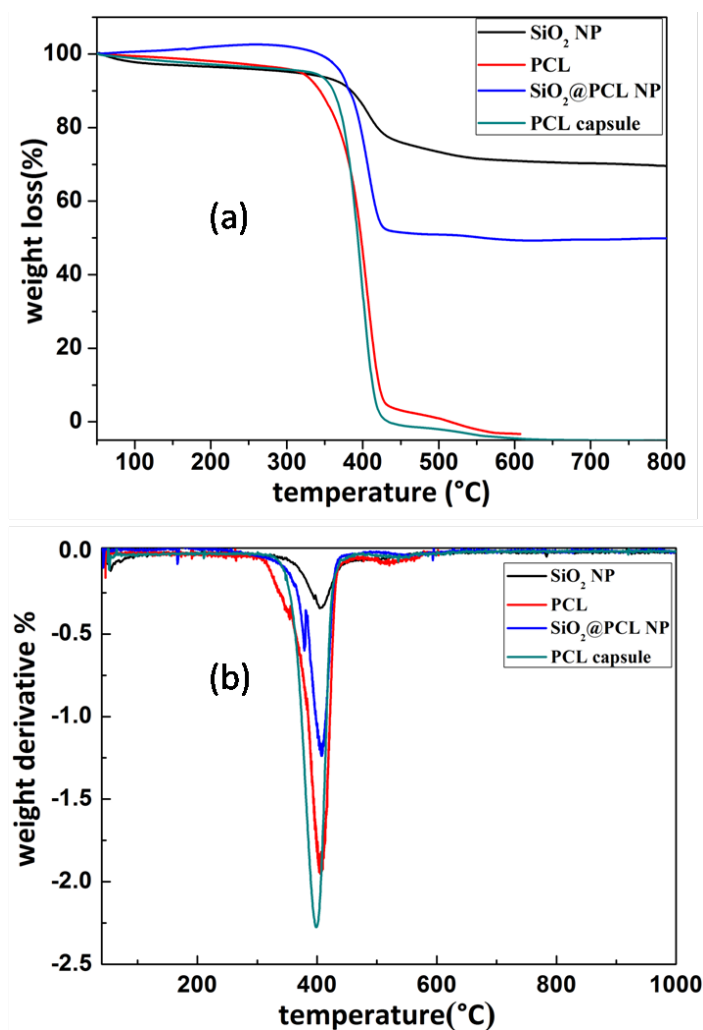


**Figure 3.1.7.** (a) TGA for SiO<sub>2</sub> NPs, pure PCL (commercial), PCL- SiO<sub>2</sub> NPs and hollow porous PCL capsules and (b) DTGA for the same, respectively.

The complete removal of SiO<sub>2</sub> NPs has further been confirmed through TGA showed in **Figure 3.1.7** and powder XRD analysis showed in **Figure 3.1.8**. For TGA, all samples SiO<sub>2</sub> NPs, pure PCL, core shell PCL-SiO<sub>2</sub> NPs and PCL NCs were heated in the range of 40°C-1000°C with a heating rate 10°C/min. TGA thermograms (**Figure 3.1.7**) show 15% weight loss occurred in between 50-450°C due to the loss of free water molecules/moisture from the surface of template SiO<sub>2</sub> and throughout the whole temperature range weight loss remained constant. However, for core shell PCL-SiO<sub>2</sub> NPs weight loss occurred around 350°C due to the weight loss of polymer PCL (commercial pure PCL polymer has shown a firm weight loss after 350°C and continued till 560°C), beyond ~450°C weight loss became constant due to the presence of SiO<sub>2</sub> in the core. After removal of SiO<sub>2</sub>, the weight loss for PCL NCs started at

~340°C and continued upto 450°C due to the complete degradation of PCL. Therefore the porous PCL capsules are thermally stable upto 340°C.

From the XRD results, as shown in **Figure 3.1.8**, it is confirmed that the prepared porous PCL capsules are semicrystalline/amorphous in nature. XRD pattern of PCL-SiO<sub>2</sub> NPs (**Figure 3.1.8b**) and mesoporous PCL capsules (**Figure 3.1.8c**) show diffraction peaks at  $2\theta = 21.4^\circ$  and  $23.0^\circ$ , corresponding to the orthorhombic planes (110) and (200) of PCL, respectively [205,206]. However, SiO<sub>2</sub> NPs showed amorphous behaviour, showed in **Figure 3.1.8a**.

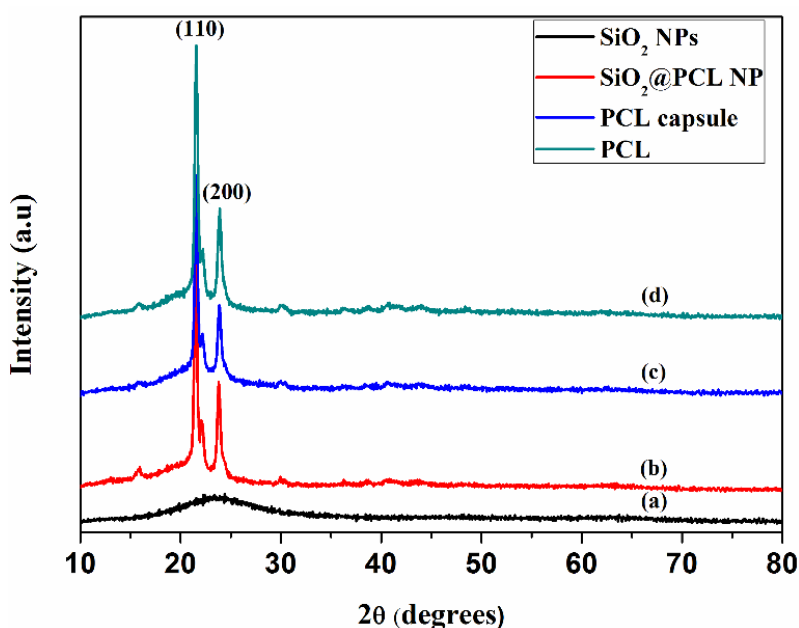


**Figure 3.1.8.** XRD for (a) SiO<sub>2</sub> NPs, (b) core shell PCL-SiO<sub>2</sub> NPs, (c) hollow porous PCL capsules and for (d) pure PCL (commercial).

Further, the DSC results (**Figure 3.1.9**) confirmed that there was no modification on the chemical structure of the PCL chain, in PCL-SiO<sub>2</sub> NPs (**Figure 3.1.9b**) and hollow mesoporous PCL capsules (**Figure 3.1.9c**), rather  $T_m$  (melting temperature) shifted little from PCL-SiO<sub>2</sub> NPs ( $T_m \sim 61^\circ\text{C}$ ) to PCL capsules ( $T_m \sim 63^\circ\text{C}$ ) due to the rearrangement of the polymer chains during processing.

To check the zeta potential value, 500 $\mu\text{g}$  of PCL NCs have been dispersed in 1mL of DI water. The value has been recorded at temperature  $25^\circ\text{C}$  by using He-Ne LASER wavelength of 633 nm. **Figure 3.1.10**, showed the zeta potential value of PCL NCs which has been found as  $-30.6\text{ mV}$  and standard deviation  $\pm 5.93$  (single peak).

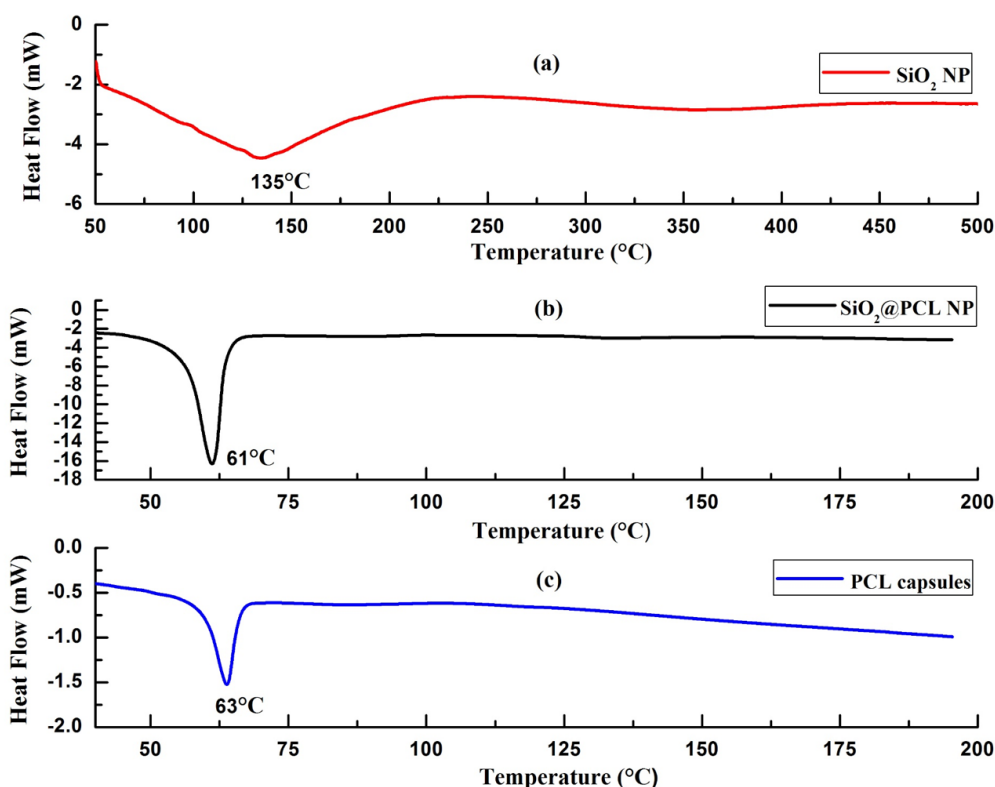


Figure 3.1.9. DSC for (a) SiO<sub>2</sub> NPs, (b) PCL-SiO<sub>2</sub> NPs and (c) hollow porous PCL capsules.

Table 1: Zeta potential results of hollow porous PCL capsules.

	Mean (mV)	Area (%)	St Dev (mV)
<b>Zeta Potential (mV): -30.6</b>	<b>Peak 1: -30.6</b>	100.0	5.93
<b>Zeta Deviation (mV): 5.93</b>	<b>Peak 2: 0.00</b>	0.0	0.00
<b>Conductivity (mS/cm): 0.0118</b>	<b>Peak 3: 0.00</b>	0.0	0.00
<b>Result quality : Good</b>			

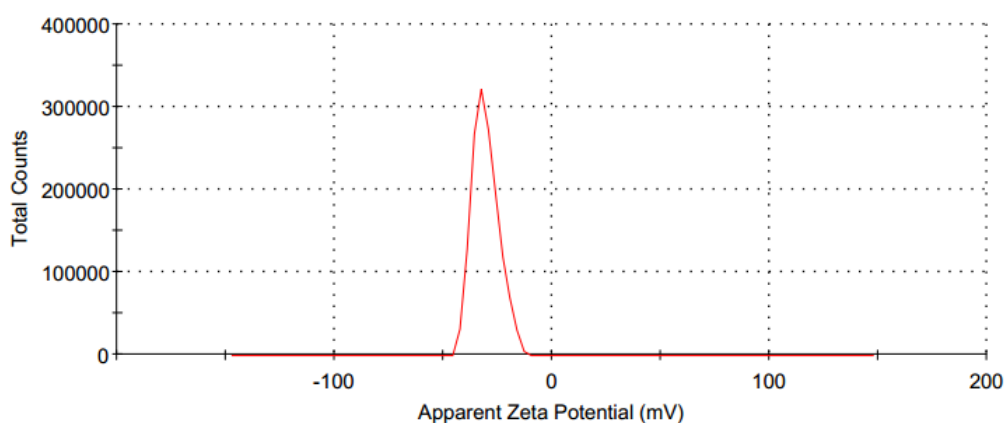
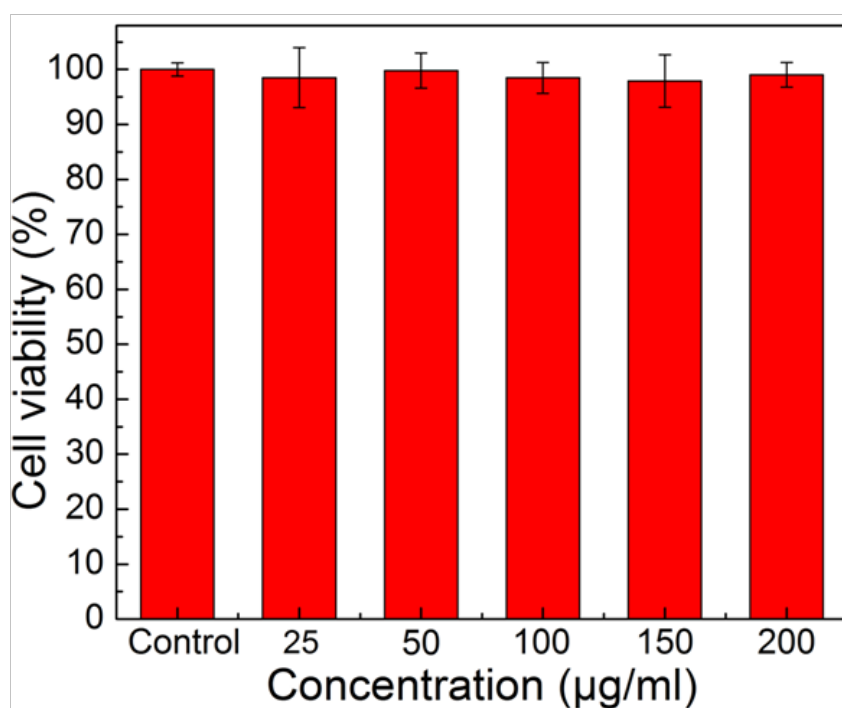


Figure 3.1.10. Zeta potential analysis of hollow porous PCL capsules.

### 3.1A.10. Cell viability analysis of bare hollow mesoporous PCL capsules with *P. falciparum* culture medium

The *in vitro* cytotoxicity assay of the hollow mesoporous PCL capsules were carried out in the culture medium by taking the different concentrations of unloaded capsules such as 25, 50, 100, 150 and 200 $\mu\text{g}\cdot\text{mL}^{-1}$ . First 500 $\mu\text{L}$  of the master solution containing fresh media, RBC and Parasitemia was centrifuged (at 500RPM for 3min at RT) and the pellet was used for the study. Working solution of different PCL (capsules) concentrations was added to the pellet and mixed thoroughly. This step was repeated three times for all concentrations as mentioned above to avoid error. The master solution without NCs was considered as control. Finally, all the solutions with different concentrations of PCL capsules, control media and RBC were pipetted into the 96 well plate. The 96 well plate with the sample was then incubated in a CO<sub>2</sub> incubator for 48h. After 48h of incubation, 100 $\mu\text{L}$  of lysis buffer containing SYBR green I (Invitrogen) dye was added to each well and further incubated for 1h at RT in dark. Then absorbance bands of the cells were recorded using the multimode reader. Cytotoxicity of the PCL-DHA and PCL-CQDP nanoformulations with *P. falciparum* cell line in 96 well plate was studied at 37°C using a Multimode Reader.



**Figure 3.1.11.** Cell viability of hollow porous PCL capsules (bear) with different concentrations of capsules incubated with *P. falciparum* cells for 48h.

Cell viability results are shown in **Figure 3.1.11**. To evaluate the cytotoxicity of the synthesized PCL capsules, the control (fresh media, RBC and Parasitemia) is considered as

100% cell viable. All the concentrations of the polymer NCs from lower to higher i.e., 25, 50, 100, 150 and 200 $\mu\text{g.mL}^{-1}$  have almost equivalent percentage of cell viability like control while comparing with the control. From the results, it was confirmed that bare hollow mesoporous PCL capsules were biocompatible in nature, non-toxic and they do not have any role in killing the parasites.

### **3.1A.11. *P. falciparum* inhibition with PCL-DHA and PCL-CQDP formulation**

The effect of PCL-DHA formulation on the *P. falciparum* infected RBCs was studied systematically with varying concentrations of nanoformulation *in vitro* by taking 2, 5, 10, 20, 50, 100, 200, 500 and 1000nM concentrations of DHA loaded in PCL capsules. In brief, the assays were conducted with the pellet obtained from 1mL culture having initial Parasitemia concentration of 1% and haematocrit of 5%. Then 1mL medium containing different concentrations of PCL-DHA formulations each were added to the pellet. The parasites were allowed to culture for 48h at 37°C and finally harvested to make blood smears. Total 1000 number of RBC were counted for each slide to estimate the Parasitemia. **Figure 3.1.12**, represented the parasitic cell inhibition by PCL-DHA nanoformulations from lower to higher concentrations of DHA. Similar experiments were performed by taking PCL-CQDP nanoformulations to study the inhibition of *P. falciparum* by taking CQDP concentration as 100, 200, 400 and 500  $\mu\text{g.mL}^{-1}$ . **Figure 3.1.13** represented the experimental parasitic inhibition analysis by PCL-CQDP nanoformulation from lower to higher CQDP concentrations in PCL NCs. It is found from the both **Figure 3.1.12** and **Figure 3.1.13**, the % of cell inhibition is decreased with increased of drug concentration in both cases i.e., PCL-DHA and PCL-CQDP nanoformulations respectively. From **Figure 3.1.12**, for the 2nM concentration of DHA the % of cell inhibition found as  $82.7\pm 2.5$  (%) and for higher concentration like 1000nM it came out as  $12.4\pm 3.4$  (%), which is very less compared to the lower concentration of the drug DHA.

In the same way, for the drug CQDP, the % of cell inhibition calculated  $85 \pm 3.1$  (%) and  $80.1\pm 1.5$  (%) for lower concentration 100 $\mu\text{g.mL}^{-1}$  and higher concentration 500  $\mu\text{g.mL}^{-1}$  of CQDP content in PCL capsules (**Figure 3.1.13**).

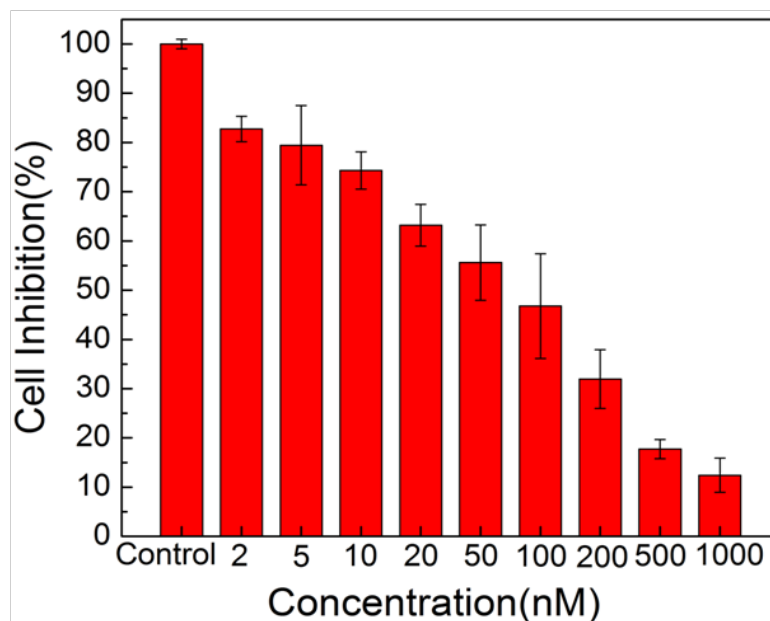


**Figure 3.1.12.** Cell inhibition by PCL-DHA nanoformulation while treated with *P. falciparum* infected RBCs by maintaining lower to higher concentrations of drug DHA (2nM to 1000nM) at 37°C after 48h of incubation.

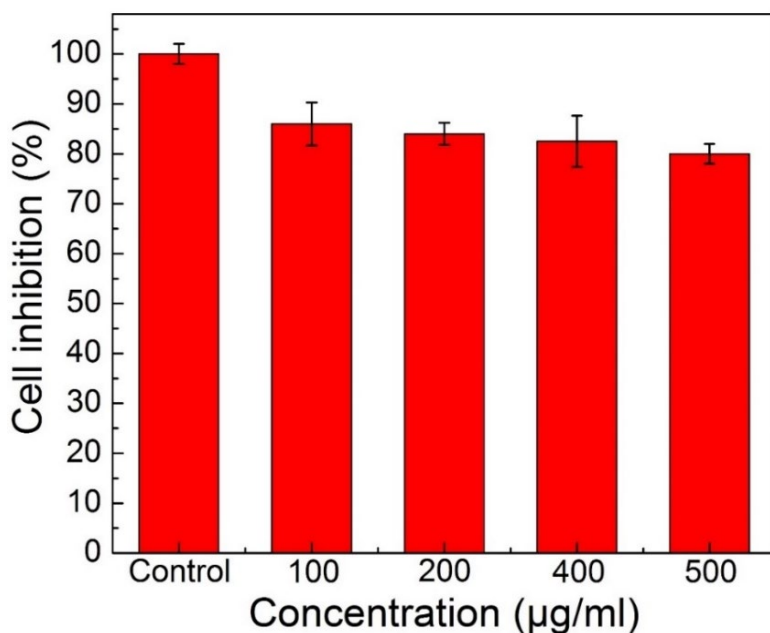


**Figure 3.1.13.** Cell inhibition by PCL-CQDP nanoformulation while treated with *P. falciparum* infected RBCs by maintaining lower to higher concentrations of drug CQDP (100 to 500µg/mL) at 37°C after 48h of incubation.

### 3.1A.12. Hollow mesoporous PCL capsules facilitate releasing of DHA and CQDP in the medium

PCL-DHA and PCL-CQDP formulations were suspended in culture medium RPMI 1640 and the release behavior has been studied. Maintaining a fixed time interval the absorbance of the released drugs in the medium was recorded at different temperatures such as 30, 37, 40 and 43°C using UV-Vis spectrometer and the extent of release of DHA and CQDP were calculated. Release amounts were calculated for 6h with a fixed time interval and then investigated the kinetics for the release. To study the release profile, 0.6mg of PCL-DHA and PCL-CQDP for each were taken with 5mL of medium in a cuvette. To calculate the extent of drug release the absorption band at 263nm for DHA were considered. Following the similar procedure, the release kinetics for CQDP were studied by considering absorption band at 260nm.

It is worth mentioning that, the loading of the DHA, CQDP and dye molecules in hollow porous PCL capsules occurred through the diffusion process. The pores present on the polymeric shell act as a channel to diffuse the drugs/dye into the hollow core. Successful loading of Rh 6G dye has been confirmed through the confocal microscopy experiments (*Figure 3.1.3c* and *3.1.3d*). A deep red light emission is detected for the loaded Rh 6G in the PCL capsules.

The release profiles of DHA and CQDP and their kinetics have studied at different temperatures and time interval showed in *Figure 3.1.14a* and *Figure 3.1.14b* respectively, to correlate with the body temperature. The temperature dependent release of DHA and CQDP are studied at different temperatures such as 30, 37, 40 and 43°C, since parasitic infection caused enhancement of body temperature periodically. The results obtained were very interesting as shown in *Figure 3.1.14a* and *3.1.14b*. It was revealed from these release profiles that with an increase in the temperature and time the extent of release of drug molecules also increased. Within 1h of incubation the percentage of release of DHA from PCL-DHA formulation (200µg per mg of PCL capsule) is found to be 16±0.8 (%), 32±1.6 (%), 21±1.05 (%), 21.5±1.07 (%) and after 5h of incubation the percentage of release obtained to be 23.1±1.5 (%), 39.4±1.8 (%), 66.1±3.3 (%), 71.6±3.5 (%) at temperatures 30, 37, 40 and 43°C, respectively. Similarly for CQDP release from PCL-CQDP formulation, within 1h the percentage of release obtained to be 41.4±2.0 (%), 46.1±2.3 (%), 55.1 ±3.7 (%) and 77.3±3.8 (%) for the temperature 30, 37, 40 and 43°C, respectively, whereas after 5h the amount of

CQDP release for these temperatures obtained to be  $45.3 \pm 2.2$  (%),  $53.1 \pm 2.4$  (%),  $71.4 \pm 4.4$  (%) and  $95.2 \pm 3.8$  (%) of the total loaded CQDP ( $18.6 \mu\text{g}$  per mg of capsules), respectively.

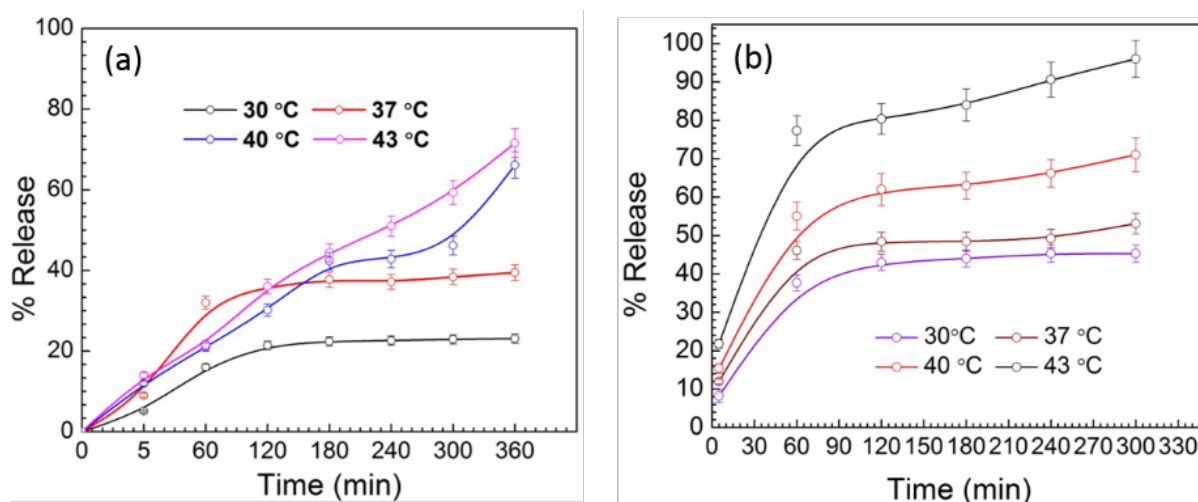


**Figure 3.1.14.** The release profile of (a) DHA from PCL-DHA and (b) CQDP from PCL-CQDP nanoformulations at different temperatures.

**Figure 3.1.15** showed the normalized percentage release profile of drug DHA maintained at room temperature ( $25^{\circ}\text{C}$ ) for 30 days where DHA showed slow and sustained release for a longer period of time and showed 79.8% release the 30<sup>th</sup> day.

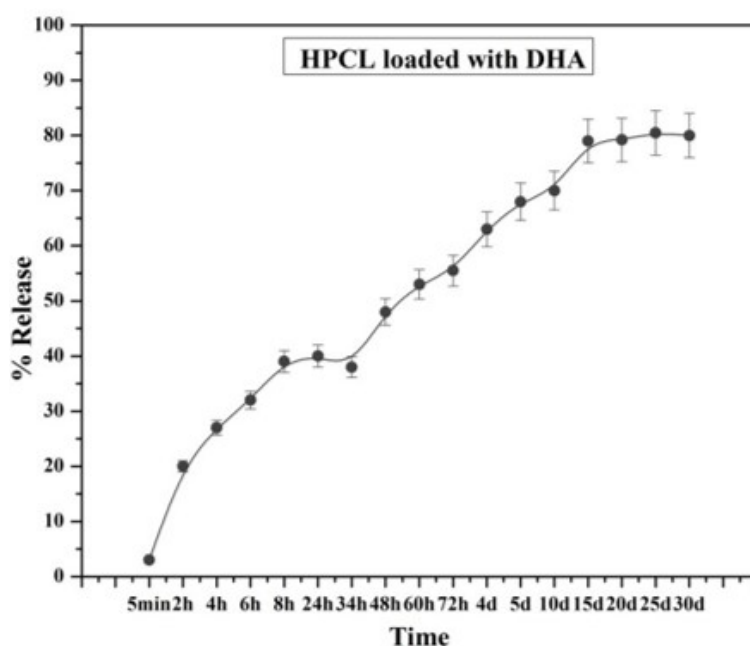


**Figure 3.1.15.** The release profile of DHA drugs from PCL-DHA nanoformulation at room temperature for 30 days.

### 3.1A.13. Release kinetics and diffusion coefficients of PCL-DHA and PCL-CQDP nanoformulations

The release kinetics of DHA and CQDP have been studied using the model kinetic equations as given below (eq. 1) and (eq. 2) [207].

Zero order release kinetic equation (eq. 1),

$$Q_t/Q_0 = K_0 \cdot t \dots \dots \dots (1)$$

Where,  $Q_t$  is cumulative amount of drug released at time  $t$ ,  $Q_0$  is the initial amount of drug,  $K_0$  is zero order release constant,  $t$  is time in min.

The firstorder release kinetic equation,

$$Q_t/Q_0 = 1 - e^{-kt} \dots \dots \dots (2)$$

Where,  $Q_t$  is cumulative amount of drug released at time  $t$ ,  $Q_0$  is the initial amount of drug,  $k$  is first order release constant,  $t$  is time in min.

The diffusion coefficients for both DHA and CQDP, released from the formulations with four different temperatures have been calculated by using the model equation (eq. 3) [208],

$$Y = \frac{M_t}{M_\alpha} = 6 \left( \frac{D_T \cdot t}{\pi \cdot R^2} \right) \dots \dots \dots (3)$$

Where,  $Y = \left( \frac{M_t}{M_\alpha} \right)$  is a function of the extent of drug released at time  $t$ ,  $D_T$  is the diffusion coefficient of drug molecules from the hollow-porous polymer capsules at a temperature (T) and at time  $t$ ,  $R$  is the diameter of the pores of hollow-porous polymer capsules.

Where the diffusion coefficient is defined by the eq. (4) below,

$$D_T = \frac{Y^2 \pi R^2}{36t} \dots \dots \dots (4)$$

At lower temperatures, such as at 30°C and 37°C, DHA released from PCL-DHA formulations exhibited characteristic of a first order release kinetics (**Figure 3.1.16**) and at higher temperatures such as at 40°C and 43°C, drug releases followed a characteristic of zero order release kinetics (**Figure 3.1.17**) in culture medium. To analyses the release kinetics, the

experimental data were fitted in both zero order and first order release kinetic equations (eq. 1 and 2) which are shown in **Figure 3.1.16** and **Figure 3.1.17**. Whereas, the release of CQDP followed characteristic of a first order release behaviour during release from the PCL-CQDP formulation at all four temperatures (30-43°C) shown in **Figure 3.1.18**.

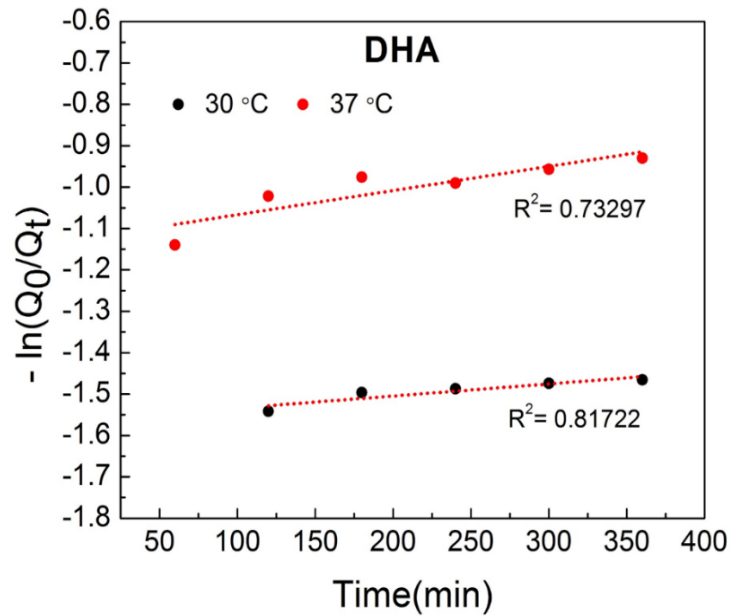


**Figure 3.1.16.** First order release kinetics at 30°C and 37°C for PCL-DHA nanoformulation.

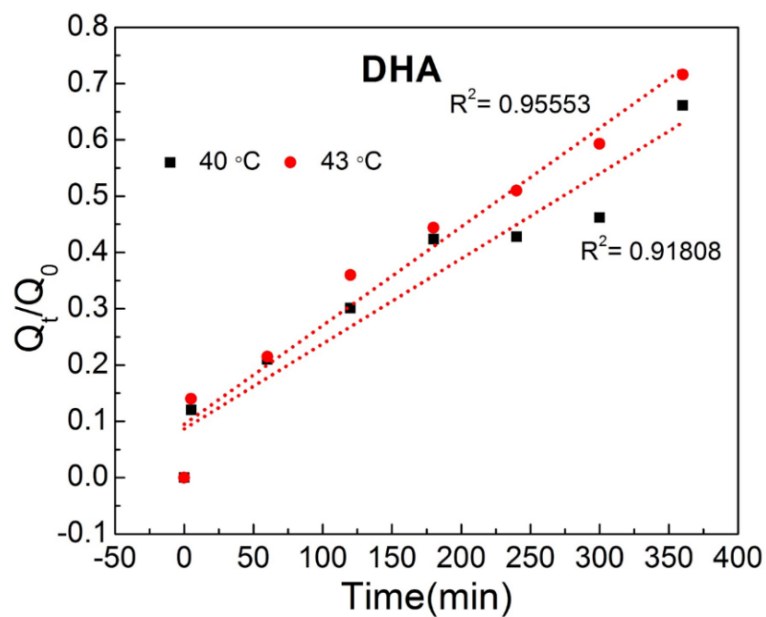


**Figure 3.1.17.** Zero order release kinetics at 40°C and 43°C for PCL-DHA nanoformulation.

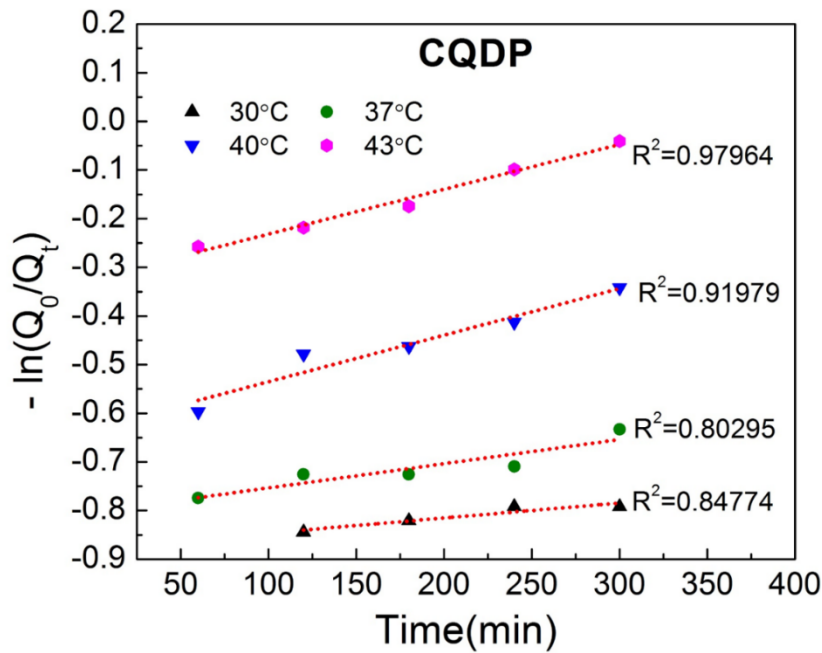


**Figure 3.1.18.** First order release kinetics at 4 different temperatures for PCL-CQDP nanoformulation.

The releases of DHA and CQDP were controlled by the temperature dependent diffusion. Therefore, diffusion coefficients for both drugs DHA and CQDP were released from the PCL-DHA and PCL-CQDP formulations, with different temperatures have been calculated (**Table 2** and **Table 3**) at different time interval with different pore sizes. From the calculated values of diffusion coefficients (**Table 2** and **Table 3**), we can confirm that the diffusion coefficient values of drug release are dependent on time, temperature and pore sizes of PCL capsules. From the **Table 2** and **Table 3**, it is very clear that the diffusion coefficients are increasing with the gradual increase in the pore sizes (from 4.5nm to 14.9nm) and temperatures (from 30°C to 43°C). For example (from **Table 2**), as the pore size increases from 4.5nm to 14.9nm, the diffusion coefficient values for DHA release from NCs increases from  $5.02 \times 10^{-19}$  to  $31.68 \times 10^{-19}$  at a fixed temperature say 37°C (after 5min). With the increase in temperature from 30°C to 43°C the diffusion coefficient increases from  $1.26 \times 10^{-19}$  to  $4.77 \times 10^{-19}$  (after 1h from 4.5 nm pore). Though with the increase of time from initial to a longer period of time (say 5 min to 5h) the diffusion coefficient decreases progressively. For example, for 37°C the diffusion coefficient value after 5min of DHA release was  $5.02 \times 10^{-19}$  whereas after 5h of DHA release, the value obtained to be  $1.45 \times 10^{-19}$  (say 4.5nm pores). A similar trend was observed for the release of CQDP (**Table 3**) i.e., at 37°C, for 5min the  $D_T$  value is  $10.43 \times 10^{-19}$  and for 5h the  $D_T$  the value calculated as  $2.76 \times 10^{-19}$  for the pore size 4.5nm.

**Table 2:** Diffusion coefficient ( $D_T$ ) of PCL- DHA nanoformulation with a range of time (5-300min) and temperature (30-43°C).

<b>Pore size 4.5nm</b>				
<b>t (min)</b>	<b><math>D_T</math> at different temperatures ( <math>\times 10^{-19}</math>)</b>			
	<b>30°C</b>	<b>37°C</b>	<b>40°C</b>	<b>43°C</b>
5	1.53	5.02	8.48	11.54
60	1.26	4.77	2.93	3.45
120	1.12	3.18	2.25	3.22
180	0.82	2.32	2.23	3.19
240	0.63	1.69	2.16	3.18
300	0.51	1.45	2.09	2.27
<b>Pore size 8.7nm</b>				
5	5.72	18.78	31.69	43.13
60	4.69	17.83	10.96	12.90
120	4.20	11.88	8.39	12.05
180	3.07	8.69	8.32	11.92
240	2.34	6.32	8.08	11.88
300	1.92	5.41	7.83	8.47
<b>Pore size 14.9nm</b>				
5	16.78	55.08	31.68	126.51
60	13.77	52.28	10.96	34.85
120	12.32	34.85	8.318	35.33
180	8.99	25.48	8.39	34.97
240	6.86	18.55	8.08	37.83
300	5.64	15.86	7.83	24.86
<b>Average pore size 9.4nm</b>				
5	6.63	21.74	36.67	49.92
60	5.43	20.63	12.69	14.93
120	4.86	13.75	9.72	13.94
180	3.55	10.05	9.63	13.80
240	2.71	7.32	9.36	13.75
300	2.23	6.25	9.06	9.81

**Table 3:** Diffusion coefficient ( $D_T$ ) of PCL- CQDP nanoformulation with a range of time (5-300min) and temperature (30-43°C).

<b>Pore size 4.5nm</b>				
<b>t (min)</b>	<b><math>D_T</math> at different temperatures ( <math>\times 10^{-19}</math>)</b>			
	<b>30°C</b>	<b>37°C</b>	<b>40°C</b>	<b>43°C</b>
5	6.95	10.43	14.87	29.32
60	3.96	8.47	13.96	27.97
120	4.53	5.75	9.42	15.85
180	3.16	3.83	6.48	11.54
240	2.52	2.96	5.36	10.06
300	2.01	2.76	4.95	9.04
<b>Pore size 8.7nm</b>				
5	26.01	38.97	55.61	109.57
60	14.81	31.68	52.18	104.58
120	16.95	21.47	35.22	59.27
180	11.83	14.32	24.23	43.13
240	9.41	11.09	20.07	37.63
300	7.53	10.34	18.51	33.80
<b>Pore size 14.9nm</b>				
5	76.27	114.31	163.11	321.41
60	43.43	92.95	153.08	306.75
120	49.73	63.00	103.31	173.85
180	34.71	42.00	71.06	126.51
240	27.59	32.55	58.87	110.38
300	22.07	30.33	54.29	99.14
<b>Pore size 9.4nm</b>				
5	30.10	45.11	64.36	126.83
60	19.62	36.67	60.41	121.05
120	17.14	24.86	40.76	68.61
180	13.69	16.57	28.04	49.92
240	10.88	12.85	23.23	43.55
300	8.71	11.97	21.43	39.12

### 3.1A.14. PCL-DHA and PCL-CQDP formulation actively inhibit *P. falciparum*

The bio-availability and inhibition of *P. falciparum* 3D7 have been investigated using PCL-DHA and PCL-CQDP nanoformulations separately through *in vitro* susceptibility assay. Three *P. falciparum* 3D7 *in vitro* cultures have been grown in parallel sets of the experiments. Set-1 was supplemented with free drugs DHA and CQDP, Set-2 was supplemented with mesoporous PCL capsules containing DHA and CQDP (formulations), and the set-3 is mock-treated (control). From the experimental results, it is observed that the bare mesoporous PCL capsules do not have any anti-parasitic effects up to 200 $\mu\text{g.mL}^{-1}$  concentration (**Figure 3.1.11**), whereas individual PCL-DHA and PCL-CQDP formulations exhibited a clear role on parasite growth even at a lower amount of drug concentrations. Based on the treatment with the formulation, the  $\text{IC}_{50}$  value was calculated and found to be 66.6nM which is almost similar to the  $\text{IC}_{50}$  obtained for free DHA (65.4nM). These results imply that formulation of hollow porous PCL NCs with DHA is effective in inhibition of parasitic growth and killing of them in a sustained manner showed in **Figure 3.1.19a**.

Then the inhibitory effects of CQDP loaded NCs (PCL-CQDP) were also evaluated by performing *in vitro* viability assay in *P. falciparum* 3D7 strain following the similar procedure used for PCL-DHA. **Figure 3.1.19b** shows the anti-malarial activities of PCL-CQDP formulation in a dose dependent manner. The  $\text{IC}_{50}$  value has been calculated for PCL-CQDP formulation and found to be 25.14nM, which is more compared to the value obtained for free CQDP (15.06nM). The  $\text{IC}_{50}$  value is in good agreement with the previously reported  $\text{IC}_{50}$  values for the free CQDP and six other available antimalarial drugs [98]. The results are evident for the release of CQDP from the hollow mesoporous PCL capsules is very effective and the marginal shift in the  $\text{IC}_{50}$  value and the rightward shift of the curve indicates that the mesoporous PCL capsules still retained in CQDP for longer period of time and thus a sustained delivery was maintained and suppress the growth of parasites. It was further can be noted that treatment efficiencies with PCL-DHA and PCL-CQDP are quite excellent with respect to the other NPs used for the same purposes.

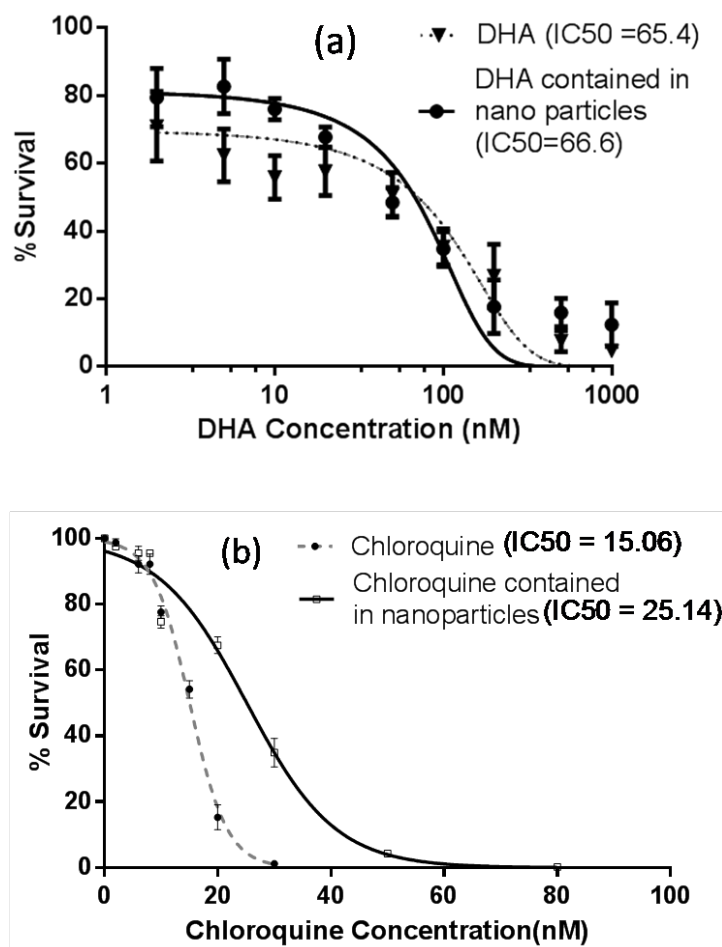


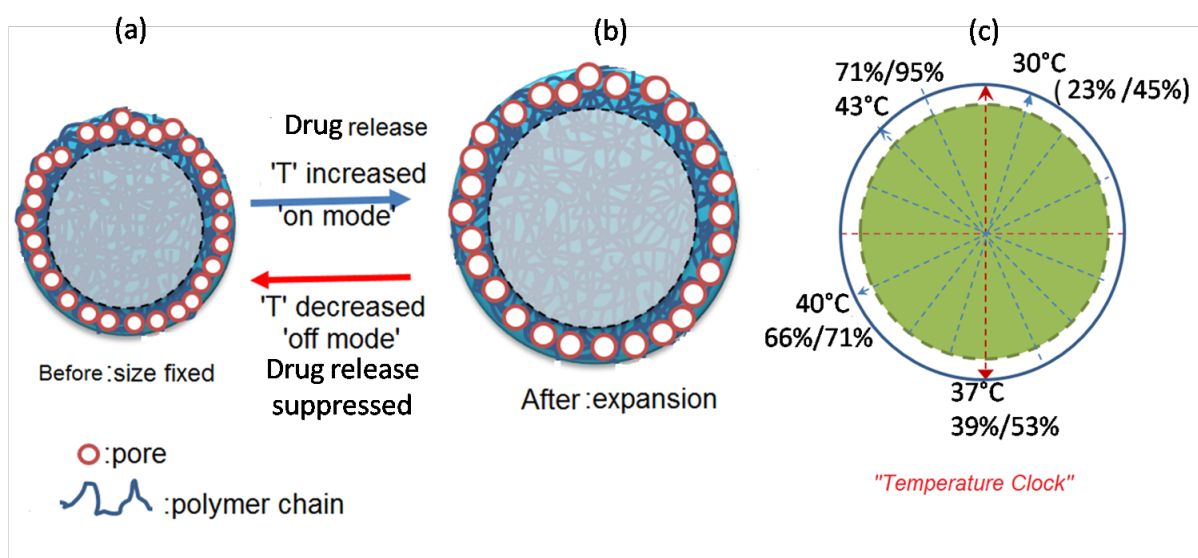
**Figure 3.1.19.** Anti-malarial activity of (a) PCL-DHA nanoformulation and (b) PCL-CQDP nanoformulation in a dose dependent manner.

### 3.1A.15. Summary of Part I (Section A)

In this **Part I (Section A)**, the synthesized hollow mesoporous PCL capsules are found as quite a stable biopolymer and possess slow degradable in a biological fluid which helps in the sustained release of antimalarial drugs such as DHA and CQDP from the nanoformulation. The PCL NCs designed here are biocompatible in nature.

Furthermore, it is evident that the novel formulation of DHA and CQDP with hollow mesoporous PCL capsules are successfully challenging *P. falciparum* growth with respect to the other six reported antimalarial drugs used alone without any carriers [98] and could be a promising choice in the treatment of malaria. The dose dependent suppression of *P. falciparum* has been studied and found that designed nanoformulations have similar IC<sub>50</sub> value for both encapsulated and free DHA and exhibited more IC<sub>50</sub> value compared to the IC<sub>50</sub> value obtained

for free CQDP and is quite efficient in killing the *P. falciparum* infection in RBCs and the efficiency is very high compared to previous reports using other NPs. Additionally, the temperature dependent extents of DHA and CQDP release are very interesting and have tremendous physiological significance in the light of the periodic change in body temperature due to *P. falciparum* infection. As soon as the body temperature increases due to the *P. falciparum* infection of RBCs, which could lead to the minor thermal expansion of the capsules as well as hollow core size and surface pore size which leads to the release of drugs DHA and CQDP from the formulations immediately to suppress the activity of *P. falciparum* and once the body temperature will be decreased then there will be contraction of the capsule's size, its pore size as well as the rate of diffusion of drugs will also be decreased. Hence, synthesized formulations show temperature dependent release of DHA and CQDP. That is with an increase in the temperature the release rate of drug molecules increase like a function of switching 'on-mode' and once the temperature decreases the release rate suppressed like a function of switching 'off-mode' as it is mechanized schematically in **Schematic 3.1.3a** and **3.1.3b**. Thus, the release process can be represented as like as a "temperature clock" and controlled by temperature dependent diffusion as it is shown in **Schematic 3.1.3c**.



**Schematic 3.1.3.** (a and b) Representative schematic showing with a change in body temperature how the DHA/CQDP release happened with "on" and "off" mode from the PCL-DHA and PCL-CQDP nanoformulations, and (c) a proposed "temperature clock" showing the different extent of release with temperature.

Further, the rate of diffusion of DHA and CQPD from hollow mesoporous PCL depends on the pore size as tabulated in **Table 2** and **Table 3**. A similar phenomenon is observed for the other materials [209]. Therefore, the formulations of DHA and CQDP with hollow porous PCL are of special kinds and are paramount for knock down the *P. falciparum* infection in RBCs and the doses can be tuned by controlling the temperature very easily.

Therefore, novel formulations are demonstrated their excellent efficiencies as a carrier in an *in vitro* anti-malaria drug delivery system and successfully abrogating *P. falciparum* growth and which is well monitored by changing temperatures. Thus designed nanoformulations act as “*temperature clock*” to suppress the normal activities of *P. falciparum* which is very unique and pioneering can be used in the treatment of malaria.

---

**Outcome:** This work has published as, “Hollow mesoporous polymer capsules with Dihydroartemisinin and Chloroquinediphosphate for knocking down *Plasmodium falciparum* infection”, Biomedical Physics and Engineering Express, 2018, 4-3.

## **Chapter 3: Result and discussion: Part I (Section B)**

### **Efficiency of hollow mesoporous PCL NCs loaded with antimalarial drug Sulfadoxine against *P. falciparum* cell line**

3.1B.1. Introduction

3.1B.2. Loading of Sulfadoxine in hollow mesoporous PCL capsules

3.1B.3. Cell inhibition study of hollow mesoporous PCL capsules loading with Sulfadoxine in the medium

3.1B.4. Hollow mesoporous PCL capsules facilitate releasing of Sulfadoxine in the medium

3.1B.5. Release kinetics and diffusion coefficients of PCL-Sulfadoxine nanoformulations

3.1B.6. Summary of Part I (Section B)

## Chapter 3

### Result and discussion: Part I (Section B)

**Objective: Efficiency of hollow mesoporous PCL NCs loaded with antimalarial drug Sulfadoxine against *P. falciparum* cell line**

#### 3.1B.1. Introduction

With the interesting results achieved from the PCL-DHA and PCL-CQDP nanoformulations mentioned in **Part I (Section A)**, subsequently we have studied the effect of the same hollow porous polymer NCs with another antimalarial drug SD by making PCL-SD nanoformulation. SD loaded PCL NCs have shown a pattern of sustained release of drug from the nanoformulation for extend period one month of time.

#### 3.1B.2. Loading of Sulfadoxine in hollow mesoporous PCL capsules

As mentioned in **Part I (Section A) 3.1A.4**, the same loading protocol have been followed for the loading of an alternative antimalarial drug SD. The dried mesoporous PCL capsules were collected and used for loading anti-malaria drug. The mesoporous PCL capsules were incubated with drug SD, with a concentration of drug to mesoporous PCL capsules of 1:1 mg.mL<sup>-1</sup> in PBS (pH 7.4). The suspensions were stirred for 1h and then kept for another 24h in dark place without stirring. The SD loaded PCL capsules were separated from PBS solution through centrifugation (at 8000RPM). These drug loaded polymer capsules were then washed thoroughly to remove the free drug molecules from the surface of the polymer capsules followed by lyophilization and stored in dark for further experiments.

### 3.1B.3. Cell inhibition study of hollow mesoporous PCL capsules loaded with Sulfadoxine

As mentioned in **Part I (Section A) 3.1A.11**, the effect of PCL-SD nanoformulations on the *P. falciparum* infected RBCs were analyzed with varying concentrations of nanoformulation *in vitro* by taking 2, 5, 10, 20, 50, 100, 200, 500 and 1000nM concentrations of SD loaded in PCL capsules. The assays were conducted with the pellet obtained from 1mL culture having initial Parasitemia concentration of 1% and haematocrit of 5%. Then 1mL medium containing different concentrations of PCL-SD formulations each were added to the pellet. The parasites were allowed to culture for 48h at 37°C and finally harvested to make blood smears. Total 1000 number of RBC were counted for each slide to estimate the Parasitemia.

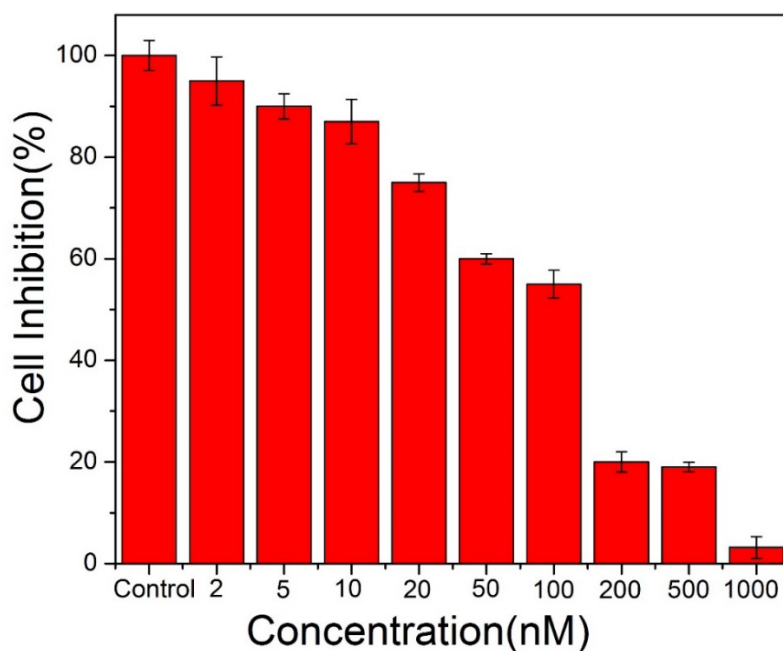


**Figure 3.1.20.** Cell inhibition by PCL-SD nanoformulation while treated with *P. falciparum* infected cells by maintaining lower to higher concentrations of SD at 37°C after incubating for 48h.

*P. falciparum* cell inhibition with antimalarial drug encapsulated polymer based nanoformulations (PCL-SD) has been analyzed here and showed in **Figure 3.1.20** and for the controlled sample 100% cell viability has considered, although the cell viability decreased with the increased concentration of SD loaded inside the polymeric NCs as shown in the **Figure 3.1.20** cell inhibition percentage vs drug concentration plot. PCL-SD formulation with the

extent of SD concentrations e.g., 2, 5, 10, 20, 50, 100, 200, 500 and 1000nM have been taken for evaluating the efficiency of the drug loaded nanoformulation for the suppression of *P. falciparum* activity. The percentages of cell inhibition have been found as  $95\pm 4.7$  (%) and  $3.17\pm 2.2$  (%) for lower (2nM) and higher (1000nM) concentrations of Sulfadoxine respectively.

### 3.1B.4. Hollow mesoporous PCL capsules facilitate releasing of SD in the culture media RPMI 1640

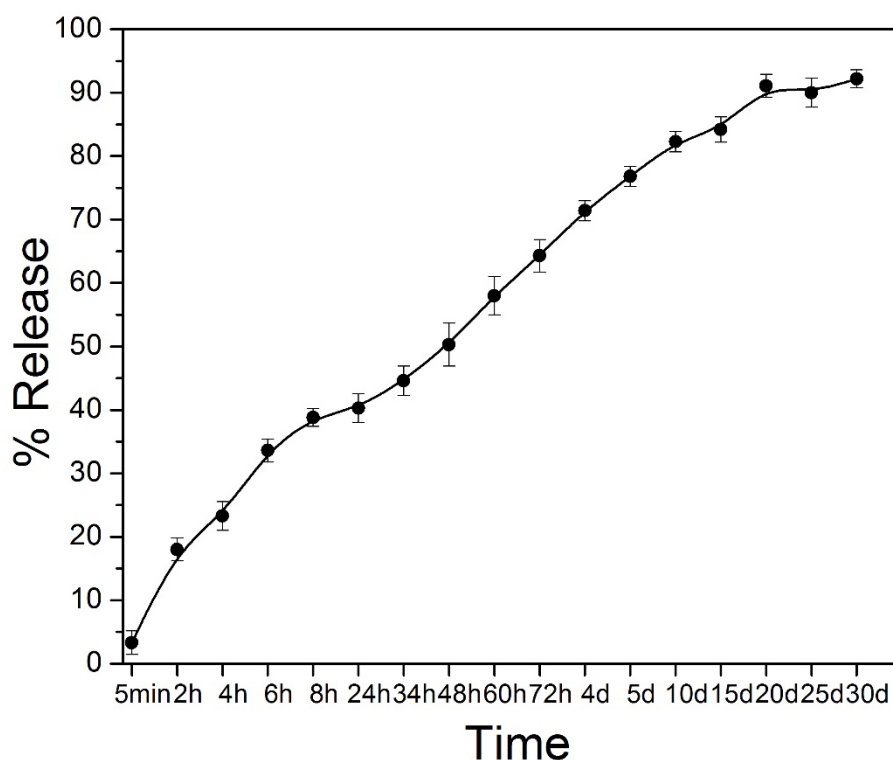


**Figure 3.1.21.** Drug release profile of SD from PCL-SD nanoformulation at room temperature for a period of one month.

To analyze the release profile of drug SD from PCL-SD nanoformulation, the same procedure was followed like the release study of PCL-DHA and PCL-CQDP formulations which are stated in **Part I (Section A)**. 0.6 mg Drug loaded nanoformulations were suspended in 5mL medium RPMI 1640 in a cuvette and the release behavior were studied by maintaining a fixed time interval for 30 days at room temperature (25°C). The absorbance of the released drugs in the medium was recorded using UV-Vis spectrometer and the extent of release of drug SD was calculated. To calculate the extent of drug release the absorption band at 276nm for SD, was considered during the experiment.

**Figure 3.1.21**, represented the drug release profile of drug SD from PCL-SD nanoformulation for 30 days and it is observed here SD exhibited 91% release on 30<sup>th</sup> day without degradation of both polymer nanocarrier and drug encapsulated inside the nanocarrier. It is revealed from these release profile (**Figure 3.1.21**) that, with an increase of time the extent of release of drug molecules are also increased. Within 2h of incubation, the percentage of release of drug from PCL-SD formulation (380µg per mg of PCL capsule) is found to be 17±1.8 (%), and after 30 days of incubation the percentage of release is obtained to be 91±0.7 (%).

### 3.1B.5. Release kinetics and diffusion coefficients of SD from PCL-SD nanoformulations

At room temperature, the pattern of SD release from PCL-SD nanoformulations exhibits the characteristic of a first order release kinetics shown in **Figure 3.1.22**. To examine the release kinetic, the experimental data obtained from a drug release profile are fitted in first order release kinetic equation,  $Q_t/Q_0 = 1 - e^{-kt}$  (eq. 2) mentioned in the **Part I (Section-A)** where,  $Q_t$  is cumulative amount of drug released at time t,  $Q_0$  is initial amount the of drug,  $k$  is first order release constant, t is time in min.

The release of drug from the nanoformulation PCL-SD is found as sustained by the time dependent diffusion as showed in **Table 4**. Diffusion coefficients for SD released from the polymer nanoformulations, at room temperature (25°C) have been calculated (showed in **Table 4**) for different pore size at a different time interval from 2h to 30days by using  $D_T = \frac{Y^2 \pi R^2}{36t}$  eq. (4) mentioned in **Part I (Section-A)**, where Y is the function of the extent of drug released at time t and R is the diameter of the pores of hollow-porous polymer capsules. From the calculated values of diffusion coefficients, we can confirm that the diffusion coefficient values are time dependent. From the **Table 4**, it is very clear that the diffusion coefficients increases with the gradual increase in the pore sizes (from 4.5nm to 14.9nm), as pore size increases from 4.5nm to 14.9nm, the diffusion coefficient for SD release increases from  $9.5 \times 10^{-19}$  to  $87.1 \times 10^{-19}$  at room temperature. Although, with increased time from 2h to 30 days the diffusion coefficient decreases i.e., diffusion coefficient after 2h of drug release was  $9.5 \times 10^{-19}$  whereas after 30 days of drug release the value obtained to be  $0.05 \times 10^{-19}$ .

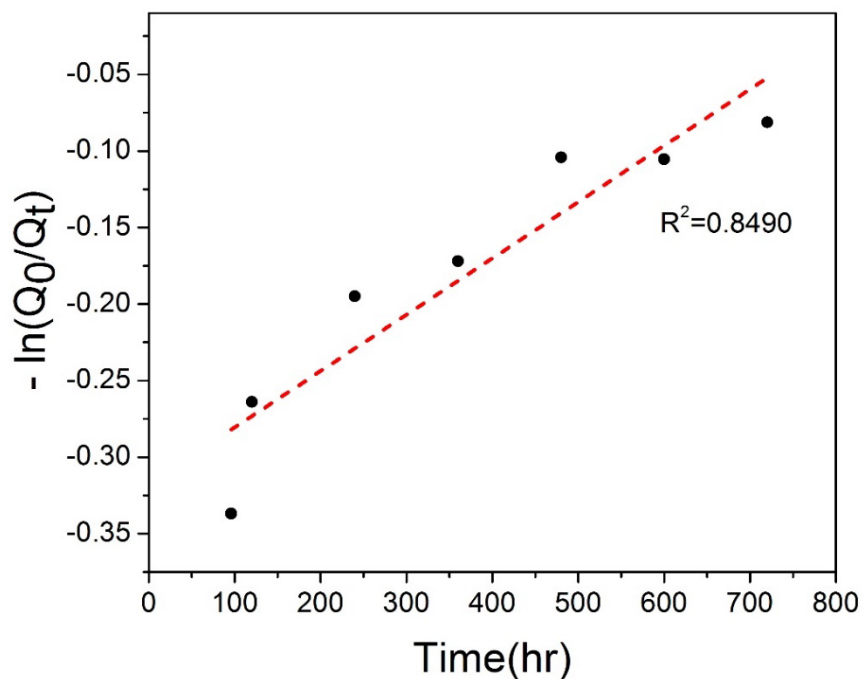


**Figure 3.1.22.** First order release kinetics of SD from PCL-SD nanoformulations maintained experiment condition at room temperature (25°C) for the duration of 30 days.

**Table 4:** Diffusion coefficient ( $D_T$ ) of PCL-SD nanoformulation with a range of time.

Time	Pore size 4.5nm	Pore size 8.7nm	Pore size 14.9nm	Average pore size 9.4nm
T (sec)	D ( $10^{-19}$ )			
7200	9.5	34.4	87.1	34.3
14400	9.3	34.1	73.0	18.8
21600	7.9	29.3	39.9	36.3
28800	6.6	24.0	39.4	31.4
86400	3.3	12.4	30.8	14.3
122400	0.28	1.07	3.01	1.24
172800	0.28	1.05	2.83	1.12
216000	0.27	1.03	2.85	1.19
259200	0.26	0.97	2.64	1.22
345600	0.25	0.96	1.51	1.12

432000	0.25	0.91	1.05	1.04
864000	0.13	0.51	1.02	0.59
1.296×10 <sup>6</sup>	0.09	0.36	1.01	0.41
1.728×10 <sup>6</sup>	0.08	0.31	0.90	0.35
2.16×10 <sup>6</sup>	0.06	0.24	0.72	0.28
2.592×10 <sup>6</sup>	0.05	0.22	0.63	0.25

### 3.1B.6. Summary of Part I (Section B)

Antimalarial drug Sulfadoxine has shown the similar kind of behavior while encapsulated with synthesized hollow mesoporous polymer NCs like other antimalarial drugs DHA and CQDP mentioned in **Part I (Section A)**. The hollow mesoporous PCL NCs can efficiently encapsulated 380µg of Sulfadoxine per mg of PCL capsules and can inhibit the growth of *P. falciparum* RBCs even at a lower concentration of drug i.e., 2nM like other two antimalarial drugs DHA and CQDP. A slow and sustained drug release pattern has been observed from the SD release profile from the PCL-SD nanoformulation in media RPMI 1640 for a longer period of time (one month) at room temperature condition. Therefore, it is proved that the synthesized nanoformulation of PCL with antimalarial drugs has the potential to eradicate the infection of *P. falciparum*.

## **Chapter 3: Result and discussion: Part II (Section A)**

### **Designing of mesoporous ZnO NCs incorporated with protein for the enhancement of immune responses**

3.2A.1. Introduction

3.2A.2. Synthesis procedure mesoporous ZnO NCs

3.2A.3. Synthesis mechanism of mesoporous ZnO NCs

3.2A.4. Designing hollow mesoporous PCL capsules: Size, Morphology and porous structure of mZnO NCs

3.2A.5. BET surface area analysis

3.2A.6. Surface chemical structure analysis of mZnO NCs

3.2A.7. Phase, solid state crystal structure study and zeta potential analysis

3.2A.8. Photoluminescence analysis, UV absorbance, optical band gap and Raman analysis

3.2A.9. Loading of Ova protein in mZnO NCs

3.2A.10. Entrapment efficiency and release of mZnO NCs

3.2A.11. Study of Ova release kinetics from mZnO NCs

3.2A.12. Immunization of mice with mZnO-Ova to analyze Immune responses

3.2A.13. Splenocytes and PBMC isolation from immunized mice

3.2A.14. Lymph node isolation

3.2A.15. Nanoformulation of mZnO-Ova elicit enhanced antigen-specific T cell responses upon immunization in mice

3.2A.16. mZnO-Ova nanoformulation elicit enhanced antigen-specific CD8<sup>+</sup> and CD4<sup>+</sup> T-cell effector responses without a booster

3.2A.17. mZnO-Ova nanoformulation elicit enhanced antigen-specific CD8<sup>+</sup> and CD4<sup>+</sup> T-cell effector responses with a booster

3.2A.18. Ova loaded mZnO NCs trigger amplified antigen specific antibody responses

3.2A.19. Summary of Part II (Section A)

## Chapter 3

### Result and discussion: Part II (Section A)

**Objective: Designing of mesoporous ZnO NCs incorporated with protein for the enhancement of immune responses**

#### 3.2A.1. Introduction

The application of nanotechnology in vaccinology has fuelled rapid advancement towards the design and development of nanovaccines. NPs have been found to enhance vaccine efficacy through the spatiotemporal orchestration of antigen delivery to secondary lymphoid organs and antigen-presentation by Antigen Presenting Cells (APCs) synchronized with stimulation of innate and adaptive immune responses. Metal based NPs (MNPs) have been extensively engineered for the generation of nanovaccines owing to their intrinsic adjuvant-like properties and immunomodulatory functions. Furthermore, mesoporous NCs of late have attracted researchers due to their precise size and exclusive capacity to encapsulate a wide range of biomolecules and their sustained release at the targeted sites.

Here, a detail about designing of mesoporous ZnO NC (mZnO) has been discussed. These mesoporous inorganic metal oxide NCs possess a size of ~12nm with an average pore

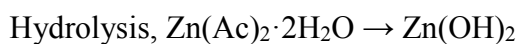
diameter of  $\sim 2.5$  nm. The surfactant-free sonochemical approach has been adapted for the designing purpose and investigated its immune modulatory properties by using protein Ova loaded mZnO NCs [mZnO-Ova] in a mice model. Findings show that mZnO-Ova administration steered the enhanced expansion of antigen specific T-cells and induction of IFN- $\gamma$  producing effector CD4<sup>+</sup> and CD8<sup>+</sup> T-cells. Also, antigen-specific IgG levels were enriched in both the serum and lymph nodes of mZnO-Ova immunized mice. Further, we noticed a substantial increase in serum IgG2a or IgG2b levels and IFN- $\gamma$  secretion in Ova re-stimulated splenocytes from mZnO-Ova immunized mice, indicating that mZnO-Ova skew Th1 type immune response. Overall, the uniqueness of mZnO NCs in terms of the defined particle to pore numbers ratio (maximum of three cavities per particle) allows loading antigens efficiently. Given these features in combination with its immunomodulatory characteristics reinforces the idea that mZnO could be used as an effective antigen-adjuvant platform for the development of novel nano-based vaccines against multiple diseases.

### **3.2A.2. Synthesis procedure mesoporous ZnO NCs**

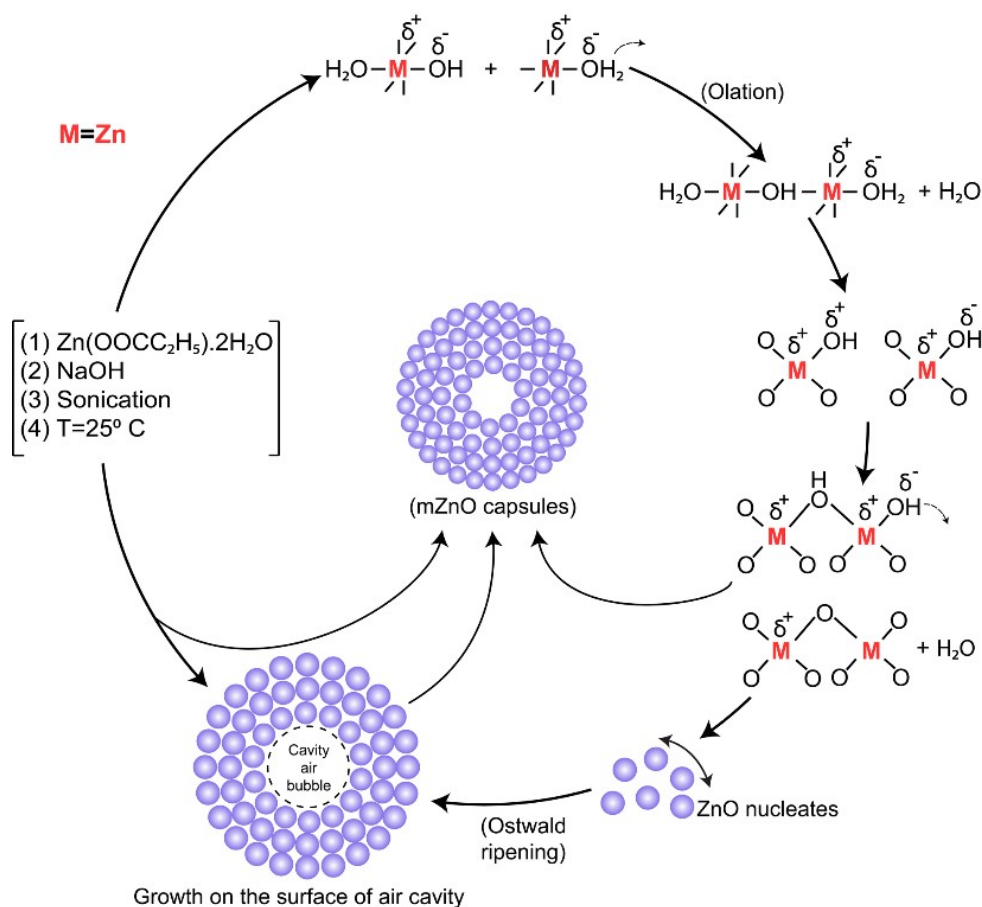
Mesoporous ZnO NCs were synthesized using high energy sonochemical method without using any surfactant. 1:2 molar ratio of Zinc acetate dehydrate ( $\text{Zn}(\text{OOCH}_3)_2 \cdot 2\text{H}_2\text{O}$ ) and sodium hydroxide were taken for the formation of ZnO NCs.  $\text{Zn}(\text{OOCH}_3)_2 \cdot 2\text{H}_2\text{O}$  which was dispersed in ethanol. NaOH solution was then added drop wise to the zinc acetate ethanol solution along with continuous sonication (ELMA S60H, peak power: 600W, frequency = 37kHz) at room temperature (25°C) and left for 12h stirring at 600RPM. The white precipitate formed after 12h was collected by centrifugation (14000RPM) followed by repeated dispersion and washing with filter sterile water-ethanol mixture (v:v = 50:50). Finally, the sample was dried for 12h at 80°C and the white colour sample in powder form was collected for characterization.

### **3.2A.3. Synthesis mechanism of mesoporous ZnO NCs**

Here, a brief explanation of surfactant-free mesoporous ZnO NCs synthesis mechanism has given and the whole mechanism has shown schematically in *Schematic 3.2.1*. Zinc acetate dehydrate [ $\text{Zn}(\text{Ac})_2 \cdot 2\text{H}_2\text{O}$ ] has used as precursor material during the synthesis of the nanosized ZnO. In the first step hydrolysis of [ $\text{Zn}(\text{Ac})_2 \cdot 2\text{H}_2\text{O}$ ] takes place to form Zinc hydroxide at pH 8–9.



In the next step dehydration ( $-n\text{H}_2\text{O}$ ) occurred resulting in the formation of metal ions. Then condensation (through olation mechanism) takes place followed by the formation of hydroxo bridges (two step associative mechanism) to form ZnO nucleates. Further, growth occurs by the Ostwald ripening mechanism where a central void space appeared by depositing ZnO nucleates around it in a spherical manner [210,211]. During the pore formation mechanism, while sonication rarefaction cycle, a stable void (or bubble/cavity) is formed in the solvent which is approximate of 2nm to 4nm in diameter and surrounding that a number of partially condensed form of ZnO nucleates assembled followed by layer by layer deposition of more nucleates within a very short period of time in such a way that the nanosized ZnO capsules formed, are having a pore size equivalent to the size of cavitation bubbles [212]. During the rarefaction cycle of the sonication process, solvent-gas interface usually become increasingly convex. Meanwhile, the rarefaction (acoustic) pressure inside the bubble increases and creates open pores.



**Schematic 3.2.1.** Schematic illustration of mesoporous ZnO formation mechanism. The first step is hydrolysis of  $[\text{Zn(Ac)}_2 \cdot 2\text{H}_2\text{O}]$ , followed by the dehydration ( $-n\text{H}_2\text{O}$ ) and condensation

(through olation mechanism). In the second step, hydroxo bridges (two step associative mechanism) formation takes place and thereby ZnO nucleates formed. In the following step, through Ostwald ripening mechanism during the rarefaction cycle of sonication, a stable cavity is formed in the solvent surrounded by partially condensed nucleates. Finally, layer by layer deposition of nucleates takes place around the cavity within a short period of time in such a manner that the nanosized ZnO capsules formed are having a pore size equivalent to the size of the cavity air bubble.

### 3.2A.4. Designing hollow mesoporous PCL capsules: Size, Morphology and porous structure of mZnO NCs

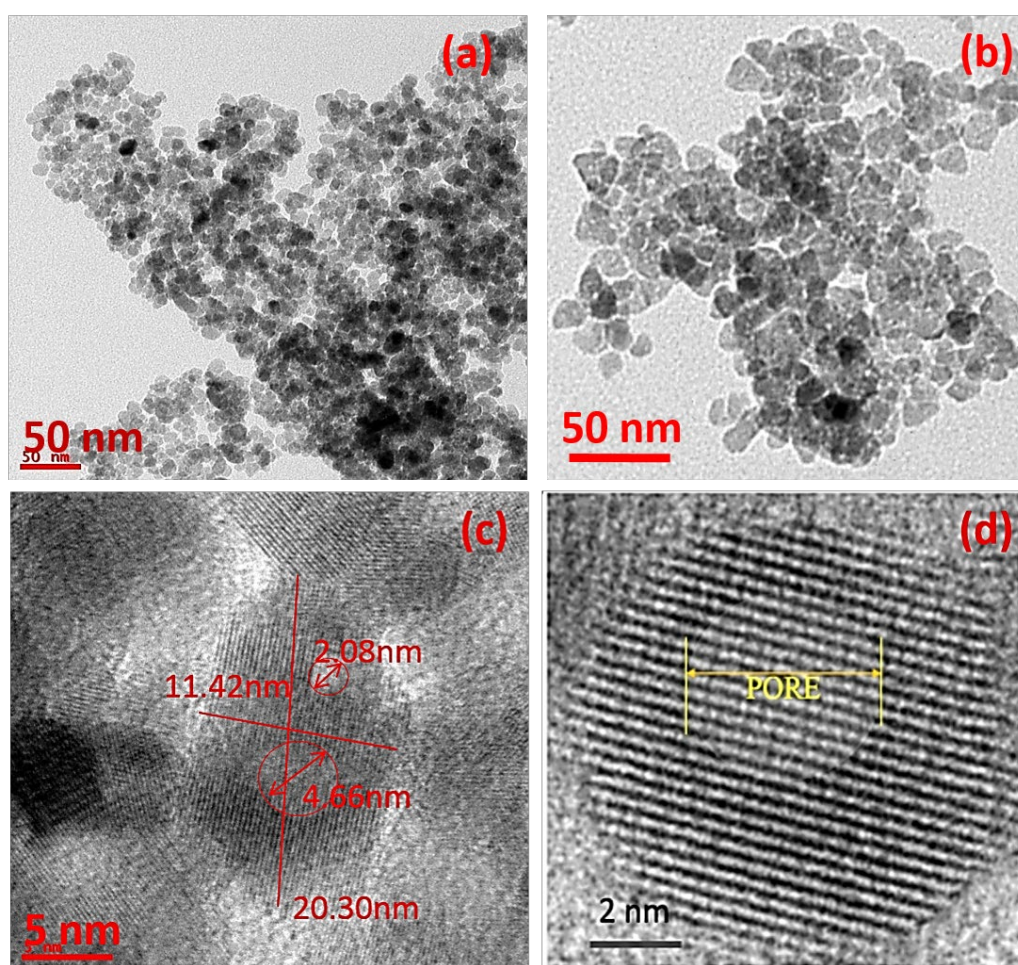


**Figure 3.2.1.** HRTEM micrographs of (a), (b) mZnO NCs and (c), (d) showed high magnification HRTEM images of a single mZnO NCs with distinct pores present inside.

The size, shape, porous structure and morphology of synthesized mZnO NCs was investigated through HRTEM micrographs (**Figure 3.2.1a-d**). **Figure 3.2.1a** and **3.2.1b** showed the HRTEM images, which confirms that the synthesized ZnO NPs are spherical and

porous in nature. For each ZnO NCs, two to three defined pores were observed, with sizes in between 2-4nm in diameter (avg. 2.5nm) showed in *Figure 3.2.1c* and *3.2.1d*. The extensive study reveals that most of the pores are open pores. The mZnO NCs exhibited uniformity in size and were found to be monodispersed. From the *Figure 3.2.2*, it can be seen that the average particle size and its distribution of sample mZnO where the average size of the NC is calculated to be 12nm in diameter. To calculate average particle size different sizes of mZnO have been measured by using HRTEM micrographs from *Figure 3.2.1a*.

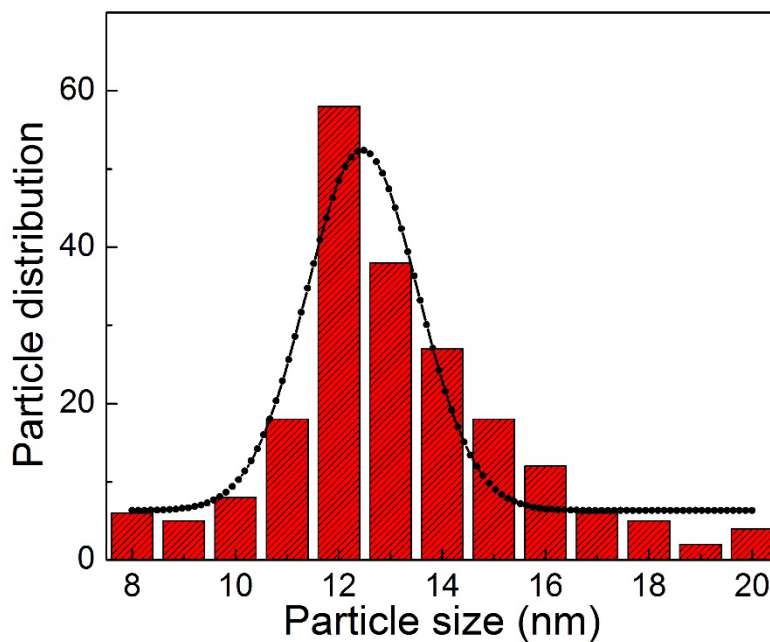


*Figure 3.2.2.* Histogram for the average particle size distribution of mZnO NPs calculated from HRTEM micrograph (*Figure 1a*).

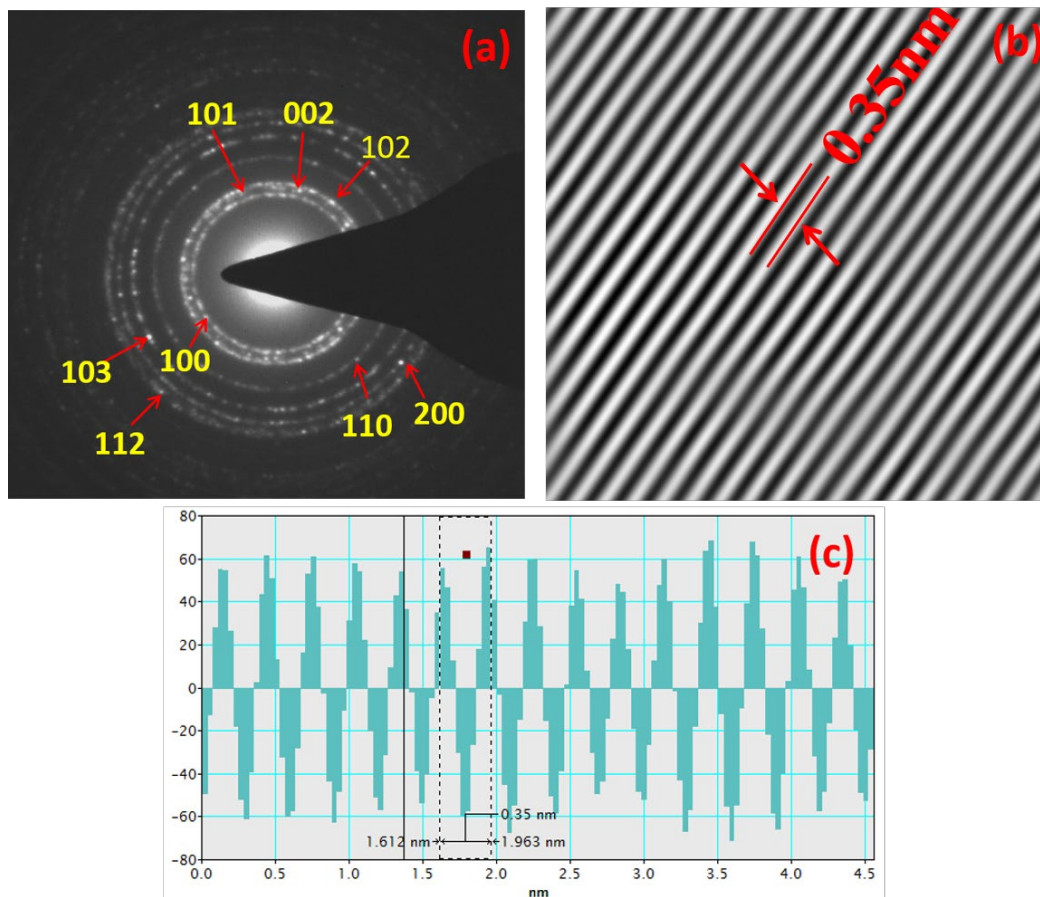


**Figure 3.2.3.** HRTEM micrographs of (a) SAED pattern of mZnO NCs and (b) lattice d-spacing (c) which counted as 0.35 nm from the TEM histogram.

**Figure 3.2.3**, showed the selected area diffraction (SAED) pattern for the mZnO NCs. **Figure 3.2.3a** demonstrates the pattern of diffused rings, which is the evidence for the formation of polycrystalline ZnO NCs. The magnified HRTEM image revealed that the separation between two lattice planes is approximately 3.5 Å which is shown in **Figure 3.2.3b** and **3.2.3c** TEM histogram.

### 3.2A.5. BET surface area analysis

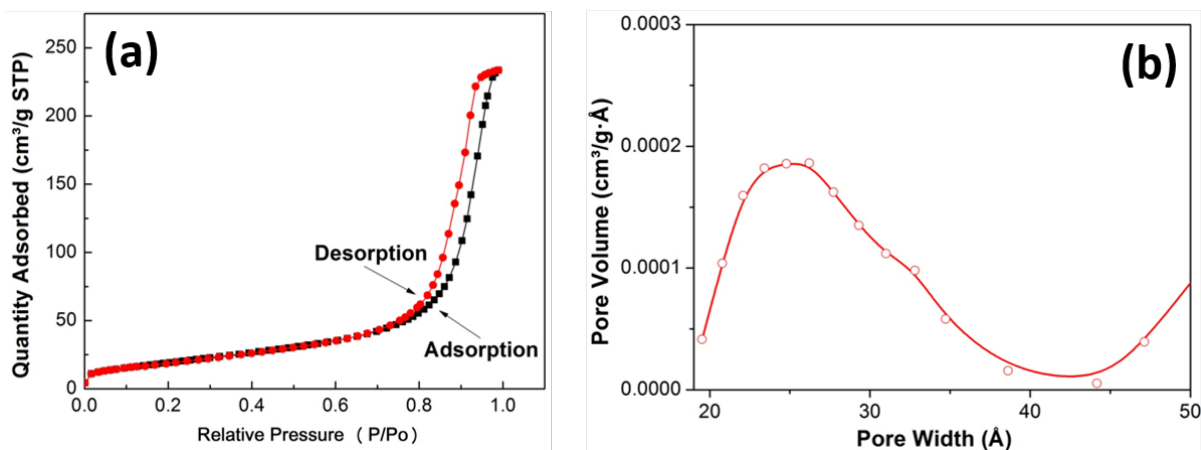


**Figure 3.2.4.** BET results (a)  $N_2$  adsorption-desorption isotherm of mZnO NCs with (b) BJH pore size distribution from an adsorption isotherm.

BET experiment was executed for the synthesized mZnO nanomaterials to further investigation of the pore size which has already been observed from the TEM micrographs and to calculate the specific surface area of the nanomaterial. **Figure 3.2.4a** and **3.2.4b** demonstrate the Nitrogen adsorption - desorption isotherm as well as pore size distribution of mZnO NCs respectively. In **Figure 3.2.4a** a clear hysteresis loop is observed which confirms the porous nature of the nanomaterial with a type-IV adsorption isotherm. BET surface area for mesoporous ZnO NCs found as  $72.4267\text{m}^2/\text{g}$  at a relative pressure  $P/P_0 = 0.285$  and adsorption average pore size achieved as  $2.5\text{nm}$  from the **Figure 3.2.4b** which is similar as the HRTEM micrograph showed in **Figure 3.2.1c**. The Langmuir surface area for the same nanomaterial has found as  $113.79\text{m}^2/\text{g}$ .

### 3.2A.6. Surface chemical structure analysis of mZnO NCs

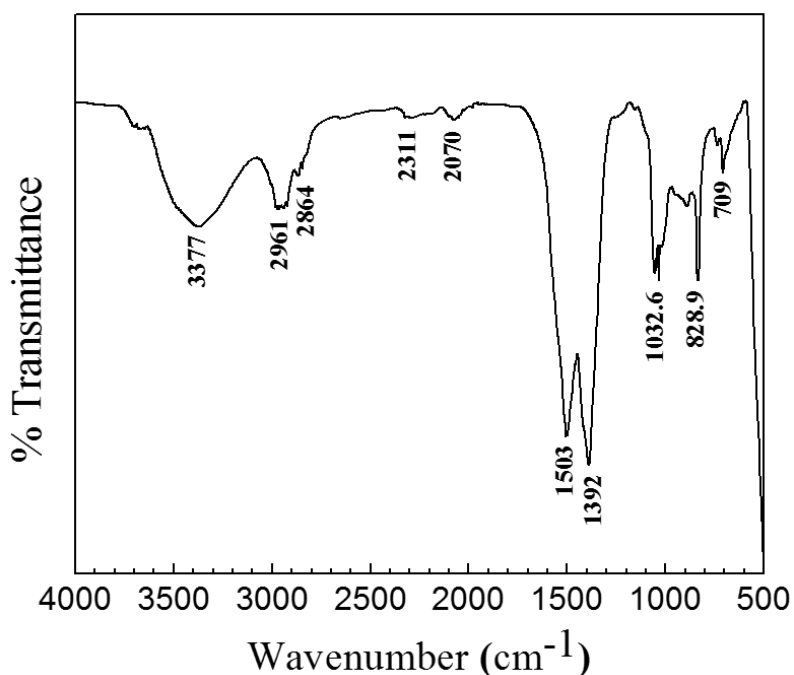


**Figure 3.2.5.** FTIR spectrum of mZnO NCs.

The purity of mZnO NCs was confirmed through FTIR spectroscopic results showed all chemical bonds existed in the mZnO NCs and presented in **Figure 3.2.5**. FTIR experiments were performed on KBr pallet. The FTIR results show a broad peak at 3377cm<sup>-1</sup> which might be possible due to the absorbed moisture or stretching of hydroxyl groups present on the NC surface. Absorption peaks present at 2961cm<sup>-1</sup> and 2864cm<sup>-1</sup> are due to the C-H stretching of the methyl group. Absorption peaks at 1503cm<sup>-1</sup> represent the asymmetric stretching and 1392cm<sup>-1</sup> represents the symmetric stretching of C=O group respectively [213,214]. At 1032.6cm<sup>-1</sup> and 828.9cm<sup>-1</sup> absorption peaks arise due to the C-O stretching vibration and C-H bending due to an alkene group respectively [215]. Because of Zn-O bond stretching an absorption peak formed at 709cm<sup>-1</sup> [216].

### **3.2A.7. Phase, solid state crystal structure study and zeta potential analysis**

The solid-state crystal structure of mZnO NC has been characterized through powder XRD and the diffraction pattern as shown in **Figure 3.2.6**. mZnO capsules were found to exhibit hexagonal crystal structure with characteristic diffraction peaks at  $2\theta = 32.2^\circ, 34.6^\circ, 36.6^\circ, 47.9^\circ, 57.1^\circ, 63.1^\circ, 66.8^\circ, 68.4^\circ, 69.6^\circ, 72.8^\circ, 77.3^\circ$  and  $81.8^\circ$  for the preferred orientation of plane such as (100), (002), (101), (102), (110), (103), (200), (112), (201), (004) and (202), respectively. The crystal structure corresponds to the phase pure Wurtzite-type ZnO

(hexagonal phase with space group  $P6_3mc$ , JCPDS card no. 36-1451, a polar axis parallel to c axis) with the lattice parameters,  $a=3.2 \text{ \AA}$ ,  $b=3.2 \text{ \AA}$  and  $c=5.2 \text{ \AA}$ .

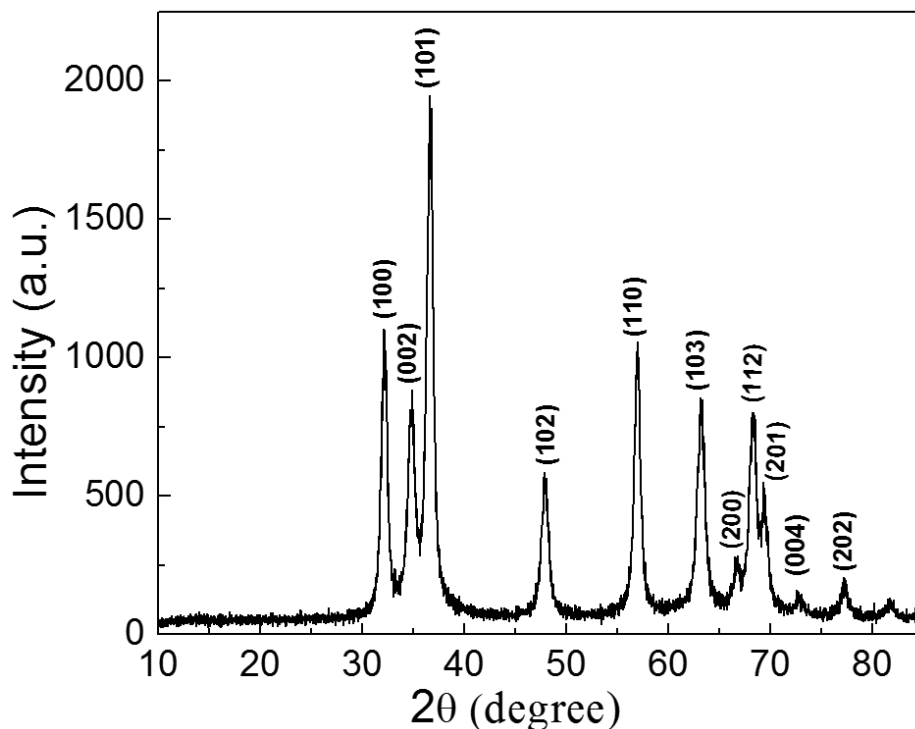


**Figure 3.2.6.** XRD powder diffraction pattern of mesoporous ZnO NCs.

To check the zeta potential value of mesoporous PCL (HPZ), 500 $\mu$ g of the sample has been dispersed in 1mL of DI water. In **Figure 3.2.7**, Zeta potential value for mZnO have been shown and the value obtained to be  $-30.8 \text{ mV} \pm 3.84$  (single peak). Whereas, after loading Ova (mZnO-Ova), the values obtained were  $-42.8 \text{ mV} \pm 5.4$  and  $-58 \text{ mV} \pm 4.18$  for  $pK_{a1}$  and  $pK_{a2}$ , respectively as shown in **Figure 3.2.8**, which is due to two ionic functional groups ( $-\text{COO}^-$  and  $\text{NH}_3^+$ ) present in Ova and is zwitterionic in nature. Zeta potential value has been calculated for three batches of mZnO and mZnO-Ova NCs to avoid any kind of error, however, it is not showing much variation in the zeta potential values. In conclusion, both mZnO and mZnO-Ova are colloidal stable.

**Table 1:** Zeta potential results of mZnO NCs.

	Mean (mV)	Area (%)	St Dev (mV)
<b>Zeta Potential (mV):</b> -30.8	<b>Peak 1:</b> -30.8	100.0	3.84
<b>Zeta Deviation (mV):</b> 3.84	<b>Peak 2:</b> 0.00	0.0	0.00
<b>Conductivity (mS/cm):</b> 0.0225	<b>Peak 3:</b> 0.00	0.0	0.00
<b>Result quality :</b> Good			

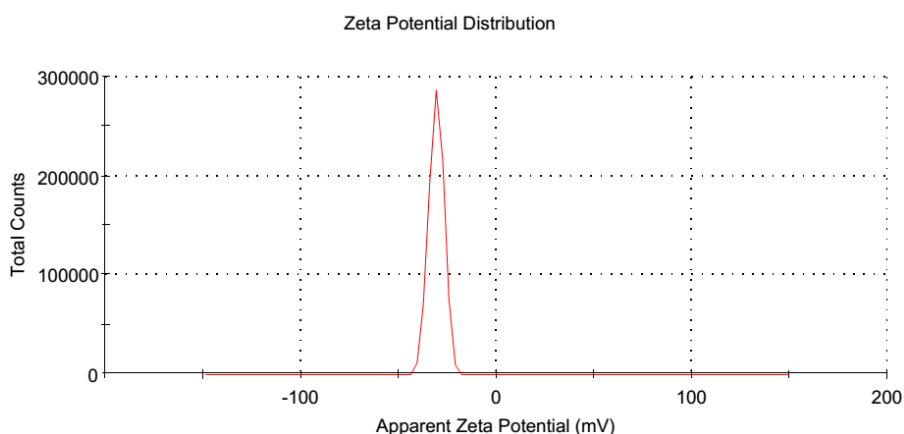


*Figure 3.2.7. Zeta potential results of mZnO NCs recorded at 25°C in DI water.*

**Table 2:** Zeta potential of nanoformulation of mZnO-Ova.

	Mean (mV)	Area (%)	St Dev (mV)
<b>Zeta Potential (mV):</b> -42.8	<b>Peak 1:</b> -40.9	86.7	5.40
<b>Zeta Deviation (mV):</b> 7.69	<b>Peak 2:</b> -58.0	13.3	4.18
<b>Conductivity (mS/cm):</b> 0.0745	<b>Peak 3:</b> 0.00	0.0	0.00
<b>Result quality :</b> Good			

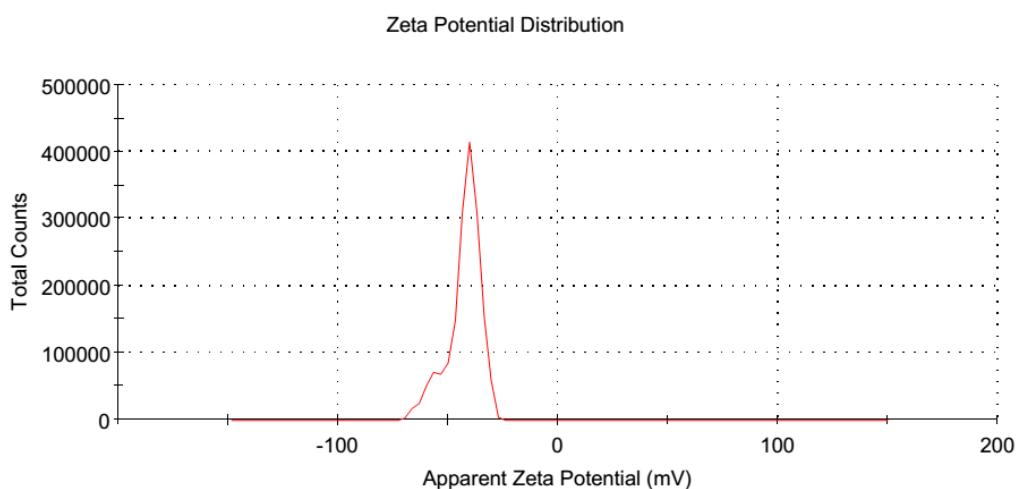


*Figure 3.2.8. Zeta potential of nanoformulation of mZnO-OVA recorded at 25°C in DI water.*

### 3.2A.8. Photoluminescence analysis, UV absorbance, optical band gap and Raman analysis

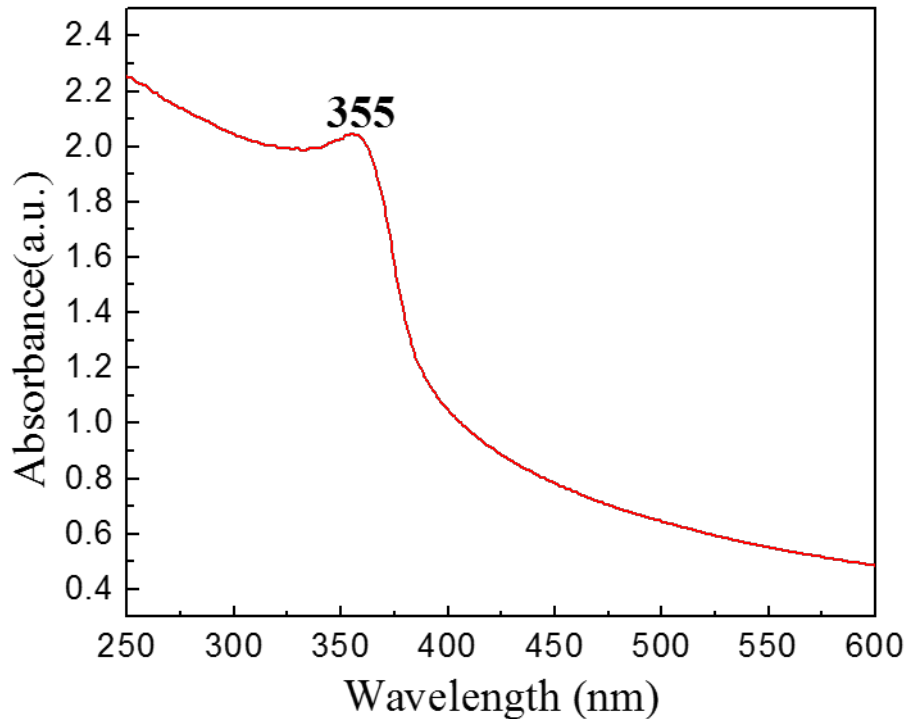


**Figure 3.2.9.** UV-Vis absorbance spectrum of mZnO NCs recorded at 25°C in PBS (~7.2pH).

ZnO particles irrespective of bulk and nanomaterials have an intrinsic ability to absorb UV. Therefore, the UV-Vis absorption behavior of synthesized mZnO NCs has studied by taking 0.3mg of nanomaterials dispersed in 5mL of PBS (~7.2 pH) medium and absorption peak has recorded with the help of UV-Vis Spectrometer at room temperature 25°C. UV absorbance peak highlighted a characteristic band at  $\lambda_{\text{max}}=355$  nm as shown in **Figure 3.2.9**.

The band gap energy using the Tauc equation represented as shown in eq1 [217]

$$\alpha h\nu = A(h\nu - E_g)^n \dots \dots \dots (1)$$

Where  $\alpha$  is absorption coefficient,  $h\nu$  is the photon energy,  $A$  is a constant,  $E_g$  is the band gap energy and exponent  $n$  is 2 for indirect transition and  $\frac{1}{2}$  for direct transition.

By following Tauc equation (eq 1) the band gap energy for the synthesized mZnO NCs have been calculated and showed in **Figure 3.2.10** with the Tauc plot, where it has followed direct transition energy and the calculated value of  $E_g$  is 3.1eV for the NCs.

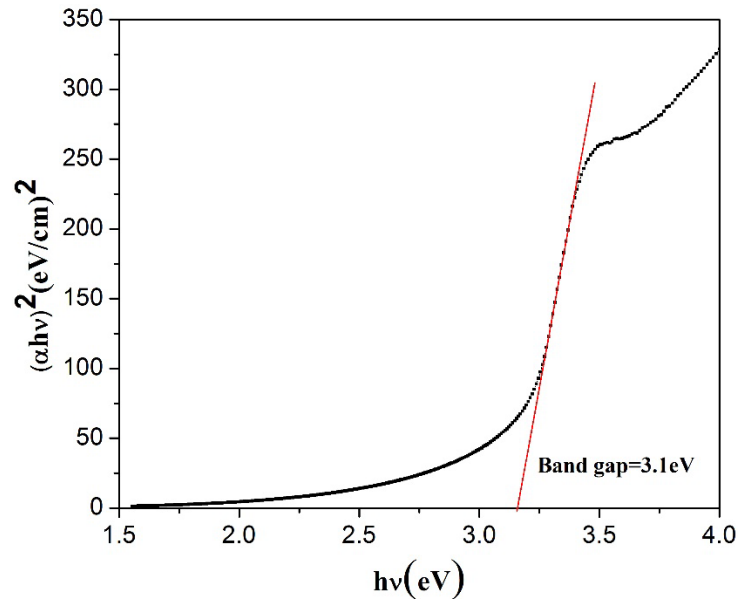


**Figure 3.2.10.** Tauc plot for the optical band gap measurement of mZnO NCs drawn from the UV-Vis absorbance spectrum of mZnO NCs (Figure 3.2.9).

The PL spectra for mZnO showed in **Figure 3.2.11a**, exhibited four defined peaks at  $\lambda = 345\text{nm}$ ,  $378\text{nm}$ ,  $406\text{nm}$  and  $460\text{nm}$  due to the presence of structural defects (pores) and also due to the presence of huge oxygen vacancies in the mZnO NC. In **Figure 3.2.11b**, the PL spectra for mZnO-Ova NCs showed peaks at  $\lambda = 350\text{nm}$ ,  $376\text{nm}$ ,  $400\text{nm}$  and  $460\text{nm}$ . The difference in peaks in mZnO-Ova from mZnO NC spectrum indicates that mZnO NCs are loaded with Ova antigen.

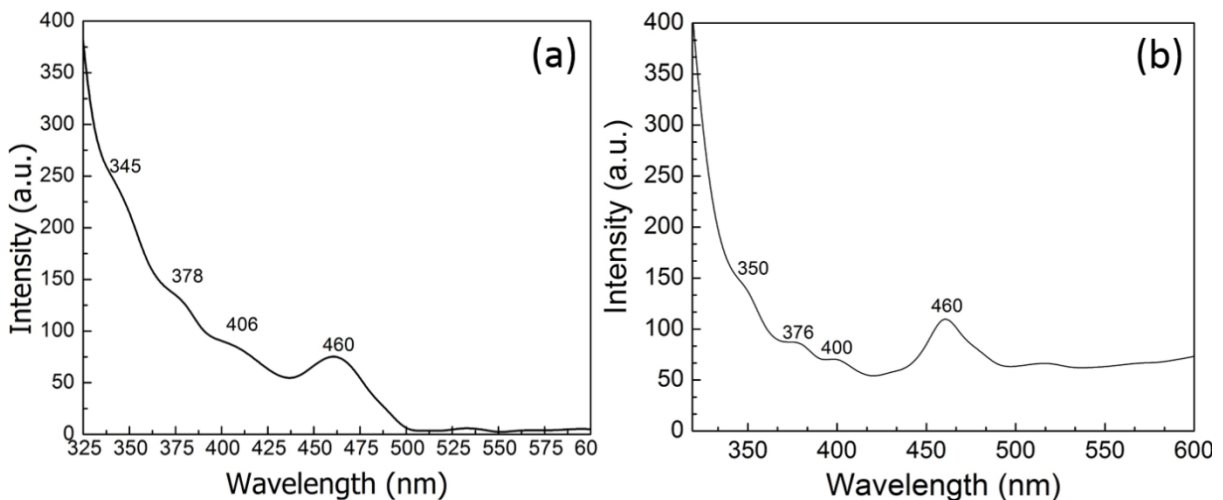


**Figure 3.2.11.** PL spectra of (a) bare mZnO and (b) mZnO-Ova NCs.

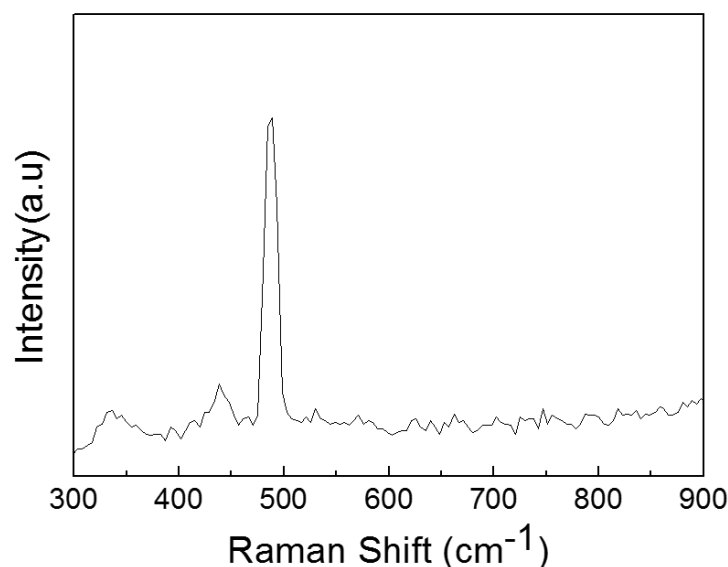


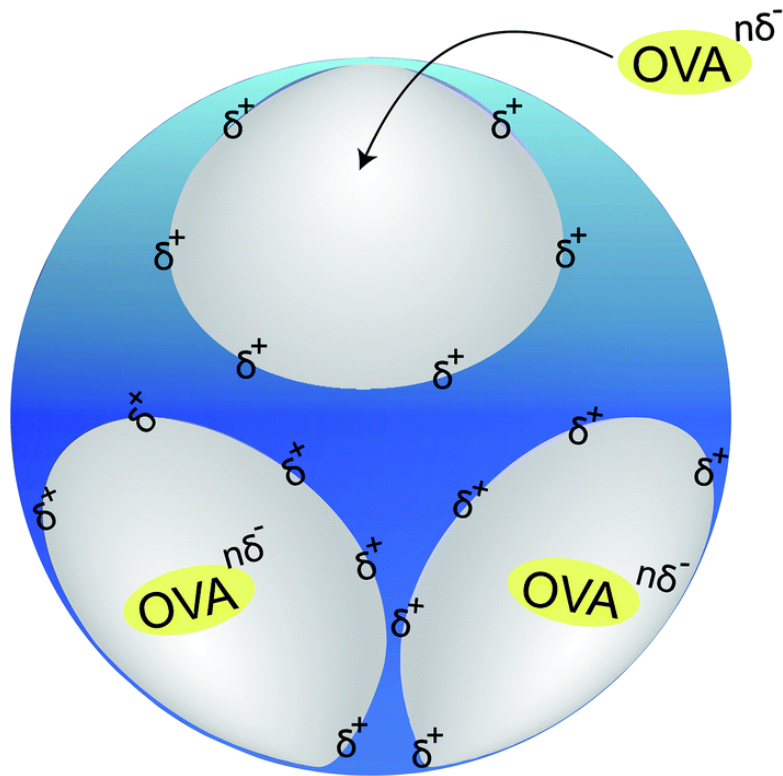
**Figure 3.2.12.** Raman spectrum for mZnO NCs at room temperature on the powdered sample.

**Figure 3.2.12** shows the Raman spectrum on the mZnO NCs. It was found that the E<sub>2</sub> (high) peak present at 437cm<sup>-1</sup> indicates more crystallinity in the material and the A<sub>1</sub> (TO) peaks were also present in the material. The little broadening of the peaks is due to the quantum confinement effect of the NCs. Also that the Raman study of mZnO NCs shows that the crystal structure is of wurtzite hexagonal type with P6<sub>3</sub> /mmc (C<sup>4</sup><sub>6v</sub>)space group and atoms in primitive cell occupying the C<sub>3v</sub> sites.

### 3.2A.9. Loading of Ova protein in mZnO NCs

The UV-Vis, PL and Raman bands of mZnO capsules appeared due to the phonon localization by defects (V<sub>o</sub><sup>+</sup>). These defects create deep energy levels (V<sub>o</sub><sup>+</sup>) which assist to entrap electron rich (δ<sup>-</sup>) small biomolecules such as proteins, amino acids, siRNA, DNA or drugs molecules. In the current study, Ova protein, as a model antigen has been loaded in mZnO capsules.

The prepared dried powdered porous ZnO nanomaterials have been loaded with Ova protein in the ratio 1:1 (mg/ml) in 1XPBS ( pH 7.2) buffer and kept in incubation for 24h at room temperature. The Ova loaded mesoporous ZnO NCs were separated from the supernatant after centrifugation. Repeated washing had been done to remove the protein particles from the surface of the NCs and finally collected Ova protein loaded ZnO NCs were dried in vacuum.



**Schematic 3.2.2.** Ova loading mechanism in mZnO NCs. Due to the electrostatic interactions Ova enters inside the pores of mZnO and subsequently forms  $(mZnO)_x-(Ova)_y$  complex. Ova protein can form strong secondary bonds with  $Zn^{2+}$  of mZnO and helps to form a stable  $(mZnO)_x-(Ova)_y$  complex (x and y are integers).

Due to the defect induced structure, mZnO capsules have huge oxygen vacancies ( $V_o^+$ ) which create a positively charged environment (cationic,  $\delta^+$ ) [218]. Thus, it enhances to entrap the electron rich ( $\delta^-$ ) small biomolecules like Ova protein (negatively charged due to C=O and -OH groups) which consists of 385 amino acids (Mw: 45kDa). Due to the electrostatic interactions Ova enters inside the pores of mZnO and subsequently forms  $(mZnO)_x-(Ova)_y$  type of complex. Ova protein has the ability to form strong secondary bonds with  $Zn^{2+}$  of mZnO and helps to form a stable  $(mZnO)_x^{\delta^+} - (Ova)_y^{\delta^-}$  complex (x and y are integers) showed in **Schematic 3.2.2.**

### 3.2A.10. Entrapment efficiency and release of mZnO NCs

Entrapment efficiency of the prepared mesoporous ZnO NCs has been calculated by using the following equation,

$$\% \text{ Entrapment efficiency} = [\text{weight of drug in NPs}/\text{weight of drug fed initially}] \times 100 \dots \dots \dots (2)$$

The entrapment efficiency of the prepared mesoporous ZnO NCs was observed to be quite high and calculated as 70.3% of the initial concentration of Ova taken in 1mL of PBS (pH 7.2).

### 3.2A.11. Study of Ova release kinetics from mZnO NCs

The release kinetics of Ova from mZnO NCs was evaluated by using UV-Vis spectrometer at 37°C for up to 3 days (considering the absorption peak of Ova at  $\lambda_{max} \approx 260\text{nm}$ ). Briefly, 0.4mg Ova loaded mZnO NCs were suspended in 5mL of media in a cuvette at room temperature and absorbance was taken at fixed time intervals of 2h up to 72h (3 days), maintaining similar conditions, until no change in the absorbance was observed for release profile. As shown in **Figure 3.2.13**, it is evident from the release profile that the initial release was very slow but with time the percentage of release increased slowly. Release was assessed at intervals of 5min, 1h, 3h, 5h, 7h, 9h, 24h, 36h, 48h, 60h and 72h and the percentage release was calculated as 1.8%, 7.6%, 9.1%, 9.6%, 10.8%, 13.1%, 28.2%, 56.2%, 76%, 79% and 89%, respectively, of the total Ova loaded in the NCs.

The release occurred mostly due to the diffusion of Ova protein from the mZnO NCs following time dependence over all semi 1st order (or semi zero order) release kinetics.

Zero order release kinetic equation (eq. 3),

$$Q_t/Q_0 = K_0 \cdot t \dots \dots \dots (3)$$

Where,  $Q_t$  is cumulative amount of drug released at time t,  $Q_0$  is the initial amount of drug,  $K_0$  is zero order release constant, t is time in min.

The first order release kinetic equation,

$$Q_t/Q_0 = 1 - e^{-kt} \dots \dots \dots (4)$$

Where,  $Q_t$  is cumulative amount of drug released at time t,  $Q_0$  is initial amount of drug,  $k$  is first order release constant, t is time in min.

The unique release behavior in the case of Ova release from mZnO-Ova NCs followed zero-order kinetics (**eq 3**) up to 30h while it followed 1<sup>st</sup> order kinetics (**eq 4**) for the rest of the time-period. This unique type of release is highly desirable for sustained delivery of drugs.

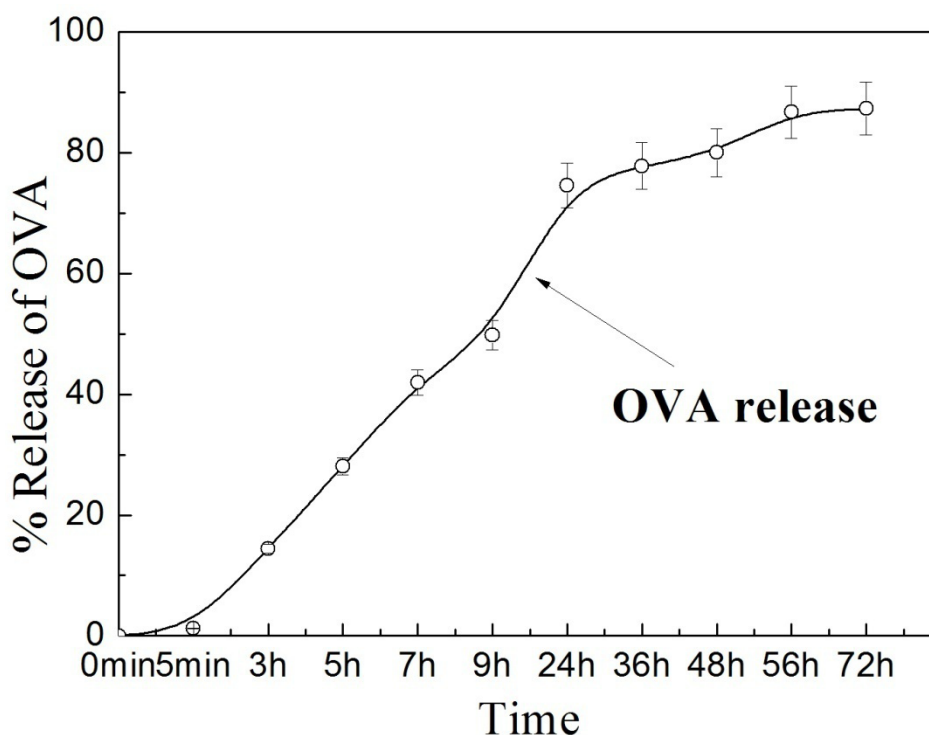


**Figure 3.2.13.** UV spectrum of time dependent Ova release from ZnO-Ova NCs at 37°C for 3days in RPMI 1640 medium.

### 3.2A.12. Immunization of mice with mZnO-Ova to analyze Immune responses

Two sets of experiments were done for *in vivo* application of mZnO-Ova nanoformulation to study their efficiency in immunization responses i.e., first one is without a booster where mice had been sacrificed on day 21 after immunization and another one is with booster where booster (identical dose like initial dose) had been given to the mice on day 14 followed by sacrifice on day 28.

In the first set of experiment, a mice of 6-8 week old male Balb/c was immunized subcutaneously at the base of the mice tails, with pure Ova (10µg dissolved in PBS of pH 7.2), Ova-adjuvant Alum (20µg.mL<sup>-1</sup>), mZnO (10µg dissolved in PBS of pH 7.2), mZnO-Ova (10µg encapsulated Ova dissolved in PBS of pH 7.2) with Alum (20µg.mL<sup>-1</sup>) and mZnO-Ova (10µg encapsulated Ova dissolved in PBS of pH 7.2). The immunized mice were bled through the tail vein at 21 days for serum collection and PBMC isolation. These mice were sacrificed and spleen and lymph nodes were also collected for further analysis.

In another set of experiment, 6-8 week old male Balb/c mice were immunized subcutaneously with pure Ova (10 $\mu$ g dissolved in PBS of pH 7.2), Ova-adjuvant Alum (20 $\mu$ g.mL<sup>-1</sup>), mZnO (10 $\mu$ g dissolved in PBS of pH 7.2), mZnO-Ova (10 $\mu$ g encapsulated Ova dissolved in PBS of pH 7.2) with Alum (20 $\mu$ g.mL<sup>-1</sup>) and mZnO-Ova (10 $\mu$ g encapsulated Ova dissolved in PBS of pH 7.2) followed by a second injection (booster) of an identical dose of pure Ova and mZnO-Ova at day 14. Finally, the mice were sacrificed at day 28 of the primary immunization for analysis of immune responses in spleen and blood. All animal experiments were performed in accordance with the animal ethical guidelines of the Institute.

### **3.2A.13. Splenocytes and PBMC isolation from immunized mice**

Spleens from immunized Balb/c mice were isolated and the single cell suspension was prepared using mechanical disruption and subsequent filtration through a 70 $\mu$ m cell strainer (BD Biosciences). The erythrocytes were lysed using the RBC lysis buffer (Sigma-Aldrich). 2 $\times$ 10<sup>5</sup> splenocytes were seeded in triplicate in a round bottom 96-well plate and restimulated with 1 $\mu$ g.mL<sup>-1</sup> Ova specific MHC class I peptide (SIINFEKL) and class II peptide (Ova 323–339). After 72h, the supernatant was collected and analyzed for IFN- $\gamma$ , IL-12p40 (BD Biosciences) and IL-4 (Biolegend) cytokines through ELISA.

Cell proliferation was assessed by pulsing the 72h splenocyte cultures with 1 $\mu$ Ci [3H] thymidine per well for another 16h. For harvesting, the cells were first fixed with 10% trichloroacetic acid (TCA) for 15min at room temperature followed by washing with 10% TCA. The cells were solubilized with 150 $\mu$ L of 1N NaOH and incubated for 15min at room temperature with agitation. After solubilization, 150 $\mu$ L of 1N HCl was immediately added. To measure the thymidine incorporation, subsequently, 300 $\mu$ L of each sample was added to a scintillation vial containing 5mL of scintillation cocktail (Sisco Research Laboratories), and the counts were measured in a scintillation counter (PerkinElmer).

CD4<sup>+</sup> and CD8<sup>+</sup> cell responses were investigated in splenocytes and peripheral blood mononuclear cells (PBMCs) following immunization with or without a booster. Briefly, PBMCs were isolated by density gradient centrifugation using Histopaque (Sigma Aldrich). Single cell suspension from isolated spleen was obtained as mentioned above. Isolated PBMCs and splenocytes were seeded in RPMI 1640 media and restimulated with Ova specific MHC class I peptide (SIINFEKL) and class II peptide (Ova 323–339) at 1 $\mu$ g.mL<sup>-1</sup> in the presence of Golgi plug and Golgi stop (BD Biosciences) at 37°C for 8h. After 8h, the stimulated cells were stained for surface CD8 using Alexa-488 labeled anti-mouse CD8 (BD Biosciences) and CD4

with Percp or FITC labeled anti-mouse CD4 (e Biosciences) for 60min at room temperature. Cells were washed with FACS buffer, fixed with 4% para-formaldehyde and permeabilized using 1×perm wash buffer (Biolegend). The cells were then stained for intracellular IFN $\gamma$  with APC conjugated anti-mouse IFN $\gamma$  (e Biosciences) and intracellular IL-2 using anti-mouse IL-2 conjugated with PE (BD Biosciences) for 60min in 1×perm wash buffer. The stained cells were washed with FACS buffer and acquired on FACS Aria (BD Biosciences). The FACS data were analyzed using Flow Jo software (Tree Star Inc, OR).

### **3.2A.14. Lymph node isolation**

Inguinal lymph nodes were isolated immunized Balb/c mice and snap frozen in moulds containing OCT embedding medium for sectioning. Sections (4 $\mu$ m) were fluorescently stained with Alexa Fluor 488 labeled antibody secreting B-Cells B220 (e Biosciences) and Alexa Fluor 647 labeled anti-mouse total IgG (Cell Signalling). Fluorescence images were captured using a  $\times$ 40 objective on a Zeiss confocal microscope.

### **3.2A.15. Nanoformulation of mZnO-Ova elicit enhanced antigen-specific T cell responses upon immunization in mice**

The ability of mZnO-Ova NCs has examined to provoke Ova-specific T-cell responses *in vivo* following subcutaneous immunization studies in mice. As a negative control, PBS and soluble pure Ova immunized groups were used. The ability of mZnO to deliver Ova antigen to Antigen Presenting Cells (APCs) was evaluated through splenocyte proliferation assay by antigen recall assay. The *ex vivo* proliferation assay was determined using 3H-thymidine incorporation in cultured splenocytes from immunized Balb/c mice in the presence of 1 $\mu$ g.mL<sup>-1</sup> of Ova peptides for 72 h. Mice were immunized with six groups i.e., control, with commercially available pure Ova, Ova-adjuvant Alum, mZnO, mZnO-Ova-Alum and mZnO-Ova.

**Figure 3.2.14a** revealed that exposure to mZnO-Ova NCs induced a significantly stronger proliferation in Ova restimulated splenocytes as compared to pure Ova immunized groups, whereas mZnO alone induced minimal proliferation in cultured splenocytes. After 21 days, splenocytes were harvested and restimulated with 1 $\mu$ g.mL<sup>-1</sup> of MHC-I restricted Ova peptide (SIINFEKL) and MHC-II peptide (Ova 323–339) for analysis of antigen specific T-cell expansion by 3H thymidine incorporation. There is a synergistic effect can observed in the proliferation rate in splenocytes isolated from mice administered with mZnO-Ova-Alum.

These results suggest that mZnO-Ova supports efficient antigen presentation to T-cells, which indeed enhanced the expansion of antigen specific T-cells.

From **Figure 3.2.14b** and **Figure 3.2.14c** it is observed, enhanced IFN- $\gamma$  and IL-12p40 secretion in the Ova restimulated splenocyte cultures from mZnO-Ova nanoformulation administered mice as compared to pure Ova immunized mice showed in respectively. A synergistic response is observed with heightened IFN- $\gamma$  and IL-12p40 levels observed during administration with mZnO-Ova-Alum. Secretion of IFN- $\gamma$  is a representative of Th1 type of T-cell response [219] and advocates a potent cellular response to mZnO-Ova.

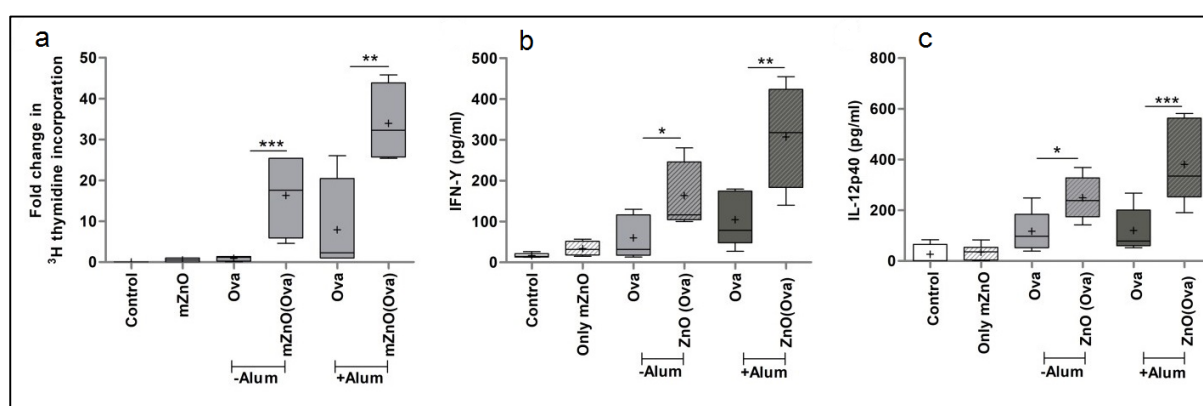


**Figure 3.2.14.** mZnO-Ova induce efficient antigen specific T-cells. (a)  $^3\text{H}$ -Thymidine incorporation, (b) IFN- $\gamma$  and (c) IL-12p40 secretion in splenocytes culture supernatants were estimated by ELISA.

### 3.2A.16. mZnO-Ova nanoformulation elicit enhanced antigen-specific CD8<sup>+</sup> and CD4<sup>+</sup> T-cell effector responses without a booster

The induction of effector CD8<sup>+</sup> and CD4<sup>+</sup> T cell responses in the splenocytes of immunized mice with all six groups (control, with commercially available pure Ova, Ova-adjuvant Alum, mZnO, mZnO-Ova-Alum and mZnO-Ova) were evaluated. Mice were immunized as per the indicated groups and were sacrificed at day 21. To examine the responsiveness of these cells, splenocytes *ex vivo* restimulated with Ova specific MHC class I peptide (SIINFEKL) and class II peptide (Ova 323–339) at  $1\mu\text{g.mL}^{-1}$  in the presence of Golgi plug and Golgi stop for 8h and analysed activation of CD4 and CD8 by measuring the frequency of IFN- $\gamma$  and IL-2 producing CD8<sup>+</sup> and CD4<sup>+</sup> cells through intracellular staining and

flow cytometry. From **Figure 3.2.15**, it is noticed a remarkable expansion in the frequency of IFN producing CD8<sup>+</sup> (**Figure 3.2.15a** and **3.2.15c**) and CD4<sup>+</sup> (**Figure 3.2.15b** and **3.2.15d**) cells in the mice immunized with mZnO-Ova NCs compared to control immunized groups.

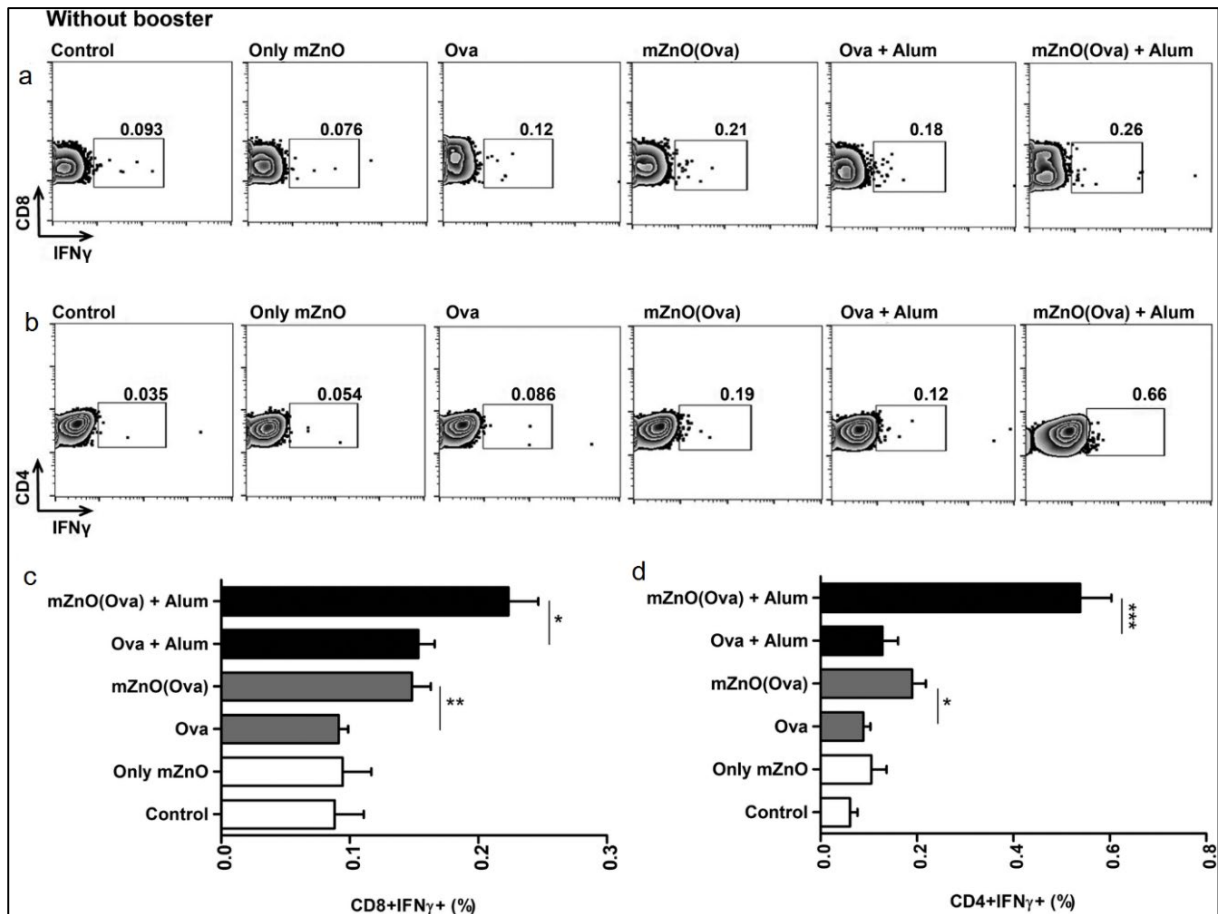


**Figure 3.2.15.** Nanoformulation of mZnO-Ova elicit enhanced antigen-specific CD8<sup>+</sup> and CD4<sup>+</sup> T-cell effector responses. (a) CD8<sup>+</sup> and (b) CD4<sup>+</sup> T cells, FACS plots for IFN $\gamma$  expression in CD8<sup>+</sup> and CD4<sup>+</sup> T cells respectively. Graphs represent average percentage of IFN- $\gamma$  producing (c) CD8<sup>+</sup> and (d) CD4<sup>+</sup> T cells.

### 3.2A.17. mZnO-Ova nanoformulation elicit enhanced antigen-specific CD8<sup>+</sup> and CD4<sup>+</sup> T-cell effector responses with a booster

*Figure 3.2.16* results revealed that booster injection with the 10 $\mu$ g dose of soluble Ova or Ova encapsulated in mZnO-Ova NCs at day 14 and sacrifice at day 28 enhanced the frequency of IFN producing CD8<sup>+</sup> showed in *Figure 3.2.16a* and *3.2.16c* and CD4<sup>+</sup> cells showed in *Figure 3.2.16b* and *3.2.16d* through Flow cytometry plots. Moreover, the percentage of IFN producing CD8<sup>+</sup> is more in case of with booster data (*Figure 3.2.16a*) compared to without booster data showed in *Figure 3.2.15a*. Graphical data in *Figure 3.2.16c* and *Figure 3.2.15c* has revealed the same. The same kind of enhancement in the percentage of IFN can be seen in case of CD4<sup>+</sup> cells showed in *Figure 3.2.16b*, *3.2.16d* and in case of with booster compared to *Figure 3.2.15c*, *3.2.15d* in case of without a booster data.

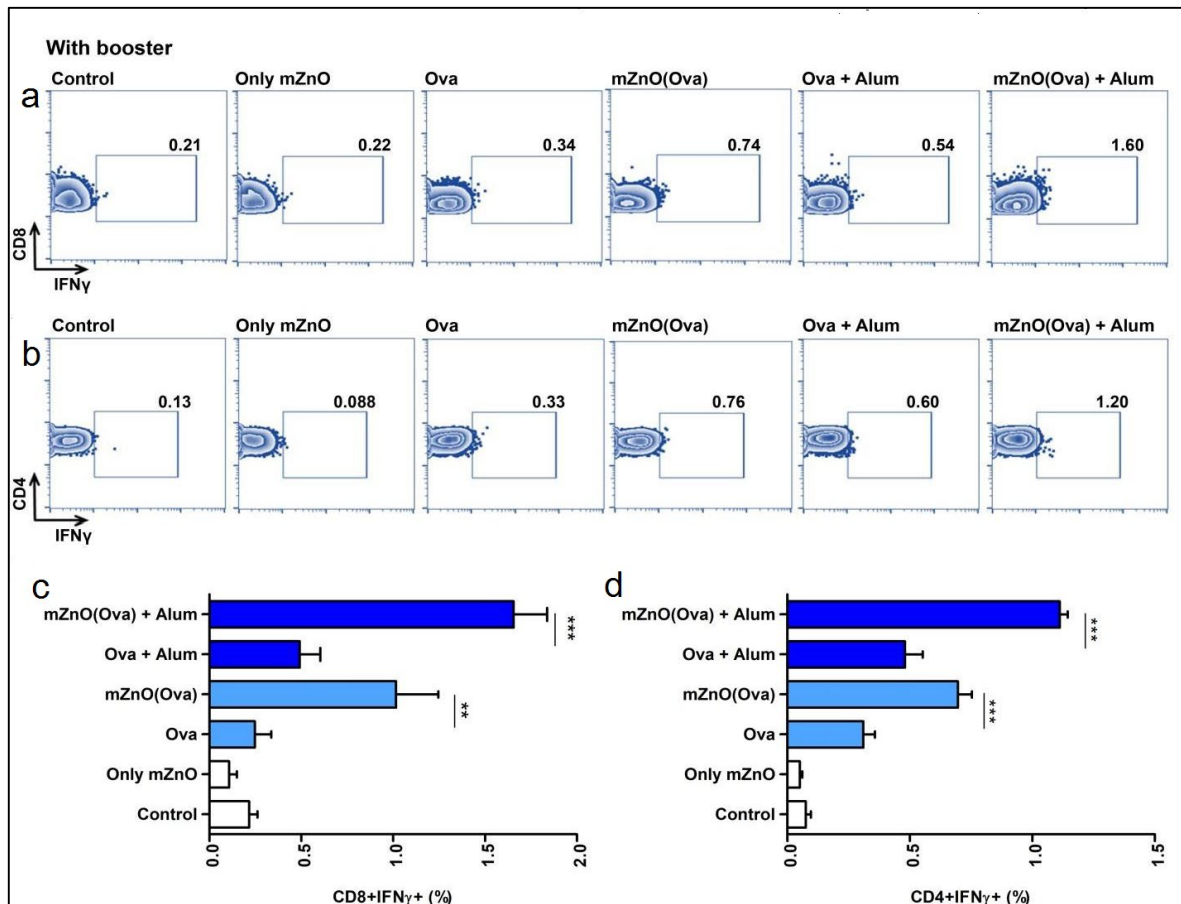


**Figure 3.2.16.** mZnO-Ova nanoformulations trigger enhancement of antigen-specific IFN- $\gamma$  producing CD8<sup>+</sup> and CD4<sup>+</sup> effector T-cells upon secondary immunization. (a) CD8<sup>+</sup> and (b) CD4<sup>+</sup> T cells through FACS Plots for IFN- $\gamma$  expression in CD8<sup>+</sup> and CD4<sup>+</sup> cells, respectively. Graphs represent average percentage of IFN- $\gamma$  producing (c) CD8<sup>+</sup> and (d) CD4<sup>+</sup> T cells.

### 3.2A.18. Ova loaded mZnO NCs trigger amplified antigen specific antibody responses

The competency of particulate antigen delivery system to induce cargo specific B-cell responses has also been evaluated. The level of IgG subtypes IgG1, IgG2a and IgG2b was estimated in the blood serum collected from all six group immunized mice. **Figure 3.2.17**, results demonstrate that the serum levels of all the IgG subtypes were higher in mZnO-Ova as compared to only pure Ova immunized group. Synergistic responses were observed with enhanced Ova specific IgG1, IgG2a and IgG2b levels produced in the group administered with mZnO-Ova-Alum as showed in **Figure 3.2.17a**.

Strikingly, profound enhancement in Ova specific antibody levels, primarily IgG2a and IgG2b, were observed in the mZnO-Ova immunized groups with booster as shown in **Figure 3.2.17b**. This anamnestic response observed after reinjection of immunogen highlights the effectiveness of mZnO-Ova NCs to act as a vaccine adjuvant and provide antigen specific long term immunity and also improved levels of IgG2a in the serum from mZnO-Ova formulation indicates that these NCs have the potential to induce a dominant antigen specific Th1 cellular response.

**Figure 3.2.17** results suggest that mZnO-Ova NCs can significantly produce higher levels of both antigen specific IgG1 and IgG2a as compared to bare mZnO NCs and control group. It is a well-established fact that IgG2a identifies a Th1- polarized immune response, while the IgG1/IgG2a ratio can identify a Th2-biased or Th1-biased immune response. The IgG1/ IgG2a isotype ratio was found to be significantly reduced in the mZnO-Ova with Alum group compared to the pure Ova-Alum immunized group (**Figure 3.2.17c**). This result clearly indicates that mZnO-Ova elicits a Th1 biased antigen specific immune response. Further, the appearance of enhanced IgG2b levels in the serum of the mZnO-Ova-Alum immunized mice and a reduced IgG1/IgG2b ratio (**Figure 3.2.17d**) calculated from the serum IgG levels from the same group provides confirmation of a Th1 bias in cellular immunity upon administration of cargo loaded mZnO NCs.

Further, from **Figure 3.2.17e**, assessment of antigen-specific IgG-secreting B220+ B-cells (indicating with green) in the lymph node sections indicated significantly higher IgG (indicating with blue) formation in mZnO-Ova immunized group versus the pure Ova immunized group (**Figure 3.2.17e**). These results suggest that mZnO-Ova generate higher antigen specific antibody-secreting plasma cells residing mostly in the germinal center of secondary lymphoid organs.

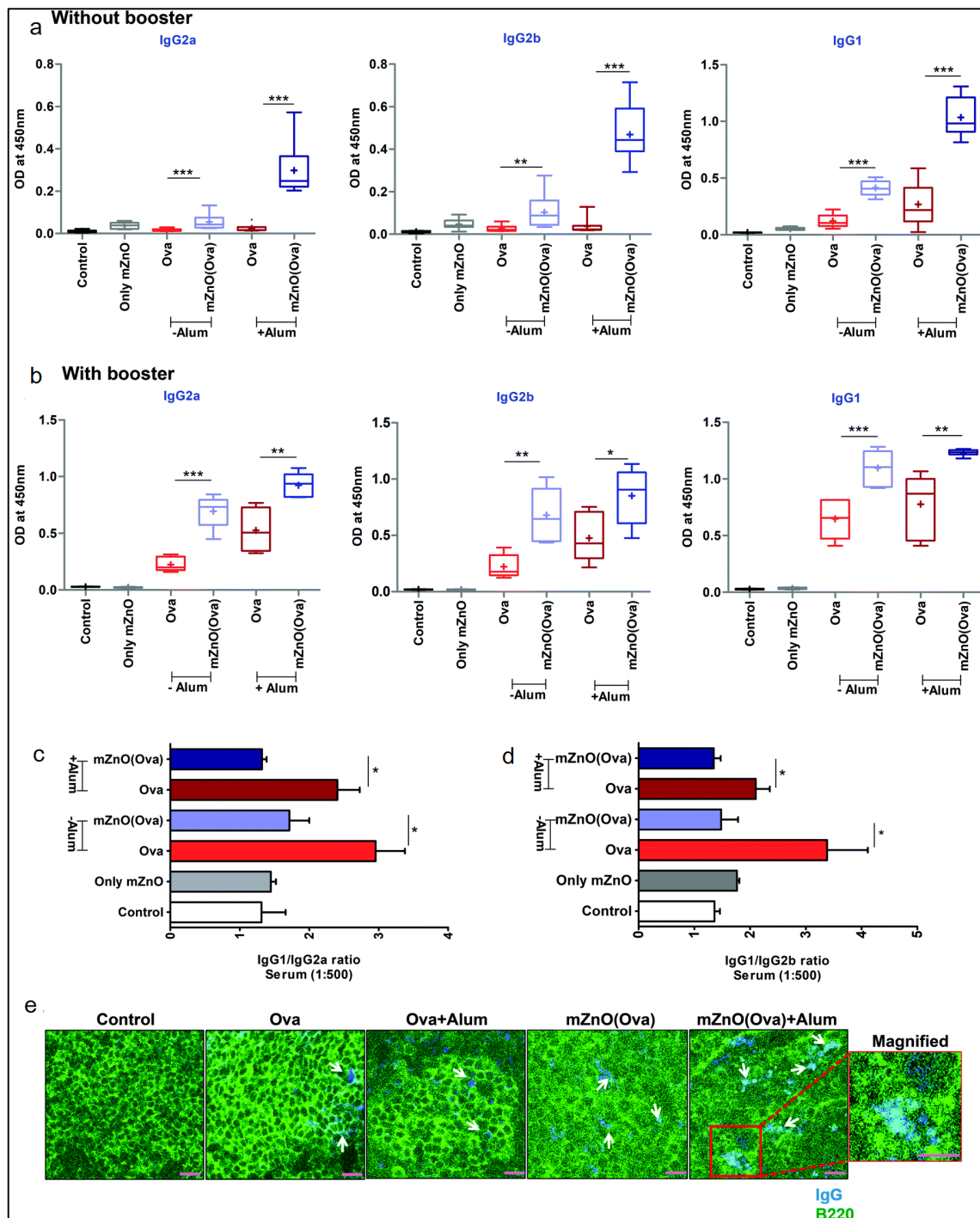


**Figure 3.2.17.** mZnO-Ova NCs elicit amplified antigen specific antibody responses. (a) Graphs represent the average Ova specific IgG2a, 2b and G1 levels after 21 days immunization in the serum of Balb/c mice as per indicated groups. (b) Graphs represent the average Ova specific serum IgG2a, 2b and G1 levels in the Balb/c mice given booster at day 14 and serum collected at day 28. Graphs represent the mean ratio IgG1/IgG2a (c) and IgG1/IgG2b (d) from mice given booster injection. (e) Draining lymph node sections from immunized Balb/c mice as per the indicated groups, stained for antibody secreting B-cells (B220, green and IgG, blue). Scale bars, 50 $\mu$ m for first five panels from left and 25 $\mu$ m for the right-hand panel.

### 3.2A.19. Summary of Part II (Section A)

In summary, mZnO NC was designed by using a surfactant free sonochemical synthesis method with uniform spherical shape and the average size of around 12nm and average pore size of 2.5nm with a high entrapment efficiency of 70.3% for Ova protein. The mZnO NCs characterization results gave a signal that it could probably interact efficiently with APCs and provoke antigen specific immune response when loaded with a specific antigen. This is possible because of the defect-induced structure of mZnO. Both mZnO and mZnO-Ova are very stable in colloidal suspension (zeta potential results). *In vivo* immunization studies revealed that mZnO NCs loaded with model Ova antigen elicit Ova specific expansion of T-cells, increased production of Ova specific IFN- $\gamma$  producing CD4<sup>+</sup> and CD8<sup>+</sup> T-cells as well increased secretion of IFN- $\gamma$  levels, a pre-requisite for an adaptive T-cell response. Although the levels in mZnO-Ova immunized groups were significant to pure Ova immunized group, they were slightly higher or comparable to Ova-Alum immunized group. These results are indicative of a self adjuvant property of mZnO-Ova NCs. Further, mZnO-Ova, when administered with already reported weak adjuvant Alum, instigates a much-heightened antigen specific response which confirms the intrinsic adjuvant property of mZnO NCs. Comparative studies depict that Alum is a weak adjuvant for antibody induction to subunit vaccines and induces a Th2 biased immune response [220]. mZnO-Ova along with Alum elicits strong antigen specific IgG responses potentiating a Th1 biased immune response as depicted by the IgG1/IgG2a or IgG2b ratios. Immunized mZnO-Ova, was also found capable of inducing antigen specific IgG2a or IgG2b levels in serum isolated from immunized mice thereby neutralizing the requirement of any co-adjuvant to trigger antigen specific adaptive T-cell or humoral responses.

Additionally, the enhanced secretion of Th1 cytokines IFN- $\gamma$  and IL-12p40 clearly highlight the ability of mZnO-Ova NCs to tailor antigen specific Th1 polarized immune responses. Further, bare mZnO NCs did not activate T or B-cells as evident from the non-existence of antigen specific CD4<sup>+</sup> IFN- $\gamma$ <sup>+</sup> or CD8<sup>+</sup> IFN- $\gamma$ <sup>+</sup> T-cells or antigen specific serum IgG levels. It is worth mentioning that, the antigen Ova used in the current study is predominantly released from the pores, without showing burst-effect for release. The immune modulatory properties of mZnO-Ova NCs reinforce its usage for a vast variety of biological and pharmacological applications. The mesoporous nature of the ZnO NCs gives it multifunctional properties and can be exploited to load a combination of drugs or antigens for

the treatment of multiple diseases like cancer. mZnO NCs act as a competent vaccine antigen-adjuvant delivery system by programming the sustained release of antigens and simultaneously providing adjuvanting functions.

---

**Outcome:** This work has published as “Mesoporous ZnO nanocapsules for the induction of enhanced antigen-specific immunological response,” Nanoscale, 2017, **9**, 14641-14653

## **Chapter 3: Result and discussion: Part II (Section B)**

### **Mesoporous ZnO NCs incorporated with different drugs for cancer therapy**

3.2B.1. Introduction

3.2B.2. Loading of dye, antimalarial drugs and anticancer drugs in mZnO NCs

3.2B.3. Biocompatibility of mZnO studied with two breast cancer cell lines

3.2B.4. Time dependent release profile of Rh6G from nanoformulation mZnO-Rh6G

3.2B.5. Time and temperature dependent drug release profiles of antimalarial drugs from mZnO NCs

3.2B.6. Time dependent drug release profile of anticancer drug from the nanoformulation of mZnO- Paclitaxel NCs

3.2B.7. Ultramicrotome HRTEM analysis of antimalarial and anticancer drugs loaded mZnO NCs interaction with cancer cell line K562

3.2B.8. Summary of Part II (Section B)

## Chapter 3

### Result and discussion: Part II (Section B)

#### **Objective: Mesoporous ZnO NCs incorporated with different drugs for cancer therapy**

##### **3.2B.1. Introduction**

When the cancer therapy concerns, already many researchers have come forward to develop something new for the betterment of human life against this life-threatening illness. The success of MSNs prompted to create the mesoporous form of a metal-based NP (MNPs). MNPs such as nano-metallic oxides (ZnO, TiO<sub>2</sub>, iron oxide, and quantum dots) [134] offers several advantages such as rigid structures, long shelf life and the capability to tailor the immunostimulatory property of an antigen. ZnO, a well-documented FDA approved material [140] has been widely used for several biomedical applications due to biocompatibility with the human body, nontoxicity, stability and cheaper cost [221]. As ZnO is biocompatible in nature and toxic to cancer cell it is a very suitable candidate for making a nanodrug delivery carrier for cancer therapy. Since ZnO NPs possess a characteristic capability to eradicate cancer T cells by the generation of reactive species of oxygen with cancer T cells resulting in cellular damage.

With the interesting results accomplished by mZnO NCs in the enhancement of immune responses as mentioned in **Part II (Section A)**, we have studied the effectiveness of these synthesized mZnO NCs with different cancer cells. **Part II (Section B)** includes experimental data of different drug conjugate mZnO NCs and their corresponding effects with two breast cancer cell lines MCF 7 and MDA-MB-231. Drugs used in this study are antimalarial drugs like Chloroquine diphosphate salt (CQDP), Dihydroartemisinin (DHA), Sulfadoxine (SD) and two anticancer drugs like DOX, Paclitaxel. Later in this part, the cellular level interaction of

antimalarial and anticancer drug DOX encapsulated nanoformulations have also checked with cancer cell line K562.

### **3.2B.2. Loading of dye, antimalarial drugs and anticancer drugs in mZnO NCs**

To investigate the efficiency of the synthesized and properly dried mZnO NCs (the detailed synthesis procedure have been discussed in the **Part II (Section A)**) were used for loading dye as well as different drugs. The mZnO NCs were incubated with dye Rhodamine 6G (Rh6G), antimalarial drugs like chloroquine diphosphate salt (CQDP), dihydroartemisinin (DHA), sulfadoxine (Sul) and two anticancer drugs like DOX, Paclitaxel with a concentration of dye/drugs to mZnO NCs were kept in the ratio of 1:1 mg.mL<sup>-1</sup> in PBS (pH 7.2). The suspensions were mixed for an hour separately and kept for another 24h without further stirring and stored in a dark place. The dye and drug particles were then separated through centrifugation (at 5000RPM). These loaded NCs were washed three times with PBS to remove the free dye and drug molecules from the surface of the mZnO NCs followed by lyophilization (at temperature -40°C and vacuum 1Pa) and stored in dark at room temperature for further experiments.

### **3.2B.3. Biocompatibility of mZnO studied with two breast cancer cell lines**

The biocompatibility of pure mZnO NCs without loading any dye/drugs have been investigated by exposing them against two breast cancer cell lines MCF 7 and MDAMB-231 through MTT assay. The cell viability of the porous NCs facilitated transfection is under the effect of the cytotoxicity affected by the chemical nature of the NPs as well as transfection reagent. To check the cell cytotoxicity of unloaded mZnO NCs with both cancer cell lines, 5×10<sup>3</sup> number of MCF 7 cells and MDAMB-231 cells were taken in each well of the 96 well plate. MTT assay has been conducted after 24h post transfection by taking various concentrations of NCs like 1000µg.mL<sup>-1</sup>, 500µg.mL<sup>-1</sup>, 250µg.mL<sup>-1</sup>, 125µg.mL<sup>-1</sup>, 62.5µg.mL<sup>-1</sup>, 31.25µg.mL<sup>-1</sup>, 15.67µg.mL<sup>-1</sup> and 7.837 µg.mL<sup>-1</sup>, where considering pure cells without any dye/drugs/NCs as control (100% cell survival) for both cell lines MCF-7 and MDAMB-231.

It can be observed from **Figure 3.2.18** and **Figure 3.2.19**, with a lower concentration of NCs i.e., 7.837µg.mL<sup>-1</sup> and 15.67µg.mL<sup>-1</sup>, are also able to kill both malignant cells. Percentage of cell survival is 72.67±5.1 % and 92.013±2.2 % for minimum mZnO

concentration  $7.837\mu\text{g.mL}^{-1}$  as well as  $11.21\pm 3.2\%$  and  $10.65\pm 1.1\%$  for highest mZnO concentration  $1000\mu\text{g.mL}^{-1}$  for both cell lines MCF 7 and MDAMB-231 respectively.

The toxicity of the unloaded bare mZnO NCs is increasing from lower to higher concentrations (i.e., from  $7.8\mu\text{g.mL}^{-1}$  to  $1000\mu\text{g.mL}^{-1}$ ) in both cell lines MCF 7 and MDAMB-231. Hence it has been confirmed that these synthesized mZnO NCs can be used as an excellent carrier for carrying anticancer drugs against cancer cells.

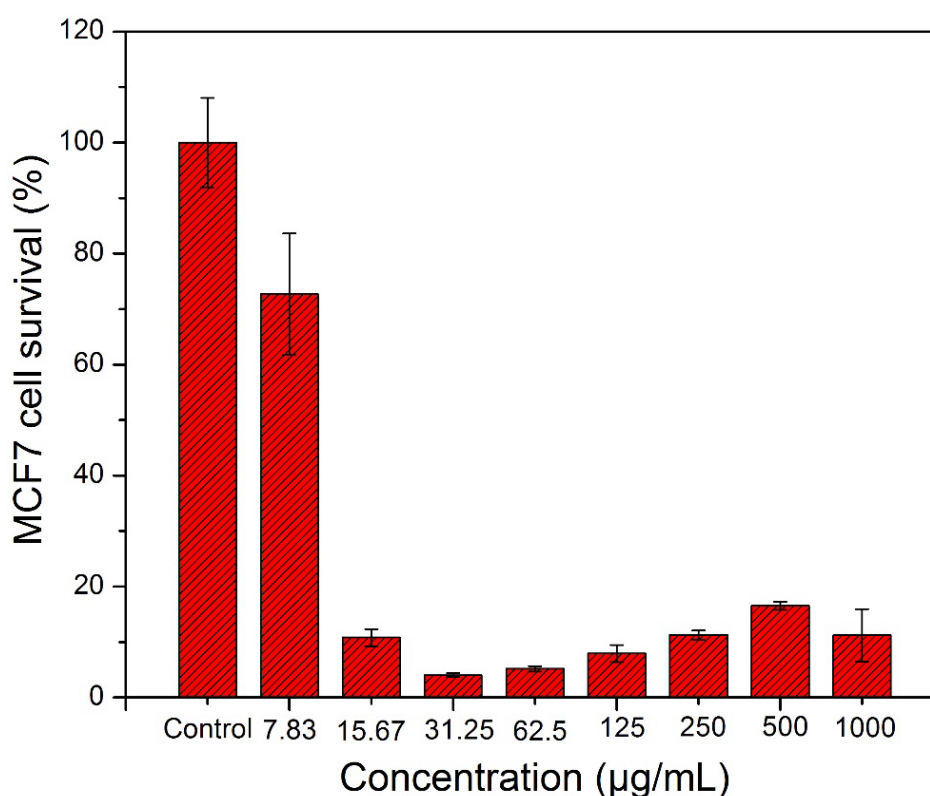


**Figure 3.2.18.** Percentage of cell survival analyzed by MTT assay while mZnO NCs were incubated with MCF 7 cell line at  $37^\circ\text{C}$  for 24h.

In **Figure 3.2.19**, with the percentage of cell survival data microscopic images of the MDA-MB-231 cells are also shown with all mZnO NC concentrations from  $1000\mu\text{g.mL}^{-1}$ ,  $500\mu\text{g.mL}^{-1}$ ,  $250\mu\text{g.mL}^{-1}$ ,  $125\mu\text{g.mL}^{-1}$ ,  $62.5\mu\text{g.mL}^{-1}$ ,  $31.25\mu\text{g.mL}^{-1}$ ,  $15.67\mu\text{g.mL}^{-1}$  and  $7.837\mu\text{g.mL}^{-1}$ . From the microscopic image showed in **Figure 3.2.19**, it is clearly visible that the cell structures started to deform at the lowest mZnO concentration ( $7.84\mu\text{g.mL}^{-1}$ ) only and it increased with an increase of NC concentrations in the cells and for the highest mZnO concentration ( $1000\mu\text{g.mL}^{-1}$ ) there is no specific shape exist for the cancer cells and only  $10.65\pm 1.1\%$  cells are survived which is very less. Thus with these experimental data mZnO

NCs are proving their toxicity behavior towards malignant cells. These microscopic images have been captured by using optical microscope Model Olympus CKX41 (10X).

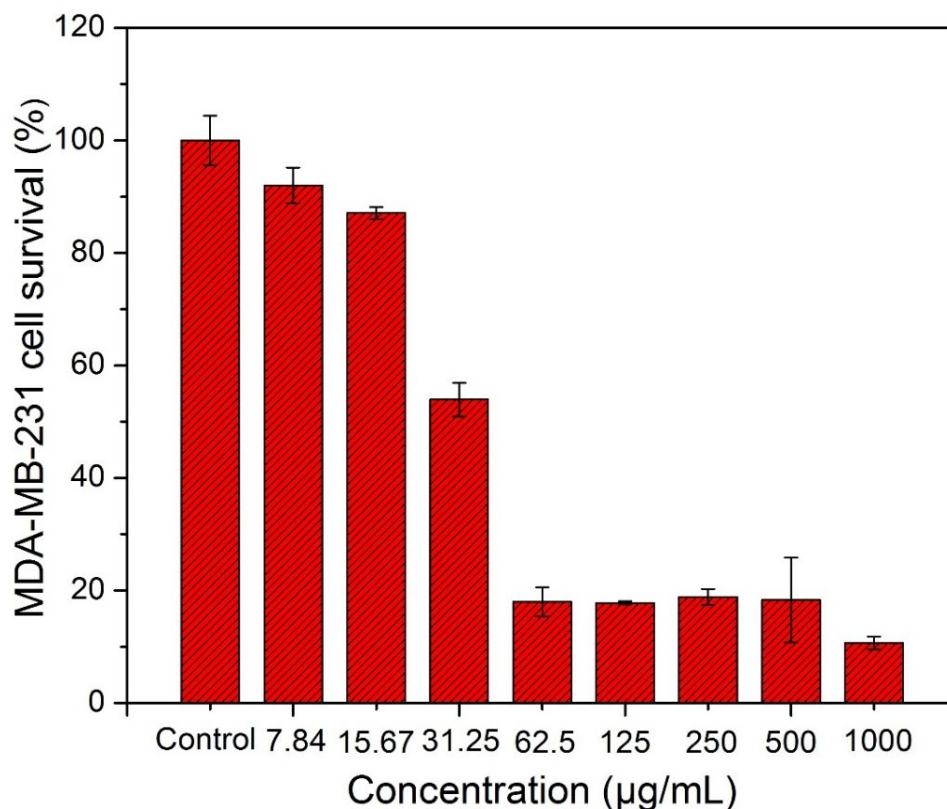


**Figure 3.2.19.** Percentage of cell survival analysed by MTT assay, while mZnO NCs were incubated with MDA-MB-231 cell line at 37°C for 24h.

Furthermore, the  $IC_{50}$  value has been calculated for the mZnO NCs on both cell lines MCF 7 and MDA-MB-231 and the values are found as  $7.056 (\pm 0.23)$  nM for MCF 7 and  $35.05 (\pm 0.6)$  nM for MDA-MB-231. We have performed some other set of experiments, (given detail in the **Chapter 3 Part 3**) where we have calculated  $IC_{50}$  value for free anticancer drug Paclitaxel treatment on MCF 7 and MDA-MB-231 and values are  $31.9 (\pm 1.3)$  nM for MCF 7 and  $37.52 (\pm 1.8)$  nM for MDA-MB-231. mZnO NCs on MDA-MB-231 shows a little less  $IC_{50}$  value compared to the free Paclitaxel on MDA-MB-231. Whereas, a more distinct difference can be seen in cases of mZnO NCs on MCF 7 and Paclitaxel on MCF 7. Thus, mZnO NCs have proved their efficiency to kill malignant cells by showing smaller  $IC_{50}$  value on both cell lines MDA-MB-231 and MCF 7 while compared with free Paclitaxel on those cell lines.

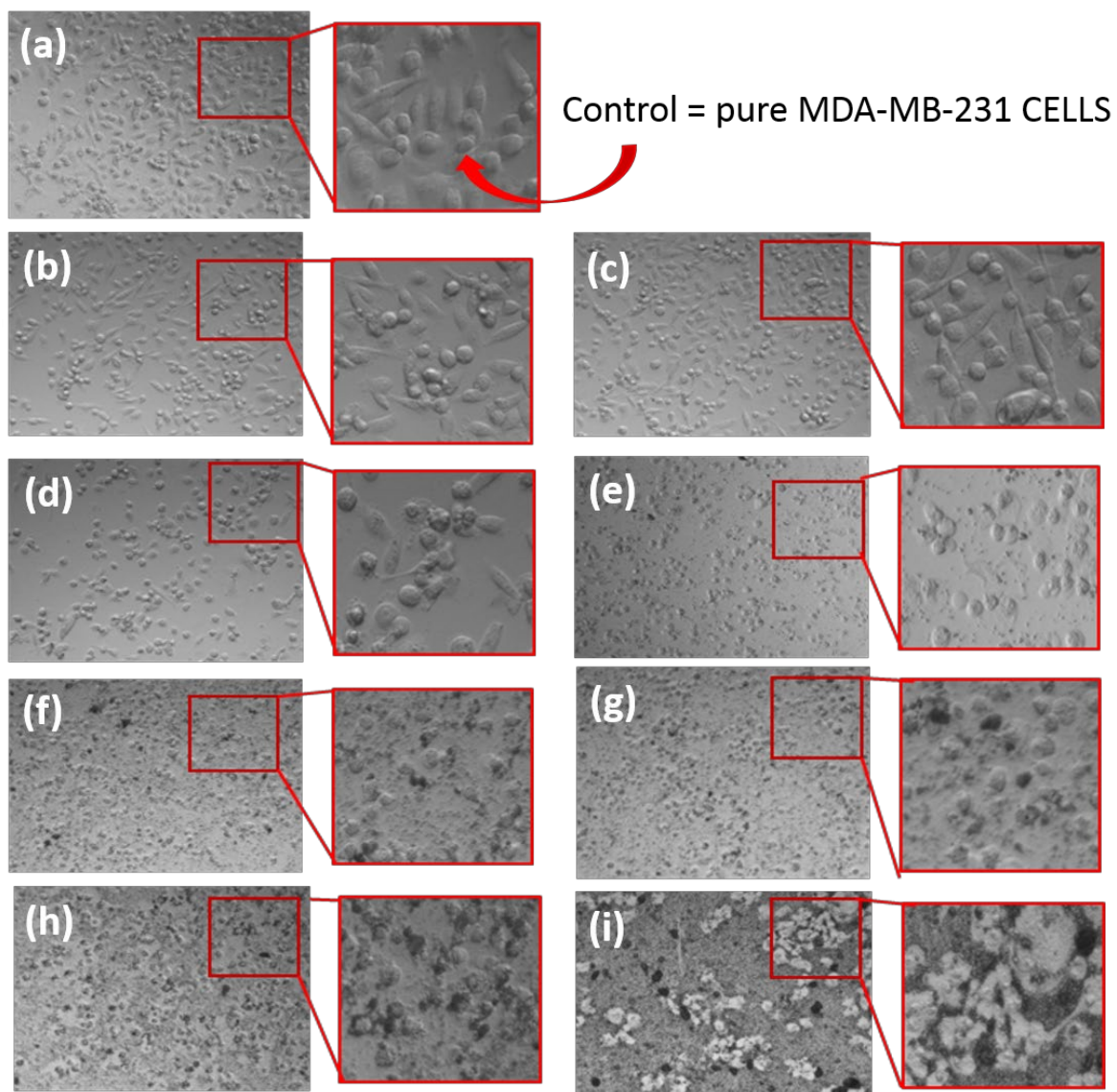


**Figure 3.2.20.** Microscopic images of the MDA-MB-231 cancer cells after incubation with increasing concentration of mZnO at 37°C for 24h (a) Control (100% cell survival), (b)  $7.84\mu\text{g.mL}^{-1}$ , (c)  $15.67\mu\text{g.mL}^{-1}$ , (d)  $31.25\mu\text{g.mL}^{-1}$ , (e)  $62.5\mu\text{g.mL}^{-1}$ , (f)  $125\mu\text{g.mL}^{-1}$ , (g)  $250\mu\text{g.mL}^{-1}$ , (h)  $500\mu\text{g.mL}^{-1}$ , (i)  $1000\mu\text{g.mL}^{-1}$ .

### 3.2B.4. Time dependent release profile of Rh6G from nanoformulation mZnO-Rh6G

The synthesized mZnO NCs were loaded with dye Rh6G in the NC to dye ratio of 1:1 mg.mL<sup>-1</sup> in PBS (pH 7.2). Dye loaded mZnO NCs (450µg) were suspended in 6mL PBS (pH 7.2) and the release behavior has been studied by maintaining a fixed time interval for 7h at room temperature (25°C).

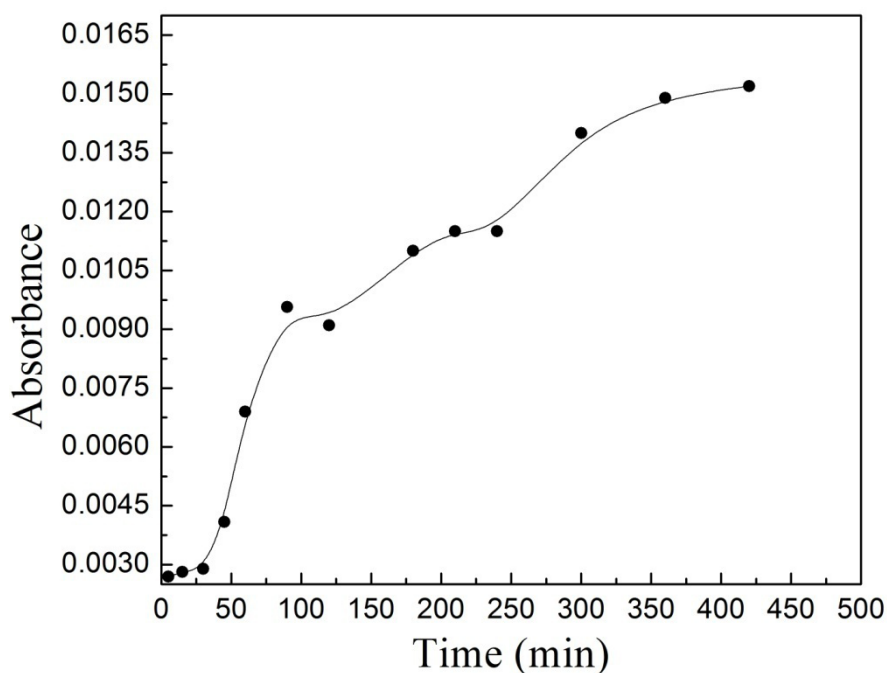


**Figure 3.2.21.** Dye release profile of Rh6G from mZnO NCs at 25°C temperatures for 7h in PBS medium (pH 7.2).

**Figure 3.2.21** shows the release profile of dye Rh6G from the mZnO NCs. The release behavior has been checked till 7h by considering absorbance peak at the  $\lambda_{\text{max}} = 535\text{nm}$  wavelength. The absorbance of the released dye in PBS was recorded by using UV-Vis spectrometer and the extent of release of dye was calculated. From the release spectrum in **Figure 3.2.21**, it is clear that mZnO NCs are capable of loading dye particles inside its pores and with an increase of time, it has the capacity to show sustained release of the loaded particles. Therefore, it is confirmed that prepared NCs are capable to load different drugs, biomolecules etc. for further biological applications.

### 3.2B.5. Time and temperature dependent drug release profiles of antimalarial drugs from mZnO NCs

The designed nanoformulations of mZnO-CQDP, mZnO-DHA and mZnO-Sulfadoxine (500 $\mu$ g each) were suspended in RPMI 1640 medium and the release behavior has been studied individually. The encapsulation efficiencies for mZnO-CQDP, mZnO-DHA and mZnO-Sulfadoxin NCs have been calculated by using [% Entrapment efficiency = {weight of drug in NPs/weight of drug fed initially} $\times$ 100] (eq. 2) mentioned in **Part II (Section A)** as 68.2%, 66.8% and 70.1% respectively. To study the drugs release profiles, three different sets of experiments were set where, 0.5mg of mZnO-CQDP, mZnO-DHA and mZnO-Sulfadoxin NCs of each were taken with 5mL of medium in three different cuvettes.

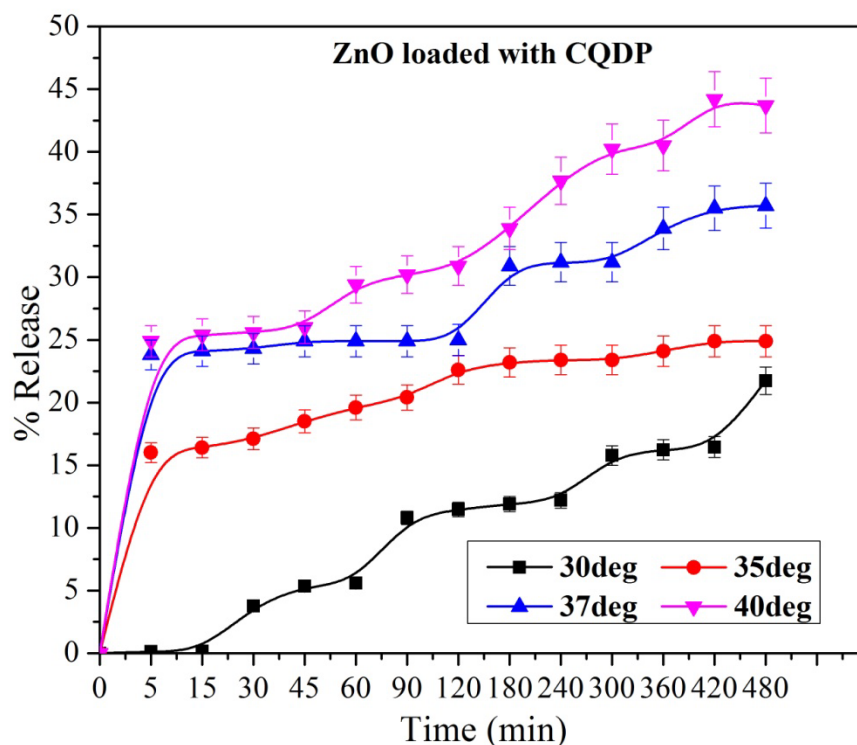


**Figure 3.2.22.** Temperature and time dependent drug release profile of CQDP loaded in nanoformulation mZnO-CQDP at 30°C, 35°C, 37°C, 40°C temperatures for 8h in RPMI 1640 medium.

In case of NC drug conjugate mZnO-CQDP, to calculate the extent of drug CQDP released from the NC the absorption peak was considered at  $\lambda_{\max} = 225\text{nm}$ . Maintaining a fixed time interval (15min) the absorbance of the released drug CQDP in the medium was recorded

at different temperatures such as 30°C, 35°C, 37°C, 40°C using UV-Vis spectrometer and the extent of release of CQDP was calculated. **Figure 3.2.22** showed the release profile of antimalarial drug CQDP loaded in the mZnO capsules. Percentage of drug release gradually increases with the increase of time (5-480min) and temperatures (30-40°C). At lower temperature 30°C, the percentage of drug release is very slow i.e., only 22±1.087 % at 8<sup>th</sup> h. The percentage of drug release are 25±1.2%, 36±1.7% and 44±2.1% at 35, 37 and 40°C after the end of 8<sup>th</sup> h. At all four temperatures, the NCs have shown a sustained release of drug CQDP upto 8h.

**Figure 3.2.23** and **Figure 3.2.24** showed the drug release profiles of two other antimalarial drugs DHA and sulfadoxine (SD) loaded in the nanoformulations of mZnO-DHA and mZnO-SD respectively. Antimalarial drugs loaded nanoformulations were suspended in PBS medium (pH 7.2) and the drug release behavior of each drug loaded NCs was studied by maintaining a time interval for 30 days at 37°C. The time interval has maintained for the drug release study as 2h for the first 8h then 12h for next 3days, then 24h till 5<sup>th</sup> day and after that 5 days upto 30 days. The absorbance of the released drugs in PBS was recorded using UV-Vis spectrometer and the extent of release of drugs DHA and sulfadoxine were calculated. To study the release profile, 0.6 mg of mZnO-DHA and mZnO-SD nanoformulations were suspended with 5mL of PBS in a cuvette. The loading of the drug in porous ZnO NCs occurred through the diffusion process.

**Figure 3.2.23** shows the release behavior of drug DHA loaded in mZnO–DHA NCs where drug release profile has been studied by maintaining a time interval for 30 days considering absorbance peak at the  $\lambda_{\text{max}} = 220\text{nm}$  wavelength. The percentage of drug release gradually increased with the increase of time and finally become constant after 15 days. The percentage of release of DHA from mZnO NCs on the 30<sup>th</sup> day is 62%.

In a similar way, the release profile of sulfadoxine from mZnO-SD has been studied by maintaining a time interval till 30 days and shows in **Figure 3.2.24**, by considering the absorbance peak at  $\lambda_{\text{max}} = 260\text{nm}$  for sulfadoxine at 37°C. Percentage of release gradually increases with the increase of time and finally become constant after 20 days. The percentage of release of Sulfadoxine from mZnO NCs on the 30<sup>th</sup> day is 82%.

All these drug release experiments have been repeated for three times to avoid all type of errors.

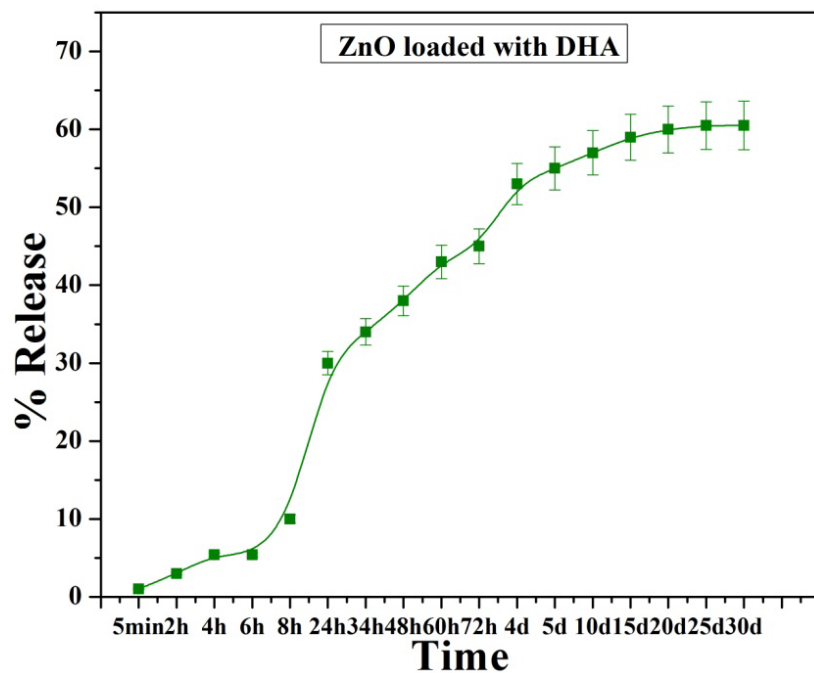


**Figure 3.2.23.** Drug release profile of DHA loaded in the nanoformulation of mZnO-DHA at 37°C for 30 days in PBS medium (pH 7.2).

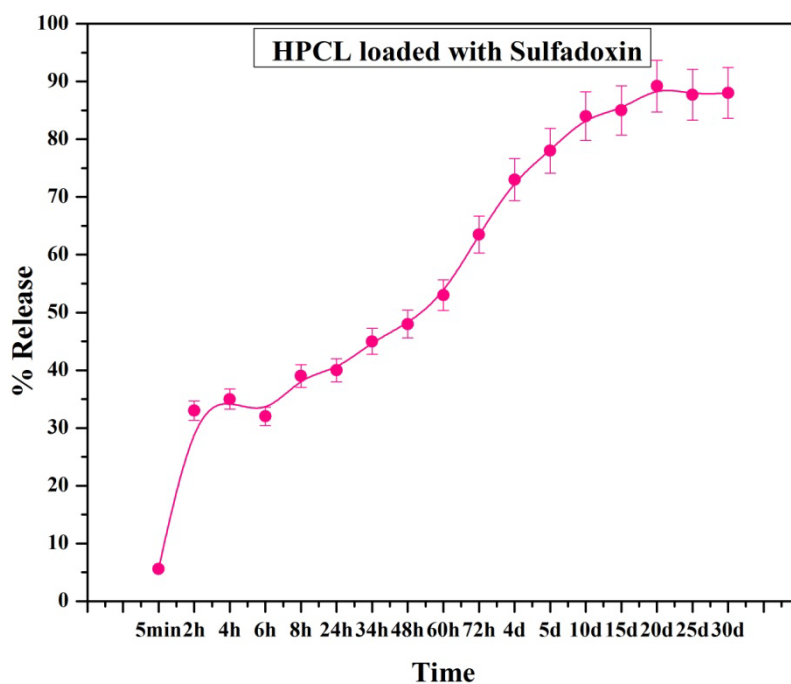


**Figure 3.2.24.** Drug release profile of Sulfadoxine loaded in the nanoformulation of mZnO-SD at 37°C for 30 days in PBS medium (pH 7.2).

### 3.2B.6. Time dependent drug release profile of anticancer drug from the nanoformulation of mZnO- Paclitaxel NCs

The same loading procedure has been followed to encapsulate anticancer drug paclitaxel in the pores of mZnO NCs. The designed mZnO-ptaxol was suspended in PBS medium (pH 7.2) and the corresponding drug release behavior has been studied. To study the release profile, 0.5mg of mZnO-ptaxol was taken with 5mL of PBS in a cuvette. All experimental parameters have been fixed in similar way like antimalarial drug release experiments, mentioned previously. The **Figure 3.2.25** shows the drug release profile of anticancer drug paclitaxel from mZnO-ptaxol NCs with a time interval till 7 days by considering the absorbance peak at  $\lambda_{\max} = 215$  nm at 37°C temperature. The percentage of release of drug is calculated as 12.5±0.62 %, 32.6±1.63 %, 41±2.05 %, 46±2.3 %, 50.7±2.53 %, 56±2.8 %, 56±2.8 %, 75±3.75 %, 78±3.9 %, 82±4.1 %, 83±4.15 %, 83.5 ±4.7 % on 2h, 4h, 6h, 8h, 24h, 36h, 48h, 3day, 4day, 5day, 6day 7day respectively.

The encapsulation efficiency for mZnO-ptaxol NCs has been calculated by using [% Entrapment efficiency = {weight of the drug in NPs/weight of drug fed initially} × 100](eq. 2) mentioned in **Part II (Section A)** as 69.8 %.

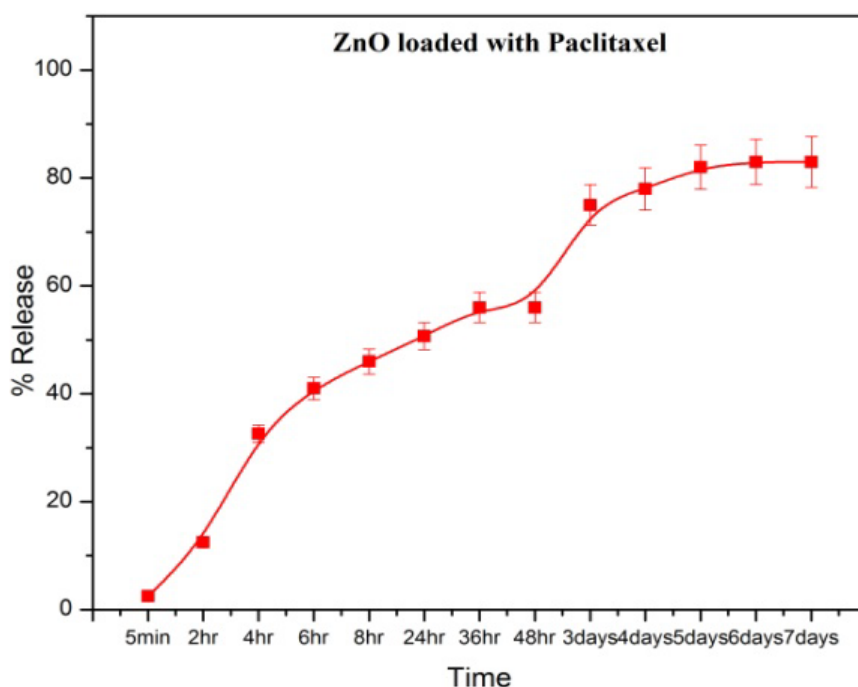


**Figure 3.2.25.** Drug release profile of Paclitaxel loaded in the nanoformulation of mZnO-ptaxol at 37°C for 30 days in PBS medium (pH 7.2).

### 3.2B.7. Ultramicrotome HRTEM analysis of antimalarial and anticancer drugs loaded mZnO NCs interaction with cancer cell line K562

The cellular level interaction of drugs loaded mZnO NCs with cancer cell line K562 can be captured with the help of HRTEM. For that regard bare mZnO NCs, nanoformulations of mZnO-CQDP and mZnO-DOX were allowed to interact with K562 cells.

K562 cells with a concentration ( $10\mu\text{g/mL}$ ) of drugs (DOX and CQDP) loaded mZnO NCs were incubated for 12h. Thereafter, cells with loaded NCs were washed and then fixed by using a cold buffer comprising 3% glutaraldehyde in 0.1M Sodium cacodylate for 30 min. After the rinsing was done with PBS, the cells were post-fixed in osmium tetroxide (1%) and embedded in Epon resin. Then, semi-thin sections of K562 with drugs loaded NCs were cut, stained with 0.5% toluidine blue and investigated under a light microscope. Ultrathin sections were stained with 2% uranyl acetate and Reynolds lead citrate and finally observed under a high definition transmission electron microscope (HRTEM).

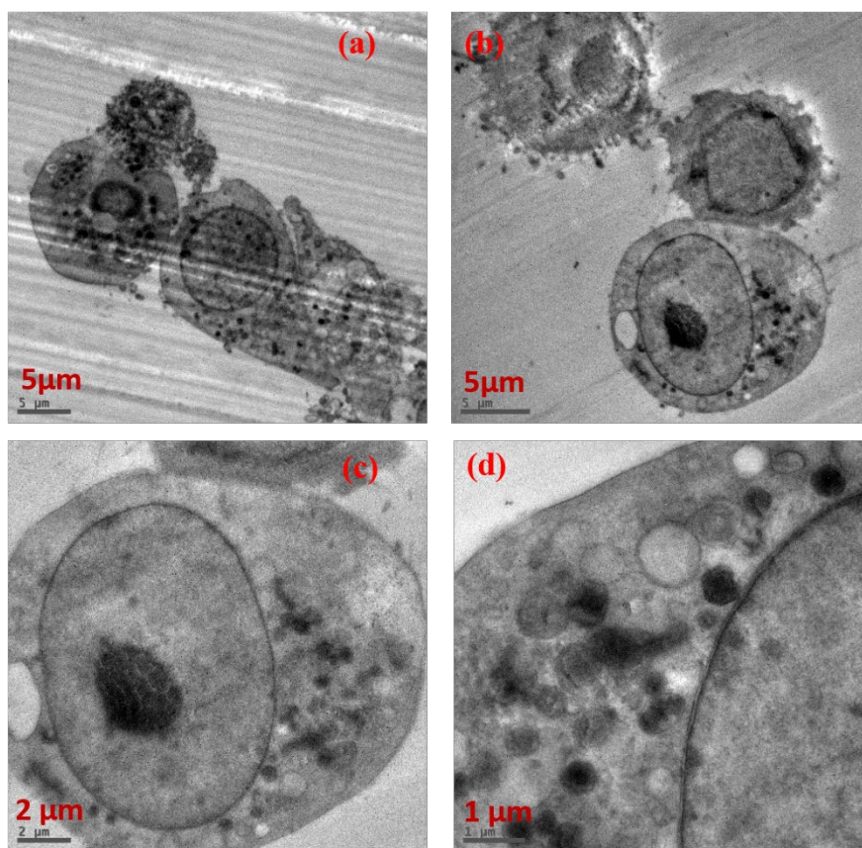


**Figure 3.2.26.** Cell sectioning HRTEM images of pure cancer cell line K562 (a-d) from lower to higher magnification.(c) and (d) showing single cells with all distinct cell components.

**Figure 3.2.26 (a-d)** represents cell sectioning HRTEM micrographs of pure cancer cells K562 without any NCs, drugs or drug loaded NCs treatment. K562 cells have proper cell morphology which exhibits definite nucleus enclosed by a defined nuclear membrane, cytoplasm surrounded by the well-defined cell membrane.

The **Figure 3.2.27 (a-d)** represented cell sectioning HRTEM micrographs of cancer cells K562 treated with bare mZnO NCs. It can be observed from the micrographs that bare mZnO NCs entered inside the cancer cells by endocytosis through the cell membrane. The deformation of the cell membrane can be observed clearly in **Figure 3.2.27b**, **3.2.10c** and **3.2.10d** due to the interaction with the NCs. Presence of small mZnO NCs inside the cell can also be observed from the HRTEM micrographs.

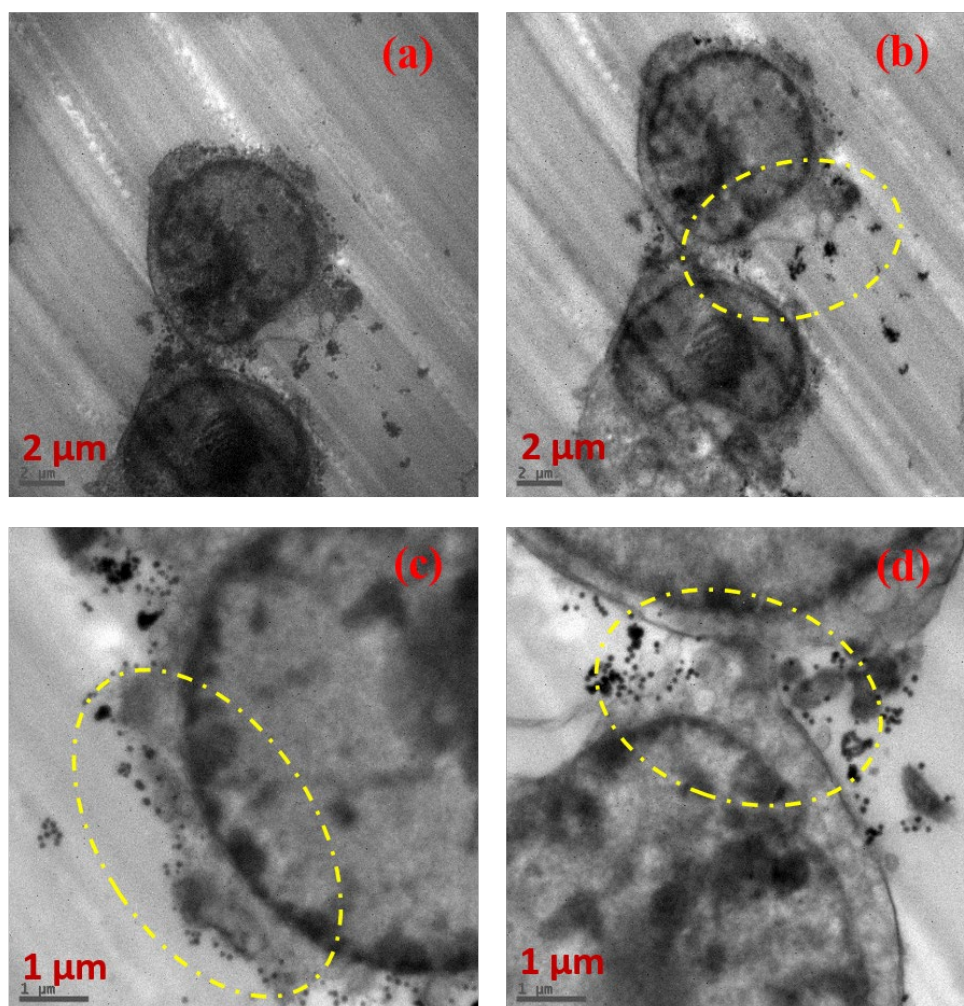


**Figure 3.2.27.** Cell sectioning images of bare mZnO NCs dispersed in PBS (pH 7.2) treated with K562 cell lines at 37°C from (a-d) lower to higher magnifications. (c) and (d) showing the single cell deformed after interaction with mZnO NCs.

This is confirmed from the TEM micrographs **Figure 3.2.27** that mZnO is toxic to the cancer cells and therefore helping it to break the cell membrane and enter inside. Cytotoxicity results of mZnO NCs in **Figure 3.2.18** and **Figure 3.2.19** are also evident with similar kind of cell killing mechanisms with different cancer cell lines i.e., MCF7 and MDA-MB-231.

**Figures 3.2.28 (a-d)** represent cell sectioning HRTEM micrographs of cancer cells K562 incubated with antimalarial as well as anticancer drug CQDP in mZnO NCs. It is observed that malignant cells got aggregated due to the presence of mZnO–CQDP NCs inside the cells through endocytosis. The loaded NCs make their way through the cell membrane resulting in the rupture of the cell membrane and thereby exposing the cellular components outside as shown in **Figure 3.2.28c**. The tiny agglomerated NCs can be observed inside the cell in **Figure 3.2.28d**. This deformation of cell structure occurred due to the release of drugs from the mZnO NCs in a sustained manner as shown in release profile data **Figure 3.2.28** with increase in time. CQDP can act as antimalarial as well as an anticancer drug in advanced medical treatments [222,223].

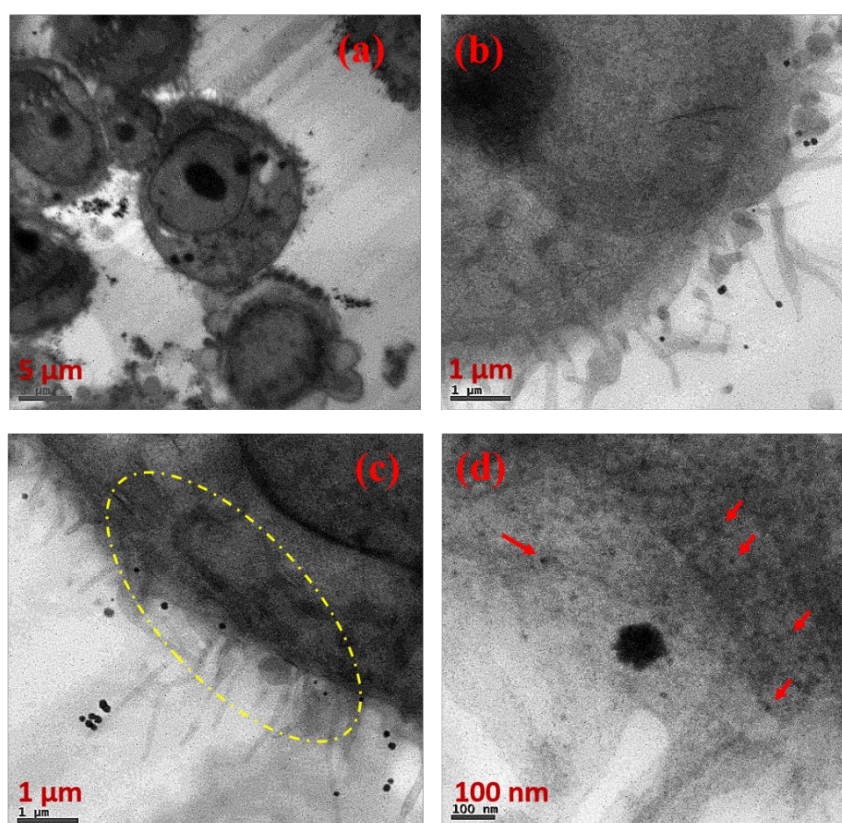


**Figure 3.2.28.** Cell sectioning HRTEM images of mZnO–CQDP nanoformulations dispersed in PBS (pH 7.2) treated with K562 cells at temperature 37°C from (a-d) lower to higher magnifications (5μm-100nm). (c) and (d) showed the single cell deformation after interaction with mZnO-CQDP nanoformulation.

**Figures 3.2.29 (a-d)** represent cell sectioning HRTEM micrographs of cancer cells K562 incubated with anticancer drug DOX loaded in mZnO nanocarriers. From the TEM micrographs, it can be observed that due to the interaction with NCs the malignant cells started to deform once drug loaded NCs entered through the cell membrane as shown in **Figure 3.2.29a** and **3.2.29b** and thereby rupturing the cell membrane completely. They are even rupturing nuclear membranes and finally resulting in the cellular components as cell debris shown in **Figure 3.2.29c** and **3.2.29d**.

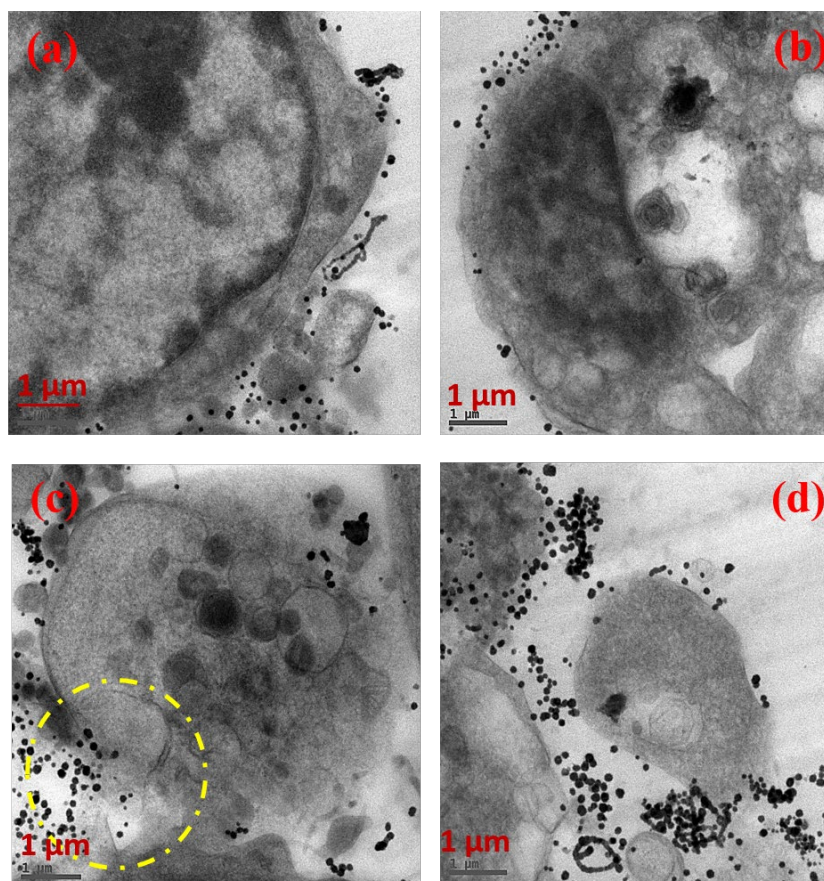


**Figure 3.2.29.** Cell sectioning HRTEM images of mZnO-DOX nanoformulations dispersed in PBS (pH 7.2) treated with K562 cells at 37°C (a-d) from lower to higher magnifications. (c) and (d) cell membrane deformation after interaction with mZnO-DOX nanoformulation.

### 3.2B.8. Summary of Part II (Section B)

The **Section B** of **Part II** includes some additional applications of surfactant free mZnO NCs. The detail surfactant free synthesis process of mZnO nanocarrier has been discussed in the **Part II (Section A)**. This porous nanosized ZnO possess very interesting physical and chemical properties which are already discussed in the **Part II (Section A)** in detail. In this

part of **Chapter 3**, the biocompatibility of the mZnO NCs has been checked with two breast cancer cell lines MCF 7 and MDA-MB-231 with different concentrations ( $1000-7.84\mu\text{g}\cdot\text{mL}^{-1}$ ) of nanosized porous ZnO where NCs have shown their toxicity towards cancer cells even with a lower concentration of NCs only. Furthermore, their toxicity towards these cancer cells was further proved by the  $\text{IC}_{50}$  values.  $\text{IC}_{50}$  for mZnO on MCF 7 is found as  $7.056 (\pm 0.23)\text{nM}$  and for mZnO on MDA-MB-231 is  $35.05 (\pm 0.6)\text{nM}$  which are more or less similar to the  $\text{IC}_{50}$  calculated by treating free Paclitaxel on MCF 7 ( $31.9\pm 1.3\text{nM}$ ) and MDA-MB-231 ( $37.52\pm 1.8\text{nM}$ ). Further, the encapsulation efficiency of the mesoporous mZnO NCs for the application of it as a drug carrier has been checked with few drugs like CQDP, DHA, SD, DOX and Paclitaxel. The nanoformulation of mZnO-CQDP, mZnO-DHA and mZnO-SD possess tremendous encapsulation efficiency to encapsulate the respective drugs as 68.2%, 66.8% and 70.1%. Among these three antimalarial drugs CQDP has selected for temperature range drug release study as CQDP is a well-established anticancer drug and for that chosen temperature range was  $30^{\circ}\text{C}$ ,  $35^{\circ}\text{C}$ ,  $37^{\circ}\text{C}$  and  $40^{\circ}\text{C}$  for 8h with a time interval of 15min in RPMI 1640 medium. The CQDP encapsulated mZnO has shown a drug release pattern where with increase with time and temperature the percentage of drug release from the NCs is also increasing i.e., for lowest temperature  $30^{\circ}\text{C}$  the drug release is  $22\pm 1.087\%$  by the end of 8<sup>th</sup> hour and for highest temperature  $40^{\circ}\text{C}$  is  $44\pm 2.1\%$  (8<sup>th</sup> hr). Both nanoformulations of mZnO-DHA and mZnO-SD are kept for two sets of long term drug release experiments where individually they have shown a sustain drug release pattern till day 30 with a drug release percentage of 62% and 82% respectively while maintaining the experimental temperature as  $37^{\circ}\text{C}$  in PBS (pH 7.2). Further drug release study has been done with nanoformulation of mZnO-ptaxol for 30 days. All experimental parameters have been fixed similar like antimalarial drug release experiments and the encapsulation efficiency has been calculated as 69.8% for mZnO-ptaxol nanoformulation. Later, these NCs have been used to encapsulate DOX a very well established anticancer drug. Nanoformulations of mZnO-DOX and mZnO-CQDP were incubated with K562 cancer cells to allow the nanosized carrier to carry drugs (DOX and CQDP) through the cell membrane of K562 cancer cells which are shown in cell sectioning part where these NCs killed the cell successfully thereby proving their efficiency as nano drug vehicle for targeted drug delivery system. Since ZnO has been previously shown to have anti-microbial properties, its usage can also be extended for the treatment of infectious diseases with a combination of pathogen specific immunogenic peptides, proteins or drugs adsorbed in the mesopores of the NP, thereby shielding it from degradation in the biological fluids.

## **Chapter 3: Result and discussion: Part III**

### **Synthesis of porous PCL nanocapsules by template removing approach to eradicate Breast Cancer cells**

3.3.1. Introduction

3.3.2. Synthesis procedure

3.3.3. Mechanism of formation of porous PCL NCs

3.3.4. Designing mesoporous PCL NCs: Size, Morphology and porous structure of NCs

3.3.5. Surface chemical structure of PCL-mZnO and mesoporous PCL NCs

3.3.6. BET surface area analysis of porous PCL NCs

3.3.7. Phase, solid state crystal structure study and zeta potential analysis

3.3.8. Loading of anticancer drug Paclitaxel in mesoporous PCL NCs

3.3.9. Time dependent drug release behavior of anticancer drug from core shell PCL-mZnO (PZ) and porous PCL (HPZ) NCs

3.3.10. Biocompatibility of core shell PCL-mZnO (PZ) studied with two breast cancer cell lines

3.3.11. Biocompatibility of mesoporous PCL (HPZ) NCs studied with two breast cancer cell lines

3.3.12. Interaction of free Paclitaxel with Cancer cell lines MCF 7 and MDA-MB-231

3.3.13. Interaction of Paclitaxel loaded HPZ with Cancer cell lines MCF 7 and MDA-MB-231

3.3.14. Summary and Conclusions of Part III

## Chapter 3

### Result and discussion: Part III

**Objective: Synthesis of porous PCL nanocapsules by template removing approach to eradicate Breast Cancer cells.**

#### 3.3.1. Introduction

Polymer based nanodrug delivery vehicles are more promising, as these polymer NPs can be engineered by encapsulating or attaching drugs and other biomolecules inside or on the surface of it and after delivered those drugs/biomolecules to the site of interest, these nanocarriers can easily degrade in physiological conditions. PCL (Poly caprolactone) is one of the proficient and vastly used biodegradable and biocompatible polymers. At the same time, when application of these polymer based nanodrug delivery vehicle in therapeutic field concerned, Cancer can be the best area to focus as it is one of the life threatening ailment and treatment related to this includes a lot of side effects, because the anticancer drugs are not only effecting the malignant cells but also effecting the other healthy cells resulting unavoidable severe side effects. Therefore, the nanobiotechnology researches are continuously trying to improve the efficiency of cancer therapy with decreasing the side effects. There are many types of research are going on in this regard [161–163]. Research in the area of cancer is very broad spectrum, therefore our focus was limited by choosing an anticancer drug Paclitaxel for the designing of drug NC conjugation and delivering it to the breast cancer cells. Paclitaxel is known for its most diverse use as well as for its outstanding effect against solid tumor malignant cells like breast, lung, ovarian, cervical, pancreatic cancer [175] etc.

However, the drug Paclitaxel has a wide range of application as an antitumoral therapeutic agent, it is still a big challenge for the application of Paclitaxel. It is hydrophobic in nature and also causing clinical complications due to the non-ionic surfactant Cremophor

EL and dehydrated ethanol present in Paclitaxel formulation used to improve the solubility of Paclitaxel for the treatment [58,59]. Considering all these limitations of antitumor drug Paclitaxel, many easy and simple approaches with polymeric drug delivery vehicles like NPs, liposomes, hydrogel, micelle etc., have been reported to increase the drug stability, permeability, solubility etc. However, as an alternative of Paclitaxel formulation, PEGylated caprolactone nanodrug carriers synthesized without using surfactant Cremophor, for Paclitaxel loading purpose has developed [224]. Biggest challenge occurred with the enhancing resistance of many anticancer drugs including paclitaxel with the ovarian carcinoma A2780 cell line. Reported oral delivery of PLGA Paclitaxel formulation could not show much potential while comparing with free Paclitaxel drug but can show a significant bioavailability of the drug to the multidrug resistant 2780 AD, which is a variant of ovarian carcinoma cell line [199].

This **Chapter 3 Part III** of the dissertation focuses on the synthesis of a nanodrug carrier of porous PCL NCs by template removing approach. A detail explanation for the designing of mesoporous ZnO (mZnO) NPs have included in the previous part (**Part II Section A**) of **Chapter 3** and these mZnO NPs have been used as templates while designing the PCL NPs in this work. Later these template NPs have been removed successfully to make polymer NPs porous in nature and to apply these porous PCL based NCs as a drug delivery carrier to encapsulate anticancer drug Paclitaxel. The cell cytotoxicity of these polymer NCs has also been studied with two different breast cancer cell lines via MTT assay. Finally, these drug loaded PCL polymer NCs have been incubated with two breast carcinoma cell lines like MCF7 and MDA-MB-231 to evaluate their inhibiting efficiency of the cancer cells *in-vitro*.

### **3.3.2. Synthesis procedure**

Detail of the experimental procedure for the synthesis of core shell PCL- mZnO NPs by using template mZnO NPs followed by mesoporous PCL NCs by template removing approach has been mentioned here. The detail of the chemicals, reagents and solvents has been included in **Chapter 2**. However, a brief of the same has been summarized below.

#### **(a) The synthesis method of mesoporous ZnO NCs**

The detail synthesis procedure of mZnO NC has been described in **Part II (Section A)** by a surfactant free ultrasonication technique. The synthesized mesoporous ZnO NCs were used as template for the further development of core shell nanostructure in this work.

### **(b) Synthesis of core shell PCL-mZnO (PZ) NCs**

For the synthesis of core shell structure, firstly 50mg of synthesized mZnO was thoroughly dispersed in 20mL acetone through ultra-sonication. Then 50mg PCL was dissolved in 20mL acetone at 45°C under constant stirring. Thereafter, dispersed mZnO and dissolved PCL were mixed together in another beaker.

Then the resultant mixture of mZnO NPs and PCL were added continuously to 150mL (water/surfactant) emulsion under sonication at a constant rate of 150 $\mu$ L.min<sup>-1</sup>. After addition, the mixture was kept under vigorous stirring for 24h. The resultant core shell NPs formed consisted of mZnO as core and PCL formed the outer shell layer. Later these particles was washed with water and isopropanol. The final product was collected after repeated washing and centrifugation (at 5000 RPM) followed by drying through lyophilization.

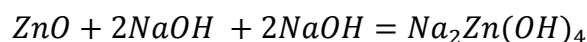
### **(c) Etching of core from core shell NCs:**

Above synthesized core-shell PCL-mZnO NPs were treated with NaOH (5M) and incubated in the same for 6h to etch out the mZnO and which leaving the porous polymeric shell. After 6h of incubation in 5M NaOH at room temperature, the etched core-shell NPs were then centrifuged to separate the particles from the solution and repeated washing was done to remove the dissolved mZnO/ NaOH. Finally, mesoporous PCL capsules were collected after freeze drying.

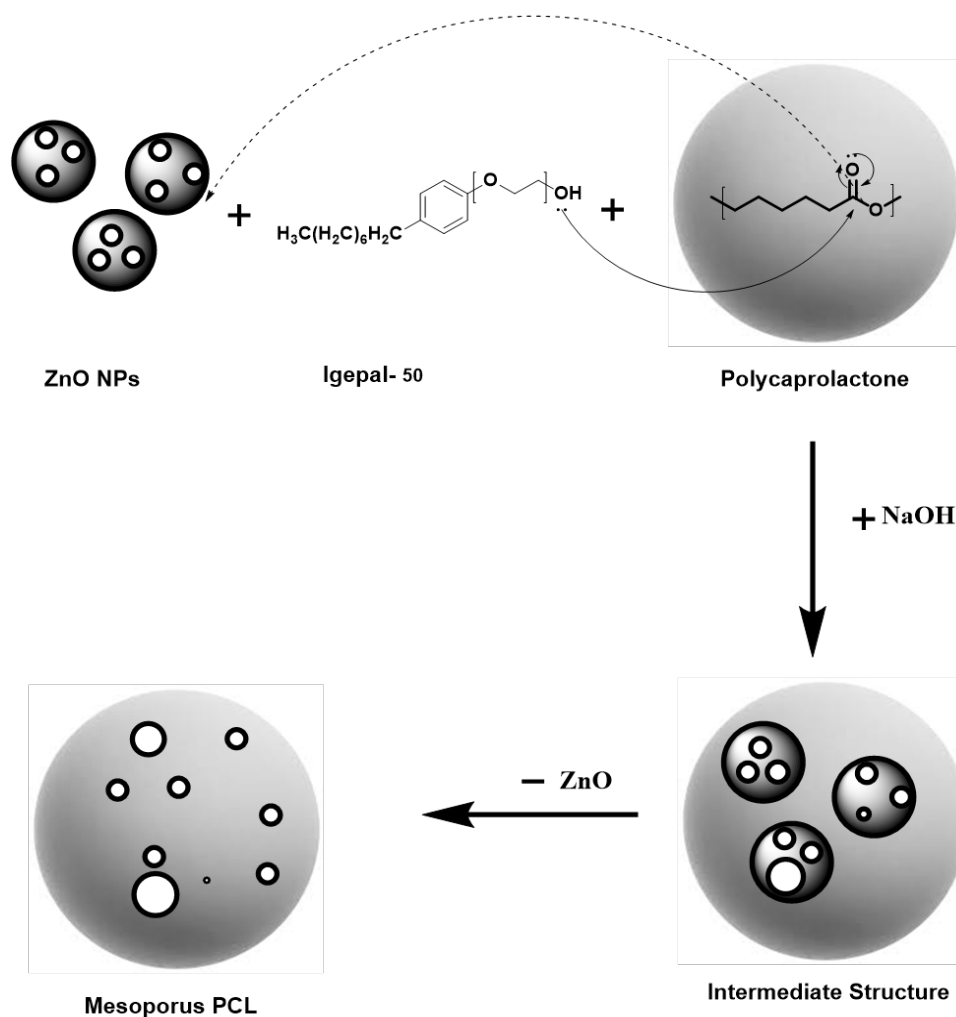
### **3.3.3. Mechanism of formation of porous PCL NCs**

During the synthesis of core shell PCL-mZnO NPs, Igepal-50 has been used as a surfactant. In the first step, the oxygen of Igepal-50 provides its pair of electrons to the electron deficient carbonyl of PCL. Various other electronic transfer has occurred with other ionic interaction for the completion of synthesis of core shell PCL-mZnO structure. Covalent interaction, van der Waal's forces of interactions etc., may have involved in the whole synthesis procedure. In the following step, to remove core mZnO from the core shell PCL-mZnO NPs, 5M NaOH was added and thereby making a porous nanostructure. Water has acted as a solvent medium in this synthesis process, resulting in a possibility to form  $Na_2Zn(OH)_4$  which will go out with water and thus PCL shell with porous structure will appear.

The proposed chemical reaction of ZnO with NaOH in aqueous medium has given below,



After repeated centrifugation at 10000RPM for 10min each, the formed  $\text{Na}_2\text{Zn}(\text{OH})_4$  has been removed completely from the PCL polymer surface leaving behind some pores in the polymer nanostructures.



**Schematic 3.3.1.** Step by step synthesis mechanism of core shells PCL-mZnO NPs and mesoporous PCL NCs after removal of core mZnO NPs In first step, PCL polymer have attached to the mesoporous ZnO NPs with the help of surfactant Igepal-50, and made the core shell structure. In the next step, NaOH was added to remove the template ZnO and finally ZnO NPs will go out leaving behind a porous polymeric nanostructure.

### 3.3.4. Designing mesoporous PCL NCs: Size, Morphology and porous structure of NCs

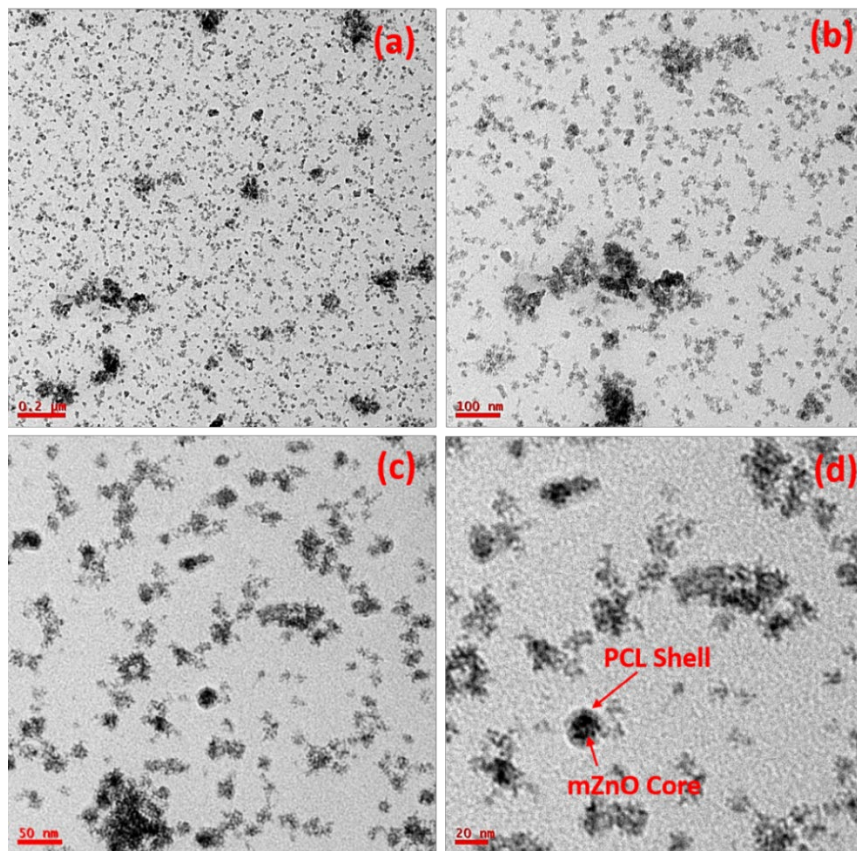


*Figure 3.3.1. TEM images of core shell PCL- mZnO NPs (PZ) from lower to higher magnifications (a-d).*

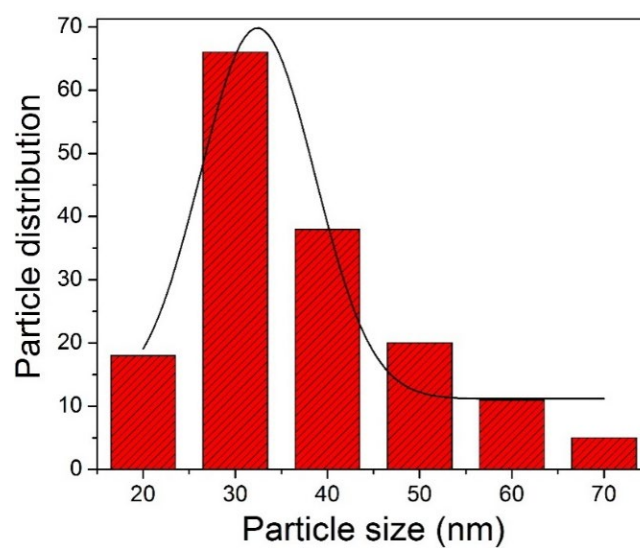


*Figure 3.3.2. Histogram for the average particle size distribution of core shell PCL-mZnO NPs (PZ), calculated from HRTEM results (Figure 3.3.1a).*

**Figure 3.3.1(a-d)** represents the TEM micrographs of synthesized core shell PCL-mZnO NPs (PZ). The NPs formed are spherical in nature and uniformly dispersed. Thus, from the size of the core, it can be assured that one to two mZnO NPs have aggregated to form the core and PCL polymer chains have surrounded them to form the shell.

**Figure 3.3.2** shows the average particle size and its distribution of sample PZ where the average size of PZ is calculated to be 32nm in dia. To calculate average particle size different sizes of PZ have been measured by using HRTEM micrographs from **Figure 3.3.1(a)**.

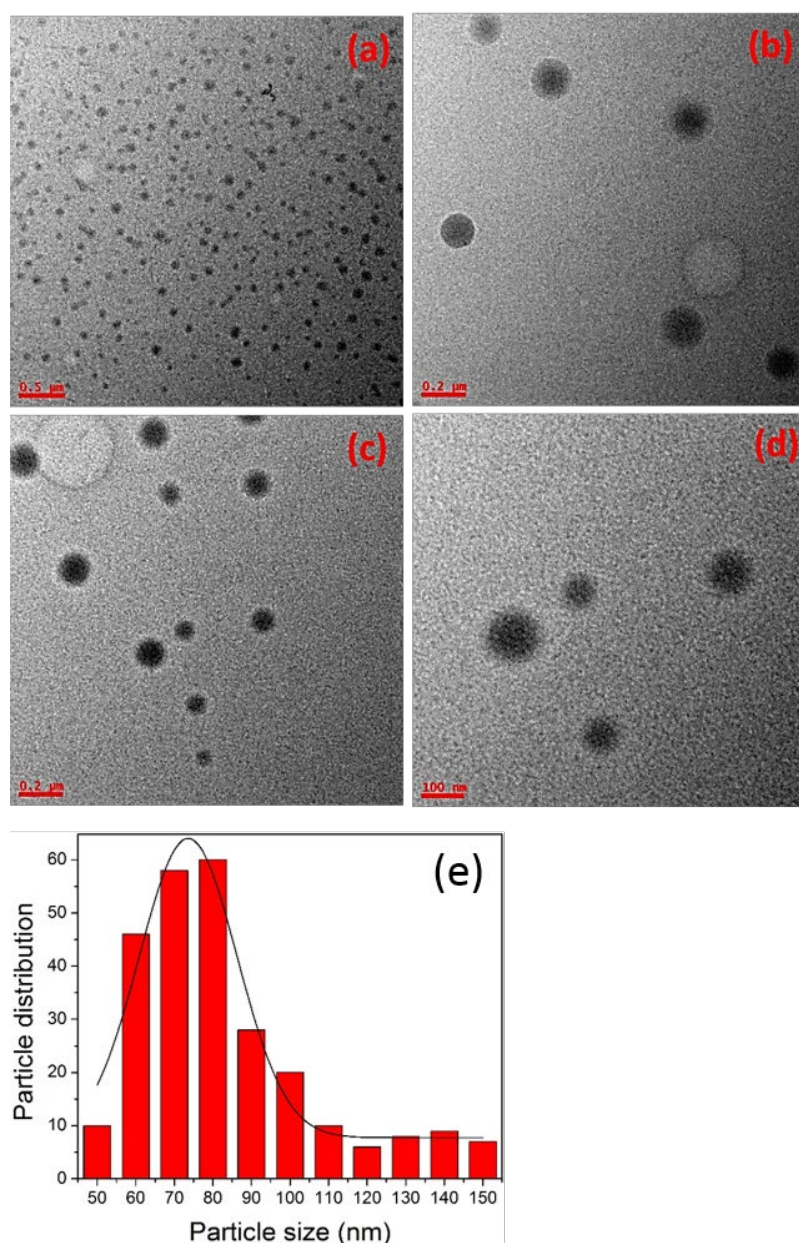


**Figure 3.3.3.** TEM images of hollow porous PCL NCs (HPZ) (a-d) from lower to higher magnifications and (e) average particle size distribution of HPZ calculated from the TEM micrograph (**Figure 3.3.3a**).

**Figure 3.3.3** showed the TEM micrographs of porous PCL NCs (HPZ) after the removal of template mZnO from the core of PCL-mZnO (PZ). From the TEM images, it can be seen that the particles are spherical and uniformly dispersed. From **Figure 3.3.3e** the average size of this HPZ are found to be around  $\sim 75\text{nm}$  in diameter which has been calculated from the HRTEM micrograph **Figure 3.3.3a**.

### 3.3.5. Surface chemical structure of PCL-mZnO and mesoporous PCL NCs

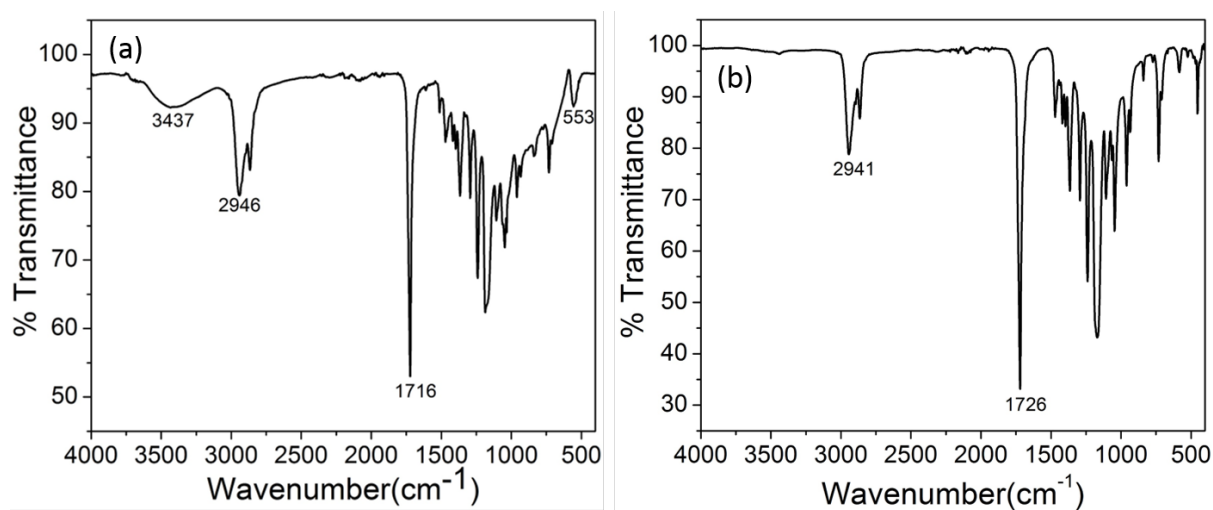


**Figure 3.3.4.** FTIR spectra of (a) PCL-mZnO core shell (PZ) NPs and (b) porous PCL (HPZ) NCs. FTIR experiments were performed on KBr pallet.

**Figure 3.3.4a** and **3.3.4b** shows the FTIR spectra for core shell PCL-mZnO and porous PCL after removal of core mZnO NCs, respectively. In **Figure 3.3.4a**, the band at  $3437\text{cm}^{-1}$  arises for stretching vibration mode of a hydroxyl group present on the sample surface of mZnO. The band at  $2946\text{cm}^{-1}$  arises for C-H(-CH<sub>2</sub>) group of PCL polymer and the band arises at  $1716\text{cm}^{-1}$  is due to the presence of -C=O group of polymer PCL [201]. At  $553\text{cm}^{-1}$ , the band arises due to the vibration mode of Zn and O bond in ZnO lattice [225,226]. Bands are overlapping in the region from  $1500\text{cm}^{-1}$  to  $750\text{cm}^{-1}$  due to the polymer coating over mZnO. The FTIR spectrum has suggested the presence of polymer PCL on the surface of mZnO NPs and thus confirmed the formation of core shell PCL-mZnO NPs. The absence of any other additional bands in the FTIR spectrum proves that the synthesised mZnO-PCL NCs are free from impurities.

**Figure 3.3.4b** show the FTIR spectrum of PCL NCs after etching the core mZnO. The band at  $2941\text{cm}^{-1}$  arises for C-H(-CH<sub>2</sub>) group of PCL and band arises at  $1726\text{cm}^{-1}$  is due to the presence of -C=O group of PCL [201]. The absence of bands responsible for mZnO proves that the template (mZnO) have been removed from the core completely and the absence of additional bands confirm the absence of impurities or the other component of Zn (II) in the PCL nanostructure.

### 3.3.6. BET surface area analysis of porous PCL NCs

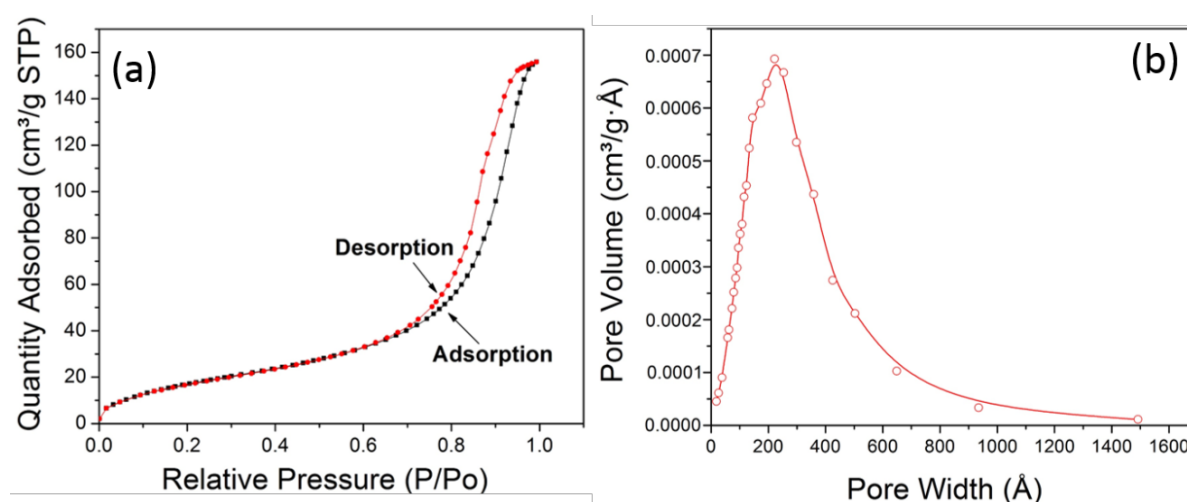


**Figure 3.3.5.** BET results (a)  $N_2$  adsorption-desorption isotherm of porous PCL NCs with (b) BJH pore size distribution from adsorption isotherm.

BET experiment was executed for the synthesized HPZ nanomaterials to further investigation of the pore size which has already been observed from the TEM micrographs and to calculate the specific surface area of the nanomaterial. **Figure 3.3.5a** and **3.3.5b** demonstrate the Nitrogen adsorption-desorption isotherm as well as pore size distribution of HPZ NCs, respectively. In **Figure 3.3.5a** the clear hysteresis loop (from relative pressure  $P/P_0$  0.7 to 0.99) is observed, which confirms the porous nature of the nanomaterial with a type-IV adsorption isotherm. BET surface area for porous HPZ NCs has calculated as  $68.67\text{m}^2/\text{g}$  at relative pressure  $P/P_0 = 0.283$  and adsorption average pore size achieved as  $22.1\text{nm}$  from the **Figure 3.3.5b**. Whereas, Langmuir surface area for the same nanomaterial was found out as  $109.29\text{m}^2/\text{g}$ .

### 3.3.7. Phase, solid state crystal structure study and zeta potential analysis

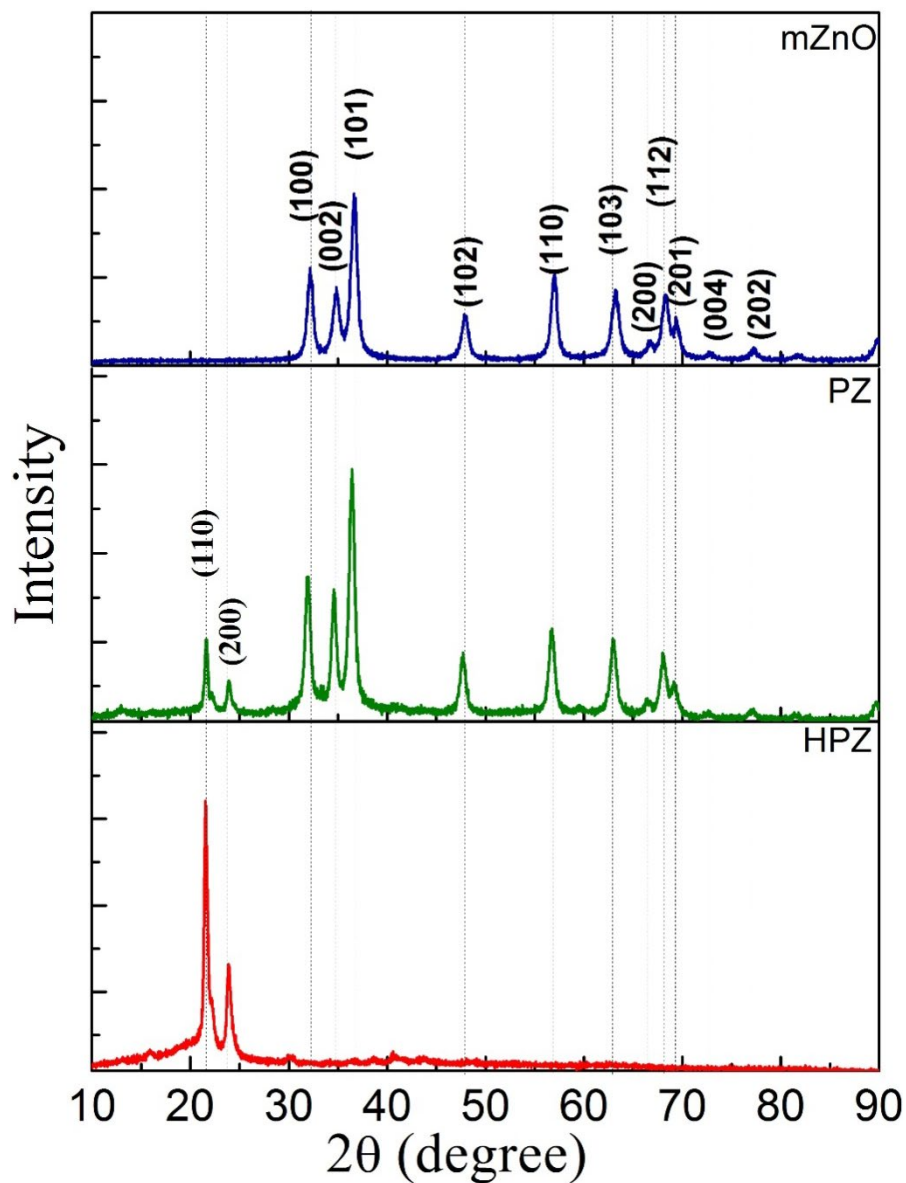


**Figure 3.3.6.** XRD pattern of *mZnO*, PCL-*mZnO* (PZ) and porous PCL NCs.

The solid-state crystal structure of the nanomaterials has been characterized through the powder XRD and the diffraction pattern has shown in *Figure 3.3.6*. *mZnO* NCs are found to have hexagonal crystal structure with characteristic diffraction peaks appeared at  $2\theta = 32.2^\circ$ ,  $34.6^\circ$ ,  $36.6^\circ$ ,  $47.9^\circ$ ,  $57.1^\circ$ ,  $63.1^\circ$ ,  $66.8^\circ$ ,  $68.4^\circ$ ,  $69.6^\circ$ ,  $72.8^\circ$ ,  $77.3^\circ$  and  $81.8^\circ$  for the corresponding preferred orientation of planes such as (100), (002), (101), (102), (110), (103), (200), (112), (201), (004) and (202), respectively. The crystal structure corresponds to the phase pure Wurtzite-type ZnO (hexagonal phase with space group  $P6_3mc$ , JCPDS card no. 36-

1451, *a* polar axis parallel to *c*-axis). XRD pattern of core shell sample PZ is found matching well with all diffraction peaks of mZnO along with some additional peaks arise at  $2\theta = 21.4^\circ$  and  $23.0^\circ$ , which corresponds to the orthorhombic planes (110) and (200) of PCL polymer, respectively. Thus the XRD pattern proves that PZ contains both mZnO (as core) and PCL (as shell). XRD pattern of HPZ sample showed the diffraction peaks only at  $2\theta = 21.4^\circ$  and  $23.0^\circ$ , corresponding to the orthorhombic crystal structure with characteristic planes (110) and (200) of PCL, respectively [205,206]. These results are the evidence for the absence of mZnO in PCL capsules.

To check the zeta potential value of mesoporous PCL (HPZ), 500 $\mu$ g of the sample has been dispersed in 1mL of DI water. The value has been recorded at temperature 25°C by using a He-Ne LASER with a wavelength of 633nm. **Figure 3.3.7**, showed the zeta potential value of mesoporous PCL capsules which has been found as  $-29.9$  mV and standard deviation  $\pm 6.45$  (single peak).

**Table 1:** Zeta potential of mesoporous PCL NCs

	Mean (mV)	Area (%)	St Dev (mV)
<b>Zeta Potential (mV):</b> -29.9	<b>Peak 1:</b> -29.9	100.0	6.45
<b>Zeta Deviation (mV):</b> 6.45	<b>Peak 2:</b> 0.00	0.0	0.00
<b>Conductivity (mS/cm):</b> 0.00965	<b>Peak 3:</b> 0.00	0.0	0.00
<b>Result quality :</b> Good			

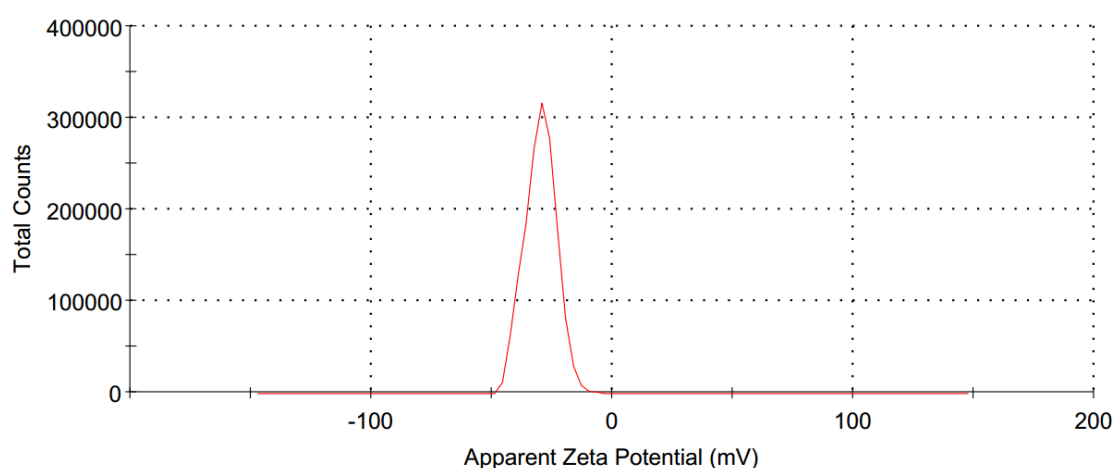


**Figure 3.3.7.** Zeta potential of mesoporous PCL NCs recorded at 25°C in DI water.

### 3.3.8. Loading of anticancer drug Paclitaxel in mesoporous PCL NCs

The dried mesoporous PCL NCs were collected and loaded with an anti-cancer drug, namely 'Paclitaxel'. The mesoporous PCL NCs were incubated with Paclitaxel with a concentration of drug to NCs of 1:1 mg.mL<sup>-1</sup> in PBS (pH 7.4). The drug loaded NC and PBS mixture were stirred for 1h and then kept for another 24h in a dark place without stirring at room temperature. The paclitaxel loaded mesoporous PCL NCs were separated from PBS solution through centrifugation (at 8000RPM). These loaded particles were then washed three times with PBS to remove the excess free drug molecules from the surface of the NCs followed by air drying (at room temperature) for the further experiments. The whole drug loading process has been done at room temperature.

### 3.3.9. Time dependent drug release behavior of anticancer drug from core shell PCL-mZnO (PZ) and porous PCL (HPZ) NCs

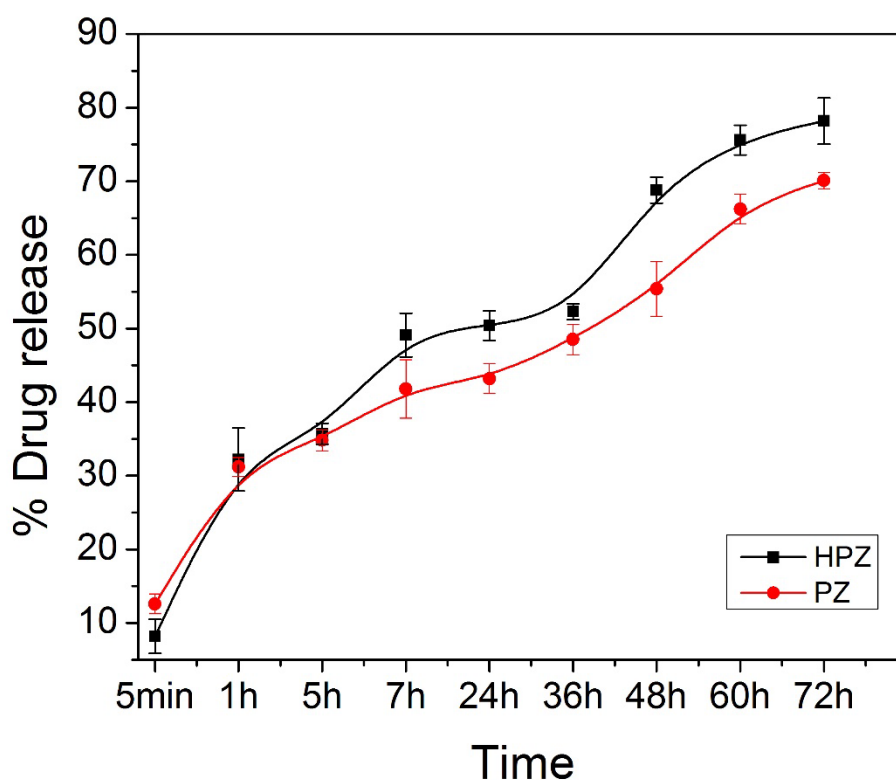


**Figure 3.3.8.** The release profile of Paclitaxel from PCL-mZnO (PZ) and mesoporous PCL NCs at 25°C temperatures for 72h in RPMI 1640 medium.

0.5mg of anticancer drug loaded NCs were suspended in RPMI 1640 medium in two different cuvettes for two different experiments and the drug release behavior of Paclitaxel drug loaded NCs have been studied by maintaining a time interval for 3 days at room temperature (25°C). **Figure 3.3.8** shows the drug release profiles of anticancer drug Paclitaxel from core shell nanostructure PZ and mesoporous nanostructure HPZ NCs, respectively. The absorbance of the released drugs in the medium was recorded by using UV-Vis spectrometer and the extent of release of drug Paclitaxel was calculated by considering the absorbance peak at  $\lambda_{\max} = 278\text{nm}$ . The percentage of drug release gradually increased with increase in time. As example, the release amounts of drug molecules calculated as  $12.6 \pm 1.33\%$ ,  $31.2 \pm 1.28\%$ ,  $34.8 \pm 1.43\%$ ,  $41.8 \pm 3.96\%$ ,  $43.2 \pm 2.02\%$ ,  $48.5 \pm 2.09\%$ ,  $55.4 \pm 3.75\%$ ,  $66.2 \pm 2.02\%$ ,  $70.1 \pm 1.13\%$  and  $8.2 \pm 2.33\%$ ,  $32.2 \pm 4.28\%$ ,  $35.7 \pm 1.43\%$ ,  $49.1 \pm 2.96\%$ ,  $50.4 \pm 2.02\%$ ,  $52.3 \pm 1.09\%$ ,  $68.8 \pm 1.75\%$ ,  $75.6 \pm 2.02\%$ ,  $78.2 \pm 3.13\%$  on time periods of 5min, 1h, 5h, 7h, 24h, 36h, 48h, 60h, 72h for PZ and HPZ, respectively.

The Paclitaxel drug encapsulation efficiencies for PZ-Paclitaxel and HPZ-Paclitaxel NCs have been calculated by using [% Entrapment efficiency = (weight of drug in NPs/weight of drug fed initially)  $\times 100$ ] (**eq. 2**) mentioned in **Part II (Section A)** as 38.6%, and 71.8%, respectively.

### **3.3.10. Biocompatibility of core shell PCL-mZnO (PZ) studied with two breast cancer cell lines**

The biocompatibility of pure PCL-mZnO (PZ) NPs without loading any drug have been investigated by exposing them against two breast cancer cell lines, e.g., MCF 7 and MDA-MB-231 through MTT assay. The cell viability of the porous NCs facilitated transfection is under the effect of the cytotoxicity affected by the chemical nature of the NPs as well as transfection reagent. To check the cell cytotoxicity of unloaded PZ NPs with both cancer cell lines,  $5 \times 10^3$  number of MCF 7 cells and MDAMB-231 cells were taken separately in each well of the 96 well plate. MTT assay has been conducted after 24h post transfection at 37°C by taking various concentrations of NCs like  $1000\mu\text{g.mL}^{-1}$ ,  $500\mu\text{g.mL}^{-1}$ ,  $250\mu\text{g.mL}^{-1}$ ,  $125\mu\text{g.mL}^{-1}$ ,  $62.5\mu\text{g.mL}^{-1}$ ,  $31.25\mu\text{g.mL}^{-1}$ ,  $15.67\mu\text{g.mL}^{-1}$  and  $7.84\mu\text{g.mL}^{-1}$ , where considering pure cell line without any drug and NCs as control (100%) for both cell lines MCF 7 and MDA-MB-231.

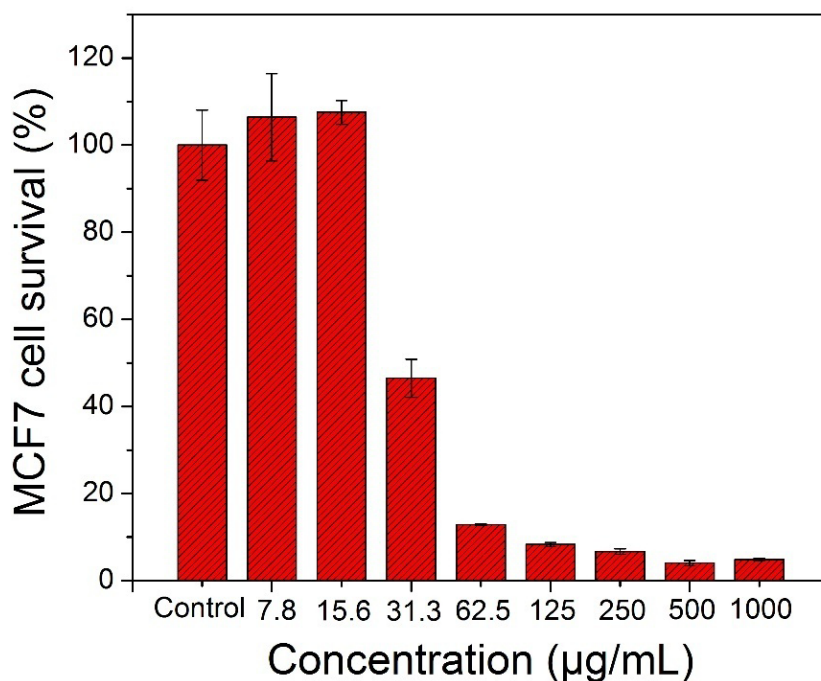


**Figure 3.3.9.** Percentage of cell survival analyzed by MTT assay, while PCL-mZnO (PZ) NCs were incubated with MCF 7 cell line at 37°C for 24h. For this experiment calculated  $IC_{50}$  value is  $35.49 (\pm 0.25) nM$ .

It can be observed from **Figure 3.3.9** and **Figure 3.3.10** that in case of PZ sample, with a lower concentration of NPs i.e.,  $7.84 \mu g \cdot mL^{-1}$  and  $15.67 \mu g \cdot mL^{-1}$ , are also able to kill both malignant cells MCF 7 and MDAMB-231. Percentage of cell survival are  $106.39 \pm 5.1\%$  and  $94.26 \pm 1.7\%$  for minimum concentration  $7.84 \mu g \cdot mL^{-1}$  of PZ sample as well as  $4.87 \pm 0.23\%$  and  $5.98 \pm 2.7\%$  for highest concentration  $1000 \mu g \cdot mL^{-1}$  of PZ sample for both cell lines MCF 7 and MDA-MB-231, respectively. This has occurred due to the presence of mZnO in the core shell structure of the PCL-mZnO (PZ) NPs.

The toxicity of the unloaded bare PZ NPs is increasing from lower to higher concentrations (i.e., from  $7.8 \mu g \cdot mL^{-1}$  to  $1000 \mu g \cdot mL^{-1}$ ) for both the cancer cell lines, e.g., for MCF 7 and MDAMB-231. **Figure 3.3.11** shows the microscopic images of MDA-MB-231 cell lines with higher ( $1000 \mu g \cdot mL^{-1}$ ) to lower ( $7.8 \mu g \cdot mL^{-1}$ ) concentrations of PZ. It is observed from the microscopic images that, with an increase of PZ concentration level in a MDAMB-231 cell line, the number of cancer cells decreased and the structure of cancer cells deformed gradually. These microscopic images have been captured by using optical microscope Model Olympus CKX41 (10X).

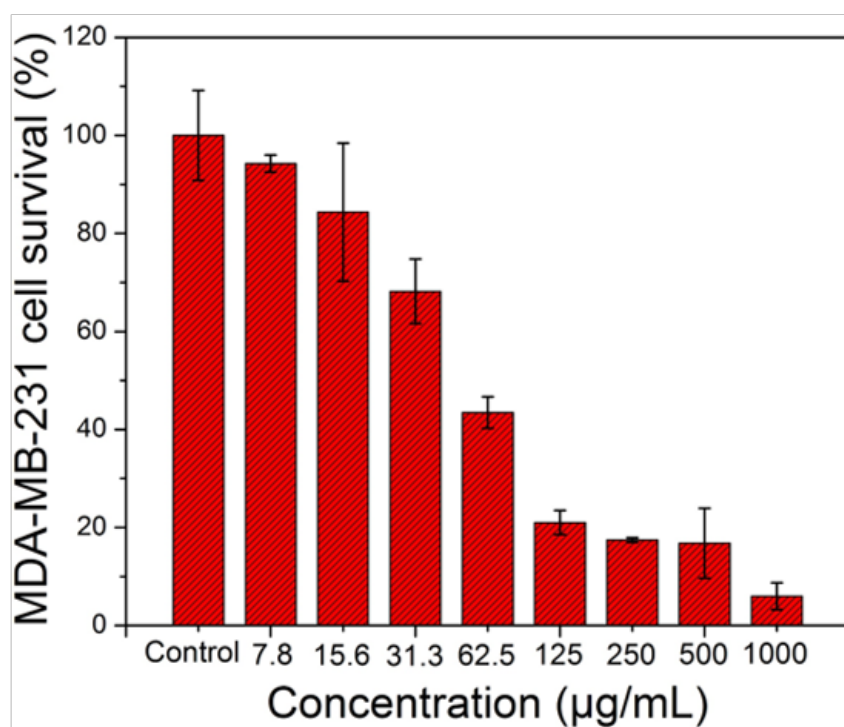


**Figure 3.3.10.** Percentage of cell survival analyzed by MTT assay while PCL-mZnO (PZ) NCs were incubated with MDA-MB-231 cell line at 37°C for 24h. For this experiment calculated  $IC_{50}$  value is 32.8 ( $\pm 0.29$ ) nM.

Furthermore, the  $IC_{50}$  value has been calculated for the PZ NCs on both cell lines MCF7 and MDA-MB-231 and the values are found as 35.49( $\pm 0.25$ )nM for MCF 7 and 32.8( $\pm 0.29$ )nM for MDA-MB-231 which are more or less similar to the  $IC_{50}$  values of free anticancer drug Paclitaxel on these two malignant cell lines (free Paclitaxel on MCF7 is 31.9 ( $\pm 1.3$ )nM and MDA-MB-231 is 37.52( $\pm 1.8$ )nM).

Thus, it has been confirmed that the synthesized PCL-mZnO (PZ) nanocapsules can be used as an anticancer drugs carrier against cancer cells due to their constant toxicity against cancer cells.

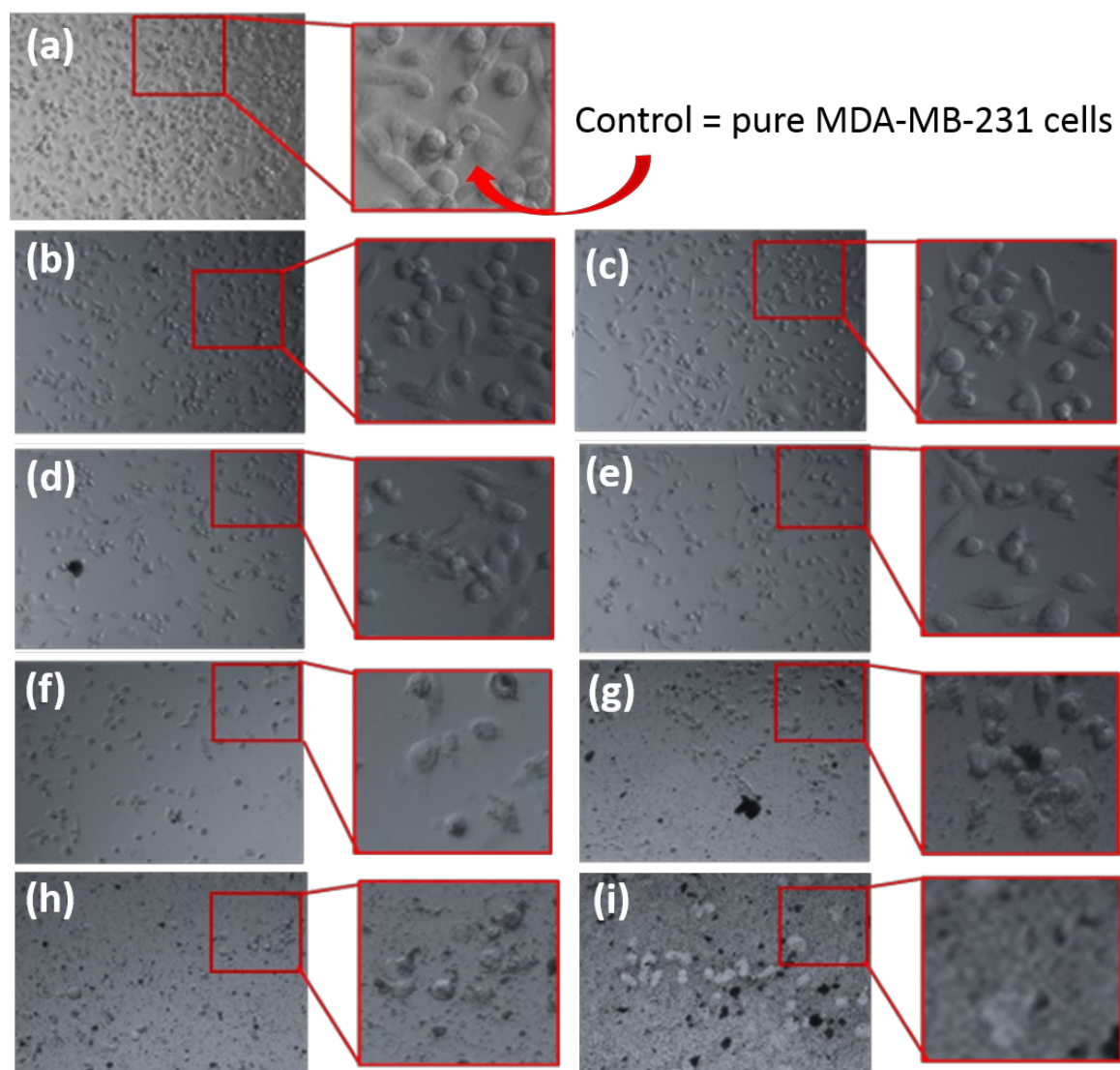


**Figure 3.3.11.** Microscopic images of the MDA-MB-231 cancer cells after incubation with increasing concentration of PZ at 37°C for 24h (a) Control (100% cell survival), (b)  $7.837\mu\text{g.mL}^{-1}$ , (c)  $15.67\mu\text{g.mL}^{-1}$ , (d)  $31.25\mu\text{g.mL}^{-1}$ , (e)  $62.5\mu\text{g.mL}^{-1}$ , (f)  $125\mu\text{g.mL}^{-1}$ , (g)  $250\mu\text{g.mL}^{-1}$ , (h)  $500\mu\text{g.mL}^{-1}$ , (i)  $1000\mu\text{g.mL}^{-1}$ .

### 3.3.11. Biocompatibility of mesoporous PCL (HPZ) NCs studied with two breast cancer cell lines

The interaction of bare PCL (HPZ) NCs without loading drug against two breast cancer cell lines MCF 7 and MDA-MB-231 has been investigated by exposing unloaded NCs to the cancer cell lines through MTT assay. The cell viability of the porous NCs facilitated transfection is under the effect of the cytotoxicity affected by the chemical nature of the NPs

as well as transfection reagent. To check the cell cytotoxicity of unloaded HPZ NCs two cancer cell lines MCF 7 cells and MDA-MB-231 of  $5 \times 10^3$  number were taken in each well of the 96-well plate. MTT assays were conducted after 24h post transfection at  $37^\circ\text{C}$  by taking various concentrations of NCs e.g.,  $1000\mu\text{g.mL}^{-1}$ ,  $500\mu\text{g.mL}^{-1}$ ,  $250\mu\text{g.mL}^{-1}$ ,  $125\mu\text{g.mL}^{-1}$ ,  $62.5\mu\text{g.mL}^{-1}$ ,  $31.25\mu\text{g.mL}^{-1}$ ,  $15.67\mu\text{g.mL}^{-1}$  and  $7.84\mu\text{g.mL}^{-1}$ , where considering pure cell line without any drug and NCs as control (100%) for both the cell lines MCF 7 and MDA-MB-231.

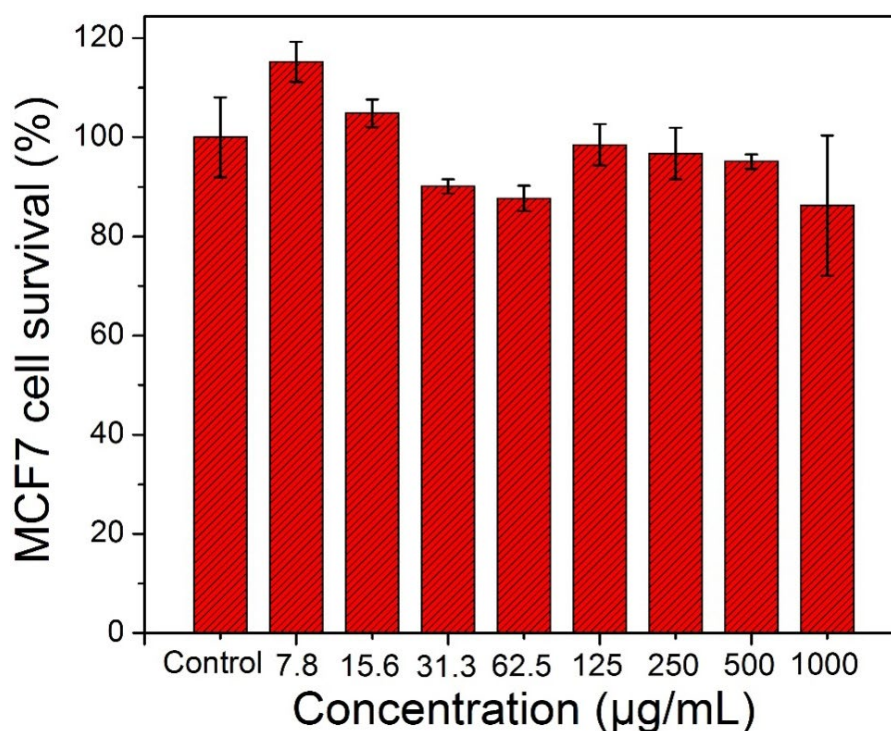


**Figure 3.3.12.** Percentage of cell survival analyzed by MTT assay while mesoporous PCL NCs were incubated with MCF 7 cell line at  $37^\circ\text{C}$  for 24h. For this experiment calculated  $IC_{50}$  value is  $52(\pm 1.0)\text{nM}$ .

It can be observed from **Figure 3.3.12** and **Figure 3.3.13** that for HPZ sample, at various concentrations i.e., from  $7.837\mu\text{g.mL}^{-1}$  to  $1000\mu\text{g.mL}^{-1}$  the cancer cell death (MCF 7 and MDA-MB-231) is less compared to the cell death occurred in case of PZ sample. Since mZnO is toxic towards the cancer cells [227] and that is the reason behind the death of more cancer cells in case of PZ as mZnO formed the core of PZ nanostructure. Again, the core mZnO were removed from the HPZ nanostructure, therefore, the percentage of cancer cell survival is more in case of HPZ compared to PZ sample.

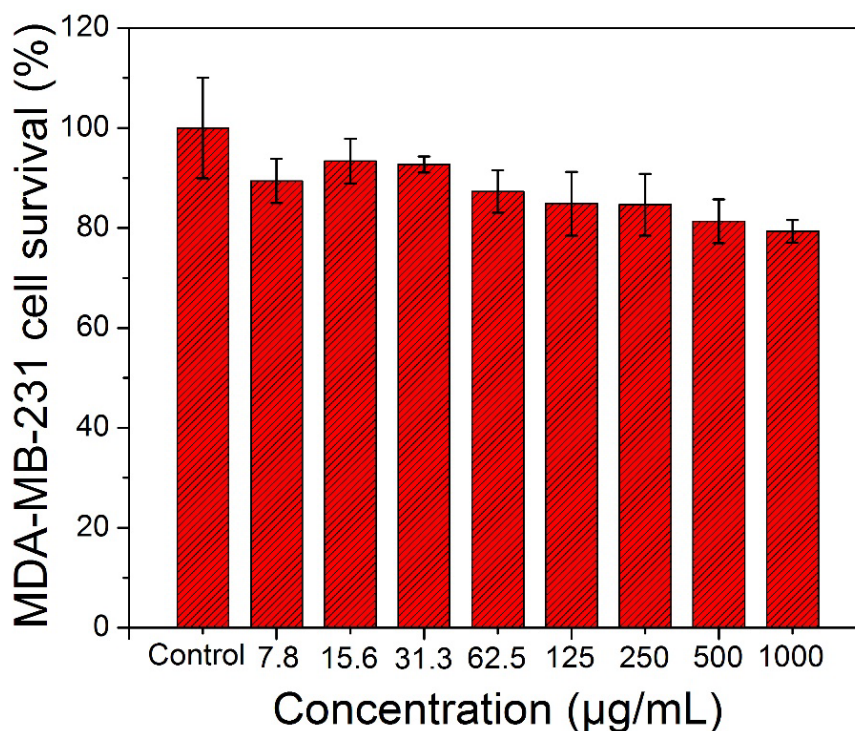


**Figure 3.3.13.** Percentage of cell survival analysed by MTT assay while mesoporous PCL NCs (HPZ) were incubated with MDA-MB-231 cell line at 37°C for 24h. For this experiment calculated  $IC_{50}$  value is  $55 (\pm 1.05)$  nM.

From **Figure 3.3.12** and **Figure 3.3.13**, it is clear that percentage of cell survival is more or less the same as the control sample (100% cell survival). At the concentration of  $7.8 \mu\text{g.mL}^{-1}$  cell survival results are found to be  $115.22 \pm 4.06$  % and  $89.40 \pm 4.42$  % as well as at  $1000 \mu\text{g.mL}^{-1}$  cell survival results found to be  $86.24 \pm 14.15$  % and  $79.34 \pm 2.25$  % for MCF 7 and MDA-MB-231 cell lines, respectively.

However, **Figure 3.3.14** showed the optical microscopic images of MDA-MB-231 cells with each increasing concentration of HPZ (0 -  $1000 \mu\text{g.mL}^{-1}$ ). It can be observed from those optical microscopic images (**Figure 3.3.14**), that interaction of different concentrations of HPZ with the malignant cells are not effecting much to the structures of the malignant cells even after 24h of incubation. Thus, these mesoporous PCL (HPZ) capsules are biocompatible in nature.

The biocompatibility of these HPZ NCs were again proved with the  $IC_{50}$  values which have been found as  $52 (\pm 1.0)$  nM for HPZ on MCF 7 and  $55 (\pm 1.05)$  nM for HPZ on MDA-MB-231 which are more than the  $IC_{50}$  values of free anticancer drug Paclitaxel on these two malignant cell lines (free Paclitaxel on MCF 7 is 31.9 nM and MDA-MB-231 is 37.52 nM).

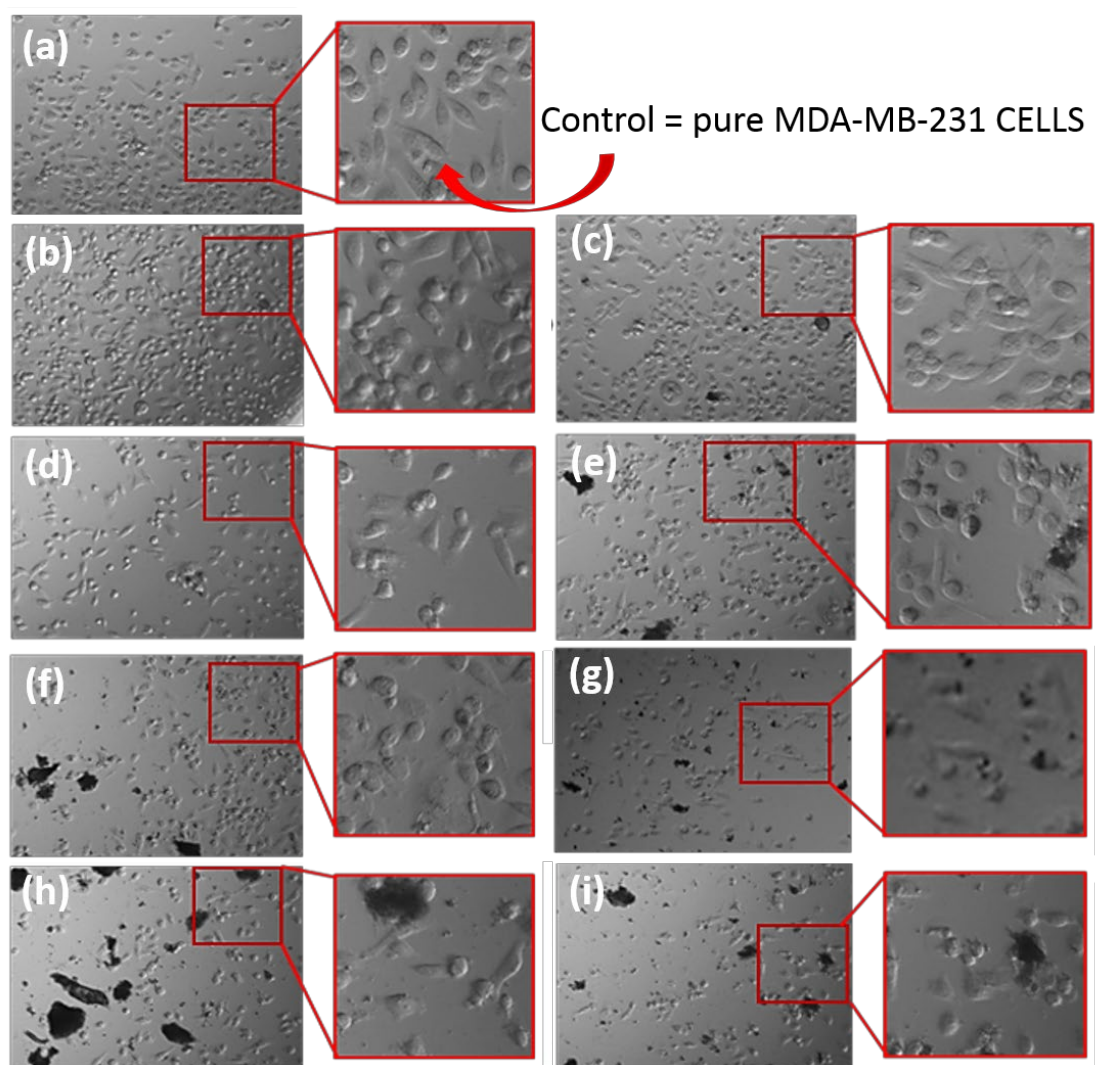


**Figure 14.** Microscopic images of the MDA-MB-231 cancer cells after incubation with increasing concentration of HPZ at 37°C for 24h (a) Control (100% cell survival), (b) 7.837  $\mu\text{g.mL}^{-1}$ , (c) 15.67  $\mu\text{g.mL}^{-1}$ , (d) 31.25  $\mu\text{g.mL}^{-1}$ , (e) 62.5  $\mu\text{g.mL}^{-1}$ , (f) 125  $\mu\text{g.mL}^{-1}$ , (g) 250  $\mu\text{g.mL}^{-1}$ , (h) 500  $\mu\text{g.mL}^{-1}$ , (i) 1000  $\mu\text{g.mL}^{-1}$ .

### 3.3.12. Interaction of free Paclitaxel with Cancer cell lines MCF 7 and MDA-MB-231

Finally, different increasing concentrations of anticancer drug Paclitaxel incubated with both cancer cell lines MCF 7 and MDA-MB-231 and the percentage of cell survival in both cases have been studied. From **Figure 3.3.15** and **Figure 3.3.16**, it can be seen that the percentage of cell survival decreases gradually as the concentration of the drug increases from 1.95  $\mu\text{g.mL}^{-1}$  to 250  $\mu\text{g.mL}^{-1}$ . **Figure 3.3.17** showed the optical microscopic images of the

MDA-MB-231 cells with increasing concentrations of Paclitaxel from  $1.95\mu\text{g.mL}^{-1}$  to  $250\mu\text{g.mL}^{-1}$ . Furthermore, the  $\text{IC}_{50}$  value has been calculated for free Paclitaxel on both cell lines MCF 7 and MDA-MB-231 and the values are found as  $31.9 (\pm 1.3)$  nM for MCF 7 and  $37.52 (\pm 1.8)$  nM for MDA-MB-231.

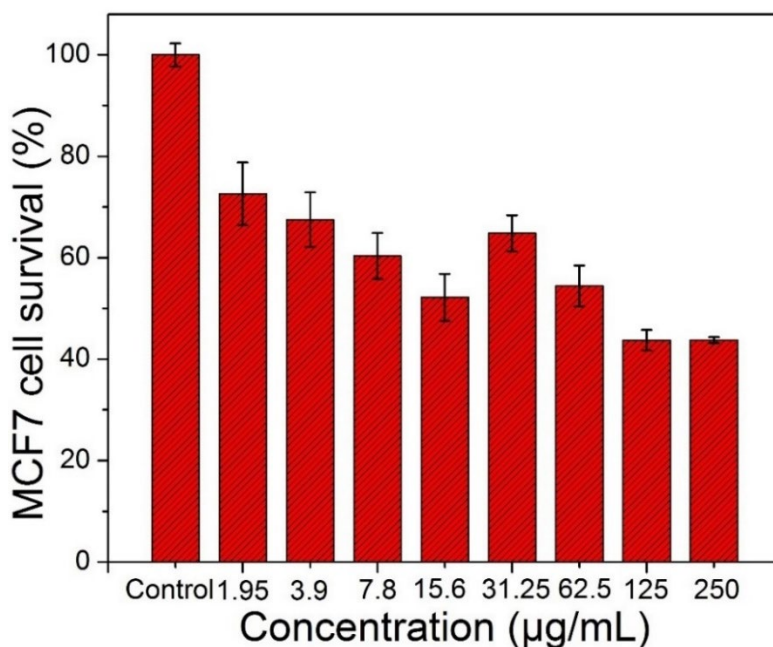


**Figure 3.3.15.** Percentage cell survival of MCF 7 while incubated with pure Paclitaxel drug for 24h at  $37^{\circ}\text{C}$ . For this experiment calculated  $\text{IC}_{50}$  value is  $31.9 (\pm 1.3)$  nM.

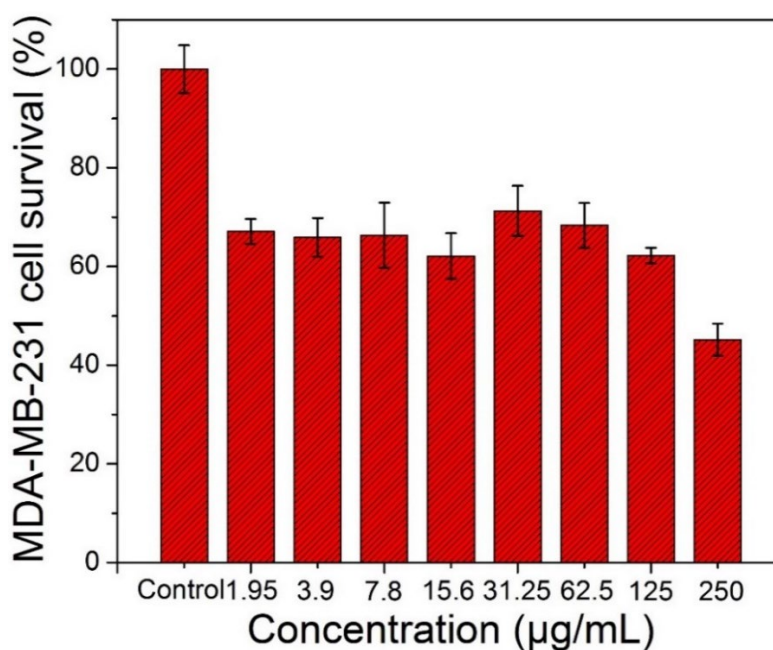


**Figure 3.3.16.** Percentage of cell survival of MDA-MB-231 while incubated with pure Paclitaxel drug for 24h at  $37^{\circ}\text{C}$ . For this experiment the calculated  $\text{IC}_{50}$  value is  $37.52 (\pm 1.8)$  nM.

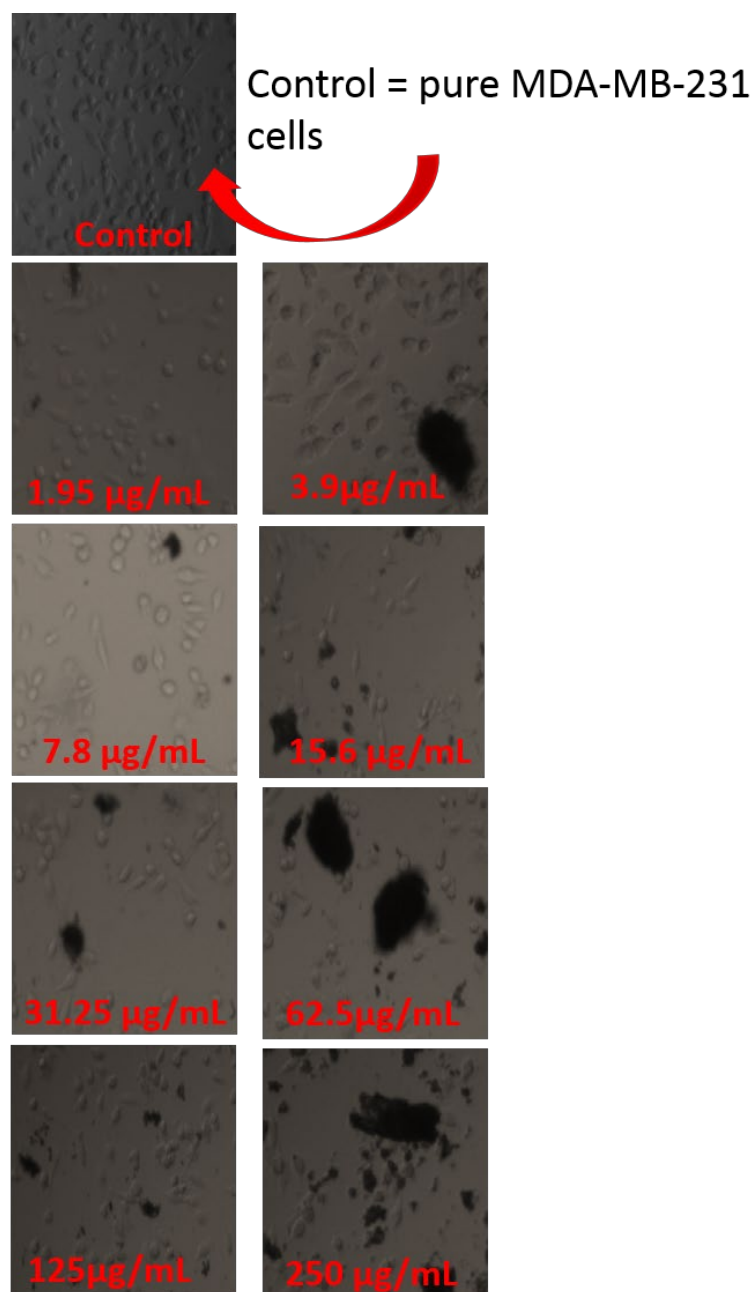


*Figure 3.3.17. Optical microscopic images of MDA-MB-231 cancer cells at different concentrations (1.95-250 µg.mL<sup>-1</sup>) of drug Paclitaxel.*

### **3.3.13. Interaction of Paclitaxel loaded HPZ with Cancer cell lines MCF 7 and MDA-MB-231**

Different concentrations of anticancer drug Paclitaxel i.e., 1.56 µg.mL<sup>-1</sup>, 3.12 µg.mL<sup>-1</sup>, 6.25 µg.mL<sup>-1</sup>, 12.5 µg.mL<sup>-1</sup>, 25 µg.mL<sup>-1</sup>, 50 µg.mL<sup>-1</sup>, 100 µg.mL<sup>-1</sup>, 1000 µg.mL<sup>-1</sup> were loaded in HPZ and incubated with both the cancer cell lines MCF 7 and MDA-MB-231 to check the

percentage of cell survival in both the cases. From **Figure 3.3.18** and **Figure 3.3.19**, it can be observed that with an increase in the concentration of Paclitaxel from  $1.56\mu\text{g.mL}^{-1}$  to  $1000\mu\text{g.mL}^{-1}$  the percentage of cell survival decreases gradually. **Figure 3.3.18**, in case of MCF7, HPZ-Paclitaxel nanoformulations can kill  $70.9\pm 1.5\%$  of cells at concentration  $25\mu\text{g.mL}^{-1}$ , which is more than half of the cells at  $50\mu\text{g.mL}^{-1}$  i.e.,  $25.70\pm 3.18\%$ . At the highest concentration, i.e.,  $1000\mu\text{g.mL}^{-1}$  the NC killed almost all the malignant cells, i.e., and the cell survival found to be only  $4.49\pm 0.36\%$ .

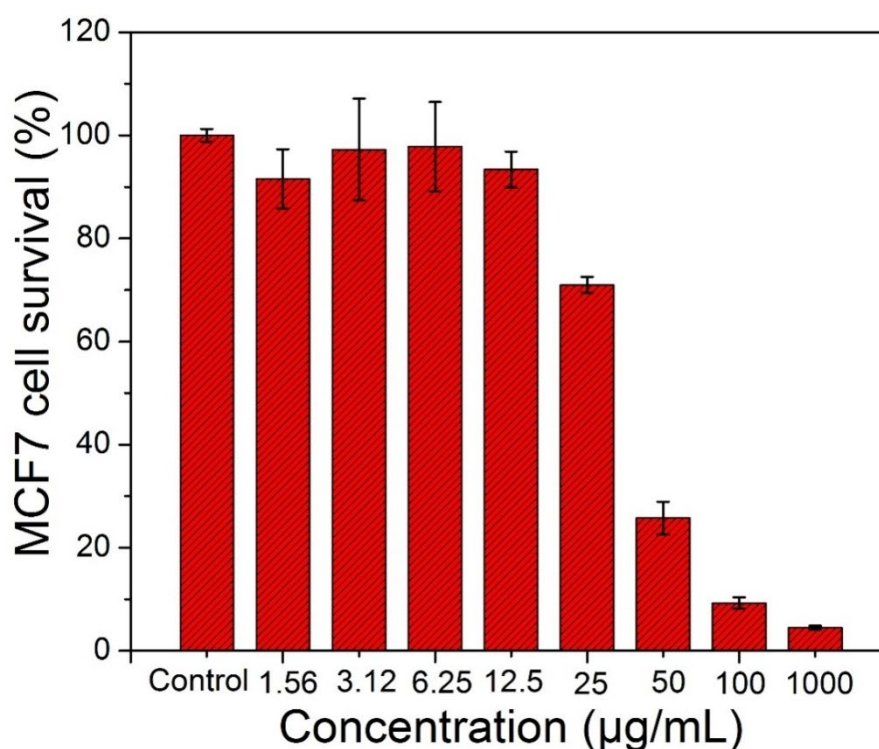


**Figure 3.3.18.** Percentage of cell survival analyzed by MTT assay while HPZ-Paclitaxel nanoformulation incubated with MCF 7 cell line at  $37^\circ\text{C}$  for 24h. The  $\text{IC}_{50}$  value is found in this case as  $33.9(\pm 1.5)\text{nM}$ .

**Figure 3.3.19** shows the treatment of MDA-MB- 231 cells with paclitaxel encapsulated inside HPZ. It is observed that for  $50\mu\text{g.mL}^{-1}$  concentration of HPZ-Paclitaxel formulation,  $43.30\pm 3.5\%$  cancer cells killed and at the highest concentration i.e.,  $1000\mu\text{g.mL}^{-1}$  the same formulation killed  $\sim 93\%$  of cancer cells (survival is only  $6.72\pm 2.90\%$ ). However, **Figure 3.3.20** showed the optical microscopic images of MDA-MB-231 cells with each increasing concentration of paclitaxel ( $0 - 1000\mu\text{g.mL}^{-1}$ ). It can be observed from those optical microscopic images (**Figure 3.3.20**), that interaction of different concentrations of paclitaxel

with the malignant cell are not effecting much to the structures of the malignant cells after 24h of incubation also. These microscopic images have been captured by using optical microscope Model Olympus CKX41 (10X).

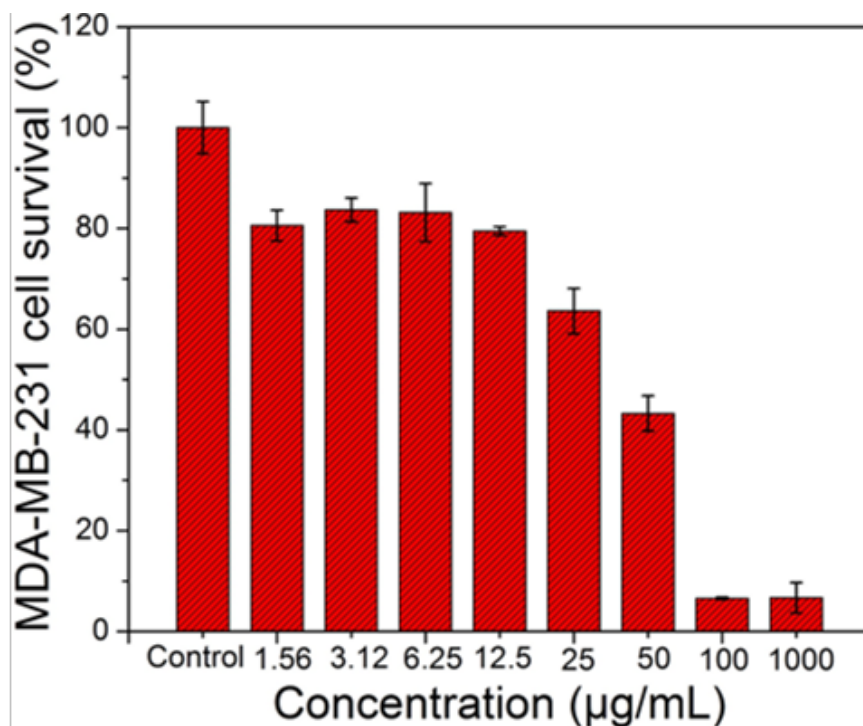


**Figure 3.3.19.** Percentage of cell survival analyzed by MTT assay while HPZ- Paclitaxel nanoformulations were incubated with MDA-MB-231 cell line at 37°C for 24h. The  $IC_{50}$  value is found in this case as  $45.62(\pm 1.86)$ .

Furthermore, the  $IC_{50}$  value has been calculated for the nanoformulated HPZ-Paclitaxel on both cell lines MCF 7 and MDA-MB-231 and the values are found as  $33.9(\pm 1.5)$ nM for MCF 7 and  $45.62(\pm 1.86)$ nM for MDA-MB-231. In the case of nanoformulated HPZ-Paclitaxel on cell line MCF 7, the  $IC_{50}$  is almost matching with the  $IC_{50}$  of free paclitaxel on MCF 7 ( $31.9\pm 1.3$ nM) which proved the efficiency of HPZ as a drug carrier. Whereas, the HPZ-Paclitaxel on cell line MDA-MB-231 gives an  $IC_{50}$  value which is quite high while comparing with free paclitaxel on MDA-MB-231 ( $37.52\pm 1.8$ nM). This increase in  $IC_{50}$  may be due to the stability of drug inside the NC followed by sustained release of drug from the PCL nanodrug carrier. However, the optical microscopic images are evidence of the inhibition ability of these drug encapsulated HPZ NCs against malignant cells and can be used as a vehicle to deliver drug for further biological applications.

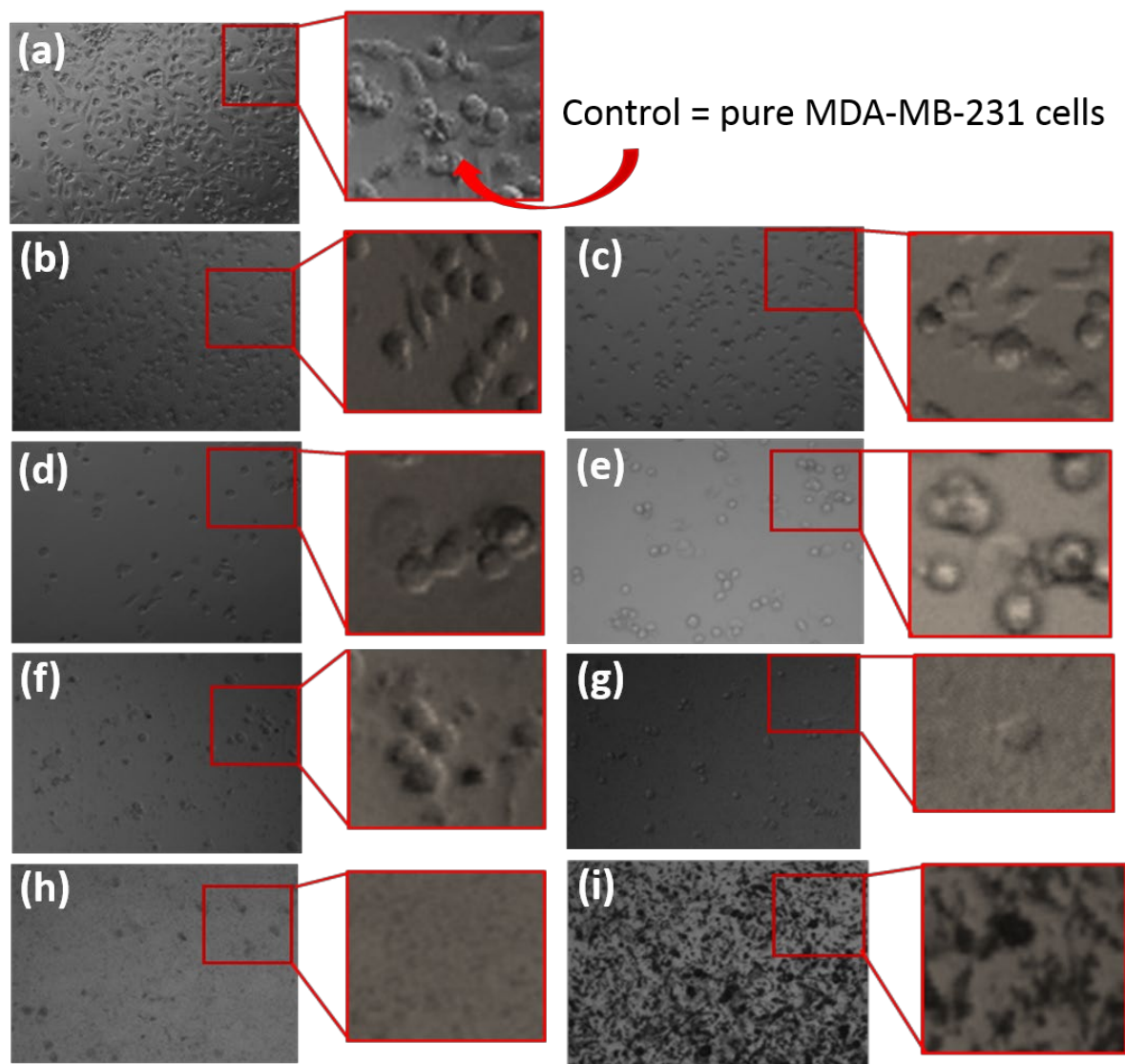


**Figure 3.3.20.** Microscopic images of the MDA-MB-231 cancer cells after incubation with increasing concentration of HPZ at 37°C for 24h (a) Control (100% cell survival), (b)  $1.56\mu\text{g.mL}^{-1}$ , (c)  $3.12\mu\text{g.mL}^{-1}$ , (d)  $6.25\mu\text{g.mL}^{-1}$ , (e)  $12.5\mu\text{g.mL}^{-1}$ , (f)  $25\mu\text{g.mL}^{-1}$ , (g)  $50\mu\text{g.mL}^{-1}$ , (h)  $100\mu\text{g.mL}^{-1}$ , (i)  $1000\mu\text{g.mL}^{-1}$ .

### 3.3.14. Summary and Conclusions of Part III

**Chapter 3 Part III** includes a porous polymer NC synthesized by the template removal wet chemical approach. PCL formed the outer shell of the capsule whereas mZnO has used as templates (on an average two mZnO per PZ) for the formation of this NC (PZ) with dia  $\sim 32\text{nm}$ . The synthesis of template mZnO with dia  $\sim 12\text{nm}$  has been discussed in previous **Part II (Section A)**. After removal of core mZnO, some pores of dia.  $\sim 22.1\text{nm}$  will appear on the PCL nanostructure (HPZ). The average particle size of the mesoporous PCL NC has been calculated as  $\sim 75\text{nm}$  in dia. The BET surface area for porous HPZ NCs has calculated as  $68.67\text{m}^2/\text{g}$  and

adsorption average pore size achieved as 22.1nm. Zeta potential value of mesoporous PCL capsules (HPZ) which has been found as  $-29.9$  mV and standard deviation  $\pm 6.45$  (single peak). For the biological application, the biocompatibility test of synthesized NCs is required. While performing biocompatibility experiment through MTT assay, of these HPZ and PZ NCs on breast cancer cell lines MCF 7 and MDA-MB-231, HPZ showed more biocompatibility towards the cancer cells compared to core shell PCL-mZnO NPs (PZ). Later the  $IC_{50}$  have been calculated for both NPs on both cancer cell lines and found as  $IC_{50}$  for HPZ on MCF 7 is  $52(\pm 1.0)$ nM, HPZ on MDA-MB-231 is  $55(\pm 1.05)$ nM and for PZ on MCF 7 is  $35.49(\pm 0.25)$ nM, PZ on MDA-MB-231 is  $32.8(\pm 0.29)$ . Thus, the calculated  $IC_{50}$  values have also proved the toxicity of PZ towards both cell lines MCF 7 and MDA-MB-231 with more or less similar to the  $IC_{50}$  values of free anticancer drug Paclitaxel on these two malignant cell lines (free Paclitaxel on MCF 7 is  $31.9(\pm 1.3)$ nM and MDA-MB-231 is  $37.52(\pm 1.8)$ nM). However, the calculated higher  $IC_{50}$  value of HPZ on both the cancer cell lines is the evidence of the biocompatible nature of synthesized HPZ NCs. It is also found that HPZ (71.8%) has more encapsulation efficiency compared to the PZ (38.6%) while loading the anticancer drug Paclitaxel in both NCs. Therefore, it can be used as a nano drug carrier for future biological applications. The drug release profile for HPZ and PZ have been studied for 3 days where HPZ showed  $78.2\pm 3.13$  % paclitaxel release on day 3 and PZ showed  $70.1\pm 1.13$  % on the 3<sup>rd</sup> day. Finally, anticancer drug Paclitaxel loaded HPZ has been incubated with breast cancer cell lines MCF 7 and MDA-MB-231 at  $37^{\circ}C$  for 24h and it has been observed that these drug loaded NPs are efficient in killing cancer cells with low concentration of drugs only than bare Paclitaxel drug and thereby minimizing side effect caused due to the anticancer drug associated application. However, the calculated  $IC_{50}$  value for HPZ-Paclitaxel on both cell lines MCF 7 and MDA-MB-231 are found as  $33.9(\pm 1.5)$ nM and  $45.62(\pm 1.86)$ nM respectively which is quite high compared to the bare drug Paclitaxel (free Paclitaxel on MCF7 is  $31.9(\pm 1.3)$ nM and MDA-MB-231 is  $37.52(\pm 1.8)$ nM). This increase in  $IC_{50}$  may be due to the stability of drug inside the NC and also due to the steady sustained release of drug from the PCL nanodrug carrier for 3 days. Consequently, these drug encapsulated inside the pores of this NC can give more bioavailability by minimizing the concentration of toxic drug for a longer period of time thereby reducing the possible side effects. However, the microscopic images of HPZ-Paclitaxel on MDA-MB-231 showed the decrease of cell survival with an increase of the concentration of Paclitaxel encapsulated by HPZ. Thus these synthesized polymer based HPZ and PZ NCs can use as drug delivery vehicle for further biological use.

# **Chapter 4**

## **Summary and Conclusions**

# Chapter 4

## Summary and Conclusions

### 4.1. Summary and conclusion

The comprehensive summary of this dissertation has been discussed in this **Chapter 4**, comprising all three chapters systematically.

In the first chapter (**Chapter 1**), a brief introduction of nanomaterials involved in the area of biotechnology with the recent achievements of this in the nanobiotechnology field by citing different excellent works by different researchers worldwide. Following part of this chapter includes a detail literature review on topics where nanomaterials involved in therapeutic fields particularly like Malaria, Immunology, and cancer as those were the application fields focused in this Ph.D. work. Later part of this chapter included the motivation to carry out this work followed by the final objectives of the dissertation.

In the second chapter (**Chapter 2**), summaries all materials used to carry out the entire synthesis of three different nanocarriers i.e., hollow porous PCL NCs, mesoporous mZnO NCs, mesoporous PCL NCs along with a detail of all three synthesis procedures of them. Finally, this chapter was also incorporated with a brief of the basic working principles of all characterization techniques utilized to analyze these synthesized nanomaterials.

The third chapter (**Chapter 3**) is divided into three parts (Part I-III) according to the synthesis and application of the three nanomaterials along with subsequent sections (Section A and B) for first two parts (Part I and Part II). This chapter discussed all characterization results of all three batches of nanomaterials with all required microscopic images, plots and data.

The third chapter (**Chapter 3**) **Part I (Section A)**, deals with the designing of hollow mesoporous PCL capsules by removing templates of SiO<sub>2</sub> (~455nm and ~10nm) and establishing their application in therapeutic field Malaria. These polymeric NCs are quite stable, biocompatible and slow degradable in a biological fluid with a very excellent loading

capacity (200 $\mu$ g DHA per mg of PCL capsule and 18.6 $\mu$ g CQDP per mg of capsules) and thus can be used as an efficient drug carrier in further studies. Two nanoformulations of PCL-DHA and PCL-CQDP with two antimalarial drugs DHA and CQDP have been used for effective knocking down the Malaria causing parasite *P. falciparum* and paramount for the treatment of malaria. In addition, it is proposed that these drug loaded nanoformulations possess a unique sustained release behavior like a ‘temperature clock’ module to further accelerate the inhibition rate of *P. falciparum* infection with increase of body temperature during the malaria infection where minor thermal expansion occurs in the capsule, hollow core, surface pores leading to the release of drugs immediately. As soon as the body temperature will be decreased then there will be a contraction of the capsule’s size, its pore size, as well as the rate of diffusion of drugs, will also be decreased. Thus, the efficiency of these polymer based nanoformulations for inhibition of growth of *P. falciparum* has been well monitored by changing temperatures.

**Chapter 3 Part I (Section B)** is the further continuation of the work on the hollow porous PCL capsules mentioned in the previous section **Part I (Section A)**. This section deals with the incorporation of PCL NCs with another antimalarial drug Sulfadoxin with the loading of 380 $\mu$ g drug per mg of PCL capsules. There is a successful sustained drug release profile from the PCL-Sulfadoxin nanoformulations, can be observed for an elongated period of time (30 days) at room temperature. Thus this synthesized polymer based NC has outstanding drug loading capacity and is efficient for sustain drug delivery via time dependent diffusion mechanism for prolong time where the diffusion coefficients increase with the gradual increase in both pore sizes as well as a time interval.

The third chapter (**Chapter 3) Part II (Section A)** has presented a sonochemical synthesis route to design mesoporous NCs mZnO of size  $\sim$ 12 nm and with an average pore diameter of 2.5 nm in absence of any surfactant. The NCs have shown excellent encapsulation efficiency of 70.3% while loaded with Ova protein and showed a sustained release pattern for the same for 3 days. The uniqueness of mZnO NCs in terms of the defined particle to pore numbers ratio (maximum of three cavities per particle) allows loading Ova efficiently and later investigated its immune modulatory properties by using [mZnO-Ova] in a mice model. The mZnO NCs characterization results signify that it could proficiently interact with APCs and provoke antigen-specific immune response with loaded specific antigen (Ova). It enhanced expansion of antigen-specific T-cells and induction of IFN- $\gamma$  producing effector CD4<sup>+</sup> and CD8<sup>+</sup> T-cells. Moreover, antigen-specific IgG levels were enriched in both the serum and lymph nodes of mZnO-Ova immunized mice. With all the special features emphasizes the

indication to represent mZnO as a perfect contender as an effective antigen-adjuvant platform for the improvement of novel nano-based vaccines against numerous diseases

**Chapter 3 Part II (Section B)** is the further continuation of the previous section (**Part II, Section B**) and it describes the excellent encapsulation efficiency of this mesoporous metal oxide NCs mZnO while loading with different antimalarial drugs Chloroquine diphosphate salt (CQDP), Dihydroartemisinin (DHA), Sulfadoxine (SD) and anticancer drugs DOX, Paclitaxel. mZnO has shown its excellent efficiency of 68.2%, 66.8% and 70.1% for drugs CQDP, DHA and Sul and 69.8 % for Paclitaxel. Mesoporous NC has shown sustained release pattern with each drug separately, maximum upto 30 days. Toxicity of mZnO NCs has been investigated with two breast cancer cell lines MCF7 and MDA-MB-231 while incubated NCs with malignant cells and analytical results proved them as an efficient carrier with outstanding encapsulation efficiency for cancer therapy. Finally, the successful cellular level interaction of drugs (CQDP and DOX) loaded mZnO NCs with cancer cell line K562, have been captured by HRTEM where mZnO NCs have killed the malignant cells effectively and established their competence as nanodrug vehicle for targeted drug delivery system.

The third chapter (**Chapter 3**) **Part III** of result and discussion summarizes the synthesis of core-shell PCL-mZnO NPs (dia ~ 32nm) (PZ) and porous PCL NCs of (dia. ~ 75nm) (HPZ) by removing tiny nanotemplates mZnO (dia ~ 12nm) from the core of the PCL-mZnO NPs. **Part III** has also included a comparative study of core-shell NCs (PCL-mZnO) along with porous PCL NCs where porous PCL showed a better encapsulation efficiency (71.8% for HPZ and 38.6% for PZ), release behavior and biocompatibility compared to the core-shell NPs. Biocompatibility experiment has performed through MTT assay, by incubating NCs with breast cancer cell lines MCF7 and MDA-MB-231. Drug encapsulated NCs can provide more bioavailability by minimizing toxicity and possible side effects caused due to the drug. Hence this synthesized polymer based NC is an appropriate platform to attach drugs or biomolecules for the drug delivery application.

## References

- [1] Feynman R P 1960 There's Plenty of Room at the Bottom *Eng. Sci.*
- [2] Bruchez M, Moronne M, Gin P, Weiss S and Alivisatos A P 1998 Semiconductor nanocrystals as fluorescent biological labels *Science*. **281** 2013–6
- [3] Chan W C W and Nie S 1998 Quantum dot bioconjugates for ultrasensitive nonisotopic detection *Science*. **281** 2016–8
- [4] Fouriki A, Farrow N, Clements M A and Dobson J 2010 Evaluation of the magnetic field requirements for nanomagnetic gene transfection *Nano Rev.* **1** 5167
- [5] Pantarotto D, Partidos C D, Hoebeke J, Brown F, Kramer E, Briand J-P, Muller S, Prato M and Alberto B 2003 Immunization with Peptide-Functionalized Carbon Nanotubes Enhances Virus-Specific Neutralizing Antibody Responses *Chem. Biol.* **10** 961–966
- [6] Salata O V. 2004 Applications of nanoparticles in biology and medicine *J. Nanobiotechnology* **2** 1–6
- [7] Jinjun Shi, Alexander R. Votruba, Omid C. Farokhzad and R L 2010 Nanotechnology in Drug Delivery and Tissue Engineering: From Discovery to Applications *Nano Lett* **10** 3223–3230
- [8] Bell J B, Rink J S, Eckerdt F, Clymer J, Goldman S, Thaxton C S and Platanias L C 2018 HDL nanoparticles targeting sonic hedgehog subtype medulloblastoma *Sci. Rep.* **8** 1211
- [9] Usov N A, Nesmeyanov M S and Tarasov V P 2018 Magnetic Vortices as Efficient Nano Heaters in Magnetic Nanoparticle Hyperthermia *Sci. Rep.* **8** 1224
- [10] Ashwatha N B and N 2014 Applications of Nanotechnology in Cancer: A Literature Review of Imaging and Treatment *J. Nucl. Med. Radiat. Ther.* **5** 1–9
- [11] Basaran A A and I 2012 Nanotechnology in Cancer Treatment *Nanomedicine Biother. Discov.* **2** 1–3
- [12] Gupta P D, Dave M and Vasavada A R 2005 Protein nanotechnology - A powerful futuristic diagnostic technique *Indian J. Clin. Biochem.* **20** 48–53
- [13] Blasiak B, Van Veggel F C J M and Tomanek B 2013 Applications of Nanoparticles for MRI Cancer Diagnosis and Therapy *J. Nanomater.* 1–12
- [14] Danie Kingsley J, Ranjan S, Dasgupta N and Saha P 2013 Nanotechnology for tissue engineering: Need, techniques and applications *J. Pharm. Res.* **7** 200–4
- [15] Wang Y and Xia Y 2004 Bottom-up and top-down approaches to the synthesis of monodispersed spherical colloids of low melting-point metals *Nano Lett.* **4** 2047–50
- [16] Rajesh Kumar and Shatrohan Lal 2014 Synthesis of Organic Nanoparticles and their Applications in Drug Delivery and Food Nanotechnology: A Review *J. Nanomater. Mol. Nanotechnol.* **3** 1–11

- [17] Sachan R and Bajpai M 2013 Transdermal Drug Delivery System : A Review *Int. J. Res. Dev. Pharm. L. Sci.* **3** 748–65
- [18] Rasool Hassan B A 2012 Overview on Drug Delivery System *Pharm. Anal. Acta* **3**
- [19] Narang N and Sharma J 2011 Sublingual mucosa as a route for systemic drug delivery *Int. J. Pharm. Pharm. Sci.* **3** 18–22
- [20] Parth S. Patel, Ashish M. Parmar, Nilang S. Doshi , Hardik V. Patel , Raxit R. Patel C N 2013 Buccal Drug Delivery System: A Review *Int. J. Drug Dev. Res.* **5** 35–48
- [21] Shozo Miyazaki, Masako Oda, Masahiko Takada D A 1995 Thermally Gelling Poloxamine Synperonic T908 Solution as a Vehicle for Rectal Drug Delivery *Biol. Pharm. Bull* **18** 1151–3
- [22] Kadir F 1993 Intramuscular and subcutaneous drug delivery: Encapsulation in liposomes and other methods to manipulate drug availability *Pharm. World Sci.* **15** 173–5
- [23] Park K 2014 Controlled drug delivery systems : Past forward and future back *J. Control. Release* **190** 3–8
- [24] Ummadi S, Shravani B, Rao N G R, Reddy M S and Sanjeev B 2013 Overview on Controlled Release Dosage Form *Int. J. Pharma Sci.* **3** 258–69
- [25] Nidhi Mishra, Perna Pant, Ankit Porwal, Juhi Jaiswal, Mohd. Aquib Samad S T 2016 Targeted drug delivery system : A Review *Am. J. Pharm Tech Res.* **6** 1–24
- [26] Fahmy T M, Fong P M, Goyal A and Saltzman W M 2005 Targeted for Drug Delivery *nanotoday* 18–26
- [27] Tiwari G, Tiwari R, Bannerjee S, Bhati L, Pandey S, Pandey P and Sriwastawa B 2012 Drug delivery systems: An updated review *Int. J. Pharm. Investig.* **2** 2–11
- [28] Fitz J 2018 Global Liposomes Drug Delivery Market 2018 Major Players- Teva Pharmaceutical , Crucell N . V ., Gilead Sciences and Enzon 1–3
- [29] Kedar U, Phutane P, Shidhaye S and Kadam V 2010 Advances in polymeric micelles for drug delivery and tumor targeting *Nanomedicine Nanotechnology, Biol. Med.* **6** 714–29
- [30] Kim Y, Ji E, Dong P and Na H 2018 Recent progress in dendrimer-based nanomedicine development *Arch. Pharm. Res.* **41** 571–82
- [31] Li J and Mooney D J 2016 Designing hydrogels for controlled drug delivery *Nat. Rev. Mater.* **1** 1–18
- [32] Matea C T, Mocan T, Tabaran F, Pop T, Mosteanu O, Puia C, Iancu C and Mocan L 2017 Quantum dots in imaging, drug delivery and sensor applications *Int. J. Nanomedicine* **12** 5421–31
- [33] Qi L and Gao X 2008 Emerging application of quantum dots for drug delivery and therapy *Expert Opin. Drug Deliv.* **5** 263–7
- [34] Min Y, Mao C, Xu D and Liu Y 2010 Gold nanorods for platinum based prodrug delivery *Chem. Commun.* **46** 8424–6
- [35] Cortés H, Alcalá-alcalá S, Ávalos-fuentes A and Mendoza-muñoz N 2017

Nanotechnology As Potential Tool for siRNA Delivery in Parkinson's Disease  
*Curr. Drug Targets* **18**

- [36] Singh A, Garg G and Sharma P K 2010 NANOSPHERES : A NOVEL APPROACH FOR TARGETED DRUG DELIVERY SYSTEM *Int. J. Pharm. Sci. Rev. Res.* **5** 84–8
- [37] Kumar V B, Medhi H, Yong Z and Paik P 2016 Designing idiosyncratic hmPCL-siRNA nanoformulated capsules for silencing and cancer therapy *Nanomedicine Nanotechnology, Biol. Med.* **12** 579–88
- [38] Rouquerol J, Avnir D, Fairbridge C W, Everett D H, Haynes J H, Pernicone N, Ramsay J D F, Sing K S W and Unger K K 1994 Recommendations for the characterization of porous solids *Pure Appl. Chem.* **66** 1739–58
- [39] Liu Y, He L, Mustapha A, Li H, Hu Z Q and Lin M 2009 Antibacterial activities of zinc oxide nanoparticles against Escherichia coli O157 : H7 *J. Appl. Microbiol.* **107** 1193–201
- [40] 2013 Zinc Oxide (ZnO) Nanoparticles – Properties, Applications
- [41] Sabir S, Arshad M and Chaudhari S K 2014 Zinc Oxide Nanoparticles for Revolutionizing Agriculture : Synthesis and Applications *Sci. World J.* **2014**
- [42] Rasmussen J W, Martinez E, Louka P and Wingett D G 2010 Zinc Oxide Nanoparticles for Selective Destruction of Tumor Cells and Potential for Drug Delivery Applications *Expert Opin Drug Deliv* **7** 1063–77
- [43] Rasmussen J W, Martinez E, Louka P and Wingett D G 2010 Zinc oxide nanoparticles for selective destruction of tumor cells and potential for drug delivery applications. *Expert Opin. Drug Deliv.* **7** 1063–77
- [44] Van Natta F J, Hill J W and Carothers W H 1934 Studies of Polymerization and Ring Formation. XXIII.  $\epsilon$ -Caprolactone and its Polymers *J. Am. Chem. Soc.* **56** 455–7
- [45] Labet M and Thielemans W 2009 Synthesis of polycaprolactone : a review w 3484–504
- [46] Woodruff M A and Hutmacher D W 2010 The return of a forgotten polymer : Polycaprolactone in the 21st century *Prog. Polym. Sci.* **35** 1217–56
- [47] Avella M, Bondioli F, Cannillo V, Di Pace E, Errico M E, Ferrari A M, Focher B and Malinconico M 2006 Poly( $\epsilon$ -caprolactone)-based nanocomposites: Influence of compatibilization on properties of poly( $\epsilon$ -caprolactone)-silica nanocomposites *Compos. Sci. Technol.* **66** 886–94
- [48] Coulembier O, Degée P, Hedrick J L and Dubois P 2006 From controlled ring-opening polymerization to biodegradable aliphatic polyester: Especially poly( $\beta$ -malic acid) derivatives *Prog. Polym. Sci.* **31** 723–47
- [49] Rajapakse C S K, Martinez A, Naoulou B, Jarzecki A A, Suárez L, Deregnacourt C, Sinou V, Schrével J, Musi E, Ambrosini G, Schwartz G K and Sanchez-Delgado R A 2009 Synthesis, Characterization and in vitro Antimalarial and Antitumor Activity of New Ruthenium(II) Complexes of Chloroquine *Inorg. Chem.* **48** 1122–31
- [50] Jiang P Du, Zhao Y L, Deng X Q, Mao Y Q, Shi W, Tang Q Q, Li Z G, Zheng Y Z, Yang S Y and Wei Y Q 2010 Antitumor and antimetastatic activities of chloroquine diphosphate in a murine model of breast cancer *Biomed. Pharmacother.* **64** 609–14

- [51] Fan C, Wang W, Zhao B, Zhang S and Miao J 2006 Chloroquine inhibits cell growth and induces cell death in A549 lung cancer cells *Bioorganic Med. Chem.* **14** 3218–22
- [52] Kakuru A, Jagannathan P, Muhindo M K, Natureeba P, Awori P, Nakalembe M, Opira B, Olwoch P, Ategeka J, Nayebare P, Clark T D, Feeney M E, Charlebois E D, Rizzuto G, Muehlenbachs A, Havlir D V., Kanya M R and Dorsey G 2016 Dihydroartemisinin–Piperaquine for the Prevention of Malaria in Pregnancy *N. Engl. J. Med.* **374** 928–39
- [53] Efferth T 2006 Molecular Pharmacology and Pharmacogenomics of Artemisinin and its Derivatives in Cancer Cells *Curr. Drug Targets* **7** 407–21
- [54] Cabello C M, Lamore S D, Bair W B, Qiao S, Azimian S, Lesson J L and Wondrak G T 2012 The redox antimalarial dihydroartemisinin targets human metastatic melanoma cells but not primary melanocytes with induction of NOXA-dependent apoptosis *Invest. New Drugs* **30** 1289–301
- [55] Sulphadoxin  
[https://ncit.nci.nih.gov/ncitbrowser/ConceptReport.jsp?dictionary=NCI\\_Thesaurus&ns=NCI\\_Thesaurus&code=C47735](https://ncit.nci.nih.gov/ncitbrowser/ConceptReport.jsp?dictionary=NCI_Thesaurus&ns=NCI_Thesaurus&code=C47735)
- [56] Sulfadoxin <https://www.ncbi.nlm.nih.gov/mesh/68013413>
- [57] Yamamoto K, Kawamura I, Tominaga T, Nomura T, Kohda C, Ito J and Mitsuyama M 2005 Listeriolysin O, a cytolysin derived from *Listeria monocytogenes*, inhibits generation of ovalbumin-specific Th2 immune response by skewing maturation of antigen-specific T cells into Th1 cells *Clin. Exp. Immunol.* **142** 268–74
- [58] Alves R C, Fernandes R P, Eloy J O, Salgado H R N and Chorilli M 2018 Characteristics, Properties and Analytical Methods of Paclitaxel: A Review *Crit. Rev. Anal. Chem.* **48** 110–8
- [59] Deepa G, Ashwanikumar N, Pillai J J and Kumar G S V 2012 Polymer Nanoparticles - A Novel Strategy for Administration of Paclitaxel in Cancer Chemotherapy *Curr. Med. Chem.* **19** 6207–13
- [60] [Http://www.who.int/ith/diseases/malaria/en/](http://www.who.int/ith/diseases/malaria/en/) 2018 Malaria *WHO* 1–4
- [61] Balbir Singh C D 2013 Human Infections and Detection of *Plasmodium knowlesi* *Clin. Microbiol. Rev.* **26** 165–84
- [62] Cannella A P and Archibald L 2017 *Plasmodium* species ( Malaria ) *Infect. Dis. Advis.* 1–12
- [63] Kirk K 2001 Membrane transport in the malaria-infected erythrocyte. *Physiol. Rev.* **81** 495–537
- [64] <https://www.cdc.gov/dpdx/malaria/index.html>
- [65] <http://scientistsagainstmalaria.net/parasite/plasmodium-falciparum>
- [66] <https://www.cancer.org/latest-news/facts-and-figures-2018-rate-of-deaths-from-cancer-continues-decline.html>
- [67] Ahmadian S, Barar J, Saei A A, Fakhree M A A and Omidi Y 2009 Cellular Toxicity of Nanogenomedicine in MCF-7 Cell Line: MTT assay *J. Vis. Exp.* 1–2
- [68] Relda Cailleau, Matilde Olive A and Cruciger Q V J 1978 Long-Term Human Breast

- Carcinoma Cell Lines Of Metastatic Origin: Preliminary Characterization *Soc. Vitr. Biol. Springer* **14** 911–5
- [69] Kathryn J C, Sireesha V G and Stanley L 2010 Triple Negative Breast Cancer Cell Lines: One Tool in the Search for Better Treatment of Triple Negative Breast Cancer *Breast Dis.* **32** 35–48
- [70] Moghimi S M, Hunter A C and Murray J C 2005 Nanomedicine: current status and future prospects *FASEB J.* **19** 311–30
- [71] De Temmerman M L, Rejman J, Demeester J, Irvine D J, Gander B and De Smedt S C 2011 Particulate vaccines: On the quest for optimal delivery and immune response *Drug Discov. Today* **16** 569–82
- [72] K. JK. James J H and P E 2014 Nanotechnology market-nanotechnology markets in healthcare & medicine *Drug Dev. Deliv.* **14** 1–4
- [73] Jennings G T and Bachmann M F 2009 Immunodrugs: Therapeutic VLP-Based Vaccines for Chronic Diseases *Annu. Rev. Pharmacol. Toxicol.* **49** 303–26
- [74] Buonaguro, L., Tagliamonte, M., Tornesello M L & and Buonaguro F M 2011 Developments in virus-like particlebased vaccines for infectious diseases and cancer *Expert Rev. Vaccines* **10** 1569–83
- [75] Chackerian B 2010 Virus-like particle based vaccines for Alzheimer disease *Hum. Vaccin.* **6** 926–30
- [76] Bolhassani A, Safaiyan S and Rafati S 2011 Improvement of different vaccine delivery systems for cancer therapy. *Mol. Cancer* **10** 3
- [77] Yogita Krishnamachari, Sean M. Geary, Caitlin D. Lemke And A K S 2011 Nanoparticle Delivery Systems In Cancer Vaccines *Pharm Res.* **28** 215–36
- [78] Hamdy S, Haddadi A, Hung R W and Lavasanifar A 2011 Targeting dendritic cells with nano-particulate PLGA cancer vaccine formulations *Adv. Drug Deliv. Rev.* **63** 943–55
- [79] Maurer P, Jennings G T, Willers J, Rohner F, Lindman Y, Roubicek K, Renner W A, Müller P and Bachmann M F 2005 A therapeutic vaccine for nicotine dependence: Preclinical efficacy, and phase I safety and immunogenicity *Eur. J. Immunol.* **35** 2031–40
- [80] Vogel, F. R., Caillet, C., Kusters, I. C. & Haensler J 2009 Emulsion-based adjuvants for influenza vaccines *Expert Rev. Vaccines* **8** 483–892
- [81] Bharali D J, Pradhan V, Elkin G, Qi W, Hutson A, Mousa S A and Thanavala Y 2008 Novel nanoparticles for the delivery of recombinant hepatitis B vaccine *Nanomedicine Nanotechnology, Biol. Med.* **4** 311–7
- [82] Khairunnisa Abdul Ghaffar, Ashwini Kumar Giddam, Mehfuz Zaman, Mariusz Skwarczynski I T 2014 Liposomes as Nanovaccine Delivery Systems *Curr. Top. Med. Chem.* **14** 1194–1208
- [83] Van Riet E, Ainai A, Suzuki T, Kersten G and Hasegawa H 2014 Combatting infectious diseases; Nanotechnology as a platform for rational vaccine design *Adv. Drug Deliv. Rev.* **74** 28–34
- [84] S. Y. Kim, H. J. Doh, M. H. Jang, Y. J. Ha S I C and and Park H J 1999 Oral

- Immunization with Helicobacter pylori -Loaded Poly( D , L -Lactide-Co-Glycolide) Nanoparticles *Helicobacter* **4** 33–9
- [85] Torres-Sangiao E, Holban A M and Gestal M C 2016 Advanced nanobiomaterials: Vaccines, diagnosis and treatment of infectious diseases *Molecules* **21**
- [86] Smith D M, Simon J K and Baker J R 2013 Applications of nanotechnology for immunology. *Nat. Rev. Immunol.* **13** 592–605
- [87] Zhao L, Seth A, Wibowo N, Zhao C X, Mitter N, Yu C and Middelberg A P J 2014 Nanoparticle vaccines *Vaccine* **32** 327–37
- [88] Luo Y-H, Chang L W and Lin P 2015 Metal-Based Nanoparticles and the Immune System: Activation, Inflammation, and Potential Applications *Biomed Res. Int.* **2015** 1–12
- [89] Joo S H, Choi S J, Oh I, Kwak J, Liu Z, Terasaki O and Ryoo R 2001 Ordered nanoporous arrays of carbon supporting high dispersions of platinum nanoparticles. *Nature* **412** 169–72
- [90] Wang Z L 2004 Zinc oxide nanostructures: growth, properties and applications *J. Phys. Condens. Matter* **16** R829–58
- [91] WHO World Malar. Rep. December 2016 <http://www.who.int/malaria/en/>
- [92] Peters W 1990 Plasmodium: resistance to antimalarial drugs *Ann. Parasitol. Hum. Comp* **65** 103–6
- [93] Packard R M 2014 The Origins of Antimalarial-Drug Resistance *N Engl J Med.* **371** 397–9
- [94] Farooq U and Mahajan R C 2004 Drug resistance in malaria *J. Vector Borne Dis.* **41** 45–53
- [95] Zalis M G, Pang L, Silveira M S, Milhous W K And Wirth D F 1998 Characterization Of Plasmodium Falciparum Isolated From The Amazon Region Of Brazil : Evidence For Quinine Resistance *Am. J. Trop. Med. Hyg.* **58** 630–7
- [96] Arjen M. Dondorp, M.D., François Nosten, M.D., Poravuth Yi, M.D., Debashish Das, M.D., Aung Phae Phyo, M.D., Joel Tarning P D, Khin Maung Lwin, M.D., Frederic Ariey, M.D., Warunee Hanpithakpong, Ph.D., Sue J. Lee, Ph.D., Pascal Ringwald, M.D., Kamolrat Silamut, Ph.D., Mallika Imwong, Ph.D., Kesinee Chotivanich, Ph.D., Pharath Lim, M.D., Trent Herdman, Ph.D., Sen Sam An, Shunmay Y P D and Pratap Singhasivanon, M.D., Nicholas P.J. Day, D.M., Niklas Lindegardh, Ph.D., Duong Socheat, M.D., and Nicholas J. White F R S 2009 Artemisinin Resistance in Plasmodium falciparum Malaria *N Engl J Med* **361** 455–67
- [97] 2006 WHO guidelines for the treatment of malaria. Geneva: World Health Organization,
- [98] Mu J, Myers R A, Jiang H, Liu S, Ricklefs S, Waisberg M, Chotivanich K, Wilairatana P, Krudsood S, White N J, Udomsangpetch R, Cui L, Ho M, Ou F, Li H, Song J, Li G, Wang X, Seila S, Sokunthea S, Socheat D, Sturdevant D E, Porcella S F, Fairhurst R M, Wellems T E, Awadalla P and Su X 2010 Plasmodium falciparum genome-wide scans for positive selection , recombination hot spots and resistance to antimalarial drugs *Nat. Genet.* **42** 268–71

- [99] John C. Wootton, Xiaorong Feng M T F, Roland A. Cooper, Jianbing Mu, Dror I. Baruch A J M and Su X 2002 Genetic diversity and chloroquine selective sweeps in *Plasmodium falciparum* *Nature* **418** 320–3
- [100] Roper C, Pearce R, Nair S, Sharp B, Nosten F and Anderson T 2004 Intercontinental Spread of Pyrimethamine-Resistant Malaria *Science (80-. )*. **305** 1124
- [101] Vreden S G, Bansie R D, Jitan J K and Adhin M R 2016 Assessing parasite clearance during uncomplicated *Plasmodium falciparum* infection treated with artesunate monotherapy in Suriname *Infect. Drug Resist.* **9** 261–7
- [102] Malaria vaccine RTS,S/AS01 <http://www.who.int/malaria/media/rtss-phase-3-trial-qa/en/>
- [103] Wanta M Y, Islamuddin M, Chouhan G, Ozbak H A, Hemegb H A, Dasgupta A K, Chattopadhyay A P and Afrin F 2015 Therapeutic efficacy of artemisinin-loaded nanoparticles in experimental visceral leishmaniasis *Colloids Surfaces B Biointerfaces* **130** 215–21
- [104] Jeong S Y and Kim S W 1986 Biodegradable Polymeric Drug Delivery Systems *Arch. Pharm* **9** 63–73
- [105] Venkataraman S, Hedrick J L, Ong Z Y, Yang C, Ee P L R, Hammond P T and Yang Y Y 2011 The effects of polymeric nanostructure shape on drug delivery *Adv. Drug Deliv. Rev.* **63** 1228–46
- [106] Kumari A, Yadav S K and Yadav S C 2010 Colloids and Surfaces B : Biointerfaces Biodegradable polymeric nanoparticles based drug delivery systems *Colloids Surfaces B Biointerfaces* **75** 1–18
- [107] Mora-Huertas C E, Fessi H and Elaissari A 2010 Polymer-based nanocapsules for drug delivery *Int. J. Pharm.* **385** 113–42
- [108] Fredenberg S, Wahlgren M, Reslow M and Axelsson A 2011 The mechanisms of drug release in poly(lactic-co-glycolic acid)-based drug delivery systems--a review. *Int. J. Pharm.* **415** 34–52
- [109] Makadia H K and Siegel S J 2011 Poly Lactic-co-Glycolic Acid (PLGA) as Biodegradable Controlled Drug Delivery Carrier *Polymers (Basel)*. **3** 1377–97
- [110] Golenser J, Buchholz V, Bagheri A, Nasereddin A, Dzikowski R, Guo J, Hunt N H, Eyal S, Vakruk N and Greiner A 2017 Controlled release of artemisone for the treatment of experimental cerebral malaria *Parasit. Vectors* **10:117** 1–10
- [111] Föger F, Noonpakdee W, Loretz B, Joojuntr S, Salvenmoser W, Thaler M and Bernkop-Schnürch A 2006 Corrigendum to “Inhibition of malarial topoisomerase II in *Plasmodium falciparum* by antisense nanoparticles” *Int. J. Pharm.* **319** 139–46
- [112] Memvanga P B, Coco R and Pr eat V 2013 An oral malaria therapy: Curcumin-loaded lipid-based drug delivery systems combined with  $\beta$ -arteether *J. Control. Release* **172** 904–13
- [113] Owais M, Varshney G C, Choudhury A, Chandra S and Gupta C M 1995 Chloroquine encapsulated in malaria-infected erythrocyte-specific antibody-bearing liposomes effectively controls chloroquine-resistant *Plasmodium berghei* infections in mice *Antimicrob. Agents Chemother.* **39** 180–4

- [114] Urbán P, Estelrich J, Cortés A and Fernández-Busquets X 2011 A nanovector with complete discrimination for targeted delivery to Plasmodium falciparum-infected versus non-infected red blood cells in vitro *J. Control. Release* **151** 202–11
- [115] Urbán P, Estelrich J, Adeva A, Cortés A and Fernández-Busquets X 2011 Study of the efficacy of antimalarial drugs delivered inside targeted immunoliposomal nanovectors *Nanoscale Res. Lett.* **6** 1–9
- [116] Mosqueira V C F, Loiseau P M, Bories C, Legrand P, Devissaguet J P and Barratt G 2004 Efficacy and Pharmacokinetics of Intravenous Nanocapsule Formulations of Halofantrine in Plasmodium berghei-Infected Mice *Antimicrob. Agents Chemother.* **48** 1222–8
- [117] Bakker-Woudenberg I A J M 2002 Long-circulating sterically stabilized liposomes as carriers of agents for treatment of infection or for imaging infectious foci *International Journal of Antimicrobial Agents* vol 19pp 299–311
- [118] Wesche D L, Schuster B G, Wang W-X and Woosley R L 2000 Mechanism of cardiotoxicity of halofantrine *Clin. Pharmacol. Ther.* **67** 521–529
- [119] Bouchaud O, Imbert P, Touze J E, Doodoo A N O, Danis M and Legros F 2009 Fatal cardiotoxicity related to halofantrine: a review based on a worldwide safety data base. *Malar. J.* **8:289** 1–8
- [120] Jacob Inbaneson S and Ravikumar S 2013 In vitro antiplasmodial activity of PDDS-coated metal oxide nanoparticles against Plasmodium falciparum *Appl. Nanosci.* **3** 197–201
- [121] Singh K K and Vingkar S K 2008 Formulation, antimalarial activity and biodistribution of oral lipid nanoemulsion of primaquine *Int. J. Pharm.* **347** 136–43
- [122] Souza A C M, Mosqueira V C F, Silveira A P A, Antunes L R, Richard S, Guimarães H N and Grabe-Guimarães A 2018 Reduced cardiotoxicity and increased oral efficacy of artemether polymeric nanocapsules in Plasmodium berghei-infected mice *Parasitology* **145** 1075–83
- [123] Velasques K, Maciel T R, de Castro Dal Forno A H, Teixeira F E G, da Fonseca A L, Varotti F de P, Fajardo A R, Ávila D S de and Haas S E 2018 Co-nanoencapsulation of antimalarial drugs increases their in vitro efficacy against Plasmodium falciparum and decreases their toxicity to Caenorhabditis elegans *Eur. J. Pharm. Sci.* **118** 1–12
- [124] Gomes G S, Maciel T R, Piegas E M, Michels L R, Colomé L M, Freddo R J, Ávila D S de, Gundel A and Haas S E 2018 Optimization of Curcuma Oil/Quinine-Loaded Nanocapsules for Malaria Treatment *AAPS PharmSciTech* **19** 551–64
- [125] Leite E A, Grabe-Guimarães A, Guimarães H N, Machado-Coelho G L L, Barratt G and Mosqueira V C F 2007 Cardiotoxicity reduction induced by halofantrine entrapped in nanocapsule devices *Life Sci.* **80** 1327–34
- [126] Muga J O, Gathirwa J W, Tukulula M and Jura W G Z O 2018 In vitro evaluation of chloroquine-loaded and heparin surface-functionalized solid lipid nanoparticles *Malar. J.* **17** 1–7
- [127] Maestrelli F, Mura P and Alonso M J 2004 Formulation and characterization of triclosan sub-micron emulsions and nanocapsules *J. Microencapsul.* **21** 857–64

- [128] Kashyap A, Kaur R, Baldi A, Jain U K, Chandra R and Madan J 2018 Chloroquine diphosphate bearing dextran nanoparticles augmented drug delivery and overwhelmed drug resistance in *Plasmodium falciparum* parasites *Int. J. Biol. Macromol.* **114** 161–8
- [129] Pulendran B and Ahmed R 2011 Immunological mechanisms of vaccination *Nat. Immunol.* **12** 509–17
- [130] Fauci A S, Touchette N A and Folkers G K 2005 Emerging infectious diseases: A 10-year perspective from the National Institute of Allergy and Infectious Diseases *Emerg. Infect. Dis.* **11** 519–25
- [131] Kasturi S P, Skountzou I, Albrecht R A, Koutsonanos D, Hua T, Nakaya H I, Ravindran R, Stewart S, Alam M, Kwissa M, Villinger F, Murthy N, Steel J, Jacob J, Hogan R J, García-Sastre A, Compans R and Pulendran B 2011 Programming the magnitude and persistence of antibody responses with innate immunity. *Nature* **470** 543–7
- [132] Fahmy T M, Demento S L, Caplan M J, Mellman I and Saltzman W M 2008 Design opportunities for actively targeted nanoparticle vaccines. *Nanomedicine (Lond).* **3** 343–55
- [133] Mant A, Chinnery F, Elliott T and Williams A P 2012 The pathway of cross-presentation is influenced by the particle size of phagocytosed antigen *Immunology* **136** 163–75
- [134] Luo Y H, Chang L W and Lin P 2015 Metal-Based Nanoparticles and the Immune System: Activation, Inflammation, and Potential Applications *Biomed Res. Int.* **2015** 1–12
- [135] Lucarelli M, Gatti A M, Savarino G, Quattroni P, Martinelli L, Monari E and Boraschi D 2004 Innate defence functions of macrophages can be biased by nano-sized ceramic and metallic particles *Eur. Cytokine Netw.* **15** 339–46
- [136] Cui Y, Liu H, Zhou M, Duan Y, Li N, Gong X, Hu R, Hong M and Hong F 2011 Signaling pathway of inflammatory responses in the mouse liver caused by TiO<sub>2</sub> nanoparticles *J. Biomed. Mater. Res. - Part A* **96 A** 221–9
- [137] Petrarca C, Clemente E, Amato V, Pedata P, Sabbioni E, Bernardini G, Iavicoli I, Cortese S, Niu Q, Otsuki T, Paganelli R and Di Gioacchino M 2015 Engineered metal based nanoparticles and innate immunity *Clin. Mol. Allergy* **13**
- [138] Vigneshwaran N, Kumar S, Katha a a, Varadarajan P V and Prasad V 2006 Functional finishing of cotton fabrics using zinc oxide–soluble starch nanocomposites *Nanotechnology* **17** 5087–95
- [139] He H, Yang Q, Wang J and Ye Z 2011 Layer-structured ZnO nanowire arrays with dominant surface- and acceptor-related emissions *Mater. Lett.* **65** 1351–4
- [140] Emamifar A, Kadivar M, Shahedi M and Solimanian-Zad S 2012 Effect of nanocomposite packaging containing Ag and ZnO on reducing pasteurization temperature of orange juice *J. Food Process. Preserv.* **36** 104–12
- [141] Chang H, Ho C C, Yang C S, Chang W H, Tsai M H, Tsai H T and Lin P 2013 Involvement of MyD88 in zinc oxide nanoparticle-induced lung inflammation *Exp. Toxicol. Pathol.* **65** 887–96
- [142] Cho N-H, Cheong T-C, Min J H, Wu J H, Lee S J, Kim D, Yang J-S, Kim S, Kim Y K and Seong S-Y 2011 A multifunctional core–shell nanoparticle for dendritic cell-based

- cancer immunotherapy *Nat. Nanotechnol.* **6** 675–82
- [143] Liu Y, Tan J, Thomas A, Ou-Yang D and Muzykantov V R 2012 The shape of things to come: importance of design in nanotechnology for drug delivery *Ther. Deliv.* **3** 181–94
- [144] Paik P and Zhang Y 2011 Synthesis of hollow and mesoporous polycaprolactone nanocapsules. *Nanoscale* **3** 2215–9
- [145] Meier W 2000 Polymer nanocapsules *Chem. Soc. Rev.* **29** 295–303
- [146] Kupferschmidt N, Qazi K R, Kemi C, Vallhov H, Garcia-Bennett A E, Gabrielsson S and Scheynius A 2013 Mesoporous silica particles potentiate antigen-specific T-cell responses *Nanomedicine* **9** 1835–46
- [147] Kupferschmidt N, Qazi K R, Kemi C, Vallhov H, Garcia-Bennett A E, Gabrielsson S and Scheynius A 2014 Mesoporous silica particles potentiate antigen-specific T-cell responses *Nanomedicine* **9** 1835–46
- [148] Heidegger S, Göbl D, Schmidt A, Niedermayer S, Argyo C, Endres S, Bein T and Bourquin C 2016 Immune response to functionalized mesoporous silica nanoparticles for targeted drug delivery *Nanoscale* **8** 938–48
- [149] Immunology: Ovalbumin (OVA) Challenge *Immunol. Ovalbumin Chall. | Taconic Biosci.* 1–3
- [150] T. Zhang, Y. Maekawa, J. Hanba, T. Dainichi, B. F. Nashed, H. Hisaeda, T Sakai T A And K. Himeno R A G & N K 2000 Lysosomal cathepsin B plays an important role in antigen processing , while cathepsin D is involved in degradation of the invariant chain in ovalbumin-immunized mice *Immunology* **100** 13–20
- [151] Slütter B and Jiskoot W 2010 Dual role of CpG as immune modulator and physical crosslinker in ovalbumin loaded N-trimethyl chitosan ( TMC ) nanoparticles for nasal vaccination *J. Control. Release* **148** 117–21
- [152] Slütter B, Bal S, Keijzer C, Mallants R, Hagenaaers N, Que I, Kaijzel E, Eden W Van, Augustijns P, Löwik C, Bouwstra J, Broere F and Jiskoot W 2010 Nasal vaccination with N-trimethyl chitosan and PLGA based nanoparticles : Nanoparticle characteristics determine quality and strength of the antibody response in mice against the encapsulated antigen *Vaccine* **28** 6282–91
- [153] Keijzer C, Slütter B, van der Zee R, Jiskoot W, van Eden W and Broere F 2011 PLGA, PLGA-TMC and TMC-TPP nanoparticles differentially modulate the outcome of nasal vaccination by inducing tolerance or enhancing humoral immunity *PLoS One* **6** 1–10
- [154] Rahimian S, Willem J, Fransen M F, Mezzanotte L, Gold H, Wisse P, Overkleeft H, Amidi M, Jiskoot W, Clemens W L and Ferry Ossendorp W E H 2015 Near-infrared labeled , ovalbumin loaded polymeric nanoparticles based on a hydrophilic polyester as model vaccine : In vivo tracking and evaluation of antigen-specific CD8  $\beta$  T cell immune response *Biomaterials* **37** 469–77
- [155] Kim S, Noh Y, Heung T, Kim J, Kim S, Ho S, Oh D, Park Y and Lim Y T 2017 Synthetic vaccine nanoparticles target to lymph node triggering enhanced innate and adaptive antitumor immunity *Biomaterials* **130** 56–66
- [156] Marit A, Groot D, Du G, Mönkäre J, Platteel A C M, Broere F, Bouwstra J A and Sijts A J A M 2017 Hollow microneedle-mediated intradermal delivery of model vaccine

- antigen-loaded PLGA nanoparticles elicits protective T cell-mediated immunity to an intracellular bacterium *J. Control. Release* **266** 27–35
- [157] Yohei Mukai, Tomoyo Yoshinaga, Mai Yoshikawa, Kazuhiko Matsuo, Tomoaki Yoshikawa, Keisuke Matsuo, Kazuyuki Niki, Yasuo Yoshioka N O and S N 2011 Induction of Endoplasmic Reticulum – Endosome Fusion for Antigen Cross-Presentation Induced by Poly (  $\gamma$  -Glutamic Acid) Nanoparticles *J. Immunol.* **187** 6249–55
- [158] Mukai Y, Yoshinaga T, Yoshikawa M, Matsuo K, Yoshikawa T, Matsuo K, Niki K, Yoshioka Y, Okada N and Nakagawa S 2011 Induction of Endoplasmic Reticulum-Endosome Fusion for Antigen Cross-Presentation Induced by Poly ( -Glutamic Acid) Nanoparticles *J. Immunol.* **187** 6249–55
- [159] Nembrini C, Stano A, Dane K Y, Ballester M, van der Vlies A J, Marsland B J, Swartz M A and Hubbell J A 2011 Nanoparticle conjugation of antigen enhances cytotoxic T-cell responses in pulmonary vaccination *Proc. Natl. Acad. Sci.* **108** E989–97
- [160] Kuai R, Ochyl L J, Bahjat K S, Schwendeman A and Moon J J 2017 Designer vaccine nanodiscs for personalized cancer immunotherapy *Nat. Mater.* **16** 489–98
- [161] Paciotti G F, Myer L, Weinreich D, Goia D, Pavel N, McLaughlin R E and Tamarkin L 2004 Colloidal gold: A novel nanoparticle vector for tumor directed drug delivery *Drug Deliv.* **11** 169–83
- [162] Wu X, Liu H, Liu J, Haley K N, Treadway J A, Larson J P, Ge N, Peale F and Bruchez M P 2003 Immunofluorescent labeling of cancer marker Her2 and other cellular targets with semiconductor quantum dots *Nat. Biotechnol.* **21** 41–6
- [163] Hirsch L R, Stafford R J, Bankson J A, Sershen S R, Rivera B, Price R E, Hazle J D, Halas N J and West J L 2003 Nanoshell-mediated near-infrared thermal therapy of tumors under magnetic resonance guidance *Proc. Natl. Acad. Sci.* **100** 13549–54
- [164] Huang X, El-Sayed I H, Qian W and El-Sayed M A 2006 Cancer cell imaging and photothermal therapy in the near-infrared region by using gold nanorods *J. Am. Chem. Soc.* **128** 2115–20
- [165] El-Sayed I H, Huang X and El-Sayed M A 2005 Surface plasmon resonance scattering and absorption of anti-EGFR antibody conjugated gold nanoparticles in cancer diagnostics: Applications in oral cancer *Nano Lett.* **5** 829–34
- [166] Jingyi Chen, Danling Wang, Jiefeng Xi, Leslie Au, Andy Siekkinen, Addie Warsen, Zhi-Yuan Li, Hui Zhang, Younan Xia and X L 2007 Immuno Gold Nanocages with Tailored Optical Properties for Targeted Photothermal Destruction of Cancer Cells *Nano Lett.* **7** 1318–1322
- [167] Shi Kam N W, O’Connell M, Wisdom J A and Dai H 2005 Carbon nanotubes as multifunctional biological transporters and near-infrared agents for selective cancer cell destruction *Proc. Natl. Acad. Sci.* **102** 11600–5
- [168] Bae K H, Park M, Do M J, Lee N, Ryu J H, Kim G W, Kim C, Park T G and Hyeon T 2012 Chitosan oligosaccharide-stabilized ferrimagnetic iron oxide nanocubes for magnetically modulated cancer hyperthermia *ACS Nano* **6** 5266–73
- [169] Creixell M, Bohórquez A C, Torres-Lugo M and Rinaldi C 2011 EGFR-targeted magnetic nanoparticle heaters kill cancer cells without a perceptible temperature rise

- [170] Chu M, Shao Y, Peng J, Dai X, Li H, Wu Q and Shi D 2013 Near-infrared laser light mediated cancer therapy by photothermal effect of Fe<sub>3</sub>O<sub>4</sub>magnetic nanoparticles *Biomaterials* **34** 4078–88
- [171] Liang X, Li X, Yue X and Dai Z 2011 Conjugation of porphyrin to nanohybrid cerasomes for photodynamic diagnosis and therapy of cancer *Angew. Chemie - Int. Ed.* **50** 11622–7
- [172] Cheng Y, Samia A C, Meyers J D, Panagopoulos I, Fei B and Burda C 2008 Highly Efficient Drug Delivery with Gold Nanoparticle Vectors for in Vivo Photodynamic Therapy of Cancer *J Am Chem Soc.* **130** 10643–7
- [173] Nam J, Won N, Jin H, Chung H and Kim S 2009 pH-Induced Aggregation of Gold Nanoparticles for Photothermal Cancer Therapy *J. Am. Chem. Soc.* **131** 13639–13645
- [174] Chu M, Pan X, Zhang D, Wu Q, Peng J and Hai W 2012 The therapeutic efficacy of CdTe and CdSe quantum dots for photothermal cancer therapy *Biomaterials* **33** 7071–83
- [175] <https://www.drugs.com/monograph/paclitaxel.html>
- [176] Tao L, Jiang J, Gao Y, Wu C and Liu Y 2018 Biodegradable Alginate-Chitosan Hollow Nanospheres for Codelivery of Doxorubicin and Paclitaxel for the Effect of Human Lung Cancer A549 Cells *Biomed Res. Int.* **2018** 1–11
- [177] Lv S, Tang Z, Li M, Lin J, Song W, Liu H, Huang Y, Zhang Y and Chen X 2014 Co-delivery of doxorubicin and paclitaxel by PEG-polypeptide nanovehicle for the treatment of non-small cell lung cancer *Biomaterials* **35** 6118–29
- [178] Zhang F, Khan S, Li R, Smolen J A, Zhang S, Zhu G, Su L, Jahnke A A, Elsabahy M, Chen X and Wooley K L 2017 Design and development of multifunctional polyphosphoester-based nanoparticles for ultrahigh paclitaxel dual loading *Nanoscale* **9** 15773–7
- [179] Yao S, Li L, Su X, Wang K, Lu Z, Yuan C, Feng J and Yan S 2018 Development and evaluation of novel tumor-targeting paclitaxel-loaded nano- carriers for ovarian cancer treatment: in vitro and in vivo **37** 1–13
- [180] Li X, Xu H, Dai X, Zhu Z, Liu B and Lu X 2012 Enhanced in vitro and in vivo therapeutic efficacy of codrug-loaded nanoparticles against liver cancer *Int. J. Nanomedicine* **7** 5183–90
- [181] Rejinold N S, Han Y, Yoo J, Seok H Y, Park J H and Kim Y C 2018 Evaluation of cell penetrating peptide coated Mn:ZnS nanoparticles for paclitaxel delivery to cancer cells *Sci. Rep.* **8** 1–11
- [182] De Sousa Marcial S P, Carneiro G and Leite E A 2017 Lipid-based nanoparticles as drug delivery system for paclitaxel in breast cancer treatment *J. Nanoparticle Res.* **19** 1–11
- [183] Mo J, Wang L, Huang X, Lu B, Zou C, Wei L, Chu J, Eggers P K, Chen S, Raston C L, Wu J, Lim L Y and Zhao W 2017 Multifunctional nanoparticles for co-delivery of paclitaxel and carboplatin against ovarian cancer by inactivating the JMJD3-HER2 axis *Nanoscale* **9** 13142–52

- [184] Rosière R, Van Woensel M, Gelbcke M, Mathieu V, Hecq J, Mathivet T, Vermeersch M, Van Antwerpen P, Amighi K and Wauthoz N 2018 New Folate-Grafted Chitosan Derivative to Improve Delivery of Paclitaxel-Loaded Solid Lipid Nanoparticles for Lung Tumor Therapy by Inhalation *Mol. Pharm.* **15** 899–910
- [185] Liu Y, Huang L and Liu F 2010 Paclitaxel nanocrystals for overcoming multidrug resistance in cancer *Mol. Pharm.* **7** 863–9
- [186] Li X, Lu X, Xu H, Zhu Z, Yin H, Qian X, Li R, Jiang X and Liu B 2012 Paclitaxel / Tetrandrine Coloaded Nanoparticles Effectively Promote the Apoptosis of Gastric Cancer Cells Based on “ Oxidation Therapy ” *Am. Chem. Soc.* **9** 222–9
- [187] Jiang M, Zhang R, Wang Y, Jing W, Liu Y, Ma Y, Sun B, Wang M, Chen P, Liu H and He Z 2017 Reduction-sensitive Paclitaxel Prodrug Self-assembled Nanoparticles with Tetrandrine Effectively Promote Synergistic Therapy Against Drug-sensitive and Multidrug-resistant Breast Cancer *Mol. Pharm.* **14** 3628–35
- [188] Gao Mingji, Jin Guangming, Lin Kang, Liqing Chen Z and Huang W 2018 Smart polymeric nanoparticles with pH- responsive and PEG-detachable properties for co-delivering paclitaxel and survivin siRNA to enhance antitumor outcomes 2405–26
- [189] Ji X, Lv H, Guo J, Ding C and Luo X 2018 A DNA Nanotube–Peptide Biocomplex for mRNA Detection and Its Application in Cancer Diagnosis and Targeted Therapy *Chem. Eur.J.* **24** 10171–7
- [190] Gupta B, Poudel B K, Regmi S, Pathak S, Ruttala H B, Gautam M, An G J, Jeong J H, Choi H G, Yong C S and Kim J O 2018 Paclitaxel and Erlotinib-co-loaded Solid Lipid Core Nanocapsules: Assessment of Physicochemical Characteristics and Cytotoxicity in Non-small Cell Lung Cancer *Pharm. Res.* **35** 1–11
- [191] Ding T, Wang L, Zhang J, Xing Y and Cai K 2018 Interfacially active polydopamine for nanoparticle stabilized nanocapsules in a one-pot assembly strategy toward efficient drug delivery *J. Mater. Chem. B* **6** 1754–63
- [192] He J, Ai L, Liu X, Huang H, Li Y, Zhang M, Zhao Q, Wang X, Chen W and Gu H 2018 Plasmonic CuS nanodisk assembly based composite nanocapsules for NIR-laser-driven synergistic chemo-photothermal cancer therapy *J. Mater. Chem. B* **6** 1035–43
- [193] Koutsouki K, Angelopoulou A, Ioannou E, Voulgari E, Sergides A, Magoulas G E, Bakandritsos A and Avgoustakis K 2017 TAT Peptide-Conjugated Magnetic PLA-PEG Nanocapsules for the Targeted Delivery of Paclitaxel: In Vitro and Cell Studies *AAPS PharmSciTech* **18** 769–81
- [194] Wu D Y, Ma Y, Hou X S, Zhang W J, Wang P, Chen H, Li B, Zhang C and Ding Y 2017 Co-delivery of antineoplastic and protein drugs by chitosan nanocapsules for a collaborative tumor treatment *Carbohydr. Polym.* **157** 1470–8
- [195] Sun Y, Wang Q, Chen J, Liu L, Ding L, Shen M, Li J, Han B and Duan Y 2017 Temperature-sensitive gold nanoparticle-coated Pluronic-PLL nanoparticles for drug delivery and chemo-photothermal therapy *Theranostics* **7** 4424–44
- [196] Chung J E, Yokoyama M, Yamato M, Aoyagi T, Sakurai Y and Okano T 1999 Thermo-responsive drug delivery from polymeric micelles constructed using block copolymers of poly ( N -isopropylacrylamide ) and poly ( butylmethacrylate ) *J. Control. Release* **62** 115–27

- [197] WHO World Malar. Rep. December 2016 (<http://www.who.int/features/factfiles/malaria/en/>).
- [198] D. Boraschi, L. Costantino and P I 2012 Interaction of nanoparticles with immunocompetent cells: nanosafety considerations *Nanomedicine (London)* **7** 121–131
- [199] Bhardwaj V, Plumb J A, Cassidy J and Ravi Kumar M N V 2010 Evaluating the potential of polymer nanoparticles for oral delivery of paclitaxel in drug-resistant cancer *Cancer Nanotechnol.* **1** 29–34
- [200] Werner Stober A F 1968 Controlled Growth of Monodisperse Silica Spheres in the Micron Size Range 1 *J. Colloid Interface Sci.* **26** 62–9
- [201] Bassi A K, Gough J E, Zakikhani M and Downes S 2011 The Chemical and Physical Properties of Poly( $\epsilon$ -caprolactone) Scaffolds Functionalised with Poly(vinyl phosphonic acid-co-acrylic acid). *J. Tissue Eng.* **2011** 1–9
- [202] Paik P, Gedanken A and Mastai Y 2009 Mesoporous Spherical Silica Prepared by Templating of Chiral Block Copolymers *ACS Appl. Mater. Interfaces* **1** 1834–42
- [203] Hu H, Zhou H, Liang J, An L, Dai A, Li X, Yang H, Yang S and Wu H 2011 Facile synthesis of amino-functionalized hollow silica microspheres and their potential application for ultrasound imaging *J. Colloid Interface Sci.* **358** 392–8
- [204] È A B, Sirutkaitis V, È M K, Nas R J È and Kareiva A 2004 FTIR , TEM and NMR investigations of Stöber Silica Nanoparticles *Mater. Sci.* **10** 287–90
- [205] Agarwal S and Speyerer C 2010 Degradable blends of semi-crystalline and amorphous branched poly(caprolactone): Effect of microstructure on blend properties *Polymer (Guildf).* **51** 1024–32
- [206] She H, Xiao X and Liu R 2007 Preparation and characterization of polycaprolactone-chitosan composites for tissue engineering applications *J. Mater. Sci.* **42** 8113–9
- [207] Kumar V B, Medhi H, Yong Z and Paik P 2016 Designing idiosyncratic hmPCL-siRNA nanoformulated capsules for silencing and cancer therapy *Nanomedicine Nanotechnology, Biol. Med.* **12** 579–88
- [208] Romero-cano M S and Vincent B 2002 C ontrolled release of 4-nitroanisole from poly (lactic acid) nanoparticles **82** 127–35
- [209] Balas F, Manzano M, Horcajada P and Vallet-Regı M 2006 Confinement and Controlled Release of Bisphosphonates on Ordered Mesoporous Silica-Based Materials *J. AM. CHEM. SOC.* **128** 8116–7
- [210] Yec C C and Zeng H C 2014 Synthesis of complex nanomaterials via Ostwald ripening *J. Mater. Chem. A* **2** 4843–51
- [211] Wang D P and Zeng H C 2011 Creation of interior space, architecture of shell structure, and encapsulation of functional materials for mesoporous SiO<sub>2</sub>spheres *Chem. Mater.* **23** 4886–99
- [212] Mason T J 2000 Ultrasound in synthetic organic chemistry *Chem. Soc. Rev.* **26** 443–51
- [213] Sibü C P, Kumar S R, Mukundan P and Warriar K G K 2002 Structural modifications and associated properties of lanthanum oxide doped sol-gel nanosized titanium oxide *Chem. Mater.* **14** 2876–81

- [214] Maensiri S, Laokul P and Promarak V 2006 Synthesis and optical properties of nanocrystalline ZnO powders by a simple method using zinc acetate dihydrate and poly(vinyl pyrrolidone) *J. Cryst. Growth* **289** 102–6
- [215] Thirugnanam T 2013 Effect of polymers (PEG and PVP) on sol-gel synthesis of microsized zinc oxide *J. Nanomater.* **2013**
- [216] Saoud K, Alsoubaihi R, Bensalah N, Bora T, Bertino M and Dutta J 2015 Synthesis of supported silver nano-spheres on zinc oxide nanorods for visible light photocatalytic applications *Mater. Res. Bull.* **63** 134–40
- [217] Sáenz-Trevizo A, Amézaga-Madrida P, Pizá-Ruiza P, Antúnez-Flores W and Miki-Yoshida M 2016 Optical Band Gap Estimation of ZnO Nanorods *Mater. Res.* 1–6
- [218] Kumar V B, Kumar K, Gedanken A and Paik P 2014 Facile synthesis of self-assembled spherical and mesoporous dandelion capsules of ZnO: efficient carrier for DNA and anti-cancer drugs *J. Mater. Chem. B* **2** 3956–64
- [219] Seder R A and Paul W E 1994 -Acquisition Of Lymphokine- Producing Phenotype By Cd4<sup>+</sup> T Cells *Annu. Rev. Immunol.* 635–73
- [220] Singh Manmohan O D 1999 Advances in vaccine adjuvants *Nat. Biotechnol.* 1075–1081
- [221] Vigneshwaran N, Kumar S, Kathe A A, Varadarajan P V. and Prasad V 2006 Functional finishing of cotton fabrics using zinc oxide-soluble starch nanocomposites *Nanotechnology* 5087–95
- [222] Kimura T, Takabatake Y, Takahashi A and Isaka Y 2013 Chloroquine in cancer therapy: A double-edged sword of autophagy *Cancer Res.* **73** 3–7
- [223] Joshi P, Chakraborti S, Ramirez-Vick J E, Ansari Z A, Shanker V, Chakraborti P and Singh S P 2012 The anticancer activity of chloroquine-gold nanoparticles against MCF-7 breast cancer cells *Colloids Surfaces B Biointerfaces* **95** 195–200
- [224] Colombo C, Morosi L, Bello E, Ferrari R, Licandro S A, Lupi M, Ubezio P, Morbidelli M, Zucchetti M, DIncalci M, Moscatelli D and Frapolli R 2016 PEGylated Nanoparticles Obtained through Emulsion Polymerization as Paclitaxel Carriers *Mol. Pharm.* **13** 40–6
- [225] Handore K, Bhavsar S, Horne A, Chhattise P, Mohite K, Ambekar J, Pande N and Chabukswar V 2014 Novel Green Route of Synthesis of ZnO Nanoparticles by Using Natural Biodegradable Polymer and Its Application as a Catalyst for Oxidation of Aldehydes *J. Macromol. Sci. Part A* **51** 941–7
- [226] Mallakpour S and Madani M 2012 Use of silane coupling agent for surface modification of zinc oxide as inorganic filler and preparation of poly(amide-imide)/zinc oxide nanocomposite containing phenylalanine moieties *Bull. Mater. Sci.* **35** 333–9
- [227] Bisht G and Rayamajhi S 2016 ZnO Nanoparticles: A Promising Anticancer Agent *Nanobiomedicine* **3**